Spring 1996

Meandering and eddy formation in separating western boundary currents

Ilson Carlos Almeida da Silveira
University of New Hampshire, Durham

Recommended Citation

da Silveira, Ilson Carlos Almeida, "Meandering and eddy formation in separating western boundary currents" (1996). *Doctoral Dissertations*. 1887.
https://scholars.unh.edu/dissertation/1887

INFORMATION TO USERS

This manuscript has been reproduced from the microfilm master. UMI films the text directly from the original or copy submitted. Thus, some thesis and dissertation copies are in typewriter face, while others may be from any type of computer printer.

The quality of this reproduction is dependent upon the quality of the copy submitted. Broken or indistinct print, colored or poor quality illustrations and photographs, print bleedthrough, substandard margins, and improper alignment can adversely affect reproduction.

In the unlikely event that the author did not send UMI a complete manuscript and there are missing pages, these will be noted. Also, if unauthorized copyright material had to be removed, a note will indicate the deletion.

Oversize materials (e.g., maps, drawings, charts) are reproduced by sectioning the original, beginning at the upper left-hand corner and continuing from left to right in equal sections with small overlaps. Each original is also photographed in one exposure and is included in reduced form at the back of the book.

Photographs included in the original manuscript have been reproduced xerographically in this copy. Higher quality 6" x 9" black and white photographic prints are available for any photographs or illustrations appearing in this copy for an additional charge. Contact UMI directly to order.

UMI

A Bell & Howell Information Company
300 North Zeeb Road, Ann Arbor MI 48106-1346 USA
313/761-4700 800/521-0600

Reproduced with permission of the copyright owner. Further reproduction prohibited without permission.

MEANDERING AND EDDY FORMATION IN SEPARATING WESTERN BOUNDARY CURRENTS

BY

ILSON CARLOS ALMEIDA DA SILVEIRA

B. Sc., Universidade do Estado do Rio de Janeiro, 1984
M. Sc., Universidade de São Paulo, 1990

DISSERTATION

Submitted to the University of New Hampshire
in Partial Fulfillment of
the Requirements for the Degree of

Doctor of Philosophy
in
Earth Sciences: Oceanography

May, 1996

UMI Number: 9627154

UMI
300 North Zeeb Road
Ann Arbor, MI 48103

This dissertation has been examined and approved.

Wendell S. Brown

Dissertation Co-Director
Dr. Wendell S. Brown
Professor of Earth Sciences
and Earth, Oceans and Space
University of New Hampshire

Glenn R. Flierl

Dissertation Co-Director
Dr. Glenn R. Flierl
Professor of Physical Oceanography
Massachusetts Institute of Technology

Martin A. Lee

Dr. Martin A. Lee
Professor of Physics
and Earth, Oceans and Space
University of New Hampshire

John McHugh

Dr. John P. McHugh
Associate Professor of Mechanical Engineering
University of New Hampshire

Larry J. Pratt

Dr. Lawrence J. Pratt
Associate Scientist, Physical Oceanography
Woods Hole Oceanographic Institution

4/30/96

Date

DEDICATED TO THE MEMORY OF

Ilson da S. Almeida, my beloved grandfather,

AND

Magdalena E. Cataldo, my beloved grandaunt,

AND

M. Aparecida Magalhães, my nanny and very special friend.

Three people that I love and miss dearly and to whom, because of my stay in the U.S., I never got a chance to say goodbye.

Acknowledgements

There are no words adequate to express my gratitude to my wife, partner and best friend, Martha da Silveira. I could simply not have done it without her. Her unconditional love, constant support and permanent understanding carried me through these five years as a graduate student. This degree is as much hers as it is mine. I also thank my daughter Camila da Silveira for brightening my life and teaching me about feelings that I did not know existed.

I had the good fortune to have Wendell Brown and Glenn Flierl as advisors in this doctoral program. I thank Wendell for guiding me at both professional and personal levels. He taught me a good part of what I know about data analysis and supported all my initiatives as a student, even when they diverged from our lab's main research line. I am also indebted to Glenn, whom I met at the semester I spent at MIT as a special student. I thank him for teaching me most of the GFD I know, for the long hours we spent discussing my research, and for guiding me through the difficulties of theoretical modeling, always with patience and good humor. I will treasure the memories of our meetings at MIT and, in particular, our summer meetings at Back Bay station.

My heartfelt appreciation is extended to the other three members of my thesis committee: John McHugh, Marty Lee and Larry Pratt. I particularly thank Larry for his effort in commuting from WHOI to MIT and UNH on several occasions to meet me and discuss my work.

I also thank my "unofficial" committee members, David Meeker and Janet Campbell, for always being available to help me with math and statistics questions.

I want to thank my dear friend Frank Bub for the five years of daily insightful scientific discussions that we shared (share) as classmates and officemates. The first third of this dissertation was done with his strong support and encouragement. I extend my gratitude to his family, Susan and Kristen Bub, who have been friends of Martha and I since our first day in the U.S.

I also need to thank the OPAL staff, Mariellen Carpenter Lee, Karen Garrison, Russell Gelinas and especially, my friend Frank "Chico" Smith. Chico, who helped me with the editing of this dissertation and gave me hours of lessons in English writing, has become part of my family here in the U.S.

I deeply thank the "Conselho Nacional de Desenvolvimento Científico e Tecnológico – CNPq" for supporting my doctoral program for 4.5 years. I thank the Institute of Earth, Oceans and Space (EOS) of the University of New Hampshire for providing most of the additional funding I needed to complete my studies.

I thank my family in Brazil (Rio and Fortaleza) for the continuous support and love during these five years abroad. In particular, I thank my parents, Olga and Carlos Alberto da Silveira, for having taught me most of the values I use in my life. I hope to raise my daughter with the same standards.

Finally, I thank the Brazilian community at UNH for always providing a warm, and caring environment for my family throughout our stay in NH.

Contents

Dedication iii

Acknowledgments iv

List of Tables ix

List of Figures xi

Abstract xxi

1 Introduction **1**

1.1 Western Boundary Current Separation: The Atlantic Ocean Context 1

1.2 Previous Modeling Efforts 5

1.3 Overview of the Dissertation 11

References 14

2 The North Brazil Current Retroflection Region **17**

Abstract 17

2.1 Introduction 18

2.2 How useful is the Quasi-Geostrophic Approximation in the near-equatorial NBC Retroflection Region? 26

2.3 A Quasi-Geostrophic Modal Structure for the NBC 34

2.4 The NBC Retroflection Region as a Three-Layer, Quasi-Geostrophic Ocean 45

2.5 Summary and Conclusions 65

Appendix: The Three-Layer Calibration Scheme 67

References 69

3 **Dynamics of $1\frac{1}{2}$-Layer Separating Jets** **73**

Abstract 73

3.1 Introduction 74

3.2 The Model Formulation 79

3.2.1 The Symmetric Front Model 81

3.2.2 The Asymmetric Front Model 93

3.3 Numerical Experiments 98

3.3.1 The Symmetric Model Results 98

3.3.2 The Asymmetric Model Results 113

3.4 Applications 121

3.4.1 The Gulf Stream 123

3.4.2 The Brazil-Malvinas Confluence 125

3.4.3 The North Brazil Current 126

3.5 Summary and Conclusions 127

Appendix: The Linear Symmetric Model 129

References 138

4 **Eddy Formation in $2\frac{1}{2}$-Layer Jets** **141**

Abstract 141

4.1 Introduction 142

4.2 The $2\frac{1}{2}$-Layer Model Formulation 145

4.3 Infinite Jets 151

4.3.1 Linear Stability 152

4.3.2 The Nonlinear Model 153

4.3.3 Numerical Results 155

4.4 Separating Jets 175

4.4.1 The Symmetric Model 177

4.4.2 The Asymmetric Model 191
4.5 Summary and Conclusions 204
Appendix: Two-layer Separating Jets 208
References 218
Complete List of References **221**

List of Tables

2.1 The water mass layer structure used in the *Bub and Brown* [1996a] classification: rest thicknesses, standard deviations, and Rossby number estimates based on a normal distribution. 33

2.2 The first six deformation radii (in km) and the corresponding equivalent-depths (in m) for the WESTRAX average Brunt-Väisälä profile. The central latitude and ocean depth considered are respectively 5°N and 4000 m. 37

2.3 Root mean square differences for the optimal fits of QG dynamical modes onto the DEOF modes 1 and 2 41

2.4 The *Frantantoni et al.* [1995] model as six-layer, QG ocean: rest thicknesses, layered density values and the corresponding internal deformation radii 47

2.5 The *Bub and Brown* [1996a] model as six-layer, QG ocean: rest thicknesses, layered density values and the corresponding internal deformation radii 48

3.1 The model variable scales 80

3.2 Summary of numerical experiments with the symmetric model 99

3.3 Summary of numerical experiments with the asymmetric model . . . 114

3.4 Scales and nondimensional parameters for the three study cases . . . 122

4.1 Scales and corresponding nondimensional quantities 148

4.2 Experiment Set 1: $\delta = 1$, $R = 6.25$, $\mu = 2.21$ and $\epsilon = 1.28$ 157

4.3 Experiment Set 2: $\delta = 1$, $R = 6.25$, $\mu = 1.41$ and $\epsilon = 3.13$ 158

4.4 Experiment Set 3: $\delta = 0.2$, $R = 6.25$, $\mu = 5.0$ and $\epsilon = 1.25$ 163

4.5 Experiment Set 4: Symmetric Separating Jets ($\delta = 0.2$, $R = 6.25$, $\mu = 5.0$ and $\epsilon = 1.25$) 180

4.6 Experiment Set 5: Asymmetric Separating Jets ($\delta = 0.2$, $R = 6.25$, $\mu = 5.0$, $\bar{u}_2(\infty, 0) = -0.125$) 195

List of Figures

1.1 Schematic representation of surface current patterns for the Atlantic Ocean. The North Brazil Current retroflection region is shaded. From *Bub and Brown* [1996]. 2

1.2 Schematic representation of Gulf Stream ring formation based on satellite images. From *Richardson* [1980]. 4

1.3 The surface (a) temperature and (b) salinity signatures of the eddies in the Brazil-Malvinas Confluence (October 1984). From *Gordon* [1989]. 6

1.4 (a) Schematic representation of the North Brazil Current eddy-shedding; (b) meander growth and eddy-shedding on the North Brazil Current retroflection based on *Johns et al.* [1990] CZCS images. From *Richardson et al.* [1994]. 7

1.5 Current paths for different critical angles θ_c. Positive values for θ_c correspond to northeastward orientations of the coastline. Negative values for θ_c correspond to northwestward orientations of the coastline. From *Ou and De Ruijter* [1986]. 8

1.6 Stream function fields from *Cessi*'s [1991] quasi-geostrophic, barotropic, converging-jet model: (a) the maximum "asymmetry" case, where northern current transport is zero; (b) the "symmetric" case, with identical converging currents; and (c) an asymmetric case, with a stronger southern current and formation of a steady "boundary" eddy. 10

2.1 *Cochrane et al.*'s [1979] acceleration potentials, which correspond to dynamic heights on isosteric coordinates, at the 140 cl/t isosteric surface ($\approx$200 m) for: (a) late winter-early spring, and (b) late summer-early fall. 20

2.2 The "Western Tropical Atlantic Experiment (WESTRAX)" Pegasus/CTD stations during the four surveys. The thick line represents the actual shape of the 200-m isobath and the light gray shaded area, its rectilinear approximation. 23

2.3 *Bub and Brown*'s [1996b] average intermediate layer (150-1300 m) flow structure for the four WESTRAX cruises. The stream function fields were computed from observed velocities by the Pegasus profiler. 24

2.4 (a) The sample correlation function for the WX2 100-1200 db geostrophic stream function differences. The correlation length l_C is 411.5 km and the bandwidth truncation error $\mathcal{E}$ is 0.08. (b) The typical root mean square errors associated with the OA horizontally gridded fields, using the data of the stations displayed in Figure 2.2 and the OA parameters above. 30

2.5 Comparison between the 100-1200m (a) Pegasus stream function differences, and (b) geostrophic stream function differences for the WX2 survey. Contours in 1×10^5 m^2/s. 32

2.6 The departures δH_i from the rest thickness H_i for the *Bub and Brown* [1996a] surface layer (upper panel) and upper intermediate layer (lower panel). Contours in meters. 35

2.7 (a) The 10m-average Brunt-Väisälä frequency profile for the four WESTRAX surveys, (b) the vertical modal structure for the barotropic and first five baroclinic modes. 38

2.8 The vertical structure of the WX2 Depth Empirical Orthogonal Function (DEOF) modes 1 (left panel) and 2 (right panel). The dashed line represents the optimal fit of the first three dynamical modes on the DEOF modes. The *rms* difference values are indicated in the lower right corner of each panel. 40
2.9 The stream function amplitude functions Ψ_i for the first three dynamical modes (i=0, 1 and 2). Units: 1×10^5 m^2/s. 43
2.10 Comparison between the Pegasus-derived stream function (left panels) and the corresponding three-mode truncation at the levels: 50 m (upper), 350 m (middle), and 1000 m (lower). 44
2.11 (a) The calibrated WESTRAX density profile under the three-layer approximation, and (b) the corresponding three discrete dynamical modes. 50
2.12 The three-layer QG stream function fields for WX2 (left panels) and WX3 (right panels). Units: 1×10^5 m^2/s. 52
2.13 The three-layer QG potential vorticity fields for WX2 (left panels) and WX3 (right panels). Units $1\times10^{-5}/s$. 54
2.14 Meridional variation of the upper layer QG potential vorticity (solid line) along 44°W. The vorticity (dashed line), the stretching (dashed-dotted lines), and the "beta" (dotted line) terms are also represented. 55
2.15 The anomalous full potential vorticity fields for WX2 (left panels) and WX3 (right panels). Units: $1\times10^{-5}/s$. 58
2.16 Scattered plots between stream function and potential vorticity fields for the three layers in WX3. The correlation coefficients are indicated on the upper right corner of each panel. 59
2.17 Scattered plot between upper-layer stream function and surface temperature fields in WX3. The correlation coefficient is indicated on the upper right corner of the panel. 60

2.18 The WX2 interior stream function (top panels) and boundary stream function (bottom panels). Upper layer fields on the left, and middle layer fields on the right. 63

2.19 The WX2 interior stream function components. On the left panels: $\psi_{1(1)}$ (top), $\psi_{1(2)}$ (center), and $\psi_{1(3)}$ (bottom). On the right panels: $\psi_{2(1)}$ (top), $\psi_{2(2)}$ (center), and $\psi_{2(3)}$ (bottom). 64

3.1 Schematic separation of western boundary currents: (a) The Gulf Stream, and (b) the Brazil Current. 75

3.2 The model geometry. The model coordinate system is rotated by an angle θ relative to the "Earth" cartesian coordinates (x_e, y_e). 78

3.3 (a) The total potential vorticity field q for the symmetric model is composed of: (b) q_0, the part of the field associated with the "undisturbed" position $\bar{y}(x)$ of the front; and (c) q_1, part of the field associated with the deviations from the "undisturbed" field q_0. The arrows indicate the integration direction. 82

3.4 The "undisturbed" stream function ψ_0 solution for the symmetric model, in which: (a) $\theta = 0$, (b) $\theta = \pi/4$ and (c) $\theta = \pi/4$, a closeup of the region around the origin. Results are expressed in the model coordinates (x, y). The potential vorticity discontinuity is represented by a solid line, and the streamlines by dashed lines. 85

3.5 The results for the β-related stream function ψ_β: (a) $\theta = 0$, and (b) $\theta = \pi/4$. Results expressed in the model coordinates (x, y). 86

3.6 Physical processes involved in the evolution of a potential vorticity front: (a) advection of a passive front by the the background shear flow; (b) vortex induction mechanisms where the basic shear flow has been "turned off"; and (c) the *Pratt and Stern* [1986] balance which is a superposition of the effects in (a) and (b). The basic jet profile is represented by the dashed line 91

3.7 The dipole effect associated with the presence of a boundary in a anticyclonic anomaly. In an inviscid system, the zero normal flow condition at the boundary is satisfied by pairing of the vortex with its image. The net result is the movement of an anticyclonic anomaly along the boundary, toward larger y-values. The net motion is in the opposite direction for a cyclonic anomaly. 92

3.8 (a) The total potential vorticity field q for the asymmetric model is composed of: (b) q_0, the part of the field associated with the "undisturbed" position $\bar{y}(x)$ of the front; and (c) q_1, the part of the field associated with the deviations from the "undisturbed" field q_0 field. The arrows indicate the integration direction. 96

3.9 The "undisturbed" stream function ψ_0 solution for the asymmetric model ($\alpha = 0.65$), in which: (a) $\theta = 0$, and (b) $\theta = \pi/4$. Results are expressed in the model coordinates (x, y). The potential vorticity discontinuity is represented by a solid line, and the streamlines by dashed lines. 97

3.10 The "anomaly" model run, in which only vortex mechanisms are present, for: (a) $t = 0$, (b) $t = 4$, and (c) $t = 8$. 101

3.11 Symmetric model experiment with $\theta = 0$ and $\beta = 0$. Initial conditions given by Eq. (3.24) in main text with a disturbance amplitude of $A = 0.5$ (*Run s1*). The y-axis scale is amplified about four times relative to the x-axis scale. 102

3.12 Same as Figure 3.11, but using a disturbance amplitude of $A = 2$ (*Run s2*). The y-axis scale is amplified about four times relative to the x-axis scale. 104

3.13 Same as Figure 3.12, but using $\beta = 0.1$ (*Run s3*). The y-axis scale is amplified about four times relative to the x-axis scale. 105

3.14 Linearized phase speed for *Pratt and Stern*'s [1986] infinite jet, using: $\beta = 0$ (solid curve), and $\beta = 0.1$ (dashed curve). 109

3.15 Symmetric model experiment with $\theta = \pi/4$, $\beta = 0$ (*Run s8*) Initial conditions given by the shape of the streamline $\psi_0 = 0$. The y-axis scale is amplified about four times relative to the x-axis scale. 111

3.16 Same as Figure 3.15, but using $\beta = 0.1$ (*Run s9*). The y-axis scale is amplified about four times relative to the x-axis scale. 112

3.17 Asymmetric model experiment results with $\theta = 0$, $\beta = 0$ at $t = 100$ for: (a) $\alpha = 0.05$ (*Run a1*), (b) $\alpha = 0.22$ (*Run a2*), and (c) $\alpha = 0.65$ (*Run a3*). The y-axis scale is amplified about four times relative to the x-axis scale. 116

3.18 Position of the northernmost particle in the front at $t = 100$ as a function of the asymmetry parameter α for $\theta = 0$ (circled curve) and $\theta = \pi/4$ (starred curve). The black cross corresponds to the steady solution found at $\alpha = -0.38$. β is zero for all the simulations. 117

3.19 Asymmetric model experiment results with $\theta = \pi/4$, $\beta = 0$ at $t = 100$ for: (a) $\alpha = 0.05$ (*Run a4*), (b) $\alpha = -0.05$ (*Run a5*), (c) $\alpha = 0.22$ (*Run a6*), (d) $\alpha = -0.22$ (*Run a7*), (e) $\alpha = 0.65$ (*Run a8*) and (f) $\alpha = -0.65$ (*Run a9*).The y-axis scale is amplified about four times relative to the x-axis scale. 119

3.20 The steady state obtained for asymmetric model experiment *Run a10*, with $\theta = 0$, $\beta = 0$ and $\alpha = -0.38$. The y-axis scale is amplified about four times relative to the x-axis scale. 121

3.21 The boundary current applications: (a) the Gulf Stream case at $t = 100$ ($\theta = \pi/4$, $\beta = 0.014$, $\alpha = -0.55$); (b) the Brazil-Malvinas Confluence case at $t = 100$ ($\theta = \pi/6$ $\beta = 0.033$, $\alpha = 0.33$); and (c) the North Brazil Current case at $t = 40$ ($\theta = \pi/4$, $\beta = 0.348$, $\alpha = 0.3$). 124

A.1 The "mismatch" stream function $\hat{\psi}_{11}$ in the (x, ξ) space: (a) in the model domain, (b) along $\xi = 0$, and (c) its zonal gradient along $\xi = 0$. 132

A.2 Linear symmetric model experiment results at $t = 100$ for: (a) $\theta = 0$, $\beta = 0$ (*Run l1*), (b) $\theta = \frac{\pi}{4}$, $\beta = 0$ (*Run l2*), and (c)$\theta = \frac{\pi}{4}$, $\beta = 0.1$ (*Run l3*). The y-axis scale is amplified about four times relative to the x-axis scale. 137

4.1 The quasi-geostrophic $2\frac{1}{2}$-layer model. The western boundary is included in the semi-infinite jet models of Section 4.3. 146

4.2 Experiment Set 1 ($\delta = 1$, $R = 6.25$, $\mu = 2.21$, and $\epsilon = 1.28$)-linear model results. (a) Jet profiles: the lower layer jets (dashed curves), from left to right, correspond to $\bar{u}_2(0)$ = -1.0 (*Run j1*), -0.5 (*Run j2*), -0.25 (*Run j3*), 0.0 (*Run j4*), 0.1 (*Run j5*), and 0.25 (*Run j6*). The upper layer jets are very similar in all cases and the thick solid line should be regarded as an envelope enclosing all six profiles. (b) Growth rates corresponding to $\bar{u}_2(0)$ = -1.0 ('o' curve, *Run j1*), -0.5 ('+' curve, *Run j2*), -0.25 ('.-.' curve, *Run j3*), 0.0 ('–' curve, *Run j4*), 0.1 ('-' curve, *Run j5*), and 0.25 ('x' curve, *Run j6*). The thick solid line represents the growth rate for M91's two-layer model with $\delta = 1$ and $\bar{u}_2(0)$ = -1.0. 159

4.3 Experiment Set 2 ($\delta = 1$, $R = 6.25$, $\mu = 1.41$, and $\epsilon = 3.13$)-linear model results. (a) Jet profiles: the lower layer jets (dashed curves), from left to right, correspond to $\bar{u}_2(0)$ = -1.0 (*Run k1*), -0.35 (*Run k2*), -0.25 (*Run k3*), 0.0 (*Run k4*), 0.1 (*Run k5*). The upper layer jets are very similar in all cases and the thick solid line should be regarded as an envelope enclosing all five profiles. (b) Growth rates corresponding to $\bar{u}_2(0)$ = -1.0 ('o' curve, *Run k1*), -0.35 ('+' curve, *Run k2*), -0.25 ('.-.' curve, *Run k3*), 0.0 ('–' curve, *Run k4*), and 0.1 ('-' curve, *Run k5*). The thick solid line represents the growth rate for M91's two-layer model with $\delta = 1$ and $\bar{u}_2(0)$ = -1.0. 160

4.4 Experiment Set 3 ($\delta = 0.2$, $R = 6.25$, $\mu = 5.0$, and $\epsilon = 1.25$)-linear model results. (a) Jet profiles: the lower layer jets (dashed curves), from left to right, correspond to $\bar{u}_2(0)$ = -0.5 (*Run l1*), -0.125 (*Run l2*), and 0.0 (*Run l3*). From left to right, the upper layer jets (solid curves) also correspond to *Runs l1, l2* and *l3*. (b) Growth rates corresponding to $\bar{u}_2(0)$ = -0.5 ('o' curve, *Run l1*), -0.125 ('+' curve, *Run l2*), and 0.0 ('-' curve, *Run l3*). The thick solid line represents the growth rate for M91's two-layer model with $\delta = 0.2$ and $\bar{u}_2(0)$ = -0.2. 164

4.5 *Run j1*: (a) t=0, (b) t=10, (c) t=20 and (d) t=25. 167

4.6 *Run j4*: (a) t=0, (b) t=15, (c) t=30 and (d) t=50. 168

4.7 *Run j5*: (a) t=0, (b) t=25, (c) t=45, (d) t=60, and (d) 80. 169

4.8 *Run k4*: (a) t=0, (b) t=30, and (c) t=60. 171

4.9 *Run j6*: (a) t=0, (b) t=15, and (c) t=50. 172

4.10 *Run k6*: (a) t=0, (b) t=30, and (c) t=65. 174

4.11 *Run k7*: (a) t=0, (b) t=30, (c) 45 and (d) t=60. 176

4.12 *Run m1*: (a) t=0, (b) t=10, (c) t=15 and (d) t=20. 182

4.13 Phase speeds for the unstable waves of Experiment Set 3, corresponding to $\bar{u}_2(0)$ = -0.5 ('o' curve, *Run l1*), -0.125 ('+' curve, *Run l2*), and 0.0 ('-' curve, *Run l3*). 183

4.14 *Run m3*: (a) t=0, (b) t=10, (c) t=25 and (d) t=50. 184

4.15 *Run m4*: (a) t=0, (b) t=25, (c) t=45, and (d) t=60. 186

4.16 *Run m5*: (a) t=0, (b) t=25, and (c) t=65. 188

4.17 *Run m6*: (a) t=0, (b) t=30, (c) t=60 and (d) t=80. 189

4.18 *Farrell*'s [1982] pinch singularity method: the local envelope growth rate ν, corresponding to $\bar{u}_2(\infty,0)$ = -0.5 (thick curve, *Runs m1* and *m2*), -0.125 (solid curve, *Runs m3* and *m4*), and 0.0 (dashed curve, *Runs m5* and *m6*). 190

4.19 Background coastal current profiles as $y \rightarrow \infty$ (dashed line) and $y \rightarrow -\infty$ (solid line) for *Runs*: (a) *m3*, (b) *n1*, (c) *n2*, (d) *n3*, and (e) *n4*. Left (right) panels correspond to upper (lower) layer currents. . . 197

4.20 *Run n1*: (a) t=0, (b) t=15, (c) t=40 and (d) t=65. 198

4.21 *Run n2*: (a) t=0, (b) t=30, and (c) t=65. 200

4.22 *Run n3*: (a) t=0, (b) t=30, and (c) t=65. 201

4.23 *Run n4*: (a) t=0, (b) t=10, (c) t=25 and (d) t=65. 203

4.24 *Run n5*: (a) t=0, (b) t=10, and (c) t=45. 205

A.1 The *Meacham* [1991] double front, two-layer model- (a) Jet profiles: the lower layer jets (dashed curves), from left to right, correspond to $\bar{u}_2(0) = -\delta$ -1.0, -0.50, -0.33, -0.20, -0.125; the upper layer center jet $\bar{u}_1(0)$ is equal to 1.0 in all cases (solid curves). (b) Growth rates,corresponding to $\bar{u}_2(0) = -\delta$=-1.0 ('o' curve), -0.5 ('+' curve), -0.33 ('.-.' curve), -0.2 ('–' curve), and -0.125 ('-' curve). 211

A.2 The *Meacham* [1991] double front, two-layer model– phase speeds of unstable waves, corresponding to $\bar{u}_2(0) = -\delta$=-1.0 ('o' curve), -0.5 ('+' curve), -0.33 ('.-.' curve), -0.2 ('–' curve), and -0.125 ('-' curve). 212

A.3 *Run a1*: (a) t=10, (b) t=20, (c) t=50 and (d) t=90. 213
A.4 *Run a2*: (a) t=0, (b) t=40, (c) t=60, and (d) t=80. 214
A.5 *Run a3*: (a) t=0, (b) t=20, (c) t=40, and (d) t=100. 216
A.6 *Run a4*: (a) t=0, (b) t=40, and (c) t=50. 217

ABSTRACT

MEANDERING AND EDDY FORMATION IN SEPARATING WESTERN BOUNDARY CURRENTS

by

Ilson Carlos Almeida da Silveira

University of New Hampshire, May, 1996

The dynamics of meandering and eddy detachment in separating western boundary currents are explored by considering inviscid, quasi-geostrophic current systems with both data analysis and modeling.

In chapter two, hydrographic and velocity observations of the North Brazil Current (NBC) retroflection region during the 1990-1991 Western Tropical Atlantic Experiment are examined. A three-layer quasi-geostrophic approximation to the NBC region is built. Stream function and potential vorticity (PV) fields are presented. The upper and middle layer flows simulate the retroflection of the NBC waters at surface and subthermocline levels, respectively. The deepest layer is represented by a meandering weak southward flow that resembles the Deep Western Boundary Current. The participation of baroclinic instability in the NBC eddy-shedding is verified by isolating the effect of PV anomalies in each of the layers on each of the layers.

In chapter three, a $1\frac{1}{2}$ layer "contour dynamical" model of two converging western boundary currents that form a zonal jet is built. It is intended to investigate the role of the coastline tilt and transport asymmetry between the converging currents in meander formation. The respective effects of coastline tilt and coastal current asymmetry can reinforce or cancel each other. In the former case, a retroflection type of boundary current separation, as observed in the Brazil Current separation, is obtained. In the latter case, a much smoother separation results, as observed in the Gulf Stream.

In chapter four, a $2\frac{1}{2}$-layer "contour dynamical" model is built to investigate the role of baroclinic instability in forming eddies. The upper active layer flow structure is similar to that of the $1\frac{1}{2}$-layer model (chapter three). The lower active layer flow structure ranges from converging to diverging coastal current configurations. Unstable waves must either propagate westward or slowly in the eastward direction to allow coast/retroflection eddy formation. When retroflection eddies pinch off, both upper and lower layers present opposite-signed, closed, PV contours. This characterizes a dipolar vortex which can self-propagate away from the jet axis.

Chapter 1

Introduction

1.1 Western Boundary Current Separation: The Atlantic Ocean Context

The large-scale surface circulation of the ocean is characterized by the presence of wind-driven meridionally organized cells: the gyre system. It is well known that the currents at the western border of these gyres are more intense and faster than their counterparts at the eastern border. These are commonly referred to in the literature as the western boundary currents. In the case of the Atlantic Ocean (Figure 1.1), perhaps the two most renowned examples are the Gulf Stream and the Brazil Current (BC), which close the mid-latitude anticyclonic gyres of the northern and southern hemispheres, respectively.

Regions where these mid-latitude western boundary currents separate from continental coasts are generally associated with strong thermal fronts. These fronts usually represent a boundary between the warm waters of the subtropical gyre and the cold waters of the subpolar gyre. When low-latitude boundary currents separate, the thermal contrast is obviously smaller but still delimits the boundary between two gyres: the equatorial and the tropical (Figure 1.1). In the tropical Atlantic

Ocean, that is the case of the North Brazil Current (NBC).

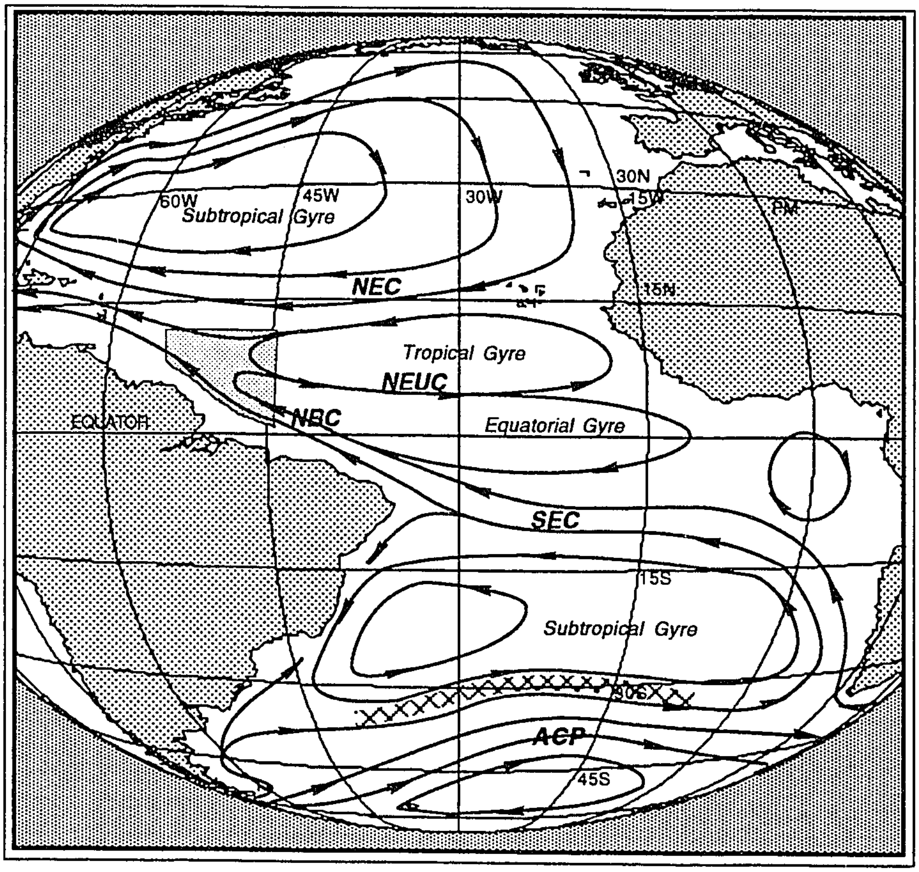

Figure 1.1: Schematic representation of surface current patterns for the Atlantic Ocean. The North Brazil Current retroflection region is shaded. From *Bub and Brown* [1996].

Fronts can become unstable, leading to meandering and eddy-shedding by western boundary currents. These phenomena occur in different ways, depending on how the boundary currents separate from the coast. For example, when the separation is smooth, the current tends to exhibit meanders that increase in amplitude toward the ocean interior. In this case, the eddies pinch off in the downstream region where the western boundary current extension may be regarded as a free jet. When the current overshoots its separation latitude and retroflects (i.e., turns back on itself), it forms a large amplitude lobe near the coast followed by meanders that decay downstream. Eddies then detach from the first or second meander closer to the coast.

At North Atlantic mid-latitudes, the Gulf Stream exhibits a smooth separation near Cape Hatteras, and the ring formation that results downstream in the western North Atlantic basin has been extensively studied, both experimentally and theoretically. *Richardson* [1993] summarized observational evidence about the Gulf Stream rings: they are mostly associated with the "necking off" of meanders and appear to occur randomly between 50° and 75°W (see Figure 1.2 for an example). The average Gulf Stream ring diameter is 150 km and, based on population estimates, there seems to be a ratio of approximately 2:1 in terms of cyclonic (cold core) and anticyclonic (warm core) ring formation.

At southern hemisphere mid-latitudes, the Brazil Current retroflects as it leaves the South American continental shelf break at around 36°S, closing the South Atlantic subtropical gyre. It separates at the point of convergence with the colder, subpolar Malvinas Current. Temporal and spatial variability of the Brazil-Malvinas Confluence (BMC) region and the associated eddy-shedding activity was investigated by *Garzoli and Garrafo* [1989] and *Olson et al.* [1989]. The former authors used inverted echo-sounder time series, while the latter examined satellite imagery and drifter data. Both studies seemed to indicate a 30-60 day pulsation of the Brazil-Malvinas front. Meander wavelengths were typically 400-500 km. The Brazil Current retroflection bulge periodically elongates southward and sheds large anticyclonic eddies in the subpolar gyre. Cyclonic eddies shed from the subsequent meander in the wave-like pattern were also reported by both works. The temperature and salinity signatures of the BMC eddy structure in 1984 was presented by *Gordon* [1989] (Figure 1.3), whose hydrographic surveys captured the BMC front shedding an anticyclone and resolved previously detached cyclones and anticyclones.

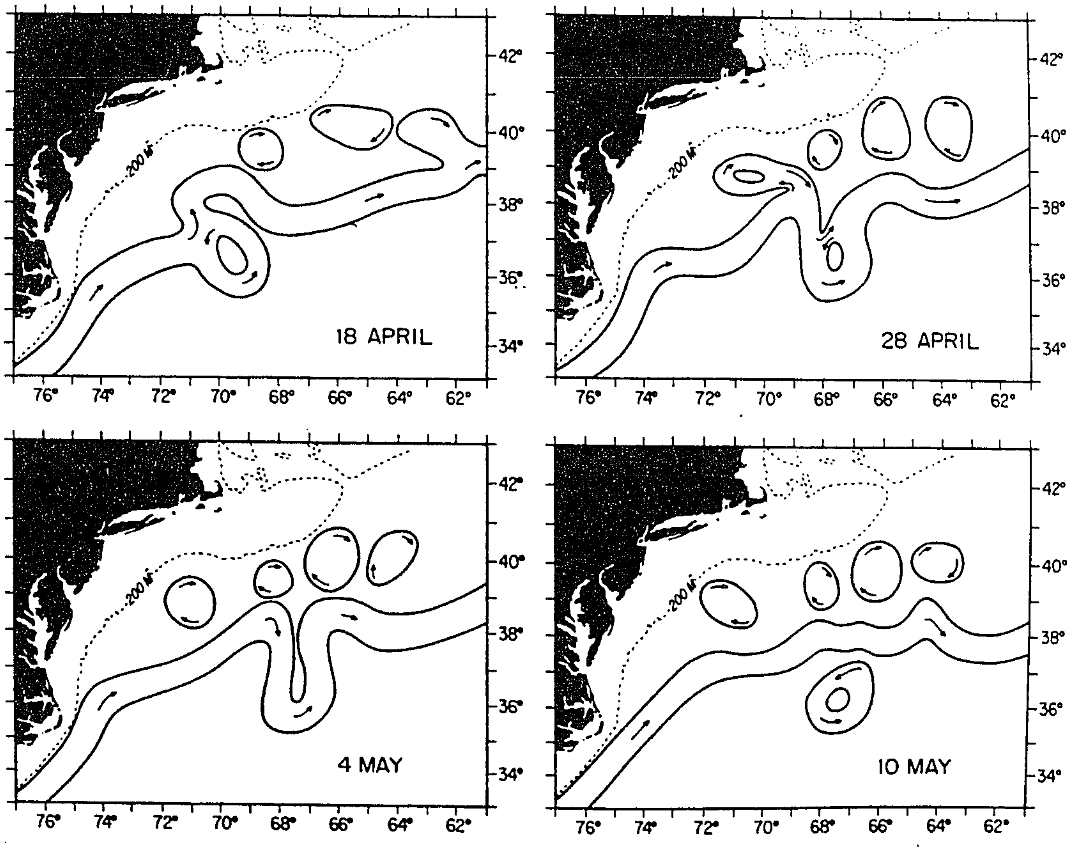

Figure 1.2: Schematic representation of Gulf Stream ring formation based on satellite images. From *Richardson* [1980].

As can be seen in Figure 1.3, ring diameters were about 200-300 km. There is no detailed information about the average annual BMC ring production in the literature. However, we speculate, based on *Gordon*'s [1989] and *Garzoli and Garrafo*'s [1989] findings, that the BMC eddy-shedding favors anticyclonic ring production by a factor of 3.

The NBC retroflection occurs at approximately 7°N. *Johns et al.* [1990] verified in their analysis of moored current meters and composite satellite images that large anticyclonic eddies are shed from the NBC retroflection bulge (Figure 1.4a). Observations show that these anticyclones are about 400km wide and 1300m deep [*Richardson et al.*, 1994; *Bub and Brown*, 1996]. The temporal evolution of the NBC eddy-shedding as depicted from satellite imagery [*Johns et al.*, 1990; *Didden and Schott*, 1993] seemed to be similar to the BMC anticyclone shedding (Figure 1.4b). Marked by a robust seasonal cycle, the NBC retroflection in the surface layers is significantly diminished during March-June. Only during this period, weak cyclonic eddies were observed to form in this region [*Didden and Schott*, 1993]. Meanders in the eastward-flowing North Equatorial Countercurrent (NECC), which is fed by the NBC retroflection, are somewhat larger than for the BMC case: 600-900km long [*Richardson and Reverdin*, 1987; *McClean and Klinck*, 1995]. The NBC ring production estimated by *Fratantoni et al.* [1995] using observations and numerical simulations is 1-3 anticyclones/year.

1.2 Previous Modeling Efforts

Several idealized physical models have been developed to explain why there are distinct separation patterns/eddy formation scenarios among western boundary currents. For example, *Ou and De Ruijter* [1986] reproduced both types of boundary current separation using a steady, inviscid, semi-geostrophic, $1\frac{1}{2}$-layer model that employed only current inertia and the variation of the Coriolis parameter in

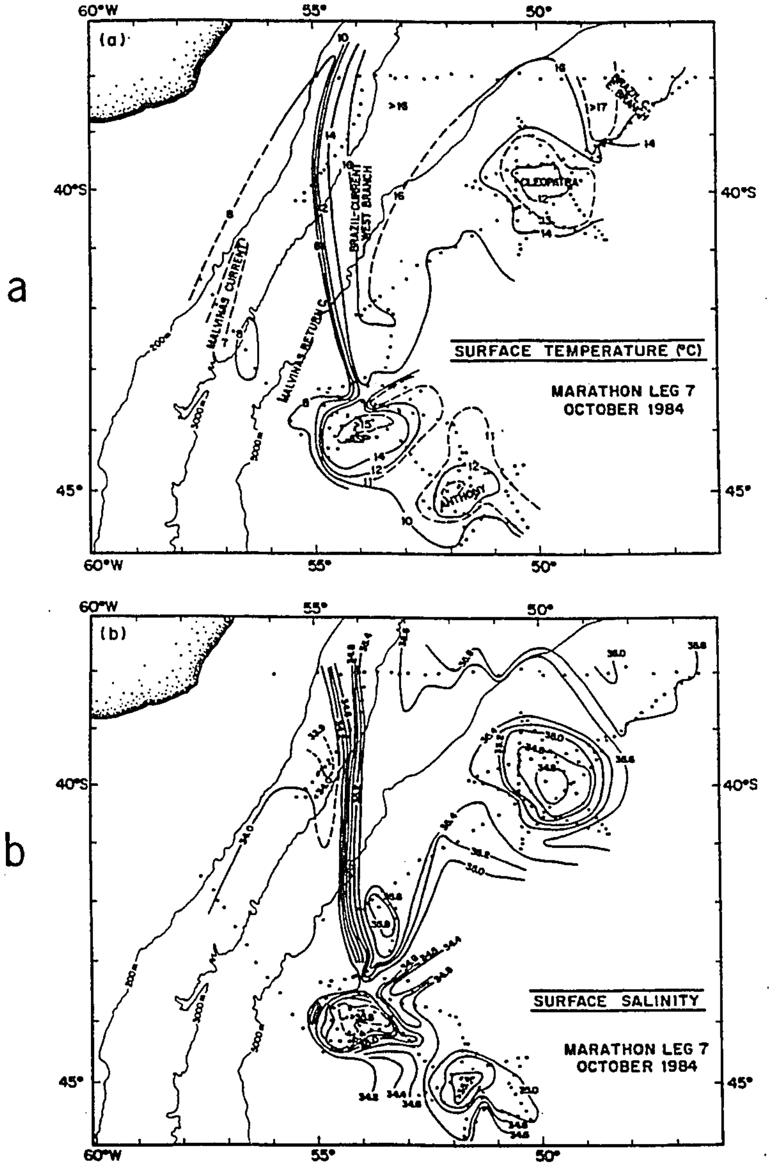

Figure 1.3: The surface (a) temperature and (b) salinity signatures of the eddies in the Brazil-Malvinas Confluence (October 1984). From *Gordon* [1989].

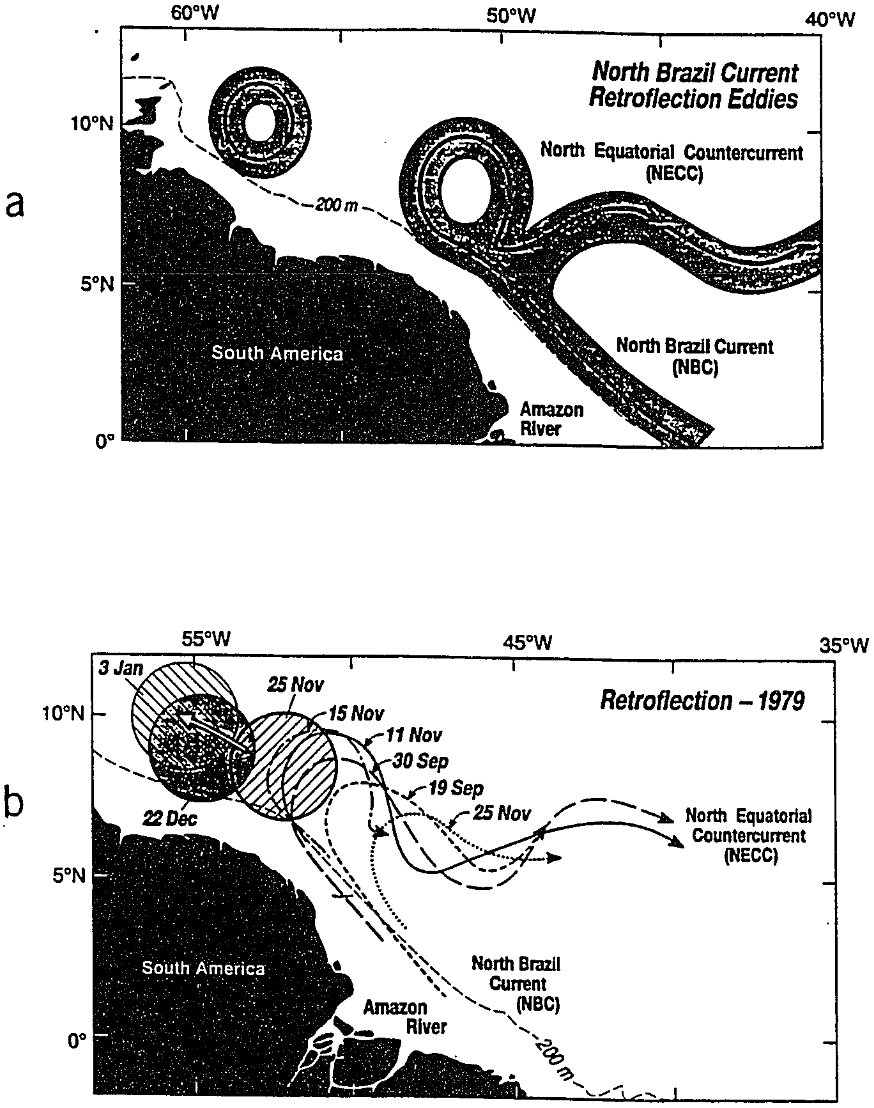

Figure 1.4: (a) Schematic representation of the North Brazil Current eddy-shedding; (b) meander growth and eddy-shedding on the North Brazil Current retroflection based on *Johns et al.* [1990] CZCS images. From *Richardson et al.* [1994].

a constant potential vorticity field. The structure by which the current left the coast was governed by the current volume transport and the coastline angle relative to the north-south direction. The former dictated the separation latitude; the latter dictated the type of separation. As Figure 1.5 shows, when the coast was oriented in the northwestward-southeastward direction ($\theta_c < 0$), the boundary currents retroflected (as do the BMC and NBC). When the coast was oriented in the northeastward-southwestward direction ($\theta_c > 0$), the boundary current underwent a smooth separation with long standing-wave patterns in the ocean interior (as in the Gulf Stream).

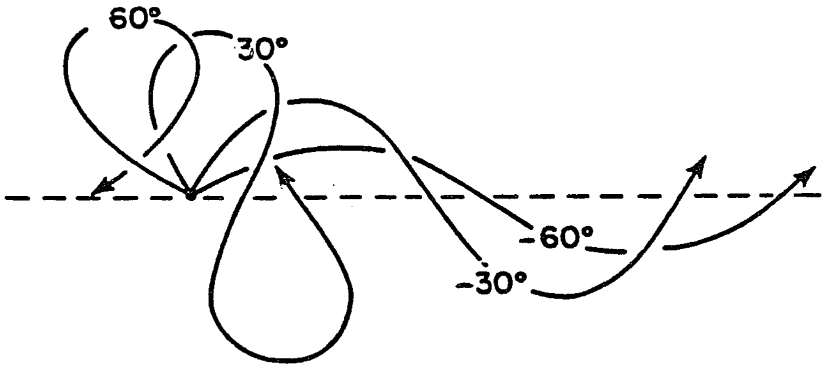

Figure 1.5: Current paths for different critical angles θ_c. Positive values for θ_c correspond to northeastward orientations of the coastline. Negative values for θ_c correspond to northwestward orientations of the coastline. From *Ou and De Ruijter* [1986].

Cessi [1993] in her steady, viscous, quasi-geostrophic barotropic model on a beta-plane assumed that the western boundary current separation was a natural consequence of the convergence of two asymmetric boundary currents. Considering a rectangular basin and a meridional western boundary, *Cessi*'s [1993] results can be summarized as follows. For the extreme case of highly asymmetric converging boundary currents (i.e., single intense current coming from the south and stagnant water in the north of the model domain), the flow overshot the latitude of the eastward interior flow and a damped Rossby wave pattern was formed (Figure 1.6a). For the case of two symmetric converging boundary currents, two large recirculation gyres were obtained (Figure 1.6b). For the intermediate cases between the extremes described above, a damped wave pattern was also obtained but a boundary (or retroflection) eddy was formed (Figure 1.6c).

Models with more vertical structure were used to investigate baroclinic effects in boundary current dynamics. Among those, *Campos and Olson*'s [1991] two-layer model is relevant to retroflecting boundary currents, in particular, the BMC case. These authors used the Miami isopycnic coordinate model forced by steady, meridionally sinusoidal winds. Their model domain was a closed basin with a tilted western boundary which was intended to simulate the orientation of the South American coastline. Their experiments showed that eddies were shed from the first two meanders and released into the subpolar and subtropical gyres, in agreement with the BMC region observations. In this case, the eddies detached at intervals of about 250 days. The authors then speculated that the eddy formation and detachment occurred due to combined barotropic/baroclinic instability.

The models discussed above answered some basic questions about the dynamics of separating western boundary currents. However, steady-state models obviously exclude the transient (or the time-dependent) part of the problem. In more complex numerical models, it becomes difficult to isolate and understand the dynamical processes involved in the temporal evolution of the current system. Hence, it is still necessary to address questions like: how do the meanders in the (spatially) quasi-stationary pattern grow in separating western boundary currents? How does the eddy detachment occur? What are the mechanisms by which the eddy propagates away from the main current axis? As we shall see summarized in the next section and described in the following chapters, this dissertation aims to answer these questions

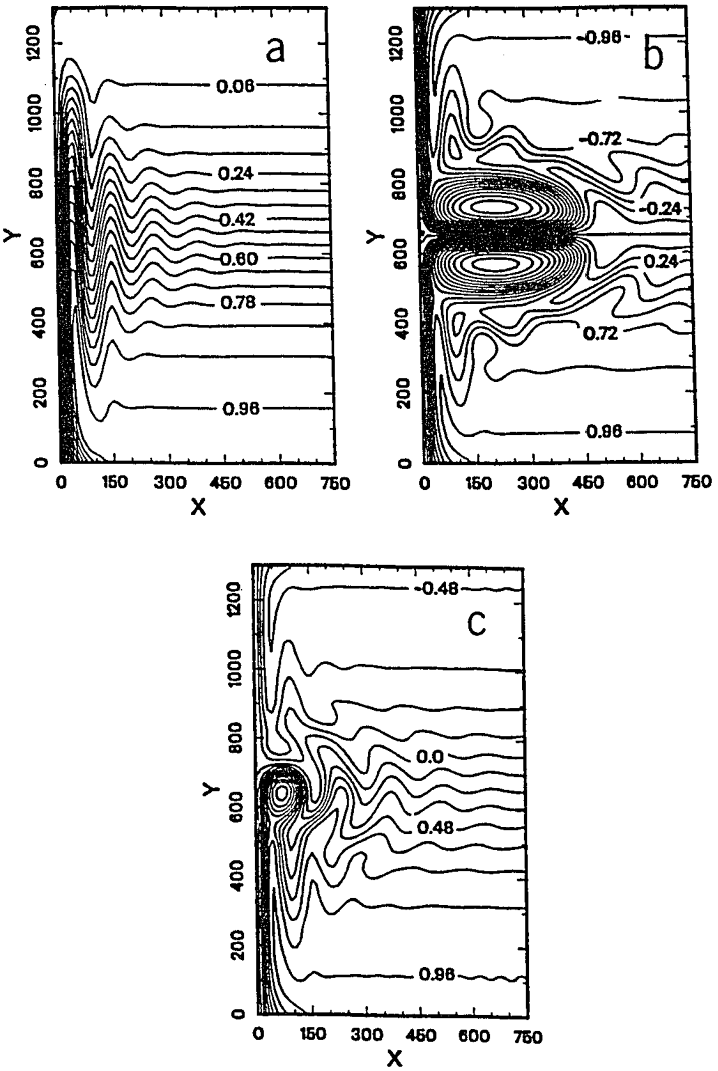

Figure 1.6: Stream function fields from *Cessi*'s [1991] quasi-geostrophic, barotropic, converging-jet model: (a) the maximum "asymmetry" case, where northern current transport is zero; (b) the "symmetric" case, with identical converging currents; and (c) an asymmetric case, with a stronger southern current and formation of a steady "boundary" eddy.

using both information obtained from data analysis and experimentation with simple time-dependent, idealized dynamic models.

1.3 Overview of the Dissertation

In this dissertation research, the dynamics of meandering and eddy formation in separating boundary currents is explored with both data analysis and modeling. Inviscid quasi-geostrophic theory is employed in both approaches. The invertibility principle – the linear relationship between quasi-geostrophic (QG) potential vorticity (PV) and streamfunction to recover the flow field from PV fields and vice-versa [*Hoskins et al.*, 1985]– is applied throughout this work.

The dissertation research is presented in the context of three self-contained papers, each a chapter. Thus, each chapter contains its own abstract, introduction, methodology, conclusions, appendices, and reference list. Some overlapping and cross-referencing among the chapters are to be expected because of this dissertation format. A complete list of references is included at the end of the dissertation.

In Chapter 2, the dynamical structure of the NBC, one of the Atlantic separating boundary current systems is examined. Dynamical information of about the NBC retroflection region is extracted from the Western Tropical Atlantic Experiment (WESTRAX) hydrographic and Pegasus velocity observations. After verifying that the NBC retroflection region complies with the basic assumptions of the QG theory, the observed NBC structure is decomposed into dynamical modes. It is found that only three modes account for most of the NBC structure. This result forms the basis for a three-layer approximation of the NBC system. A calibration scheme, based on *Flierl's* [1978] method, is employed to match the deformation radii of the continuously stratified ocean with its three-layer approximation. Three-layer streamfunction and potential vorticity fields are presented. Since the relationship between streamfunction and PV is linear in each layer, the superposition principle is valid. In other words, the dynamical fields can be partitioned into simpler relationships which when added represent the total dynamical solution. The invertibility principle then also applies to each of these simpler systems individually [*Davis and Emanuel*, 1991]. Thus, it is possible through the superposition-invertibility principles to isolate the effect of PV anomalies in each of the layers on each of the layers. This set of calculations is done to check the possibility of baroclinic instability as one mechanism leading to meander growth and eddy-shedding in the NBC region.

Chapter 3 addresses the issues raised by *Ou and De Ruijter* [1986] and *Cessi* [1993] regarding the role of the coastline tilt and asymmetry in current transport on meander formation of separating western boundary currents. In order to do that, *Pratt and Stern*'s [1986] "contour dynamical," $1\frac{1}{2}$-layer, infinite jet model is connected to the western boundary by a system of two converging boundary currents. The contour dynamics technique is also based on conservation of potential vorticity. The kernel of the contour dynamics technique is that the PV field is made piecewise constant, and thus, the dynamics is concentrated at the discontinuities (i.e., PV contours or fronts). The invertibility principle is then used to recover the velocities from the contour shape at each time step. Several initial value problems are solved by varying the relative strengths of the coastal jets and allowing the coastline to be tilted relative to the north-south orientation. Only configurations with one potential vorticity front are examined. The issue of how to handle the beta-effect in a piecewise constant potential vorticity field is raised in this chapter. Basically, the *Yano and Flierl* [1992] method of adding a zero potential vorticity field to the model is employed. Thus, in the presence of the western boundary, the β-term is compensated by a flow structure that resembles the diverging edge between two inertial gyres. Of course, with this approach, Rossby waves are not possible, but a steady westward tendency is introduced in the ocean interior. At the end of this chapter, the model is applied to the three Atlantic western boundary current examples mentioned in Section 1.1: the Gulf Stream, the BMC, and the NBC.

Chapter 4 investigates the role of baroclinic instability in the formation of eddies in separating boundary currents. The contour dynamics technique is used with a $2\frac{1}{2}$-layer, f-plane model. This model contains one potential vorticity front in each of the upper two (active) layers. The *Flierl and Meacham* [1995] multi-layer contour dynamics method is used to build both linear and nonlinear versions of the model. The linear model is used to determine the basic jet profiles, growth rates, phase speeds and group velocities. The nonlinear model is used to solve initial values problems. That is, the nonlinear evolution of the dynamical system is explored given a certain initial condition. The imposed flow structures in the upper layer are similar to those used in the $1\frac{1}{2}$-layer model: two converging boundary currents that form an eastward inertial jet. The imposed flow structures in the lower layer range from diverging to converging boundary currents. Asymmetric boundary current systems and the tilted western boundary effect are also studied in this baroclinic configuration. The ocean interior, where the $2\frac{1}{2}$-layer jets can be regarded as free jets, is also analyzed.

References

Bub, F.L. and W.S. Brown, Intermediate layer water masses in the Western Tropical Atlantic Ocean, *accepted for publication in J. Geophys. Res.*, 1996.

Campos, E.J.D., and D.B. Olson, stationary Rossby waves in western boundary current extensions, *J. Phys. Oceanogr., 21,* 1202-1224, 1991.

Cessi, P., Laminar separation of colliding western boundary currents, *J. Mar. Res., 49*, 697-717, 1991.

Davis, C.A. and K.A. Emanuel, Potential vorticity diagnostics of cyclogenesis, *Mon. Wea. Rev., 119(8),* 1929-1953, 1991.

Didden, N., and F. Schott, Eddies in the North Brazil Current retroflection region observed by Geosat altimetry, *J. Geophys. Res., 98*, 20121-02131, 1993.

Flierl, G.R., Models of vertical structure and the calibration of two-layer models, *Dyn. Atm. Oceans., 2*, 341-381, 1978.

Flierl, G.R., and S.P. Meacham, Instabilities and waves on thin jets, (submitted to *J. Phys. Oceanogr.*)

Fratantoni, D.M., W.E. Johns and T.L. Townsend, Rings of the North Brazil Currents: Their structure and behavior inferred from observations and a numerical simulation, *J. Geophys. Res., 100(C6)*, 10633-10654, 1995.

Garzoli, S.L. and Z. Garrafo, Transports, frontal motions and eddies at the Brazil-Malvinas currents confluence, *Deep-Sea Res., 36(5),* 681-702, 1989.

Gordon, A. L., Brazil-Malvinas Confluence–1984, *Deep-Sea Res., 36(3),* 359-384, 1989.

Hoskins, B.J., M.E. McIntyre, and A. W. Roberson, On the use and significance of isentropic potential vorticity maps, *Quart. J. R. Met. Soc., 111,* 877-946, 1985.

Johns, W.E., T.N. Lee, F. Schott, R. Zantopp and R.H. Evans, The North Brazil Current retroflection: seasonal structure and Eddy Variability, *J. Phys. Oceanogr., 95 (C12),* 22103-22120, 1990.

McClean, J.L. and J.M. Klinck, Description and Vorticity Analysis of the 50-day Oscillations in the Western Tropical Atlantic Region of the CME Model, *J. Phys. Oceanogr., 25,* 2498-2517.

Olson, D., G. Podesta, R. Evans and O. Brown, Temporal variations in the separation of Brazil and Malvinas currents, *Deep-Sea Res., 35,* 1971-1980, 1988.

Ou, H. W., and W. P. M. De Ruijter, Separation of an inertial boundary current from a curved coastline, *J. Phys. Oceanogr., 16,* 280-289, 1986.

Pratt, L.J., and M. E. Stern, Dynamics of potential vorticity fronts and eddy detachment, *J. Phys. Oceanogr., 16,*, 1101-1120, 1986.

Richardson, P.L., Gulf Stream ring trajectories, *J. Phys. Oceanogr., 10,* 90-104, 1980.

Richardson, P.L., Tracking Ocean Eddies, *American Scientist, 81,* 261-271, 1993.

Richardson, P.L., and G. Reverdin, Seasonal cycle of velocity in the Atlantic North Equatorial Countercurrent as measured by surface drifters, current meters, and ship drifts, *J. Geophys. Res., 92,* 3691-3708, 1986.

Richardson, P.L., G.E. Hufford, R. Limeburner, and W.S. Brown, North Brazil Current retroflection eddies, *J. Geophys. Res., 99 (C3),* 5081-5093, 1994.

Yano, J.-I., and G. R. Flierl, Isolated potential vorticity patches in quasi-geostrophic zonal shear flows, *Dynam. Atmos. Oceans, 16*, 439-472, 1992.

Chapter 2

The North Brazil Current Retroflection Region

Abstract

Hydrographic and velocity observations of the North Brazil Current (NBC) retroflection region during the 1990-1991 Western Tropical Atlantic Experiment (WESTRAX) are examined with the intent of extracting dynamical information about the NBC eddy-shedding. The NBC separation region, although tropical, complies with the basic quasi-geostrophic assumptions when a β-plane centered at 5°N is considered. The typical Rossby number for the WESTRAX-sampled area is 0.35. A comparison between Depth Empirical Orthogonal Function modes and the quasi-geostrophic dynamical modes indicates that about 90% of the variance of the vertical structure is explained by the barotropic and first two baroclinic modes. The first baroclinic mode dominates the NBC structure. Based on this result, a three-layer quasi-geostrophic approximation of the NBC region is built. The density values within each layer are carefully chosen to reproduce the deformation radii of the continuously stratified ocean. Stream function and potential vorticity (PV) fields are presented. In terms of flow structure, the upper layer simulates the retroflection

of the surface layers of the NBC to form the the North Equatorial Countercurrent (NECC). The intermediate layer simulates the separating subthermocline waters of the NBC to form the North Equatorial Undercurrent (NEUC). The deepest layer simulates a weak meandering southward flow that resembles the Deep Western Boundary Current (DWBC). In terms of PV, a well-defined PV front separates the NBC waters from the North Equatorial Current (NEC) in the upper layer. Both upper and middle layers exhibit closed PV contours associated with the eddy which is in the process of pinching off from the retroflecting NBC. The necessary conditions for instability based on the *Arnol'd* [1966] theorem for curved flows are satisfied in the three-layer model. Hence, by isolating the effect of PV anomalies in each of the layers on each of the layers, we verify that baroclinic interactions are a participating mechanism in the NBC eddy-shedding phenomenon.

2.1 Introduction

Cochrane et al. [1979] used geostrophic calculations to define the North Brazil Current (NBC) retroflection in terms of two anticyclonic vortices at subthermocline depths (Figure 2.1); one centered at about 3°-5°N, and other at about 7°-9°N. They named the southernmost eddy named the "Amazon" eddy because of its proximity to the mouth of the Amazon river (Figure 2.1). Cochrane and his collaborators were also the first to link the NBC retroflection flow around the southern anticyclone (at about 3°-5°N) to the eastward undercurrent now known as the North Equatorial Undercurrent (NEUC) [*Molinari et al.*, 1981]. The northern anticyclone was named the "Demerara" eddy by *Bruce* [1984] and *Bruce and Kerling* [1984], who thought that both anticyclones were semi-permanent. The latter, using earlier hydrographic surveys of the region (from 1964 and 1968) and two AXBT studies from March and September 1983, found that these eddies had a vertical extension of at least 500 m and were mainly composed of mixed layer and upper thermocline water, being larger, deeper and in the summer-fall period.

While the thermocline-subthermocline depth location of the NBC retroflection appears to be permanent (with a seasonally varying transport), the near-surface circulation is found to have a robust seasonal cycle. *Richardson and Mckee* [1984] used ship drift information to describe the seasonal cycle in the NBC retroflection surface flow. Their work showed that the upper layers of the NBC feed the North Equatorial Countercurrent (NECC) in the summer-fall period. The winter-spring ship drifts implied currents were less intense, with the major part of the NBC continuing to flow along the coast toward the Caribbean. *Arnault* [1987] showed that the ship drift surface flow patterns corresponded very closely to the estimates of the sum of geostrophic and Ekman velocities in the tropical Atlantic.

Johns et al. [1990] analysis of moored current meters and composite satellite images of the NBC retroflection region revealed a semi-periodic eddy-shedding by the NBC during the "near-surface retroflection" season (July-January) was responsible for the feature termed the "hydrographic" Demerara eddy. Their analysis provided convincing evidence that eddies were pinching off from the NBC retroflection. These "retroflection" eddies had a coherent vertical structure that extended from the surface to 900 meters depth. The *Johns at al.* [1990] current meter data exhibited an 50-day oscillatory behavior even when the surface retroflection was absent. They speculated that the eddy-shedding is modulated by short first mode baroclinic Rossby waves of the same frequency and probably generated by shearing instability in the ocean interior.

Didden and Schott [1992] estimated, by comparing GEOSAT-derived geostrophic velocities to results from simulations by the "WOCE community model–CME" [*Schott and Böning*, 1991], that the NBC retroflection region flow structure was about 80% geostrophic. *Didden and Schott* [1993] analyzed sea surface height anomaly maps obtained from GEOSAT altimetry to track the NBC retroflection eddies. These authors estimated that the average eddy radius was 200 km and were

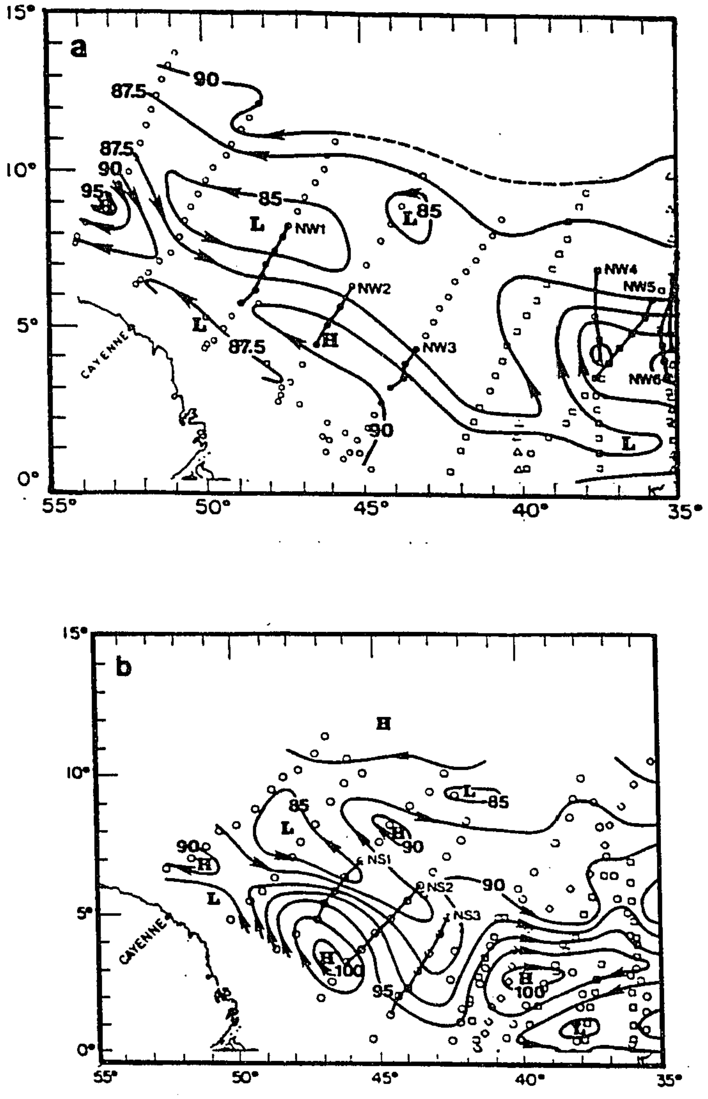

Figure 2.1: *Cochrane et al.*'s [1979] acceleration potentials, which correspond to dynamic heights on isosteric coordinates, at the 140 cl/t isosteric surface (≈200 m) for: (a) late winter-early spring, and (b) late summer-early fall.

able to track the anticyclones up to a distance of 1000 km from the NBC retroflection. However, their GEOSAT-derived (geostrophic) eddy velocities represented only 50% of those from *Johns at al.*'s [1990] moored current meters. *Didden and Schott* [1993] attributed the discrepancy to the combined effect of GEOSAT track filtering, objective mapping and ageostrophic velocities.

Richardson et al.'s [1994] analysis of surface drifters and SOFAR floats at 900 m during 1989-1992 also revealed five retroflection eddies. They found that the eddies had mean widths of 250 at the surface and 140 km at 900 m. Two very important findings of their work were that: (1) the eddy-shedding season is longer than previously thought (i.e., July-January), i.e., extends from August to April, and (2) the Guiana Current (GC) is dominated by these retroflection eddies during July-December. They speculated that the GC might just be composed of a series of eddies. *Richardson et al.* [1994] also corroborated the *Johns et al.* [1990] findings that the NBC retroflection pulsation and eddy-shedding modulation are triggered by the 50-day waves.

Fratantoni et al. [1995] simulated the generation of the NBC retroflection eddies with the U.S. Navy nonlinear, primitive equation, layered ocean model forced by climatological winds and a prescribed thermohaline meridional overturning cell (MOC). These authors verified that at least 2-3 rings per year separated from the modeled NBC. Because the model failed to shed eddies in the absence of an imposed MOC, *Fratantoni et al.* [1995] suggested that there was a causal relationship between the NBC ring formation and the MOC. After re-examining the *Johns et al.* [1990] current meter data set and the modeled eddies, they concluded that the NBC eddies were as geostrophic as the Gulf Stream eddies.

McClean and Klinck [1995] offered an explanation of the 50-day wave background in the NBC retroflection region. Their vorticity analysis on numerical simulations by the CME showed that the dominant terms are in quasi-geostrophic (QG) balance. Their reconstructed QG modal velocities helped verify that the 50-day waves were first and second baroclinic Rossby waves. Their study suggested that it was the retroflecting NBC which produced this Rossby wave pattern that slowly propagates eastward via the NECC to 35°W, where it dissipates.

The Western Tropical Atlantic Experiment (WESTRAX) synoptic data set provided a unique opportunity to reconcile geostrophically-derived information about the NBC retroflection region with the direct velocity measurements. As described by *Brown et al.* [1992], the WESTRAX observational program consisted of five ship surveys with simultaneous CTD/O_2, XBT, Acoustic Doppler Current Profiler and Pegasus Current Profiler measurements (Figure 2.2).

Bub and Brown's [1996a] analysis of the synoptic WESTRAX data set led to a water mass classification consistent with the observed hydrography and Pegasus velocity measurements (Figure 2.3). The stream function fields, which *Bub and Brown* [1996b] derived from the Pegasus velocities, confirmed the basic flow patterns for the region depicted by *Cochrane et al.* [1979] and *Bruce* [1984].

Bub and Brown [1996a, 1996b] found a 1km vertical extent of the retroflection eddies and presented synoptic pictures of the NBC retroflection at different stages of the eddy-shedding process. For example, both the winter 1990 (WX1, Figure 2.3a) and 1991 (WX3, Figure 2.3c) surveys documented eddies which had already pinched off from the NBC retroflection. The fall 1990 survey (WX2, Figure 2.3b) captured an unstable NBC retroflection in the midst of shedding an eddy. The WX4 survey (summer of 1991, Figure 2.3d) shows an inconclusive picture: although the NBC is apparently shedding an eddy, the cruise period is at the beginning of the "eddy-shedding season", and the weak anticyclone feature depicted in *Bub and Brown*'s [1996b] stream function maps could have been part of a finite amplitude 50-day Rossby wave or its accompanying anticyclones (as speculated by *Johns et al.* [1990] and *Richardson et al.* [1994]).

So while the NBC eddy-shedding process has been documented, there is little if any understanding of the eddy detachment process nor its periodic modu-

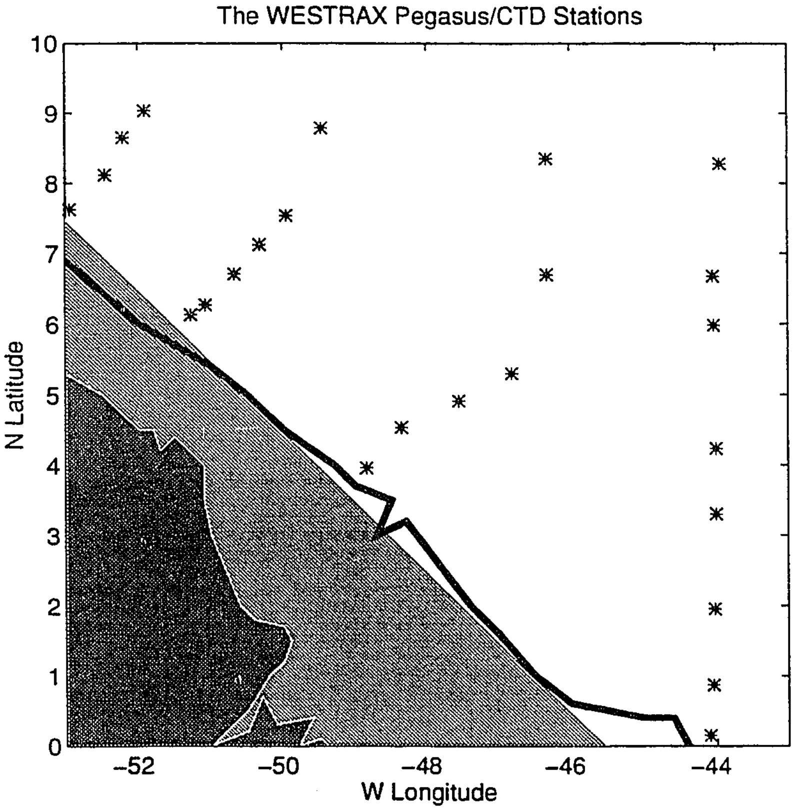

Figure 2.2: The "Western Tropical Atlantic Experiment (WESTRAX)" Pegasus/CTD stations during the four surveys. The thick line represents the actual shape of the 200-m isobath and the light gray shaded area, its rectilinear approximation.

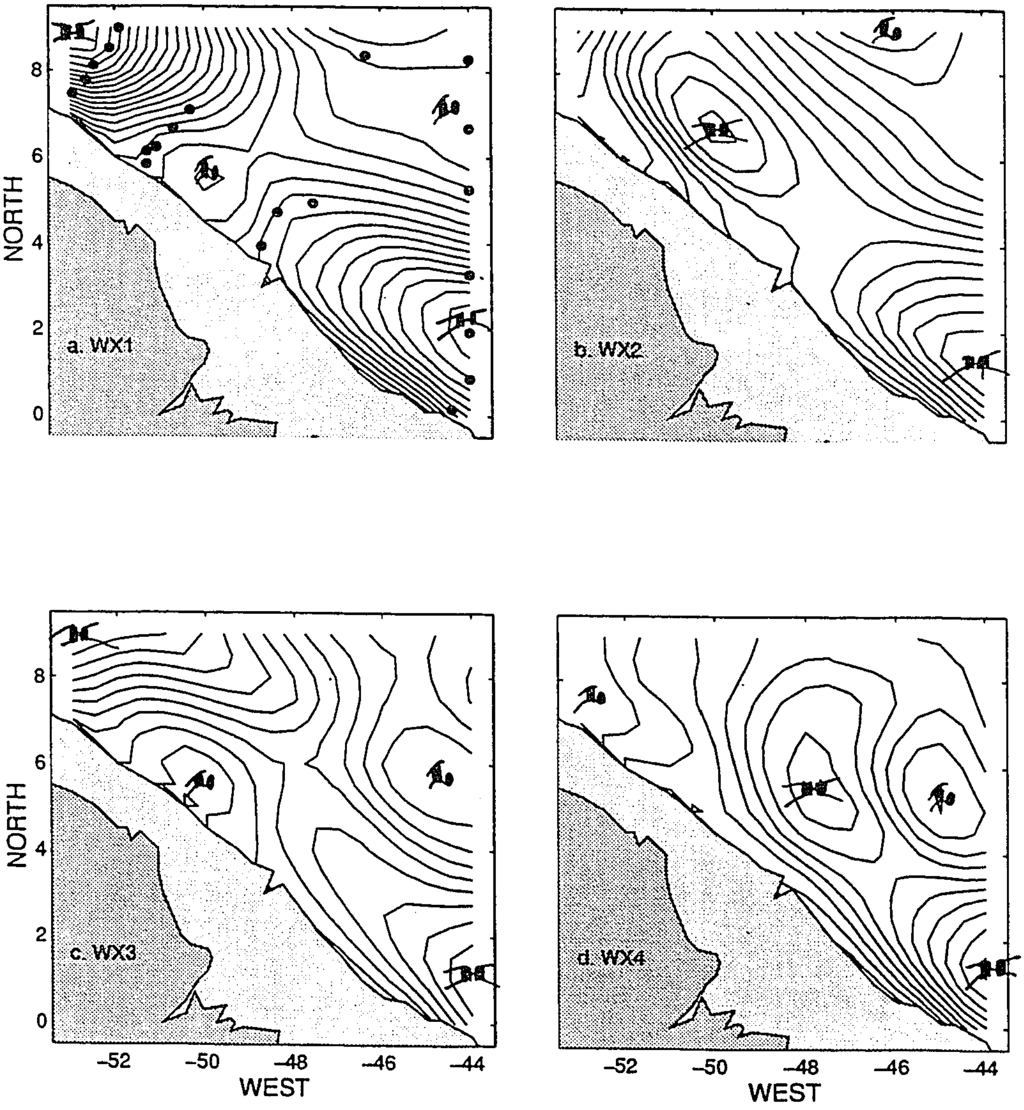

Figure 2.3: *Bub and Brown*'s [1996b] average intermediate layer (150-1300 m) flow structure for the four WESTRAX cruises. The stream function fields were computed from observed velocities by the Pegasus profiler.

lation. There is also virtually no information available on the NBC dynamical structure from observations. From the literature reviewed above, there is evidence that geostrophy accounts for the bulk flow structure within the NBC retroflection region. The purpose of this paper is to extract some dynamical information about the NBC retroflection system, from the WESTRAX data set and employing the quasi-geostrophic theory. In particular, we intend to address the following questions:

- How large are ageostrophic effects in the WESTRAX region?
- What is the dynamical modal structure of the NBC?
- What do the potential vorticity (PV) fields look like?
- How does a QG model for the NBC perform compared to other models in the literature?
- What are the dynamical processes leading to the NBC eddy-shedding?

In applying the QG theory to the WESTRAX region, we expect some of the results to be borderline for two reasons: (1) it is an equatorial region, and (2) oceanic jets are semi-geostrophic systems at best. On the other hand, since QG models have been widely used to investigate other western boundary currents and their rings, we will document possible differences between this low-latitude example and its mid-latitude counterparts (in particular, the Gulf Stream) in terms of PV.

We will address the above questions as follows. In Section 2.2, we check the viability of applying the QG approximation to the NBC retroflection region by verifying the basic QG approximations on the WESTRAX data set and evaluating ageostrophy. In Section 2.3, we decompose the NBC in QG dynamical modes. In Section 2.4, we discuss the dynamics of the NBC retroflection region in terms of a 3-layer QG model. In Section 2.5, we summarize our findings and present our conclusions.

2.2 How useful is the Quasi-Geostrophic Approximation in the near-equatorial NBC Retroflection Region?

For geophysical flows with time scales longer than the period of the Earth's rotation, inertial forces are much weaker than Coriolis forces and, thus the Rossby number (Ro) is small. The beta-plane QG equations for a continuously stratified, hydrostatic, Boussinesq fluid are obtained by invoking three different approximations (see *Pedlosky* [1979], *Gill* [1982], and *Young* [1986] for a complete derivation), namely:

(1) The "beta-plane" approximation, where the Coriolis parameter is approximated by

$$f = f_0 + \beta y \; , \tag{2.1}$$

subject to the condition that

$$\frac{\beta y}{f_0} = O(Ro) \; , \tag{2.2}$$

where f is Coriolis parameter, f_0 its central latitude value, β its constant meridional gradient, and y is the meridional coordinate;

(2) The geostrophic approximation, where the velocity $\vec{v}_p$ is approximated by its geostrophic component $\vec{v}$ according to

$$\vec{v}_p = \vec{v} + O(Ro) \; , \tag{2.3}$$

where

$$\vec{v} = \vec{k} \times \nabla \frac{p}{\rho_0 f_0} \; , \tag{2.4}$$

p is the pressure, and ρ_0 the reference density; and

(3) The layer thickness approximation, which for a continuously stratified ocean is

$$\frac{\frac{\partial z'}{\partial \sigma}}{\frac{\partial \bar{z}}{\partial \sigma}} = O(Ro) \quad , \tag{2.5}$$

where, $\bar{z} = \bar{z}(\sigma)$ represents the hydrostatic depth of a given isopycnal σ, and $z' = z'(x, y, \sigma, t)$ are the deviations from $\bar{z}$. However, it is perhaps simpler to think of the latter in terms of a layered QG ocean, which has been approximated by a finite number of homogeneous, immiscible layers. In this case, Eq. (2.5) becomes

$$\frac{\delta H_i}{H_i} = O(Ro) \quad , \tag{2.6}$$

where H_i is the rest thickness of the *ith* layer, and δH_i are the deviations of H_i.

The validity of the above approximations clearly comes into question at low latitudes (where f has smaller values). First, as the equator is approached, the inertial forces increase in relative importance in the horizontal momentum equations as the Coriolis forces weakens. Second, in the equatorial band, the meridional f gradient (i.e., β) reaches its maximum value and the corresponding length scales become large, bringing into question approximation (1).

Nevertheless we can show that the hypotheses underpinning the QG theory are reasonably applicable to the NBC region. For example, to check approximation (1), we can take the average radius of the NBC eddies (≈200 km) as our length scale L, which is very close to the first baroclinic radius of deformation in the region. Since, at 5°N,

$$\begin{aligned} f_0 &= 1.27 \times 10^{-5} s^{-1} \\ \beta &= 2.27 \times 10^{-11} (ms)^{-1} \\ Ro &= \frac{\beta L}{f_0} = 0.35 \, . \end{aligned}$$

While not small by mid-latitude standards, the beta term is about a third of f_0 and significantly less than 1.

To check approximation (2), we use Eq. (2.3) to define a stream function ψ_p which should satisfy the relation

$$\psi_p = \psi + O(Ro) \, , \tag{2.7}$$

where the index "p" refers to the Pegasus observed velocities.

The vertically integrated thermal wind relationship is

$$V_2 - V_1 = -\frac{1}{f}\frac{\partial}{\partial n}(\phi_2 - \phi_1) , \tag{2.8}$$

where V_i is defined as the geostrophic speed at the *ith* pressure level (i=1,2), n is the direction normal to V_i, ϕ_i is the geopotential anomaly (or dynamic height) at the *ith* pressure level relative to the surface, given by

$$\phi_i = \int_0^{p_i} \delta_V dp , \tag{2.9}$$

in which δ_V the specific volume anomaly.

Assuming $f = f_0$ is constant, Eq. (2.8) becomes

$$\frac{\partial}{\partial n}(\psi_2 - \psi_1) = -\frac{1}{f_0}\frac{\partial}{\partial n}(\phi_2 - \phi_1) , \tag{2.10}$$

where ψ is the geostrophic stream function.

By integrating Eq. (2.10) along the n direction, one obtains

$$(\psi_2 - \psi_1) = -\frac{1}{f_0}(\phi_2 - \phi_1) + \text{constant} . \tag{2.11}$$

We will then apply Eq. (2.11) to WX2, the fall 1990 WESTRAX survey, which according to *Bub and Brown* [1996a, 1996b], was the survey which exhibited the strongest velocities in connection with the retroflection eddy which was pinching off at the time- an extreme ageostrophic WESTRAX velocity pattern.

We focus our attention on two pressure levels, one near the depth of maximum velocity and away from the Ekman layer (100 m), and the other at a depth of substantially reduced velocities (1200 m).

Before interpolation, the geopotential anomaly differences at the 100 and 1200 db levels are computed and converted to geostrophic stream function differences, according to the right-hand side of Eq. (2.11). The mean of the 100-1200 db geostrophic stream function difference observation vector is removed and interpreted as the integration constant in Eq. (2.11). The Pegasus velocity differences between isobaric levels 100 and 1200 db are also computed.

Following *Bretherton et al.* [1975], an Objective Analysis (OA) scheme is then used to map the WX2 geostrophic stream function from hydrography and the Pegasus stream function from the velocity data. The OA spatial correlation function is estimated by fitting all the correlation pairs in the data to an assumed isotropic Gaussian shape given by

$$C(r) = (1 - \mathcal{E})e^{-r^2/l_C^2} , \tag{2.12}$$

where $r = \sqrt{x^2 + y^2}$ is the radial distance, $\mathcal{E}$ is the bandwidth truncation error, and l_C is the correlation length scale. As shown in Figure 2.4a, best fits are obtained for $l_C \approx$400 km. All the OA gridded fields were mapped with this correlation length scale. The interpolation error field, which depends solely on the station locations and the $[l_C, \mathcal{E}]$ parameter set, is presented in Figure 2.4b and is representative of the WESTRAX fields.

We force the interpolated velocity difference maps to satisfy the zero-normal-flow condition at the western boundary by employing the method of images. As shown in Figure 2.2, the almost rectilinear 200m isobath is approximated by a straight line and regarded to be the line of symmetry. Then, the data points in both scalar and vectorial fields are symmetrically projected on the land side; i.e., their mirror images with the suitable sign changes are added to this data set before their input on the OA scheme.

The 100-1200db Pegasus and geostrophic stream functions, compared in Figure 2.5, are remarkably similar and corroborate earlier hydrographic data analysis, such as *Cochrane et al.* [1979]. The present analysis has captured the NBC, which is seen to be shedding an eddy in both Figures 2.5a and 2.5b, with both the Amazon eddy and the shed eddy centered at the same latitudes. The dynamic low depicted in the northeastern corner of both maps is associated with a cyclonic turning of

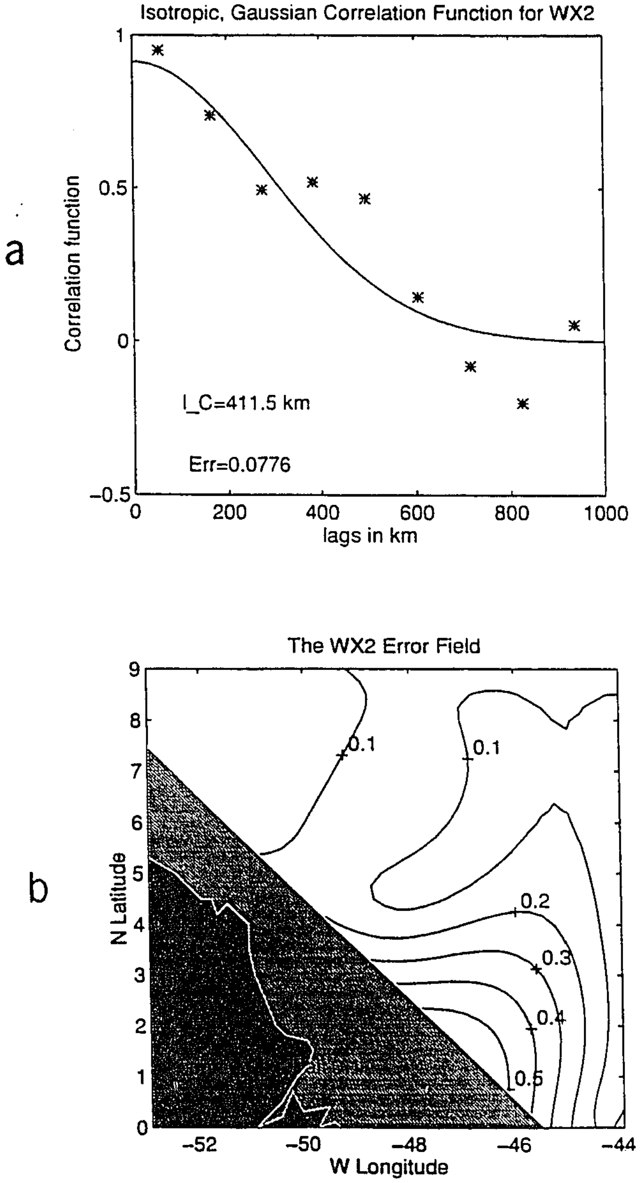

Figure 2.4: (a) The sample correlation function for the WX2 100-1200 db geostrophic stream function differences. The correlation length l_C is 411.5 km and the bandwidth truncation error $\mathcal{E}$ is 0.08. (b) The typical root mean square errors associated with the OA horizontally gridded fields, using the data of the stations displayed in Figure 2.2 and the OA parameters above.

the NEC waters, as in *Bub and Brown*'s [1996b] analysis (Figure 2.3b) The major differences between the two maps is the location of the center of the Amazon eddy. It turns out that this difference is located inside of the region of the larger OA interpolation errors (Figure 2.4b), and further more, our assumption of a constant f is more suspect so near the equator.

To qualitatively evaluate the differences between the geostrophic and Pegasus fields (Figure 2.5), we follow *Pinardi and Robinson* [1987] in computing the root-mean-square (rms) difference associated with the velocity magnitudes of geostrophic and Pegasus fields. That error is defined as

$$rms \quad = \quad \sqrt{\frac{\langle (V_p - V)^2 \rangle}{\langle (V_p)^2 \rangle}} \quad = \; 0.31 \quad ,$$

where V_p and V are respectively the Pegasus and geostrophic velocity magnitudes. The 0.31 value is based on all data except those within the latitudinal band 0°-1°N. As the rms difference represents a measurement of the deviations of the geostrophic field relative to the observed velocity field, it can be thought of as an estimate for the Rossby number within the WESTRAX region.

Another approach to estimating Ro based on approximation (2) is to find a characteristic velocity U and compute $Ro = U/(f_0 L)$. *Frantantoni et al.* [1995] considered the maximum radial velocity of the pinching-off eddy as U, which in our case is U=0.92 m/s. Thus, Ro is 0.36, a value is consistent with the rms calculation and is about 75% larger than that of *Frantantoni et al.* [1995]. Similarly, we can estimate the Rossby number as $Ro = \mid \zeta_p \mid / f_0$, where ζ_p by is the relative vorticity of the observed velocity field. In this case, we simply calculate $\zeta_p = \nabla^2 \psi_p$ from Figure 2.5a, yielding a mean value $\langle \mid \zeta_p \mid \rangle = 0.56 \times 10^{-5}$/s, and $Ro = 0.44$. This last result is larger than we would like. Nevertheless, the rms difference between ζ_p and the geostrophic vorticity ζ is 0.28, assuring that the relative vorticity is essentially geostrophic.

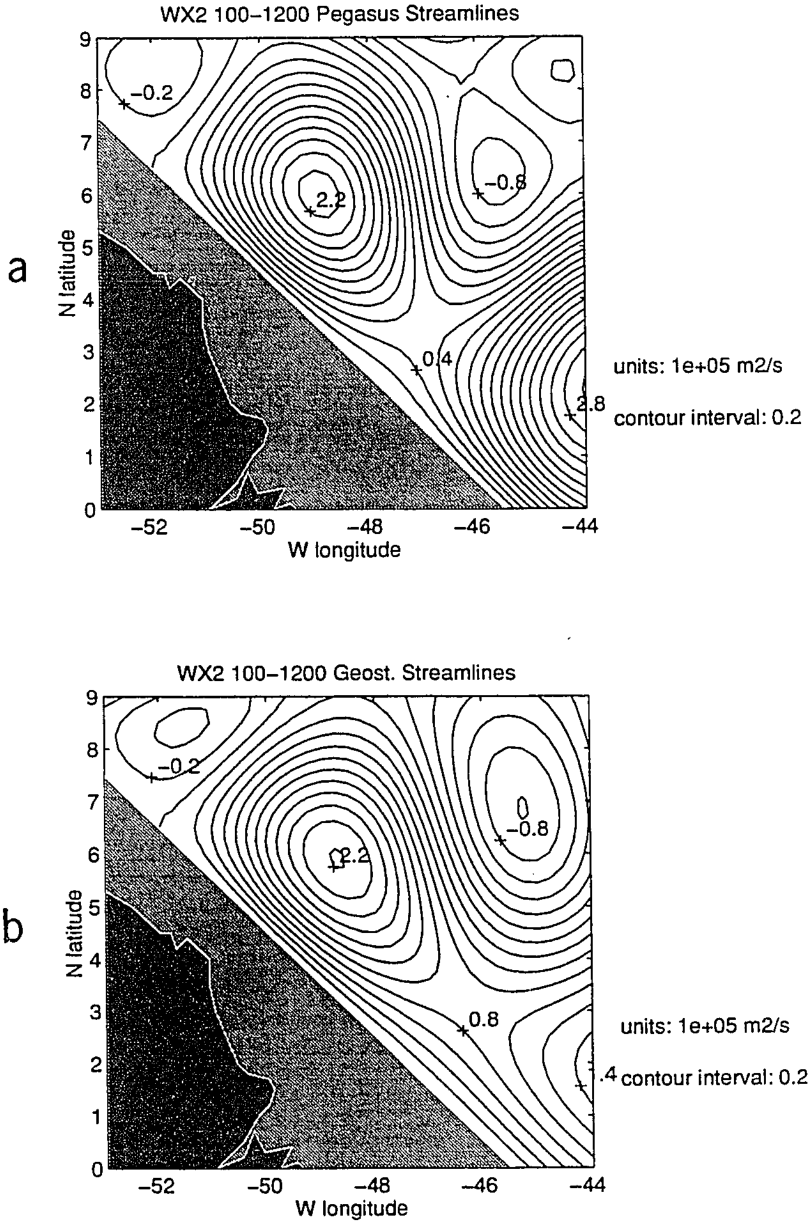

Figure 2.5: Comparison between the 100-1200m (a) Pegasus stream function differences, and (b) geostrophic stream function differences for the WX2 survey. Contours in 1×10^5 m^2/s.

To verify that changes in layer thickness are small (in the sense of our approximation 3), we examine the layers as defined by *Bub and Brown*'s [1996a] water mass classification in light of the layered model condition (Eq. 2.6). In Table 2.1, we present the mean (H_i) and corresponding standard deviations (std_i) for five of *Bub and Brown*'s layers ($i = 1, 5$) within the upper 1500 m for the WX2 survey. We included the values south of 1°N in these calculations.

Table 2.1: The water mass layer structure used in the *Bub and Brown* [1996a] classification: rest thicknesses, standard deviations, and Rossby number estimates based on a normal distribution.

i	$\sigma_{i+1} - \sigma_i$[a]	Layer	H_i (m)	std_i (m)	$Ro_i = \frac{2\,std_i}{H_i}$
1	26.00–surface [b]	surface	141.0	26.2	0.37
2	27.20–26.00	upper intermediate	451.2	71.3	0.31
3	27.35–27.20	mid intermediate	239.7	43.4	0.36
4	27.35–27.65	lower intermediate	443.6	57.2	0.26
5	27.65-27.75	upper NADW [c]	224.5	38.2	0.34

[a] σ_i refers to a potential density value expressed in (ρ_i -1000) kg/m^3; the index i indicates the density surface value bounding the top of the *ith* layer; the index $i + 1$ indicates the density surface value bounding the bottom of the *ith* layer.

[b] The ocean surface is considered a rigid lid.

[c] The acronym NADW stands for North Atlantic Deep Water.

Figure 2.6 shows the OA mapped δH_1 and δH_2, as defined in Table 2.1. If the changes in layer thickness are normally distributed, 95% of the layer thickness values should fall in the range $H_i \pm 2\,std_i$. Assuming that, estimates of Rossby numbers based on $Ro_i = (2\,std_i)/H_i$ are made and show remarkable consistency among the layers in yielding a *Ro* ≈0.35 value. These *Ro* estimates are very similar to those found in verifying approximations (1) and (2).

The analysis above shows that the three approximations (Eqs. 2.2-2.6), upon which QG is based, are reasonably satisfied in the WESTRAX region. This means that the relative vorticity is primarily geostrophic, and that the "beta" term and the vortex stretching associated with the changes in layer thicknesses are also small (≈ 35%) compared to the Coriolis parameter f_0. The QG potential vorticity q, which is the sum of these three terms, is $O(f_0)$. However, the $q = O(f_0)$ is not necessarily a consequence of the NBC being a low-latitude system. *Hall* [1985] showed that a typical q magnitude for the Gulf Stream region is 8×10^{-5}/s, the same order of magnitude as the typical mid-latitude $f_0 = 10^{-4}$/s value.

Thus, we conclude that it is reasonable to apply the QG model to the NBC region, and the Pegasus observed currents, which are about 65-70% geostrophic (with f kept constant), will be used throughout this work as the absolute geostrophic current (according to Eq. 3) in the stream function and potential vorticity calculations to be presented in the following sections.

2.3 A Quasi-Geostrophic Modal Structure for the NBC

In this section, the NBC velocity structure is decomposed into dynamical modes. The formalism used in this section follows directly from *Flierl* [1978]. It should be noted that the QG vertical modes presented in this section are identical to the ones obtained if separation of variables is used on a inviscid, primitive equation model under the hydrostatic approximation.

The QG potential vorticity equation is given by

$$\frac{D}{Dt}q = \mathcal{F} \ , \tag{2.13}$$

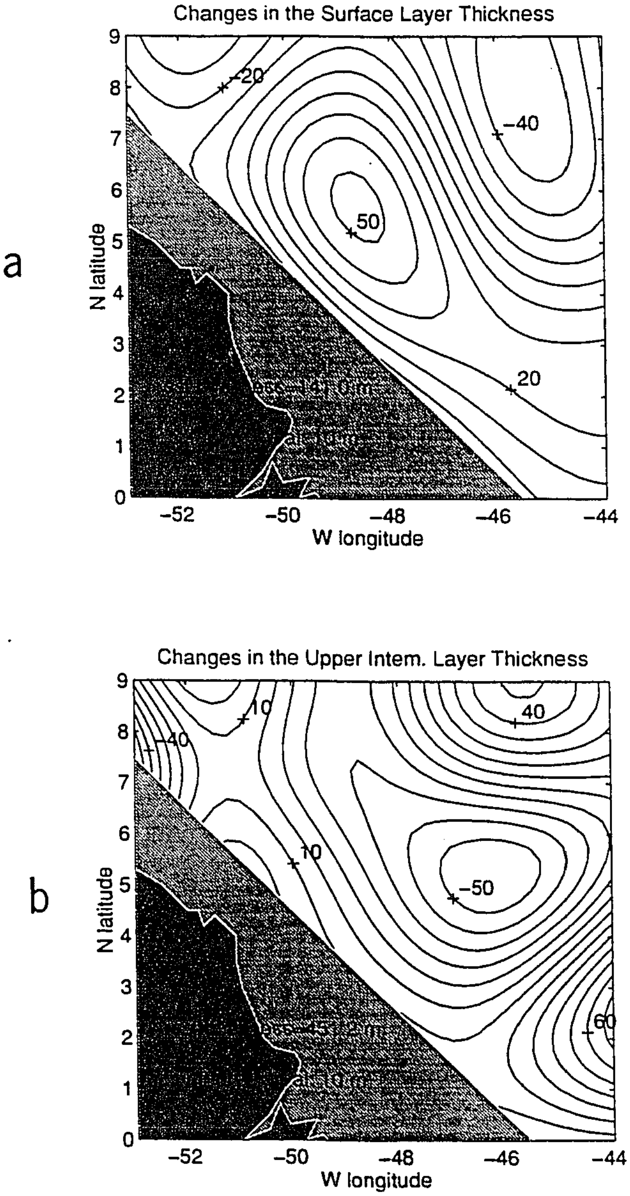

Figure 2.6: The departures δH_i from the rest thickness H_i for the *Bub and Brown* [1996a] surface layer (upper panel) and upper intermediate layer (lower panel). Contours in meters.

where the potential vorticity q relates to the geostrophic stream function ψ by

$$q = \nabla^2\psi + \beta y + \frac{\partial}{\partial z}\frac{f_0^2}{N^2(z)}\frac{\partial\psi}{\partial z} \ , \tag{2.14}$$

with

$$\frac{D}{Dt} = \frac{\partial}{\partial t} - \frac{\partial\psi}{\partial y}\frac{\partial}{\partial x} + \frac{\partial\psi}{\partial x}\frac{\partial}{\partial y} \tag{2.15}$$

being the geostrophic substantive derivative, and $\mathcal{F}$ the forcing-dissipation term.

The vertical normal modes of the geostrophic stream function can be obtained from the linearized, flat bottom, unforced form of Eq. (2.13), by assuming a separation of variables according to

$$\psi(x,y,z,t) = \Psi_i(x,y,t)\, F_i(z) \ , \tag{2.16}$$

where Ψ_i is the stream function amplitude, and F_i the vertical structure function (or the eigenfunction) of the *ith* vertical mode.

By substituting Eq. (2.16) in Eq. (2.13), one gets

$$\frac{1}{F_i(z)}\frac{\partial}{\partial z}\frac{f_0^2}{N^2(z)}\frac{\partial F_i(z)}{\partial z} = \text{constant} \ , \tag{2.17}$$

which together with the required boundary conditions of rigid lids at both surface ($z = 0$) and bottom ($z = -H$), leads to a Sturm-Liouville eigenvalue problem. Formally, we can write

$$\frac{\partial}{\partial z}\frac{f_0^2}{N^2(z)}\frac{\partial F_i(z)}{\partial z} + \lambda_i F_i(z) = 0 \tag{2.18a}$$

$$\frac{\partial F_i(z)}{\partial z} = 0 \ \text{at} \ z = 0, -H \ . \tag{2.18b}$$

The eigenvalues λ_i, which form an infinite but discrete set, are defined to be equal to the inverses of the corresponding squared deformation radii Rd_i.

To solve Eq. (2.18) for the eigenvalues and (orthonormalized) vertical eigenmodes, we use the WESTRAX four-cruise average Brunt-Väisälä profile (Figure 2.7a) with vertical resolution of 10 m and a depth of H =4000 m. As in Section 2.2, the β-plane is centered at 5°N. The result for the first six modes are shown in Figure

Table 2.2: The first six deformation radii (in km) and the corresponding equivalent-depths (in m) for the WESTRAX average Brunt-Väisälä profile. The central latitude and ocean depth considered are respectively 5°N and 4000 m.

mode i	Rd_i	$he_i = \frac{(Rd_i{}^2 f_0{}^2)}{g}$
0 [a]	15,584.6	4000
1	197.7	0.64
2	126.2	0.26
3	74.1	0.09
4	54.6	0.05
5	44.4	0.03

[a] The values for $Rd_0 = \sqrt{gH}/f_0$ and $he_0 = H$ are used instead of the $Rd_0 = he_0 = \infty$ obtained from the QG eigenvalue calculation.

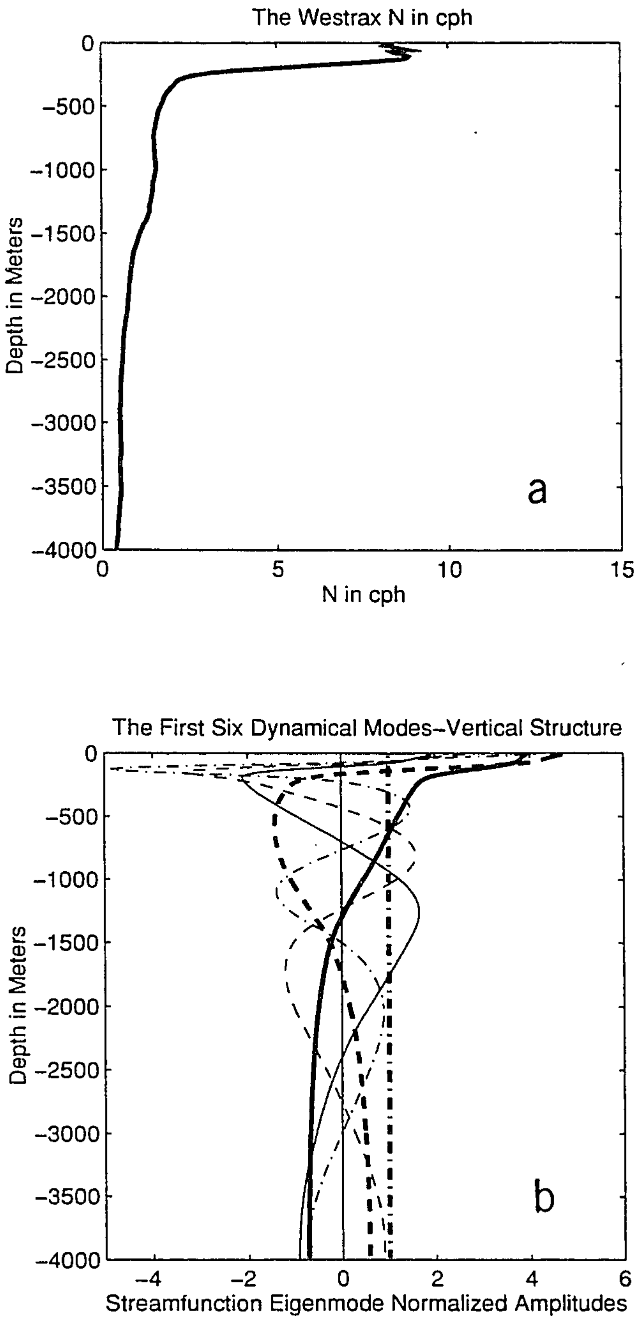

Figure 2.7: (a) The 10m-average Brunt-Väisälä frequency profile for the four WESTRAX surveys, (b) the vertical modal structure for the barotropic and first five baroclinic modes.

2.7b. The numerical values for the corresponding deformation radii and equivalent depths are presented in Table 2.2.

It is now necessary to verify how the flow in the WESTRAX region behaves in terms of a weighted sum of the orthogonal modes and to identify the dynamical modes that account for the bulk velocity structure in the NBC region. To address these issues, depth empirical orthogonal functions (DEOF) are computed for the deeper stations of WX2.

The DEOF method is analogous to the time-domain EOF calculation of *Davis* [1976] and *Klinck* [1984], who dealt with scalar quantities. We seek the stream function vertical structure function analogous to dynamical mode decomposition. All deep Pegasus u and v vertical profiles are used to obtain DEOF's of the form

$$\psi(x,y,z,t) = \Psi_i^{(E)}(x,y,t) F_i^{(E)}(z) \quad , \tag{2.19}$$

where $\Psi_i^{(E)}(x,y)$ are the orthonormalized eigenfunctions, and $F_i^{(E)}(z)$ are the dimensional vertical structure functions. Thus, Eq. (2.19) is used to convert the array of individual observed velocity profiles to a set of horizontal spatial stream function patterns that vary with depth.

The first and second DEOF modes explaining 78% and 11% of the variance of the vertical structure in WX2 respectively, are shown in Figure 2.8 (solid lines). The $F_i^{(E)}(z)$'s (for i =1,2) are nondimensionalized by their norms so that they are of the same order of magnitude as the dynamical modes displayed in Figure 2.7.

An optimal fit of the dynamical modes (Figure 2.7) to the statistical DEOF modes (Figure 2.8 and Table 2.3) shows that DEOF modes 1 and 2 are dominated by dynamical mode 1 and 2 respectively. The *rms* differences between the DEOF modes and the respective fits using a three-dynamical-mode truncation (i.e., using the barotropic and two gravest baroclinic modes) are generally less than 8.5% (see also Figure 2.7, dashed lines).

We now approximate the WX2 flow structure with three dynamical modes (i.e.,

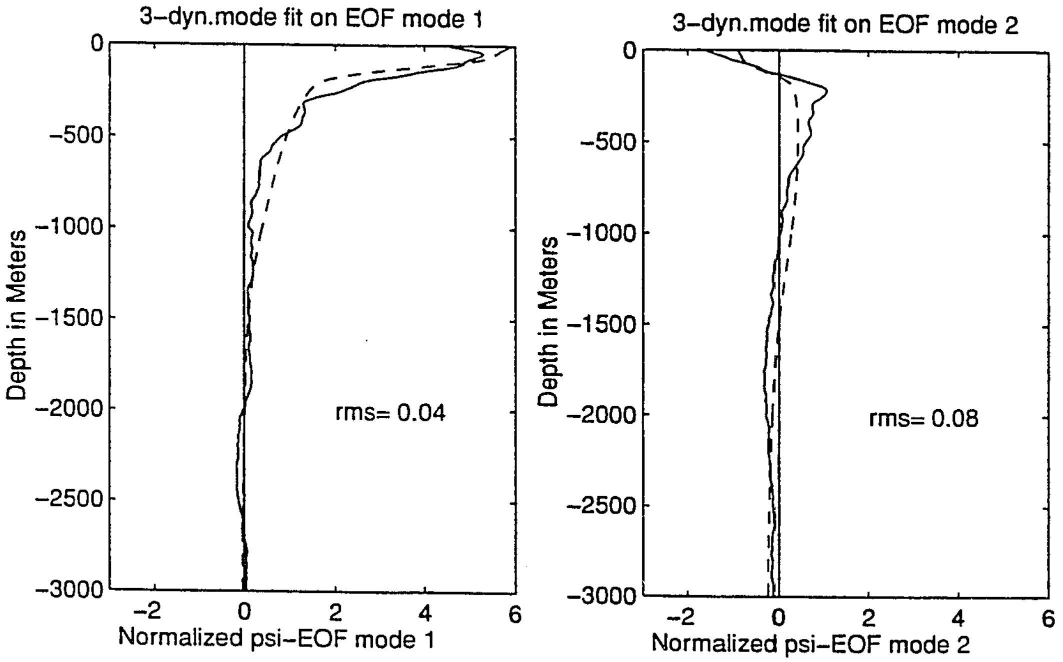

Figure 2.8: The vertical structure of the WX2 Depth Empirical Orthogonal Function (DEOF) modes 1 (left panel) and 2 (right panel). The dashed line represents the optimal fit of the first three dynamical modes on the DEOF modes. The *rms* difference values are indicated in the lower right corner of each panel.

Table 2.3: Root mean square differences for the optimal fits of QG dynamical modes onto the DEOF modes 1 and 2

	rms differences [a]	
fitted mode(s)	DEOF mode 1	DEOF mode 2
0	0.871	0.980
1	0.301	0.691
2	0.862	0.442
3	0.986	0.931
4	0.977	0.989
5	0.999	0.999
0-3	0.052	0.081
0-5	0.001	0.003

[a] The *rms* difference definition is given by $\sqrt{\langle (F_j{}^{(E)} - \sum_{i=1}^{N} \alpha_i{}^j F_i)^2 \rangle / \langle (F^{(E)}{}_j)^2 \rangle}$, where N is the total number of modes used on the fitting, and α_i is the weight obtained in the optimal fitting of the *ith* dynamical mode onto the *jth* DEOF mode.

we use Eq. (2.16) with i =0,1,2). The total stream function field at a given level $z = z_*$ is obtained by directly OA mapping the velocities measured at z_*. The three-mode approximation requires that the amplitude functions $\mathcal{U}_i$ and $\mathcal{V}_i$ for i =0,1,2 must be known. The relationships between ith-mode velocity amplitude functions and Ψ_i follow from the stream function definition, and are given by

$$[\mathcal{U}_i,\, \mathcal{V}_i] \;=\; \left[-\frac{\partial}{\partial y},\, \frac{\partial}{\partial x}\right] \Psi_i \quad . \tag{2.20}$$

These expressions allow us to write the three-mode approximation of the zonal and meridional velocities using Eq. (2.16), which yields

$$[u(x,y,z,t)\, v(x,y,z,t)] \;\approx\; [\mathcal{U}_i(x,y,t),\, \mathcal{V}_i(x,y,t)]\, F_i(z) \tag{2.21}$$

for i= 0,1,2.

Then, the $\mathcal{U}_i$ and $\mathcal{V}_i$ values at one particular location are determined by projecting the ith dynamical mode onto the u and v profiles. Mathematically, this is

$$[\mathcal{U}_i,\, \mathcal{V}_i] \;=\; \frac{1}{H}\int_{-H}^{0} [u\,,\, v]\, F_i\, dz \quad . \tag{2.22}$$

In Figure 2.9, we show the OA-mapped Ψ_i (i =0,1,2) fields based on the $\mathcal{U}_i$ and $\mathcal{V}_i$ values computed by Eq. (2.22). The three-mode approximation for ψ is obtained by directly OA mapping the three-mode approximation of u and v through the use of Eq. (2.22) in Eq. (2.21).

Figure 2.10 shows the maps for ψ (left panels) and the corresponding three-mode approximation (right panels) at three different levels: 50 m (in the mixed layer), 350 m (embedded in the thermocline), and 1000 m (at the lower boundary of the NBC eddy activity). The three-mode approximation is very similar to the total stream function field, only slightly more energetic. The three-mode approximation of ψ even captured northwestward tilt with depth in the retroflection eddy, also observed in the total stream function field (Figure 2.10, left panels), and which was described originally by *Bub and Brown* [1996b].

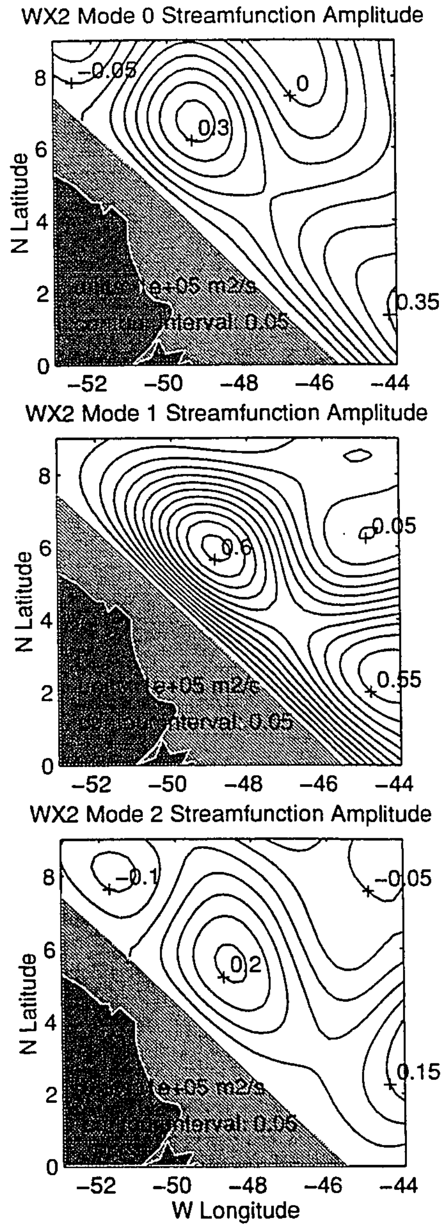

Figure 2.9: The stream function amplitude functions Ψ_i for the first three dynamical modes (i=0, 1 and 2). Units: 1×10^5 m^2/s.

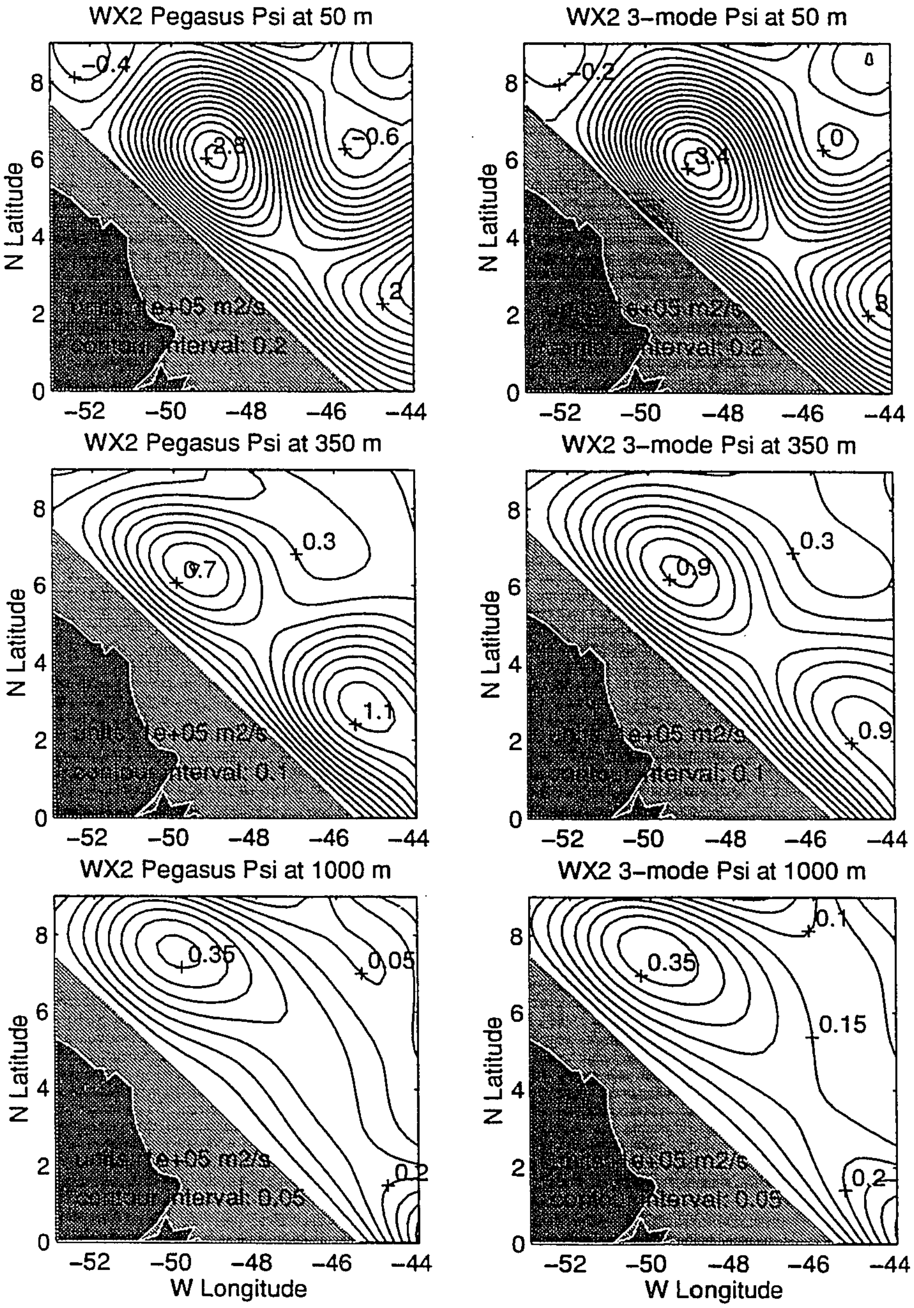

Figure 2.10: Comparison between the Pegasus-derived stream function (left panels) and the corresponding three-mode truncation at the levels: 50 m (upper), 350 m (middle), and 1000 m (lower).

2.4 The NBC Retroflection Region as a Three-Layer, Quasi-Geostrophic Ocean

When a given current system can be reasonably approximated by a small number of modes, it is common to employ a so-called layered model. In such layered models, the vertical density structure is simplified, assuming a step-like profile with successive homogeneous and usually immiscible layers. Consequently, the Brunt-Väisälä profile becomes a sum of Dirac delta functions.

We follow *Flierl*'s [1978] notation in defining a QG N-layer model, analogous to the continuously stratified system (Eqs. 2.12-2.18). The conservation of PV equation for the ith layer becomes

$$\left[\frac{\partial}{\partial t} - \frac{\partial \hat{\psi}_i}{\partial y}\frac{\partial}{\partial x} + \frac{\partial \hat{\psi}_i}{\partial x}\frac{\partial}{\partial y}\right] \hat{q}_i = \hat{\mathcal{F}}_i \tag{2.23}$$

where the hats are used to distinguish the layer model from the continuously stratified model quantities. The layer index i varies from 1 to N.

The relationship between PV and stream functions is given by

$$\hat{q}_i = \nabla^2 \hat{\psi}_i + \beta y + \frac{{f_0}^2}{\epsilon_{i-1} g H_i}(\hat{\psi}_{i-1} - \hat{\psi}_i) + \frac{{f_0}^2}{\epsilon_i g H_i}(\hat{\psi}_{i+1} - \hat{\psi}_i) \ , \tag{2.24}$$

where H_i is the rest thickness of the ith layer, $\epsilon_i = (\sigma_{i+1} - \sigma_i)/\bar{\rho}$ are the density steps between layers i and $i+1$. The assumed values of $\epsilon_0 = \epsilon_N = \infty$ are used to eliminate the extraneous stretching terms.

Analogous to the solution for the continuously stratified model (Eq. 2.16), we solve for the ith layer geostrophic stream function using separation of variables according to:

$$\hat{\psi}_i(x,y,t) = \hat{\Psi}_j(x,y,t)\hat{F}_j^{\ i} \ , \tag{2.25}$$

where $\hat{F}_j^{\ i}$ refers to the amplitude of the jth mode onto the ith layer. The $\hat{F}_j^{\ i}$'s are the orthonormalized eigenvectors.

The separability condition

$$\frac{{f_0}^2}{\epsilon_{i-1} g H_i}({\hat{F}_j}^{i-1} - {\hat{F}_j}^{i}) + \frac{{f_0}^2}{\epsilon_{i} g H_i}({\hat{F}_j}^{i+1} - {\hat{F}_j}^{i}) + \hat{\lambda}_i {\hat{F}_j}^{i} = 0 \qquad (2.26)$$

is the layered model analog to Eq. (2.18). The eigenvalues are found by requiring that the N-equation system has a nontrivial solution [*Flierl*, 1978]. Operationally, this means that the determinant of the $N \times N$ matrix formed by Eqs. (2.26) is zero. The amplitude functions $\hat{\Psi}_j$ are found using the finite difference analog of Eq. (2.22):

$$\hat{\Psi}_j = \frac{H_i}{H} \hat{\psi}_i {\hat{F}_j}^{i} \ . \qquad (2.27)$$

An obvious consequence of the conditions above is that an N-layer model is able to resolve N dynamical modes.

In order to quantitatively reproduce the correct physics of the corresponding continuously stratified ocean, the layered model must be calibrated [*Flierl*, 1978]. In particular, the fundamental length scales (i.e. the deformation radii) of the model must be similar to those of the continuously stratified model. This means that the rest depths H_i and the layer densities σ_i must be chosen carefully to make the eigenvalues of Eq. (2.26) approximately the same as those of Eq. (2.18). We have some guidance in this matter.

In the previous section, we have have shown that the NBC vertical structure is dominated by the first three dynamical modes, while a six-mode NBC reproduces almost exactly the total velocity stream function field (see Table 2.3). Coincidently or not, two of the NBC layered models found in the literature are six-layer models.

Fratantoni et al.'s [1995] six-layer primitive equation model was the only numerical simulation so far to successfully reproduce the NBC eddy-shedding. The H_i and σ_i values used by those authors are presented in Table 2.4. We then apply these values in the QG eigenvalue problem Eq. (2.26) for $N = 6$ and a beta-plane centered at 5°N. We use H_6=3000 m to be consistent with our assumption of a 4000m deep flat-bottom ocean to model the WESTRAX region. The results for the deformation radii (Table 2.4) agree reasonably well with those obtained for the continuously stratified ocean (Table 2.2). Because the external deformation radius does not depend on the stratification, it is perfectly matched. The first internal deformation radius differs from the continuously stratified one only by 10% (Table 2.2). According to our analysis in Section 2.2, the NBC dynamical structure is dominated by the first baroclinic mode. Thus, the approximately correct Rd_1 within the NBC region might have played a role in the agreement of *Fratantoni et al.*'s [1995] NBC eddy-shedding modeling with observations. The average difference between the six deformation radii in Table 2.4 and Table 2.2 is about 20%.

Table 2.4: The *Frantantoni et al.* [1995] model as six-layer, QG ocean: rest thicknesses, layered density values and the corresponding internal deformation radii

i	H_i (m)	$\sigma_i = (\rho_i - 1000)$ kg/m^3	Rd_i
1	80	24.97	179.4
2	170	26.30	91.3
3	175	26.83	61.2
4	250	27.12	45.7
5	325	27.32	34.3
6	3000	27.77	-

Bub and Brown's [1996a] descriptive model vertically sliced the NBC region according to water-mass criteria. Using the WESTRAX data set, *Bub and Brown* [1996a] defined a 150m thick surface layer, divided the intermediate layers in four layers, and defined a deeper layer extending from 1500 m to the bottom. The *Bub and Brown* [1996a] model values for H_i and σ_i are shown in Table 2.5. The same eigenvalue calculation done for the *Fratantoni et al.* [1995] model is carried out for *Bub and Brown*'s [1996a]. The results obtained for the first three baroclinic modes (Table 2.5) differ from the continuously stratified ones in Table 2.2 by only about 5%. Thus, the vertical structure of *Bub and Brown*'s [1996a] model, based solely on water mass identification, is also appropriate for six-layer dynamical studies of the NBC.

Table 2.5: The *Bub and Brown* [1996a] model as six-layer, QG ocean: rest thicknesses, layered density values and the corresponding internal deformation radii

i	H_i (m)	$\sigma_i = (\rho_i - 1000)$ kg/m^3	Rd_i
1	140	24.13	194.6
2	450	26.97	129.9
3	240	27.28	71.1
4	445	27.48	37.5
5	225	27.74	32.2
6	2500	27.87	-

However, are all these six layers needed to capture the essence of the NBC dynamics? We believe that probably not. The analysis in Section 2.3 indicates that 90% of the variance in the vertical structure is explained by the barotropic and first two baroclinic modes. Furthermore, from the literature review in Section 2.1, it seems intuitive to look for a three-layer model. The first layer should simulate the retroflection of the surface layers of the NBC to form the NECC. In the second layer, the separating subthermocline waters of NBC should feed the NEUC. The third layer should simulate the DWBC.

To build a three-layer WESTRAX model, we extend the *Silveira and Flierl* [1996] $2\frac{1}{2}$-layer calibration scheme to three layers and force $\hat{\lambda}_1 = \lambda_1$ and $\hat{\lambda}_2 = \lambda_2$ (the mathematical details of the calibration scheme are presented in the Appendix). The three-layer calibration scheme requires the input of f_0, λ_1, λ_2, and the rest depths H_1, H_2, and H_3. We choose the *Bub and Brown* [1996a] surface layer depth of H_1=150 m. We set the subthermocline layer depth as H_2=850 m. With a deep layer thickness of H_3=3000 m, our flat bottom ocean depth $H = H_1 + H_2 + H_3$ is 4000 m .

The calibration procedure (see Appendix) yields two possible sets of density jump values:

$$
\begin{aligned}
\textbf{set1}: \ \epsilon_1 &= 2.32 \times 10^{-3} \ , \ \epsilon_2 = 0.76 \times 10^{-3} \\
\textbf{set2}: \ \epsilon_1 &= 3.96 \times 10^{-3} \ , \ \epsilon_2 = 0.45 \times 10^{-3} \ .
\end{aligned}
$$

We then compute "observed" σ's in each of the layers from the mean WESTRAX density profile. The same WESTRAX density profile was previously used to generate the $N^2(z)$ (Figure 2.7a) and to compute of the eigenvalues and eigenmodes in the continuously stratified model (Figure 2.7b) is used. The "observed" σ's are used to compute the "observed" ϵ's,

$$
\epsilon_1 = 2.85 \times 10^{-3} \ , \ \epsilon_2 = 0.68 \times 10^{-3} \ .
$$

We chose the set of calibrated ϵ values which better fits the "observed" values above. In the present case, the first set is a clear choice.

The values for the calibrated σ_1, σ_2, and σ_3 are found by choosing σ_3 to be the "observed" σ_3 and using the calibrated ϵ's to get the other two σ's. The calibrated density profile is shown in Figure 2.11a. The corresponding dynamical modes for the three-layer model are displayed in Figure 2.11b.

We compute the stream function in each layer by a procedure similar to that described in Section 2.3. The obvious difference is that here the velocity amplitude

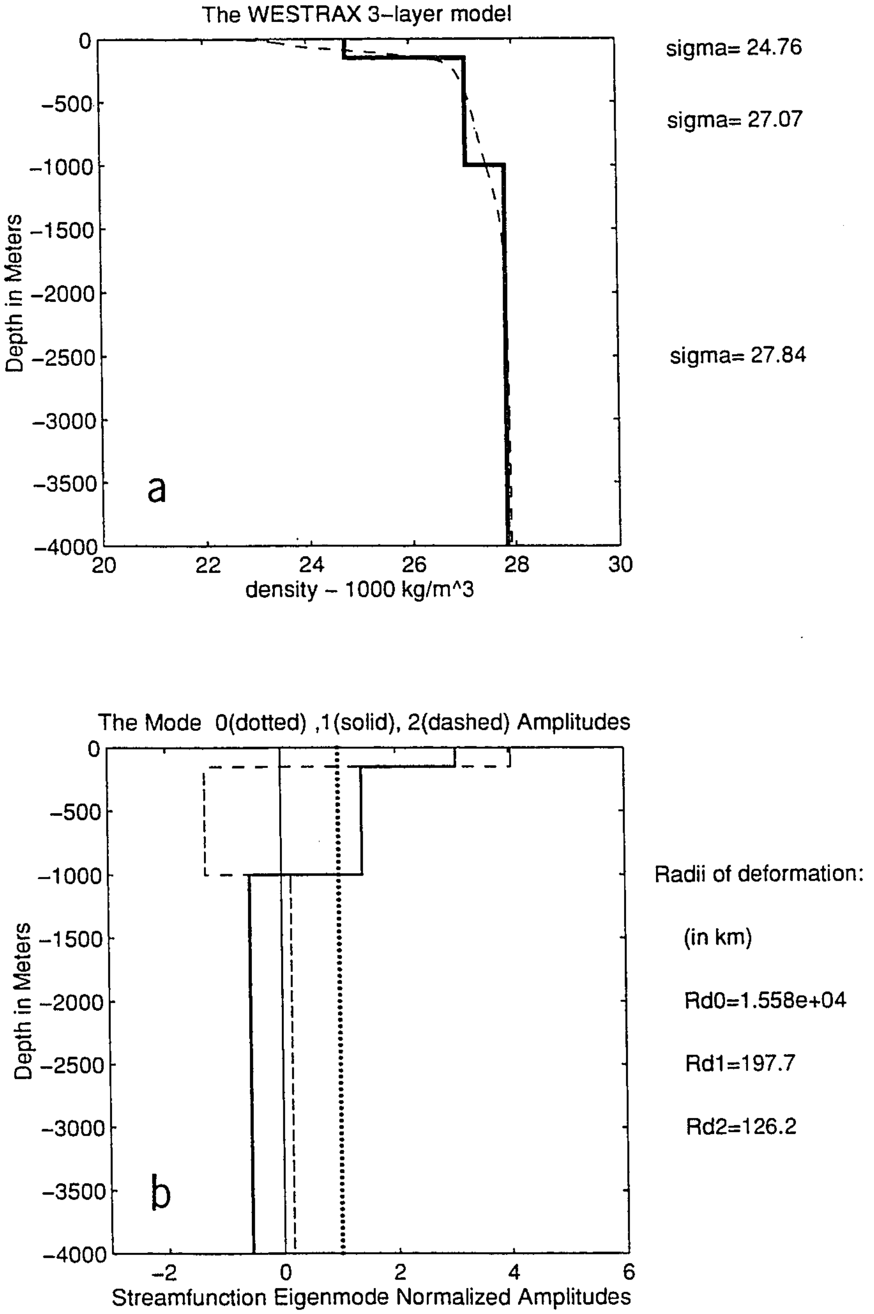

Figure 2.11: (a) The calibrated WESTRAX density profile under the three-layer approximation, and (b) the corresponding three discrete dynamical modes.

functions are obtained by projecting the discrete modes of Figure 2.11b onto u and v profiles.

We apply the model to WX2 (fall 1990) and WX3 (winter 1991) surveys, which represent two sequential stages in the NBC eddy-shedding process (Figure 2.3). The stream functions in the three layers for WX2 and WX3 are shown in Figure 2.12. There we can see that the NBC system and its eddy structure are confined to the upper two layers, while the third layer is dominated by a weaker and meandering analog to the DWBC. The velocities in the middle layer are about a fourth of those in the surface layer in both surveys. In addition, the layered-retroflection of the NBC is reproduced in this three-layer approximation: the subthermocline waters retroflect at more southern latitudes (3°-5° N) than the surface waters (6°-8° N). As reported by *Bub and Brown* [1996a, 1996b], the latitudinal difference in the location of the NBC retroflections in the upper and subthermocline layers respectively is somewhat smaller during the eddy-shedding process (Figure 2.12, left panels). We can also see that when the NBC retracts after shedding the eddy, as in WX3 fields (Figure 2.12, right panels), a cyclonic circulation exists in the subthermocline layer, northwestward of the retroflection bulge. This cyclonic feature, which is absent during the eddy-shedding phase, has been reported by *Cochrane et al.* [1978] (see Figure 2.1), *Bruce and Kerling* [1984], and by *Bub and Brown* [1996b], who have referred to it as the "French Guiana Low".

The QG potential vorticity fields (Figure 2.13) are computed using Eq. (2.24). The geostrophic relative vorticity is mapped directly from the layered velocities using an OA scheme similar to the one for the stream function (see *Hua et al.* [1986] for details). The stretching term in each layer is built using the previously gridded layered stream functions. A PV front defining the region of confluence between the retroflecting NBC and the flow associated with the cyclonic turn of the NEC water is evident in the upper-layer PV fields (Figure 2.13, upper panels). The beta-term seems to dominate the QG potential vorticity in the second and third

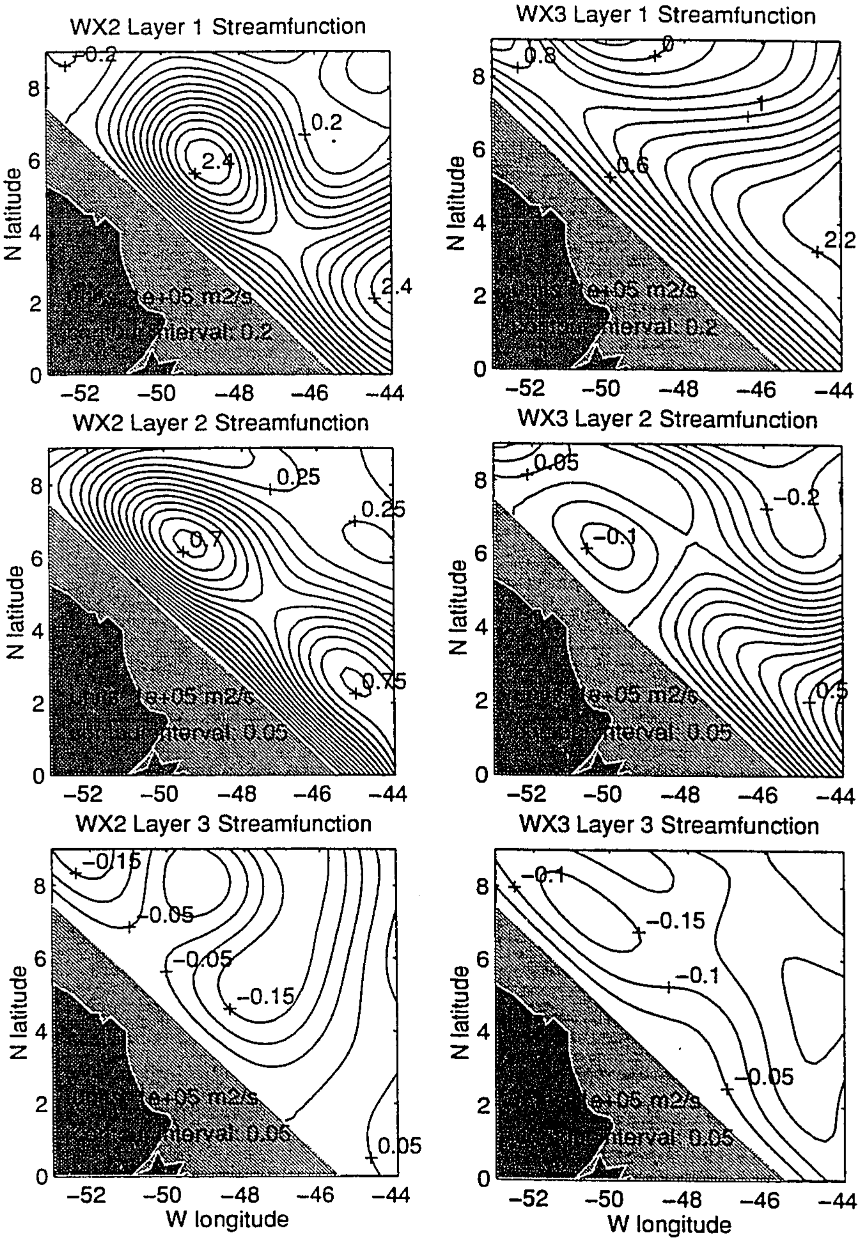

Figure 2.12: The three-layer QG stream function fields for WX2 (left panels) and WX3 (right panels). Units: 1×10^5 m^2/s.

layers. Nevertheless, in the WX2 PV fields (Figure 2.13, left panels), both upper and middle layers exhibit closed PV contours associated with the shedding eddy.

Quantitatively, the upper layer PV fields reflect the borderline character of the QG assumption in the WESTRAX region. For example, in the WX2 upper layer (Figure 2.13, left upper panel), the change in $\hat{q}_1$ over one deformation radius and across the shedding eddy is 1.74×10^{-5}/s (f_0 is 1.27×10^{-5}/s). There are comparable changes in $\hat{q}_1$ transversing the separating NBC at the eastern border of the WESTRAX area. The $\hat{q}_1$ variation with latitude along 44°W in Figure 2.14 shows that a PV front can be denied in the region of maximum PV gradient between 4°N and 6°N. The meridional variation of the three components of the PV field (the relative vorticity, the beta term and the stretching term) are also plotted in Figure 2.14. The relative vorticity is about 20% smaller than stretching term. However, the cross-frontal change in relative vorticity is two times larger than that of the stretching term.

We can compare the NBC cross-frontal variation of QG potential vorticity and its components with more poleward situations, such as the Gulf Stream's presented by *Hall* [1985]. Unlike the NBC configuration (Figure 2.14), the relative vorticity is about only 25% of the stretching term. Such difference should be examined carefully because *Hall's* [1985] transect was located 15 deformation radii away from the coast, while in the NBC case, the transect is close to the western boundary. As expected, the beta-term is one order of magnitude smaller than the other terms in the Gulf Stream case. In the NBC case, the upper layer PV cross-frontal gradient is 3.8β.

The PV cross-frontal change in Gulf Stream's upper layers over one deformation radius (about 50 km) is about 1.3×10^{-4}/s (f_0 is 0.9×10^{-4}/s) [*Hall's*, 1985], not very different from the $1.37f_0$ obtained for the NBC.

For this NBC three-layer model, we could eliminate the PV values larger in magnitude than f_0 by deepening the upper two layers (i.e., choosing other H_i's). However, due to the large size of β and less intense velocities, it is likely that the

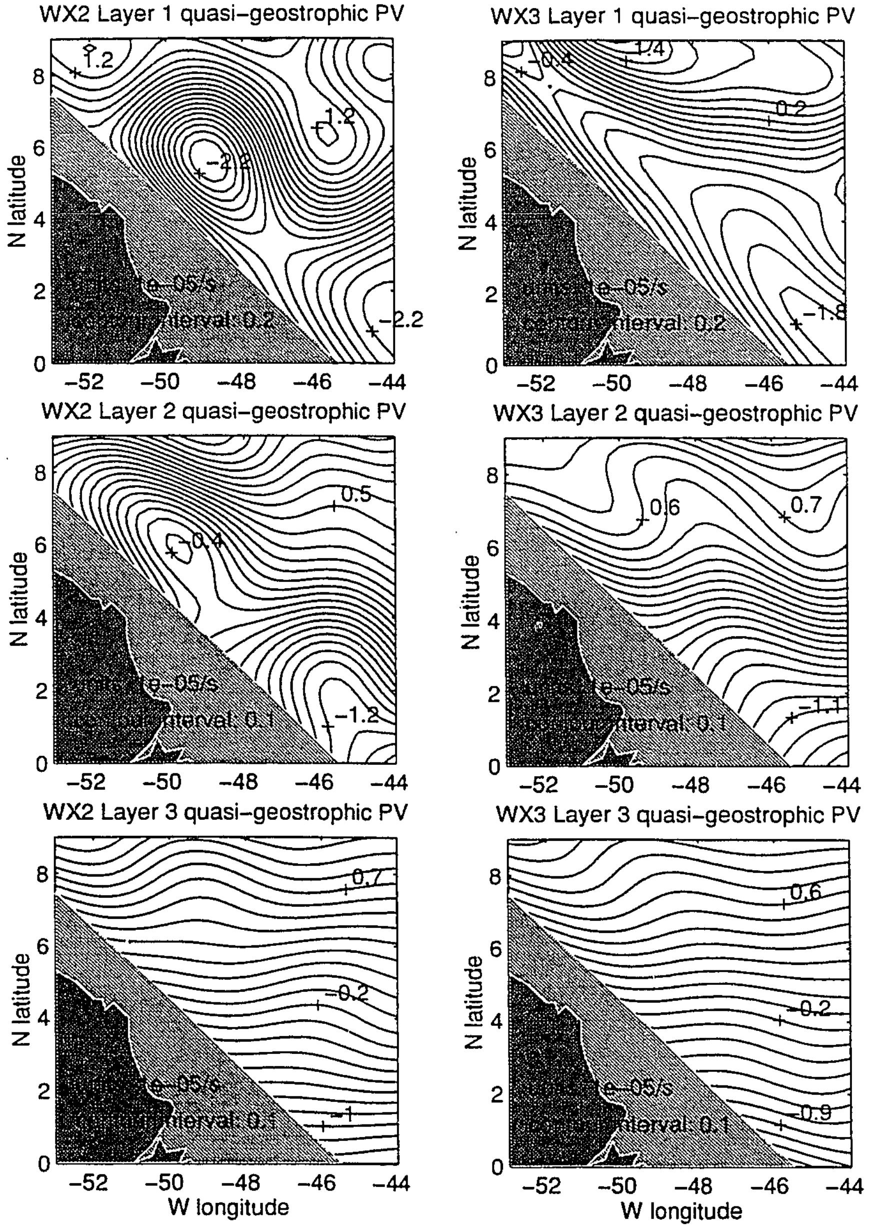

Figure 2.13: The three-layer QG potential vorticity fields for WX2 (left panels) and WX3 (right panels). Units 1×10^{-5}/s.

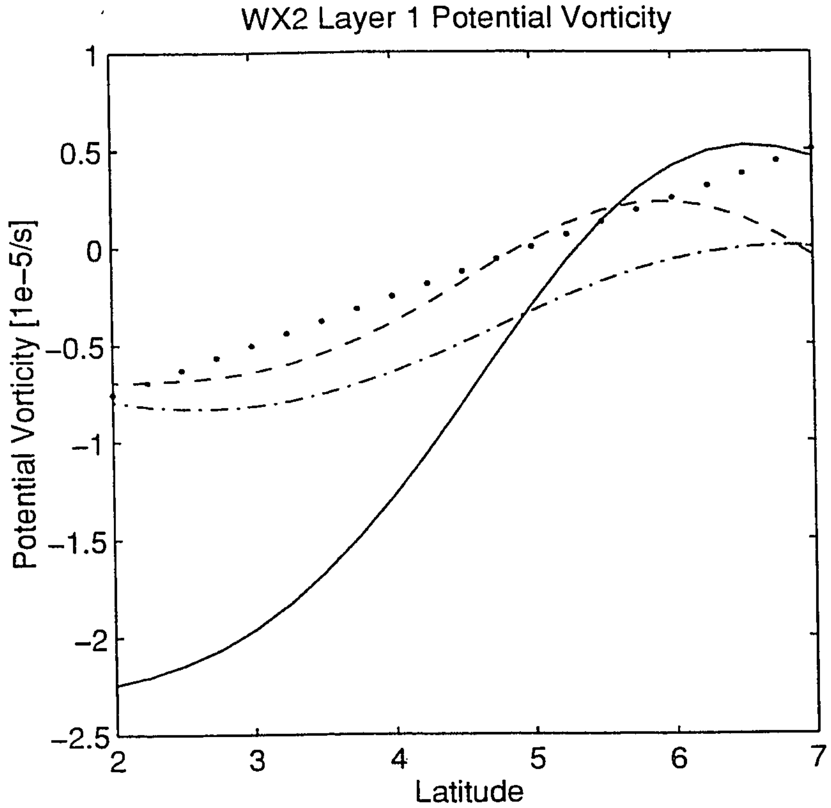

Figure 2.14: Meridional variation of the upper layer QG potential vorticity (solid line) along 44°W. The vorticity (dashed line), the stretching (dashed-dotted lines), and the "beta" (dotted line) terms are also represented.

middle layer would not then represent the pinching-off eddy properly. *Silveira et al.* [1994] approximated the NBC retroflection region as a two-layer system. Given a 750m deep upper layer, variations on $\hat{q}_1$ over one deformation radius were typically $0.7 f_0$. In that work, we were able to isolate the NBC eddy activity on the upper layer and the DWBC on the deeper layer. Nevertheless, the two-layer approximation filtered out the second baroclinic mode, which is shown by our DEOF calculation (Section 2.3) to be more important in the NBC dynamics than the barotropic mode. We believe that a three-layer approximation better represents the NBC dynamics despite the borderline values of the PV in the upper layer.

We can evaluate ageostrophy in the three-layer model by building the full PV fields and comparing to the QG ones in Figure 2.13. The full layered-PV expression is given by

$$\hat{\Pi}_i = \frac{\hat{\zeta}_{p_i} + f}{h_i} \quad , \tag{2.28}$$

where h_i is the *ith* layer thickness. We grid ζ_{p_i} using the same OA scheme used for gridding $\hat{\zeta}_i$ in the QG version. However, here the *ith*-layer velocity vectors are the averages of the Pegasus velocities over the corresponding h_i. The layer thicknesses are defined by the rigid surface lid, the topography of the σ_θ=26.10 and 27.45 and the flat bottom respectively. The hydrostatic depths of the σ_θ=26.10 and 27.45 are 150 m and 1000 m respectively. Thus, the rest thicknesses H_1=150, H_2=850 and H_3 = 3000 m are the same as in the QG model.

For direct comparisons with the quantities in Figure 2.13, it is convenient to define an anomalous full layered-PV according to

$$\hat{\Pi}'_j = H_i \hat{\Pi}_i \delta_{ij} - f_0 \quad , \tag{2.29}$$

where δ_{ij} is the Dirac delta.

The results for WX2 and WX3 shown in Figure 2.15 reveal patterns identical to the QG fields in Figure 2.13. For the upper-layer fields, the *rms* differences, defined as

$$rms = \sqrt{\frac{\langle(\hat{\Pi}_i' - \hat{q}_i)^2\rangle}{\langle(\hat{\Pi}_i')^2\rangle}} \ ,$$

are 0.36 for WX2 and 0.39 for WX3. But, PV gradients are dynamically more important then the actual values of PV itself, and in particular, we should look for cross-stream (or cross-frontal) PV gradients. We then estimate the *rms* differences between the meridional gradients along 44°W of $\hat{\Pi}_1'$ and $\hat{q}_1$ to be 0.29 for WX2 and 0.22 for WX3. These calculations are consistent with the estimates in Section 2.2, in which the ageostrophic terms are of $O(Ro)$ ≈0.35 in the WESTRAX region

Our QG analysis of the WESTRAX data set can provide some information about the processes involved in the NBC eddy-shedding phenomenon. Geophysical instability may be important [*Johns et al.*, 1990]. However, the standard QG infinite zonal jet stability theorems cannot be applied here since the NBC is a retroflecting curvilinear current system and the eddy-shedding takes place close to the coast. But it is possible to determine whether the necessary conditions for instability required by the first *Arnol'd* [1966] nonparallel flow theorem are satisfied. For a flat-bottomed, three-layer ocean, the necessary conditions for instability by the first Arnol'd [1966] theorem are reduced to simply

$$\frac{\partial \hat{q}_i}{\partial \hat{\psi}_i} < 0 \qquad (2.30a)$$

$$\frac{\partial \theta_s}{\partial \hat{\psi}_i} > 0 \ , \qquad (2.30b)$$

where θ_s is the surface temperature. Also, the *Arnol'd* [1966] conditions refer to flow and potential vorticity fields in absence of perturbations, i.e., steady states. Hence, if there exists a steady NBC, it more likely resembles the WX3 fields, in which the eddy has been shed and the NBC front has retracted.

The results displayed in Figure 2.16 show negative correlations between the $\hat{\psi}_i$ and $\hat{q}_i$ in all three layers. The same procedure is repeated for the condition of Eq. (2.23b), and the results are shown in Figure 2.17. Using Fisher's Z transformation,

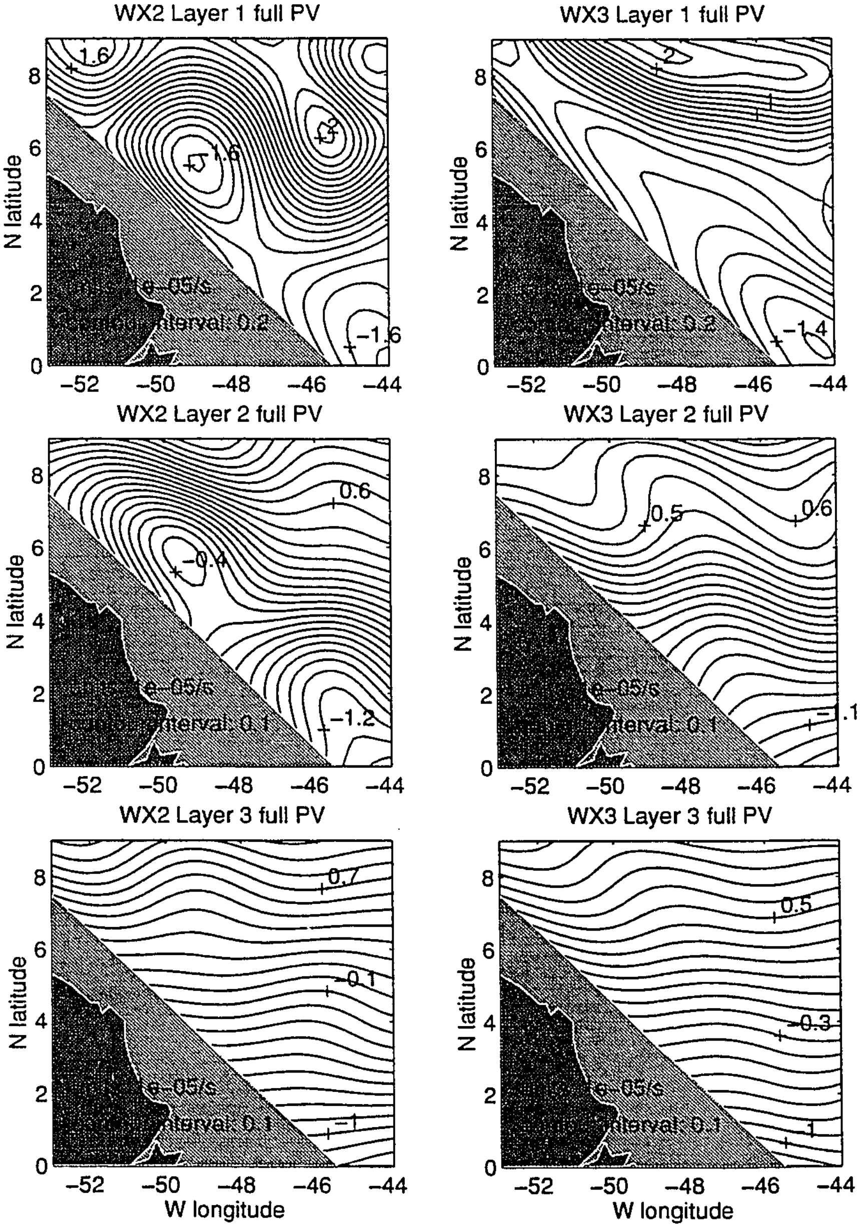

Figure 2.15: The anomalous full potential vorticity fields for WX2 (left panels) and WX3 (right panels). Units: 1×10^{-5}/s.

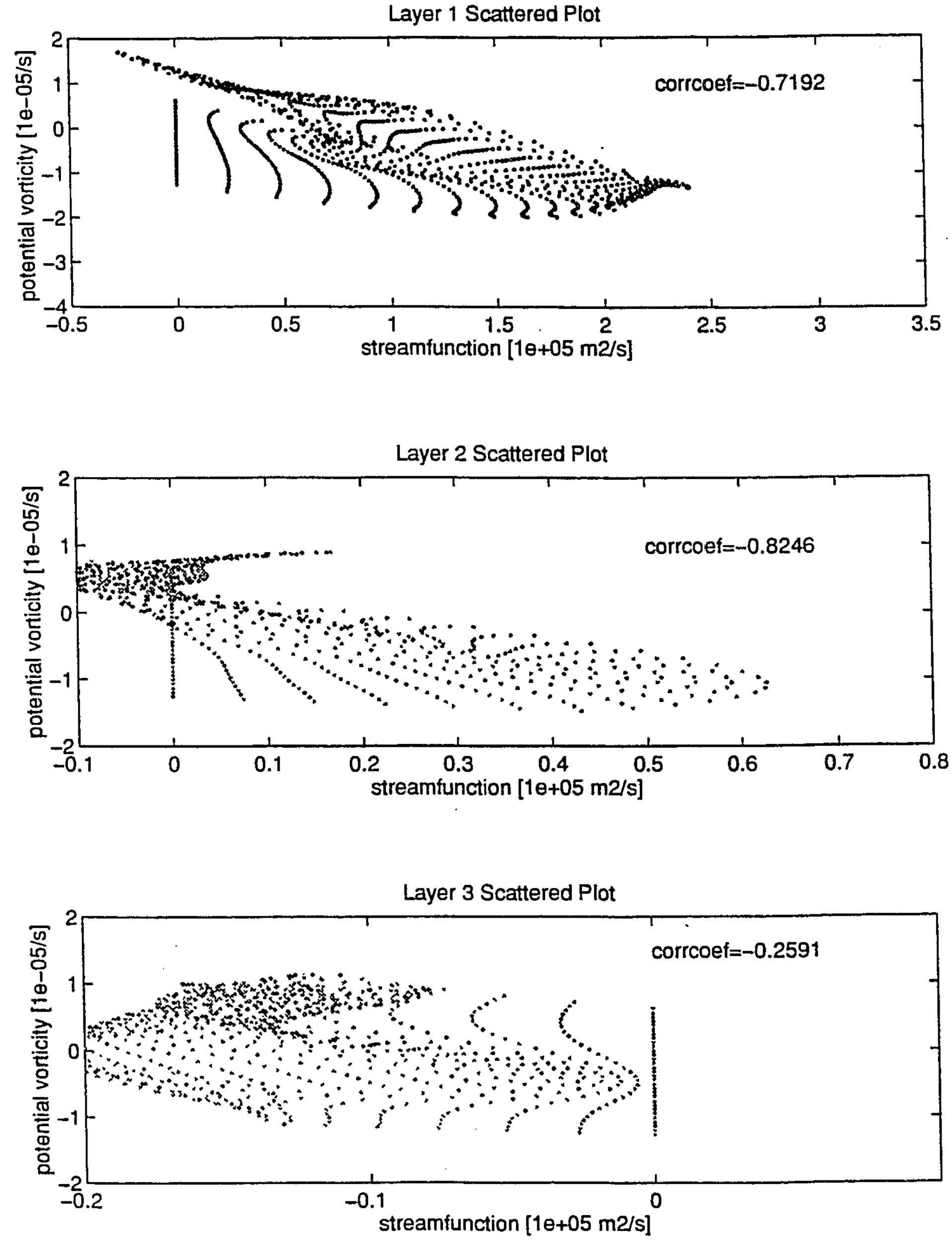

Figure 2.16: Scattered plots between stream function and potential vorticity fields for the three layers in WX3. The correlation coefficients are indicated on the upper right corner of each panel.

we find that all correlation coefficients are significant at the 95% confidence level. Therefore, the first *Arnol'd* [1966] theorem necessary (but not sufficient) conditions for instability are satisfied. Thus, it is plausible that a geophysical instability mechanism is responsible for the NBC eddy-shedding. The question then is: if there is an instability, what kind of instability is it?

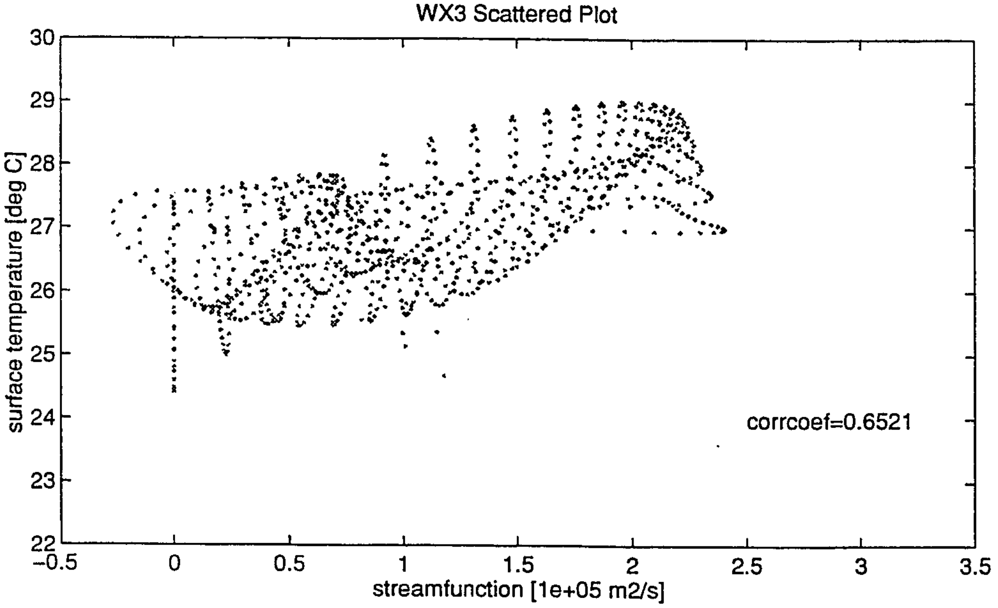

Figure 2.17: Scattered plot between upper-layer stream function and surface temperature fields in WX3. The correlation coefficient is indicated on the upper right corner of the panel.

To address this question, we build on *Davis and Emanuel's* [1991] ideas of applying the invertibility and superposition principles to verify whether there are baroclinic interactions among the layers. The WX2 three-layer fields are used in this analysis.

First, we define the *ith*-layer PV field as a sum of a mean part (i.e., the "beta" term) and an anomalous part:

$$\hat{q}_i = \beta y + \hat{q}_i'. \tag{2.31}$$

From the inversion relationship Eq. (2.24), it can be noticed that there is no flow associated with the mean PV part. Hence, the *ith*-layer stream function $\hat{\psi}_i$ is due solely to the PV anomaly field as defined in Eq. (2.31).

Second, using the superposition principle, we partition the *ith*-layer stream function field into four parts:

$$\hat{\psi}_i = \sum_{j=1}^{3} \hat{\psi}_{i(j)} + \hat{\varphi}_i \ . \tag{2.32}$$

We define $\hat{\psi}_{i(j)}$ as the *ith*-layer "interior" domain stream function induced by PV anomalies in the *jth*-layer only and $\hat{\varphi}_i$ as the *ith*-layer "boundary" domain stream function.

It is possible to orthogonalize $\hat{\psi}_{i(j)}$ and $\hat{\varphi}_i$ using Eq. (2.25), yielding

$$[\hat{\psi}_{i(j)}, \hat{\varphi}_i] = [\hat{\Psi}_m{}^{(j)}, \hat{\varphi}_m] \hat{F}_m{}^i \ , \tag{2.33}$$

where $\hat{\Psi}_m{}^{(j)}$ is the *mth*-mode "interior" domain stream function induced by PV anomalies in the *jth*-layer, and $\hat{\varphi}_m$ is the *mth*-mode "boundary" domain stream function.

Third, we solve for $\hat{\Psi}_m{}^{(j)}$ and $\hat{\varphi}_m$ using the modal inversion expressions in the WESTRAX region domain, i.e.,

$$(\nabla^2 - \hat{\lambda}_m)\hat{\Psi}_m{}^{(j)} = \hat{Q}_m{}^{(j)'} \tag{2.34a}$$

$$\hat{\Psi}_m{}^{(j)} = 0 \quad \text{at the WESTRAX region boundaries} \tag{2.34b}$$

and

$$(\nabla^2 - \hat{\lambda}_m)\hat{\varphi}_m = 0 \tag{2.35a}$$

$$\hat{\varphi}_m = \hat{\Psi}_m \quad \text{at the WESTRAX region boundaries} \tag{2.35b}$$

$\hat{Q_m}^{(j)'}$ represents the PV anomaly field in the *mth* mode due to PV anomalies in the *jth* layer only, being mathematically defined by

$$\hat{Q_m}^{(j)'} = \frac{H_i}{H}\hat{F_m}^{i} q_i \delta_{ij} \ . \tag{2.36}$$

The last step is to map $\hat{\psi}_{i(j)}$ and $\hat{\varphi}_i$ using Eq. (2.33). On the upper panels of Figure 2.18, we show the results for the sum of the three upper layer (left panels) and middle layer (right panels) interior domain stream functions (i.e., $\sum_{j=1}^{3} \hat{\psi}_{1(j)}$ and $\sum_{j=1}^{3} \hat{\psi}_{2(j)}$). On the lower panels of Figure 2.18, we show the results for the boundary domain stream functions $\hat{\varphi}_1$ (upper panel) and $\hat{\varphi}_2$ (lower panel). It is seen that in the vicinity of the pinching-off eddy in the two layers, the flow is almost entirely due to the interior stream function component (dashed lines). Then, on the right (left) panels of Figure 2.19 we show the individual $\hat{\psi}_{i(j)}$ for the upper (subthermocline) layer. The solid line represents the (total) PV contour in the center of the front for each layer. It can be seen that $\hat{\psi}_{1(2)}$ (right center panel) and $\hat{\psi}_{2(1)}$ (left upper panel) are enhancing the retroflection bulge in the two layers. In other words, the flow induced in the upper layer by the PV anomalies on the middle layer is increasing the displacement of the PV contour in the upper layer and vice-versa (see arrows in Figure 2.19). This layer interaction is indicative of baroclinic instability mechanisms.

It is also seen that cross-frontal velocities, i.e., the velocities on the right-hand corner of the bulge in the PV contour that account for the eddy pinch-off, occur in the upper layer when induced by PV anomalies in the upper layer itself. This may indicate either that another instability mechanism (such as the barotropic instability found by *Springer and Kawase* [1993] in their $1\frac{1}{2}$-layer model of low-latitude boundary currents) is also contributing or that nonlinear vortex dynamics causes the eddy occlusion. Very likely, though, both mixed-instability mechanisms and nonlinear dynamics are present in the NBC eddy-shedding phenomenon.

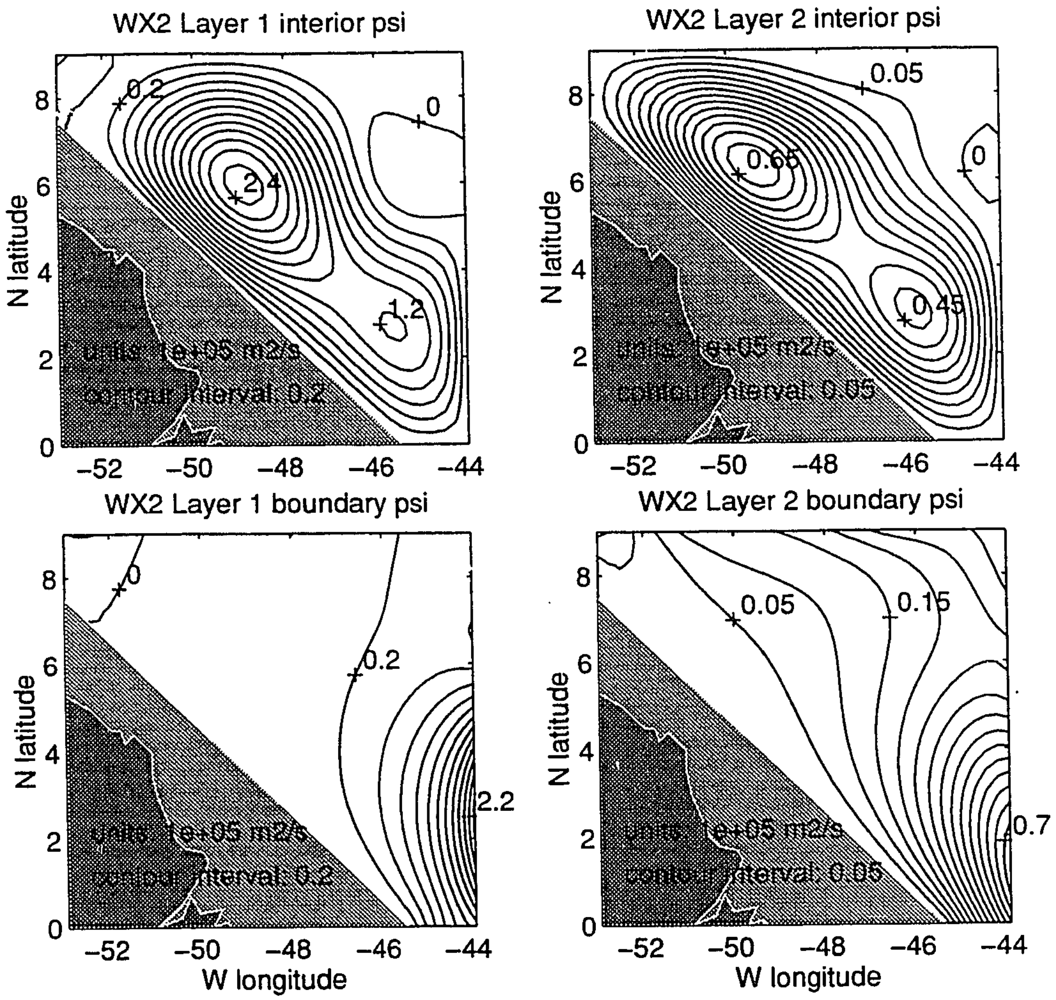

Figure 2.18: The WX2 interior stream function (top panels) and boundary stream function (bottom panels). Upper layer fields on the left, and middle layer fields on the right.

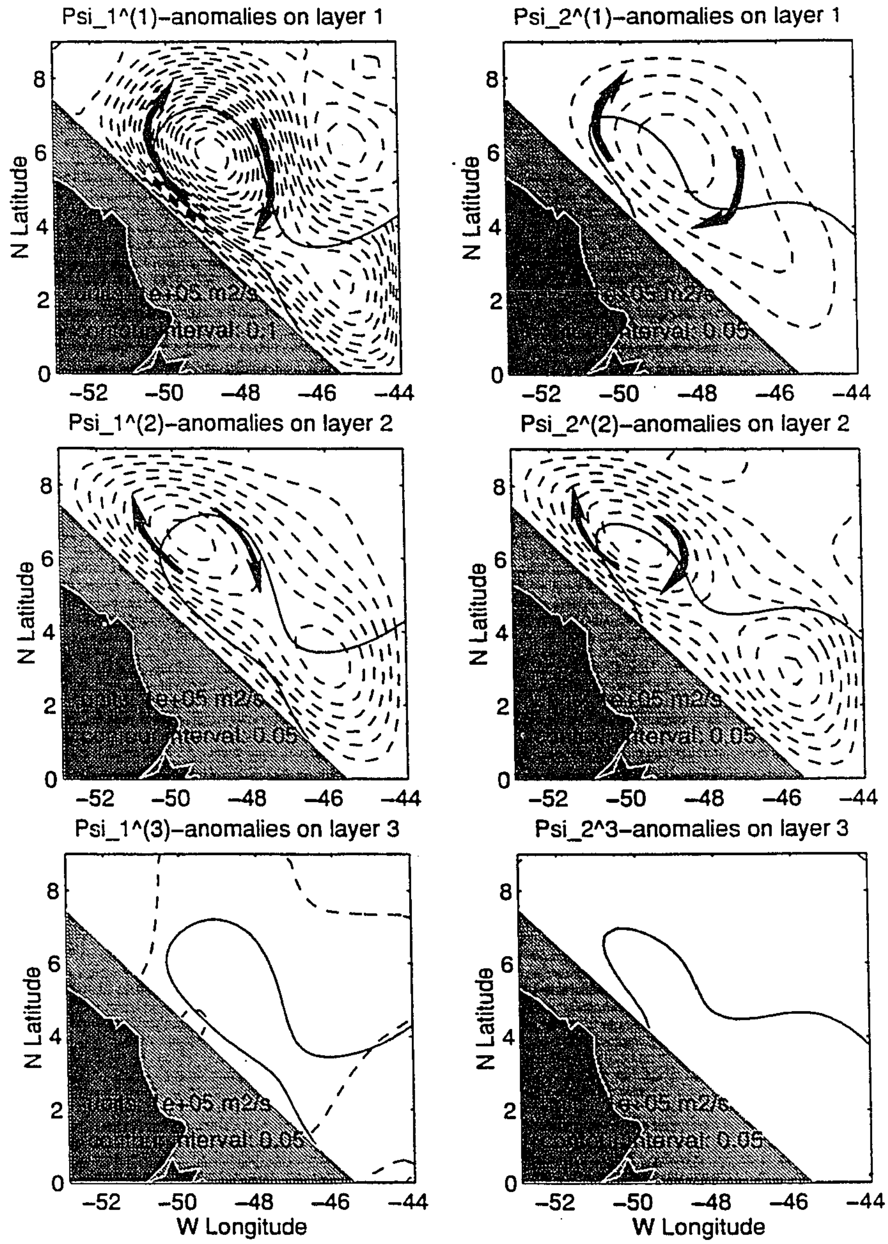

Figure 2.19: The WX2 interior stream function components. On the left panels: $\psi_{1(1)}$ (top), $\psi_{1(2)}$ (center), and $\psi_{1(3)}$ (bottom). On the right panels: $\psi_{2(1)}$ (top), $\psi_{2(2)}$ (center), and $\psi_{2(3)}$ (bottom).

2.5 Summary and Conclusions

Evidence from the literature suggests that despite being a near-equatorial region, the NBC retroflection flows are essentially geostrophic. Thus, using the Western Tropical Atlantic Experiment (WESTRAX) synoptic data set, we investigate the dynamical structure of the NBC retroflection employing the quasi-geostrophic theory.

The Rossby number for the WESTRAX region (north of 1°N) is estimated in different ways by checking the basic QG assumptions on the WX2 survey. The WX2 cruise is chosen because it captured the NBC in the act of shedding an eddy, and thus very likely represents an upper-bound in terms of nonlinearities for the WESTRAX data set. A β-plane centered at 5°N is considered in all calculations. It is found that the typical Rossby number Ro for the WESTRAX region is 0.35. In addition to quantitative estimates based on statistics, qualitative assessments based on horizontal pattern comparisons are presented. There is a remarkable resemblance between the geostrophic flows (computed from hydrography) and the Pegasus flow structure.

The QG theory is then used to determine the NBC modal structure. The QG dynamical modes and the corresponding deformation radii are computed using the average WESTRAX Brunt-Väisälä profile. The first two depth empirical orthogonal functions (DEOF) modes, computed from the Pegasus velocity profiles, explain about 90% of the variance in vertical structure of the NBC region. Optimal fits of the dynamical modes onto the DEOF modes suggest that DEOF mode 1 is dominated by dynamical mode 1, and DEOF mode 2 by dynamical mode 2. The sum of the first three dynamical modes were found to account for about 90% of the vertical structure within the WESTRAX region, with a sum of six-mode approximation reproducing the WESTRAX profiles nearly exactly. These results corroborate those from *Johns et al.* [1990] time domain EOF analysis on their moored current meter velocities and the dynamical decomposition of the CME model results by *McClean and Klinck* [1995]. Both works, like the results from the present paper, indicate a dominant first (internal) mode. A secondary role is played by the second baroclinic mode.

Based on these findings, a three-layer QG model is built for the flow in the WESTRAX region. The density values within each layer are carefully chosen to reproduce the deformation radii of the continuously stratified model. The calibration procedure used is a modified version of the $2\frac{1}{2}$-layer calibration method by *Silveira and Flierl* [1996]. The three-layer QG approximation for the WX2 survey depicts the NBC in the eddy-shedding phase, while the NBC front has retracted in the WX3 survey. The three-layer stream function fields obtained isolate the NBC eddy activity on the upper two layers. The third and deepest layer is the domain of a southward meandering flow that resembles the DWBC. The NBC retroflection in the upper layer occurs at about 7°N, forming the NECC. The middle layer is characterized by the NBC separation around 4°N to form the NEUC. QG potential vorticity fields are presented for both cruises. The variation of the upper layer PV ($\hat{q}_1$) over one deformation radius, which may define a PV scale, is about $1\frac{1}{3}$ times the Coriolis parameter. It is discussed that mid-latitude systems, such as the Gulf Stream, present similar cross-stream variations [*Hall*, 1985]. The full-layered nonlinear PV fields of flat-bottom ocean are also computed and compared with their QG counterparts. The *rms* differences between upper layer QG and full PV fields are about 0.37, and therefore consistent with our estimates for *Ro*. The *rms* differences for the second and third layer are considerably smaller since they are dominated by the beta term.

The necessary (but not sufficient) conditions for instability based on the first *Arnol'd* [1966] theorem for curved flows are evaluated for the WX3 survey. The WX3 survey is chosen because the authors believe that a retracted NBC front is likely to be closer to the steady state required for the application of the *Arnol'd* theorem. All conditions are satisfied. We then perform a calculation on the WX2 data set designed to isolate the effect of PV anomalies in each of the layers on each of the layers. Our results suggest that baroclinic interactions occur, with upper layer PV anomalies inducing extension of the middle layer eddy and vice-versa. A detailed discussion of possible mechanisms was presented by *Johns et al.* [1990]. They speculated on a local instability process modulated (or triggered) by the 50-day Rossby waves. Our results indicate that baroclinic instability is a participating process. An idealized three-layer QG model that simulates the NBC and its periodic modulation may provide some clarifications to this fascinating phenomenon.

Appendix: The Three-Layer Calibration Scheme

This calibration procedure extends the *Silveira and Flierl* [1996] $2\frac{1}{2}$-layer calibration scheme to three-layers. The goal of the calibration is to match the two internal deformation radii of the three-layer model to those of the continuously stratified ocean by obtaining special density jump values between the layers. Choices for f_0 and the rest depths (H_1, H_2, H_3) are required, as well as a previous computation of the eigenvalues (or deformation radii) of the continuously stratified model.

The determinant of Eq. (2.26) is calculated, giving

$$\begin{aligned} \hat{\lambda}_i^3 &- \frac{f_0^2}{g}\left[\frac{1}{\epsilon_1 H_1} + \frac{1}{\epsilon_1 H_2} + \frac{1}{\epsilon_2 H_2} + \frac{1}{\epsilon_2 H_3}\right]\hat{\lambda}_i^2 \\ &+ \frac{f_0^4}{g^2}\left[\frac{1}{\epsilon_1\epsilon_2 H_1 H_2} + \frac{1}{\epsilon_1\epsilon_2 H_1 H_3} + \frac{1}{\epsilon_1\epsilon_2 H_2 H_3}\right]\hat{\lambda}_i = 0 \ . \end{aligned} \tag{A1}$$

Consequently,

$$\hat{\lambda}_0 = 0 \tag{A2a}$$

$$\hat{\lambda}_1 + \hat{\lambda}_2 = \frac{f_0^2}{g}\left[\frac{1}{\epsilon_1 H_1} + \frac{1}{\epsilon_1 H_2} + \frac{1}{\epsilon_2 H_2} + \frac{1}{\epsilon_2 H_3}\right] \tag{A2b}$$

$$\hat{\lambda}_1\hat{\lambda}_2 = \frac{{f_0}^4}{g^2}\left[\frac{1}{\epsilon_1\epsilon_2H_1H_2} + \frac{1}{\epsilon_1\epsilon_2H_1H_3} + \frac{1}{\epsilon_1\epsilon_2H_2H_3}\right] \quad . \tag{A2c}$$

Eqs. (A2b) and (A2c) can be easily manipulated to obtain a quadratic expression for ϵ_1:

$$\frac{1}{{\epsilon_1}^2}\left[\frac{H(H_1+H_2)}{{H_1}^2H_2(H_2+H_3)}\right] - \frac{1}{\epsilon_1}\left[\frac{g}{{f_0}^2}(\hat{\lambda}_1+\hat{\lambda}_2)\frac{H}{H_1(H_2+H_3)}\right] + \frac{g^2}{{f_0}^4}(\hat{\lambda}_1\hat{\lambda}_2) = 0 \quad . \tag{A3}$$

The expression for ϵ_2 is simply given by

$$\frac{1}{\epsilon_2} = \left[\frac{H_2H_3}{H_2+H_3}\right]\left\{\frac{g}{{f_0}^2}(\hat{\lambda}_1+\hat{\lambda}_2) - \frac{1}{\epsilon_1}\left[\frac{H_1H_2}{H_1+H_2}\right]\right\} \quad . \tag{A4}$$

Finally, ϵ_1 and ϵ_2 are obtained by using $\hat{\lambda}_1 = \lambda_1$ and $\hat{\lambda}_2 = \lambda_2$, and therefore matching the deformation radii of the layered model to the values of the corresponding continuously stratified ocean.

It is evident from Eqs. (A3) and (A4) that, as in *Silveira and Flierl*'s [1996] method, there is some freedom left in the system and the calibration outputs two sets of values for ϵ_1 and ϵ_2. We suggest that decision between the two pairs of values be made through comparisons with ϵ's calculated from averaging the density profile used on the *Rd* computation.

References

Arnault, S., Tropical Atlantic geostrophic currents and ship drifts, *J. Geophys. Res., 92(C5)*, 5076-5088, 1987.

Arnol'd, V.I., On the a priori estimate in the theory of hydrodynamical instability, *Isv, Vyssh Uchebn. Zaved. Mat., 54(5)*, 3-5, 1966.

Bretherton, F.P., R.E. Davis and C.B. Fandry, A technique for objective analysis and design of oceanographic experiments applied to MODE-73, *Deep-Sea Res., 23*, 559-582, 1976.

Brown, W.S., W.E. Johns, K.D. Leaman, J.P. McCreary, R.L. Molinari, P.L. Richardson and Rooth, C., A western tropical Atlantic experiment (WESTRAX), *Oceanography 5(1)*, 73-77, 1992.

Bruce, J.G., Comparison of eddies off the North Brazilian and Somali Coasts, *J.Phys.Oceanogr., 14*, 825-832, 1984.

Bruce, J.G. and J.L. Kerling, Near equatorial eddies in North Atlantic. *Geophys. Res. Lett., 11(8)*, 779-782, 1984.

Bub, F.L. and W.S. Brown, Intermediate layer water masses in the western tropical Atlantic Ocean, *accepted for publication in J. Geophys. Res.*, 1996.

Bub, F.L. and W.S. Brown, Seasonal changes in the intermediate layer transport of mass and heat in the western tropical Atlantic Ocean, *submitted to in J. Geophys. Res.*, 1996.

Carter, E.F. and A.R. Robinson, Analysis models for the estimation of oceanic fields, *J.Atm.Oc.Tech., 4(1)*, 49-74, 1987.

Cochrane, J.D., F.J. Kelly and C.R. Olling, Subthermocline countercurrents in the western equatorial Atlantic Ocean. *J.Phys.Oceanogr., 9*, 724-738, 1979.

Davis, C.A. and K.A. Emanuel, Potential vorticity diagnostics of cyclogenesis, *Mon. Wea. Rev., 119 (8),* 1929-1953, 1991.

Davis, R.E., Predictability of sea surface temperature and sea level pressure anomalies over the North Pacific Ocean, *J.Phys.Oceanogr., 6(3)*, 249-266.

Didden, N, and F. Schott, Seasonal variations in the western tropical Atlantic: surface circulation from Geosat altimetry and WOCE model Results, *J. Geophys. Res., 97(C3)*, 3529-3541, 1992.

Didden, N, and F. Schott, Eddies in the North Brazil Current retroflection region observed by Geosat altimetry, *J. Geophys. Res., 98*, 20121-02131, 1993.

Frantatoni, D.M., W.E. Johns and T.L. Townsend, Rings of the North Brazil Currents: their structure and behavior inferred from observations and a numerical simulation, *J. Geophys. Res., 100(C6)*, 10633-10654, 1995.

Flierl, G.R., Models of vertical structure and the calibration of two-layer models,*Dyn.Atm.and.Oc., 2*, 341-381, 1978.

Gill, A.E., Atmosphere-ocean dynamics, *Academic Press*, 652 pp., 1982.

Hall, M.M., Horizontal and vertical structure of velocity, potential vorticity and energy in Gulf Stream, Ph.D. thesis, WHOI/MIT Joint Program in Oceanography, WHOI-85-16, 165pp, 1985.

Hua, B.L., McWilliams, J.C., and Owens, W.B., An objective analysis of the POLYMODE local dynamics experiment. Part II: stream function and potential vorticity fields during the Intensive Period, *J.Phys.Oceanogr., 16*, 506-522.

Johns, W.E., T.N. Lee, F. Schott, R. Zantopp and R.H. Evans, The North Brazil Current retroflection: seasonal structure and eddy variability, *J.Phys.Oceanogr., 95(C12)*, 22103-22120, 1990.

Klinck, J.M., EOF analysis of central Drake Passage currents from DRAKE 79, *J.Phys.Oceanogr., 15*, 288-298, 1984.

McClean, J.L. and J.M. Klinck, Description and vorticity analysis of the 50-day oscillations in the western tropical Atlantic region of the CME model, *J.Phys.Oceanogr., 25*, 2498-2517.

Molinari, R.L., B. Voituriez and P. Ducan, Observations in the subthermocline undercurrent of the equatorial South Atlantic Ocean: 1978-1980, *Oceanologica Acta, 4(4)*, 451-456, 1981.

Pedlosky, J., Geophysical fluid dynamics, Springer-Verlag, 770 pp, 1979.

Pinardi, N and A.R. Robinson, Dynamics of deep thermocline jets in the POLYMODE region, *J.Phys.Oceanogr., 17(8)*, 1163-1188.

Richardson, P.L. and T.K. McKee, Average seasonal variation of the Atlantic equatorial currents from historical ship drifts, *J.Phys.Oceanogr., 14(7)*, 1226-1238, 1984.

Schott, F., and C.W. Böning, The WOCE model in the western equatorial Atlantic: upper layer circulation, *J. Geophys. Res., 96(C4)*, 6993-7004, 1991.

Silveira, I.C.A. da, W.S. Brown and Flierl, G.R., A Quasi-geostrophic study of the North Brazil Current retroflection eddies (abstract), *EOS Trans. AGU, 75(3)*, Ocean Sciences Meeting Suppl., 225, 1994.

Silveira, I.C.A. da, and Flierl, G.R., Eddy formation in $2\frac{1}{2}$-layer, quasi-geostrophic jets (in preparation)

Springer, S.R. and M. Kawase, Nonlinear and dissipative dynamics in the connection region between western boundary currents and equatorial currents, *J. Geophys. Res., 98*, 12511-12525, 1993.

Young, W.R., Baroclinic theories of the wind driven circulation, in *General circulation of the ocean*, pp.134-200, H.D.I. Abarbanel and W.R.Young, Springer-Verlag, 1987.

Chapter 3

Dynamics of $1\frac{1}{2}$-Layer Separating Jets

Abstract

In this work, we connect *Pratt and Stern*'s [1986] quasi-geostrophic, $1\frac{1}{2}$ layer, infinite jet model to a western boundary by a system of two converging boundary currents. The model has a piecewise constant potential vorticity structure and the departing jet has a zonal cusplike profile in the ocean interior. The relative strengths of the coastal jets can be varied and the coastline can be tilted relative to the north. The coastline tilt and the coastal current asymmetry cause an alongshore momentum imbalance that creates a spatially damped, quasi-stationary wave pattern. The presence of the boundary favors the long waves on the model, which behave fairly linearly in all study cases. As a consequence, no coastal eddy detachment is obtained in this work. The effects of the coastline tilt and the coastal current asymmetry are varied to reinforce or cancel each other. In the former case, a retroflection type of boundary current separation, like the one observed in most Southern Hemisphere western boundary currents, is obtained. In the latter case, a much smoother separation results, as when the Gulf Stream leaves the North American coast. In order

to comply with the piecewise constant potential vorticity constraint, the β-effect is included in the model only very crudely. The "beta" term in the potential vorticity relationship is totally compensated by a steady flow pattern similar to the edge between two Fofonoff gyres. It is found that when β is nonzero, the wavelengths are somewhat shorter than those of f-plane cases.

3.1 Introduction

Meanders and Rossby-wave-like motion are often found in regions where western boundary currents separate from continental margins. In some cases, the current separation is smooth and the meander amplitudes increase toward the ocean interior (Figure 3.1a). In others, the current overshoots its separation latitude and retroflects (i.e., turns back on itself), forming a large amplitude lobe near the coast and meanders which decay in the downstream direction (Figure 3.1b). Eddy detachment may occur in both types of separation. When the separation is smooth, eddies are pinched off in the downstream region, where the western current extension may be regarded as a free jet. When a current retroflects, the eddy-shedding usually takes place close to the coast.

Ou and De Ruijter [1986] reproduced both types of boundary current separation using a steady, semi-geostrophic equivalent-barotropic model that employed only current inertia and the variation of the Coriolis parameter in a constant potential vorticity field. The transport magnitude dictated the separation latitude of the jets. The coastline angle (relative to the north) dictated the type of separation. Obtuse angles led to retroflection, while more acute angles produced smooth separation and long standing-wave patterns in the ocean interior.

Ou and De Ruijter's theoretical results are verified in *Campos and Olson*'s [1991] summary of types of western boundary current separation. Looking at the major mid-latitude western boundary currents, the latter authors attribute the smooth sep-

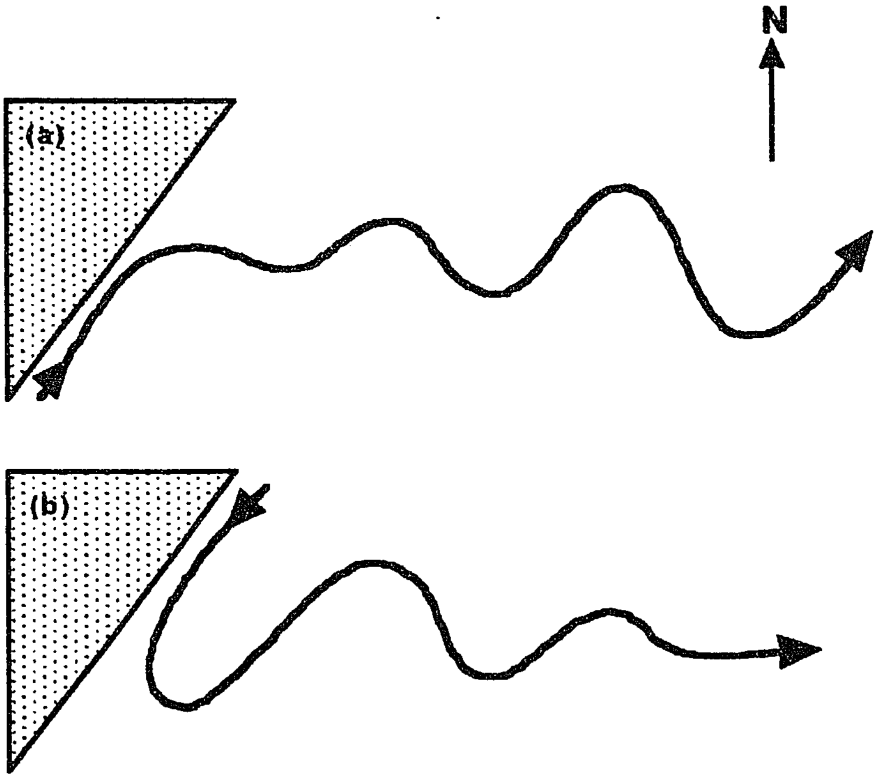

Figure 3.1: Schematic separation of western boundary currents: (a) The Gulf Stream, and (b) the Brazil Current.

aration of the Gulf Stream and the Kuroshio to the fact that both North American and Japanese coasts are tilted towards the east of their general northward direction, following the current. By contrast, all the Southern Hemisphere boundary currents (i.e., the Brazil, East Australia, and Agulhas Currents) which separate from coasts tilted towards the west (of their general southward direction) tend to retroflect.

In the present work, we theoretically investigate the wave motion and meandering associated with separating western boundary currents. Unlike *Ou and De Ruijter*'s [1986] work, we include time variability and make potential vorticity non-constant in order to account for the contrast between the boundary current water and its surroundings. We employ a "contour dynamics" approach to the problem (the reader is referred to *Pullin* [1992] for a review on the contour dynamics method). There are several examples in the literature where contour dynamics has been successfully used to investigate geophysical flows, particularly, jet and vortex dynamics. *Stern and Pratt* [1985] studied barotropic shear flows. *Pratt and Stern* [1986] (hereafter referred to as PS86) examined eddy detachment in infinite equivalent-barotropic jets. *Stern and Flierl* [1987] modeled interactions between vortices and jets. *Polvani et al.* [1989] investigated vortex dynamics in a two-layer fluid. *Meacham* [1991] examined meander development in barotropically and baroclinically unstable jets.

The model used in this work is based on PS86's jet model and has the following principal characteristics:

- Boundary current separation due to a convergence (or collision) of two coastal currents at some separation latitude (Figure 3.2). This approach was originally used by *Cessi* [1991] on viscous system, and by *Agra and Nof* [1993] on an inviscid system. As example, the Gulf Stream separation near Cape Hatteras may be interpreted as the convergence of its warm waters with the weaker southward flow of colder Slope Water. The Brazil Current retroflects as the region of the confluence between the Brazil and the Malvinas currents at about 38°S.

- The coastal current convergence forming a zonal jet downstream. The axis of the major boundary current extension (such as the Gulf Stream extension and the South Atlantic Current) is oriented mainly east-west, having motivated most theoretical models of infinite jets in the literature.

- Inertial equivalent-barotropic physics in a fully nonlinear quasi-geostrophic system. The equivalent-barotropic (or $1\frac{1}{2}$-layer) approximation, where a finite upper layer overlies an infinitely deep motionless layer, is the simplest mathematical formulation for simulating the highly baroclinic structure of the western boundary currents.

- A piecewise constant quasi-geostrophic potential vorticity field as required by the contour dynamics technique. Low uniform potential vorticity is mostly associated with the northward boundary current, and high potential vorticity with the opposing, southward-flowing current region (Figure 3.2). Thus, away from the coast, the zonal jet has uniform cyclonic (positive) potential vorticity on one side of the discontinuity and anticyclonic (negative) potential vorticity on the other side as in PS86. This structure is intended to mimic the meeting of warmer (low potential vorticity) and often stronger boundary currents with colder (higher potential vorticity) and weaker flows in the opposite direction.

- An asymmetry in the transport of the converging currents in the model, prescribed by setting different potential vorticity magnitudes in each half of the model's domain.

- A straight coastline, which can be tilted relative to north-south. It separates land from an infinitely deep ocean. *Campos and Olson*'s [1991] Figure 1 indicates that the continental shelf break for four out of the five mid-latitude basins can be reasonably approximated as a tilted straight line (the exception is the Agulhas Current).

- Incorporation of the beta-effect, but only very crudely. To comply with the piecewise constant potential vorticity constraint, a time-independent flow field, which resembles the edge between two Fofonoff gyres, is included in the model to compensate for the β term. This introduces a westward tendency but does not allow Rossby waves.

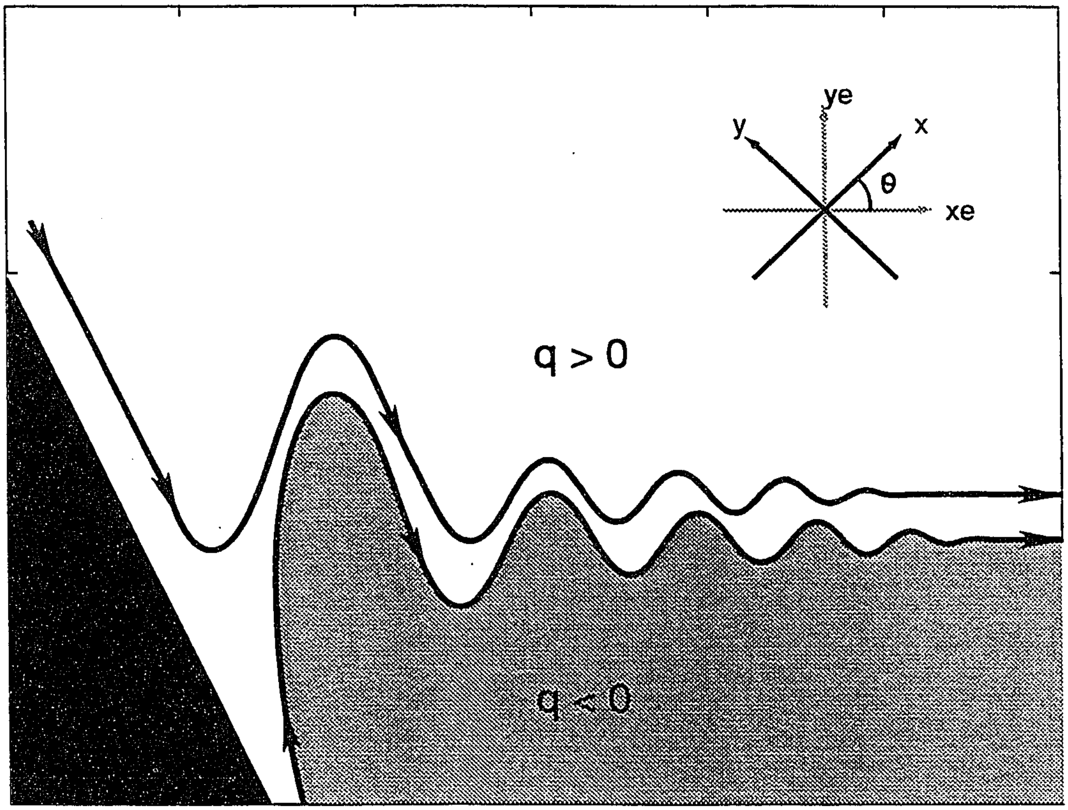

Figure 3.2: The model geometry. The model coordinate system is rotated by an angle θ relative to the "Earth" cartesian coordinates (x_e, y_e).

We intend to examine the dynamical roles of coastline angle, transport asymmetry and the beta-effect, as boundary currents separate from the coast according to the simple geometry sketched in Figure 3.2.

The mathematical formulation of the model is detailed in Section 3.2. The results of the time-dependent model experiments are reported in Section 3.3. The model is applied to the Gulf Stream, Brazil Current and North Brazil Current in Section 3.4. A summary of our main findings is presented in Section 3.5.

3.2 The Model Formulation

The flow in a contour dynamics model is governed by conservation of the quasi-geostrophic potential vorticity, q. Since q is taken to be piecewise constant, all the action in this model is confined to the discontinuity (i.e., a contour). The contour is a material line which separates two pools of uniform potential vorticity with opposite signs (Figure 3.2). If the equivalent-barotropic potential vorticity equation is non-dimensionalized, using the scales of Table 3.1, it takes the form

$$\frac{d}{dt}q = [\frac{\partial}{\partial t} - \frac{\partial\psi}{\partial y}\frac{\partial}{\partial x} + \frac{\partial\psi}{\partial x}\frac{\partial}{\partial y}]q = 0\,, \tag{3.1}$$

where

$$q = (\nabla^2 - 1)\psi + \beta y_e\,, \tag{3.2}$$

ψ is the quasi-geostrophic stream function, β is the Rossby parameter, and y_e is the northward coordinate. Eq. (3.2), known as the inversion relationship, relates the flow structure to the potential vorticity field.

The model frame of reference has been rotated anticlockwise by an angle θ from the usual "Earth" Cartesian coordinate system (x_e,y_e) to make the y-axis parallel to the western boundary (Figure 2). Hence the x and y directions in the model correspond to the cross-shore and alongshore directions, respectively. The angle θ can also be regarded as the prescribed angle that assures the outflowing jet is zonal ($y_e = constant$) at $x_e = \infty$.

Table 3.1: The model variable scales

definition	convention
horizontal length scale (=Rossby radius of deformation)	R_d
horizontal velocity (=f-plane center jet velocity)	U
time scale	$R_d U^{-1}$
potential vorticity	$U R_d^{-1}$
Rossby parameter	$U R_d^{-2}$.

In Section 3.2.1, we formulate the model for the case in which q has a "symmetric" potential vorticity distribution (same magnitude but opposite sign in each half of the model). In Section 3.2.2, we describe the model for an asymmetric potential vorticity configuration.

3.2.1 The Symmetric Front Model

The symmetric model represents two converging boundary currents that have the same transport and thus contribute equally in forming the zonal inertial jet. The non-dimensionalized q is equal to -1 in the lower half of the model, and $+1$ in the upper half. The potential vorticity front is connected to the coast (Figure 3.3a). The inversion relationship (Eq. 3.2) for this case may be rewritten as

$$(\nabla^2 - 1)\psi + \beta y_e = -1 + 2\mathcal{H}(y - \bar{y}(x) - \eta(x,t)) , \tag{3.3}$$

where

$$\bar{y}(x) = -x \tan\theta \tag{3.4}$$

is the "undisturbed" latitude of the zonal jet as x_e approaches ∞ expressed in terms of the model coordinates, $\eta(x,t)$ is the time-dependent deviation relative to $\bar{y}(x)$, and

$$\begin{aligned} \mathcal{H}(y) &= 0 \text{ for } y < 0 \\ \mathcal{H}(y) &= 1 \text{ for } y > 0 \end{aligned}$$

represents the Heaviside step function.

The two non-dimensional parameters of the symmetric model [Eq. (3.3)] are β and θ. Since we assume that the planetary vorticity gradient is much smaller than the relative vorticity, β is kept small throughout the experiments using the symmetric model, with $\beta = 0.1$ being the maximum value considered. This assumption is consistent with the fact that we intend to investigate primarily the separation of mid-latitude boundary currents, for which β is small compared to shear within the

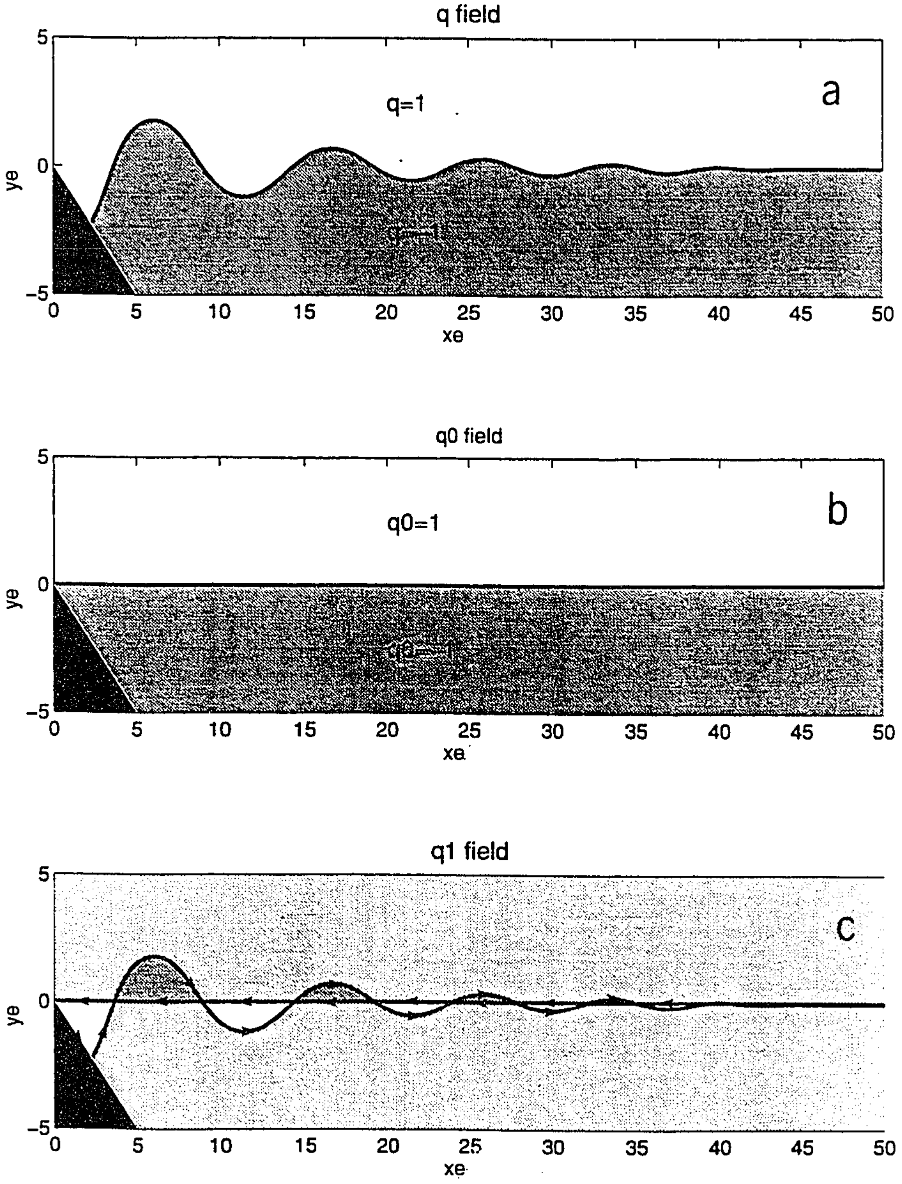

Figure 3.3: (a) The total potential vorticity field q for the symmetric model is composed of: (b) q_0, the part of the field associated with the "undisturbed" position $\bar{y}(x)$ of the front; and (c) q_1, part of the field associated with the deviations from the "undisturbed" field q_0. The arrows indicate the integration direction.

currents. Regarding θ, we will limit our study to the two cases in which the western boundary is either oriented north-south ($\theta = 0$) or tilted at $\theta = \pi/4$.

Following *Stern and Flierl* [1987], we take advantage of the linear nature of Eq. (3.3) and subdivide the stream function in three parts, namely

$$\psi = \psi_0 + \beta\psi_\beta + \psi_1 \,. \tag{3.5}$$

The ψ_0 component, associated with the "undisturbed" (or straight and zonal) position of the front (Figure 3.3b), is defined by

$$\begin{aligned} (\nabla^2 - 1)\psi_0 &= q_0 \\ &= -1 + 2\mathcal{H}(y - \bar{y}(x)) \,. \end{aligned} \tag{3.6}$$

The ψ_β component, associated with the flow due to the beta-effect in a piecewise constant potential vorticity field, is defined by

$$(\nabla^2 - 1)\psi_\beta = -y_e \,. \tag{3.7}$$

The ψ_1 component, associated with disturbances or the time-dependent deviations from the "undisturbed" position of the front, is given by

$$\begin{aligned} (\nabla^2 - 1)\psi_1 &= q_1 \\ &= 2[\mathcal{H}(y - \bar{y}(x) - \eta(x,t)) - \mathcal{H}(y - \bar{y}(x))] \,. \end{aligned} \tag{3.8}$$

All three fields satisfy the boundary condition $\psi = 0$ at the coast ($x = 0$).

The partition of ψ is done mainly for computational (operational) reasons as we shall see later. The reader should be aware that "undisturbed" and "disturbed" fields, in our cases, do not correspond to the conventional meanings of "mean" or "perturbed" fields, respectively. Therefore, the $\psi_0 + \beta\psi_\beta$ field does not (necessarily) represent a steady solution to the problem defined here.

The four boundary conditions needed to solve for ψ_0 are that of: zero normal flow at the coast,

$$\psi_0 = 0 \quad at \ x = 0\,; \tag{3.9a}$$

the two conditions establishing the symmetry of the two converging coastal currents,

$$\psi_0 = -(1 - e^{-x}) \quad \text{as} \ y \to \infty \tag{3.9b}$$

and

$$\psi_0 = (1 - e^{-x}) \quad \text{as} \ y \to -\infty\,; \tag{3.9c}$$

and the condition that assures that the separating jet has a cusplike profile in the ocean interior,

$$\psi_0 = sign(-y_e)(1 - e^{-|y_e|}) \quad \text{as} \ x_e \to \infty\,. \tag{3.9d}$$

Given θ, the ψ_0 fields are determined numerically by iteration using Eqs. (3.6) and (3.9). Figure 3.4 shows the respective ψ_0 fields for the two different coastline orientations considered.

The ψ_β component is determined analytically. To solve for ψ_β, we impose $u_\beta \to -1$ as $x_e \to \infty$ and $\psi_\beta = 0$ at the center of the zonal jet. The choice of $\psi_\beta = 0$ at $y_e = 0$ is arbitrary, meant to match the latitude of the ψ_0 centerjet streamline, and oppose the convergence of the coastal currents in the ψ_0 field. Hence, the solution is simply:

$$\psi_\beta = x \sin\theta + y \cos\theta (1 - e^{-x})\,, \tag{3.10}$$

which is shown for $\theta = 0$ and $\pi/4$ in Figure 3.5.

Given the solution for the time-independent part of ψ, why is it that $\psi_0 + \beta\psi_\beta$ may not represent a steady state solution to the problem? In a steady state system, q contours coincide with streamlines (or vice-versa). Consider the $\theta = 0$ case (Figure 3.4a), the streamline $\psi_0 = 0$ coincides with the contour $\bar{y}$. The beta streamline $\psi_\beta = 0$ (Figure 3.5a) is also a straight line along $y = y_e = 0$. Therefore in this case

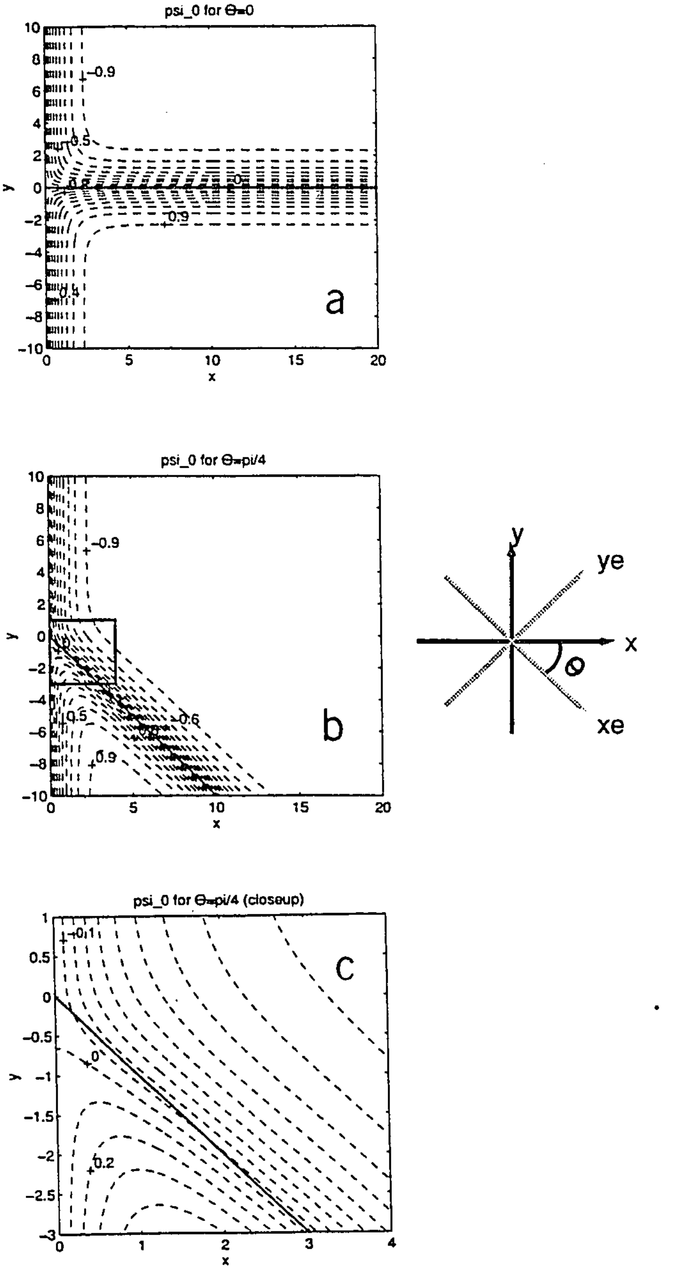

Figure 3.4: The "undisturbed" stream function ψ_0 solution for the symmetric model, in which: (a) $\theta = 0$, (b) $\theta = \pi/4$ and (c) $\theta = \pi/4$, a closeup of the region around the origin. Results are expressed in the model coordinates (x, y). The potential vorticity discontinuity is represented by a solid line, and the streamlines by dashed lines.

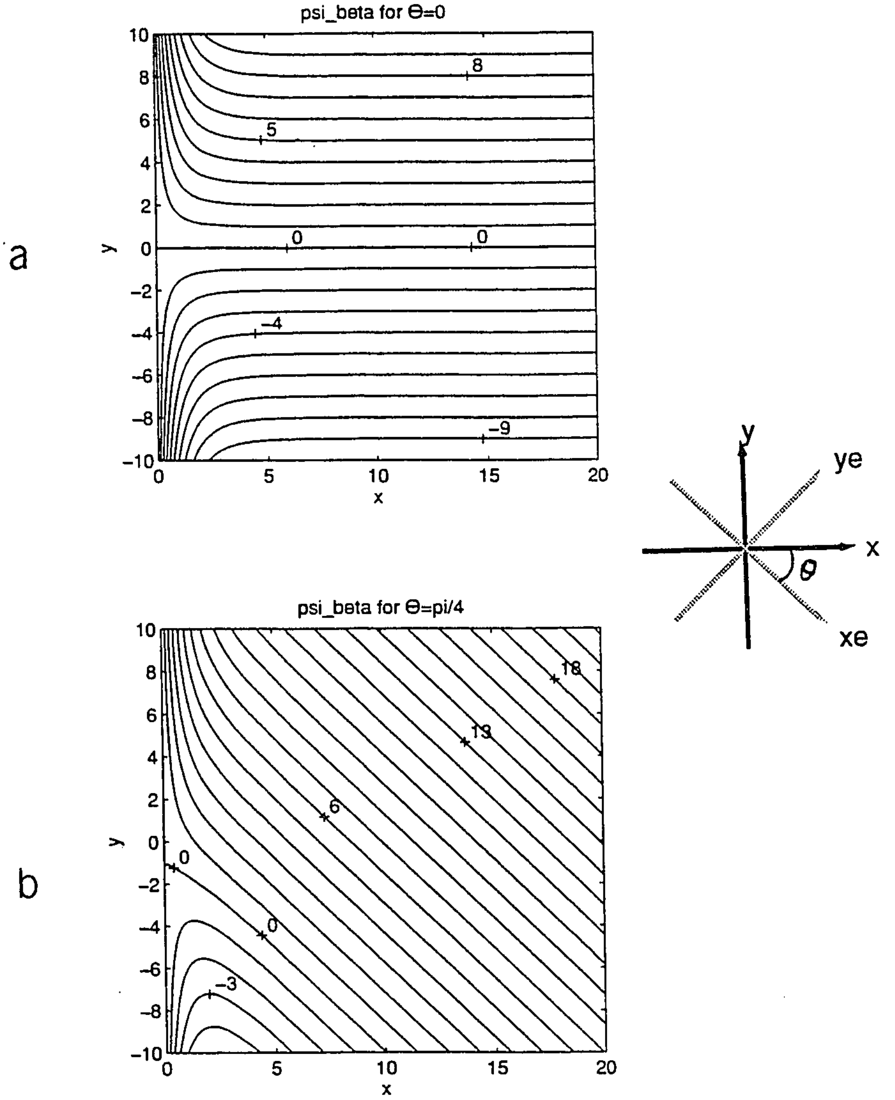

Figure 3.5: The results for the β-related stream function ψ_β: (a) $\theta = 0$, and (b) $\theta = \pi/4$. Results expressed in the model coordinates (x, y).

the $\psi_0 + \beta\psi_\beta$ solution does represent a steady state. The same is not true for the $\theta = \pi/4$ case (Figure 3.4b), in which there is a clear mismatch between the straight contour $\bar{y}$ and the $\psi_0 = 0$ streamline (which is curved) near the coast, as enlarged in Figure 3.4c. The $\psi_\beta = 0$ streamline in Figure 3.5b is also curved.

The ψ_1 field is computed by integrating Eq. (3.8) using the Green's function method,

$$\begin{aligned} \psi_1 &= \int\int G(x,y \mid x',y')\, q_1\, dx'\, dy' \\ &= -2\int\int_D G(x,y \mid x',y')\, dx'\, dy' \, , \end{aligned} \tag{3.11}$$

where D is the area between the curves $y = \bar{y}(x) + \eta(x,t)$ and $y = \bar{y}(x)$, as indicated in Figure 3.3c.

According to PS86, the Green's function takes the form

$$G = G_+ + G_- = -\frac{1}{2\pi}K_0(r_+) + \frac{1}{2\pi}K_0(r_-) \, , \tag{3.12}$$

where K_0 is the modified Bessel function of the second kind of order zero, G_- represents the image point required to satisfy $\psi_1 = 0$ at the western boundary and

$$\begin{aligned} {r_+}^2 &= (x - x')^2 + (y - y')^2 \, , \\ {r_-}^2 &= (x + x')^2 + (y - y')^2 \, . \end{aligned}$$

The "disturbed" velocity field is determined from Eq. (3.11), according to stream function definition

$$(u_1, v_1) = (-\frac{\partial}{\partial y}, \frac{\partial}{\partial x})\psi_1 \, , \tag{3.13}$$

and using Eqs. (3.11) and (3.12).

The contour dynamics technique requires Eq. (3.13) be written in terms of contour integrals. According to PS86, we need to express the x and y derivatives in terms of x' and y'. We then follow *Wang*'s [1992] derivation in using the symmetry properties of the Green's function to write

$$\begin{aligned}
\frac{\partial}{\partial x}G_+ &= -\frac{\partial}{\partial x'}G_+ && \text{(3.14a)}\\
\frac{\partial}{\partial x}G_- &= \frac{\partial}{\partial x'}G_- && \text{(3.14b)}\\
\frac{\partial}{\partial y}G_+ &= -\frac{\partial}{\partial y'}G_+ && \text{(3.14c)}\\
\frac{\partial}{\partial y}G_- &= -\frac{\partial}{\partial y'}G_- \,. && \text{(3.14d)}
\end{aligned}$$

For example, the "disturbed" alongshore velocity v_1 becomes

$$v_1 = 2\int\int_D [\frac{\partial}{\partial x'}G_+ - \frac{\partial}{\partial x'}G_-]\, dx'\, dy' \,,$$

where we have combined Eqs. (3.13) and (3.14).

We then invoke the divergence theorem

$$\begin{aligned}
v_1 &= 2\int\int_D \nabla\cdot(G_+\vec{i}' - G_-\vec{i}')\, dx'\, dy'\\
&= 2\int_{\partial D}(G_+ - G_-)(\vec{i}'\cdot\vec{n}')\, dl'\\
&= -2\int_{\partial D}(G_+ - G_-)\, dy' \,,
\end{aligned}$$

where ∂D is the contour enclosing D (see Figure 3.3c), $\vec{n}'$ is the unit vector normal to ∂D, dl' is the infinitesimal increment along ∂D, and $\vec{i}'$ is the unit vector in the x'-direction.

An analogous procedure can be applied to obtain the "disturbed" cross-shore velocity u_1 in terms of contour integrals. Using the Green's function definitions (Eq. 3.12) in the velocity expressions yields

$$u_1 = \frac{1}{\pi}\int_{\partial D}[K_0(r_+) - K_0(r_-)]\, dx' \qquad \text{(3.15a)}$$

$$v_1 = \frac{1}{\pi}\int_{\partial D}[K_0(r_+) + K_0(r_-)]\, dy' \,. \qquad \text{(3.15b)}$$

The partitioning the stream function field was chosen so that Eqs. (3.11) and (3.15) do not involve improper integrals, which potentially behave poorly [PS86]. Rather, ∂D in Eq. (3.15) has finite boundaries (see Figure 3.3c).

However, Eq. (3.15) still has a logarithmic singularity because $K_0(r) \simeq -\ln(r)$ when r is very small. The singularity is circumvented following *Polvani* [1988] through a simple integration by parts of Eq. (3.15), leading to the non-singular expressions

$$u_1 = \frac{1}{\pi}\Big[\int_{\partial D}(x-x')\,K_1(r_+)\,\frac{d{r_+}^2}{2r_+} + \int_{\partial D}(x+x')\,K_1(r_-)\,\frac{d{r_-}^2}{2r_-}\Big] \qquad (3.16a)$$

$$v_1 = \frac{1}{\pi}\Big[\int_{\partial D}(y-y')\,K_1(r_+)\,\frac{d{r_+}^2}{2r_+} + \int_{\partial D}(y-y')\,K_1(r_-)\,\frac{d{r_-}^2}{2r_-}\Big], \qquad (3.16b)$$

where K_1 is the modified Bessel function of the second kind of order one.

Finally, how does the potential vorticity front evolve? Material particles along the q front (or the contour) are moved by the total velocity, which in our case is a combination of the "undisturbed", "beta" and "disturbed" flow fields, according to

$$\frac{d}{dt}x \;=\; u \;=\; u_0(x,\bar{y}+\eta) \;+\; \beta u_\beta(x,\bar{y}+\eta) \;+\; u_1(x,\bar{y}+\eta,t) \qquad (3.17a)$$

$$\frac{d}{dt}(\bar{y}+\eta) \;=\; v \;=\; v_0(x,\bar{y}+\eta) \;+\; \beta v_\beta(x,\bar{y}+\eta) \;+ v_1(x,\bar{y}+\eta,t)\,. \qquad (3.17b)$$

The (u_0, v_0) and (u_β, v_β) velocities only advect the water parcels in the front. The (u_1, v_1) components are responsible for vortex induction mechanisms on the front [PS86]. Far from the coast, the jet does not "feel" the boundary and the "undisturbed" and "beta" components are zonal. The evolution of the jet is then governed by PS86's infinite jet physics. Mathematically, this implies that as $r_- \rightarrow \infty$, $K_1(r_-) \rightarrow 0$, and the second integral on the right hand side of Eqs. (3.16a) and (3.16b) becomes negligible. PS86 and *Pratt* [1988] have shown that advection and vortex induction generally oppose each other. This process is summarized in Figure 3.6. For example, the non-uniform eastward advection of the disturbance is illustrated in Figure 3.6a (the vortex-induction part of the model $[u_1, v_1]$ is "turned off"). Note the tendency for wave breaking on the west side of the bump. In

Figure 3.6b, the westward Rossby-wave-like motion tendency, as a result of vortex induction mechanisms, is isolated. The combined advection and vortex induction in PS86's balance may lead to meander detachment (Figure 3.6c) through simultaneous backward and forward wave breaking.

Near the coast, however, the balance is somewhat different from that of the infinite jet problem. For example, consider the meridional boundary case where $\psi_0 + \beta\psi_\beta$ represents a steady state. If the contour is perturbed northward, as in the previous case, the southward-flowing coastal current will try to restore the contour toward the $y = 0$ latitude. On the other hand, the vortex induction mechanisms will cause both the vorticity wave motion and a dipole effect. The latter results from the interaction of a contour anomaly with its image due to the presence of the western boundary. In the case of an anticyclonic disturbance, the dipole effect will tend to cause the contour to move northward by pairing with its image (see Figure 3.7).

The numerics of the contour dynamics algorithm described next follow PS86. The time-dependent position of the contour is determined by tagging parcels along the potential vorticity front and following their motion using Eq. (3.17). A second-order Runge-Kutta scheme is employed in the discretization of Eq. (3.17). At each time step, the three different contributions to the total velocities u and v must then be determined. The "undisturbed" velocity is interpolated within grids previously obtained by the iterative scheme. The "disturbed" velocity is evaluated from Eq. (3.16), which has been discretized using a midpoint integration rule, according to *Zou et al.* [1987] and *Polvani* [1988]. In order to maintain the model's resolution, a simple particle insertion-deletion scheme is applied to maintain the front particle separation at a preselected average distance δ. The model accuracy is assessed using the conservation of area arguments presented by *Bell and Pratt* [1994]. By delimiting a box defined between the coast and $x_e = 100$, and $y_e = -10$ and 10, we estimate that the area underneath (beneath) the "disturbed" contour $\bar{y}(x) + \eta(x,t)$ increases

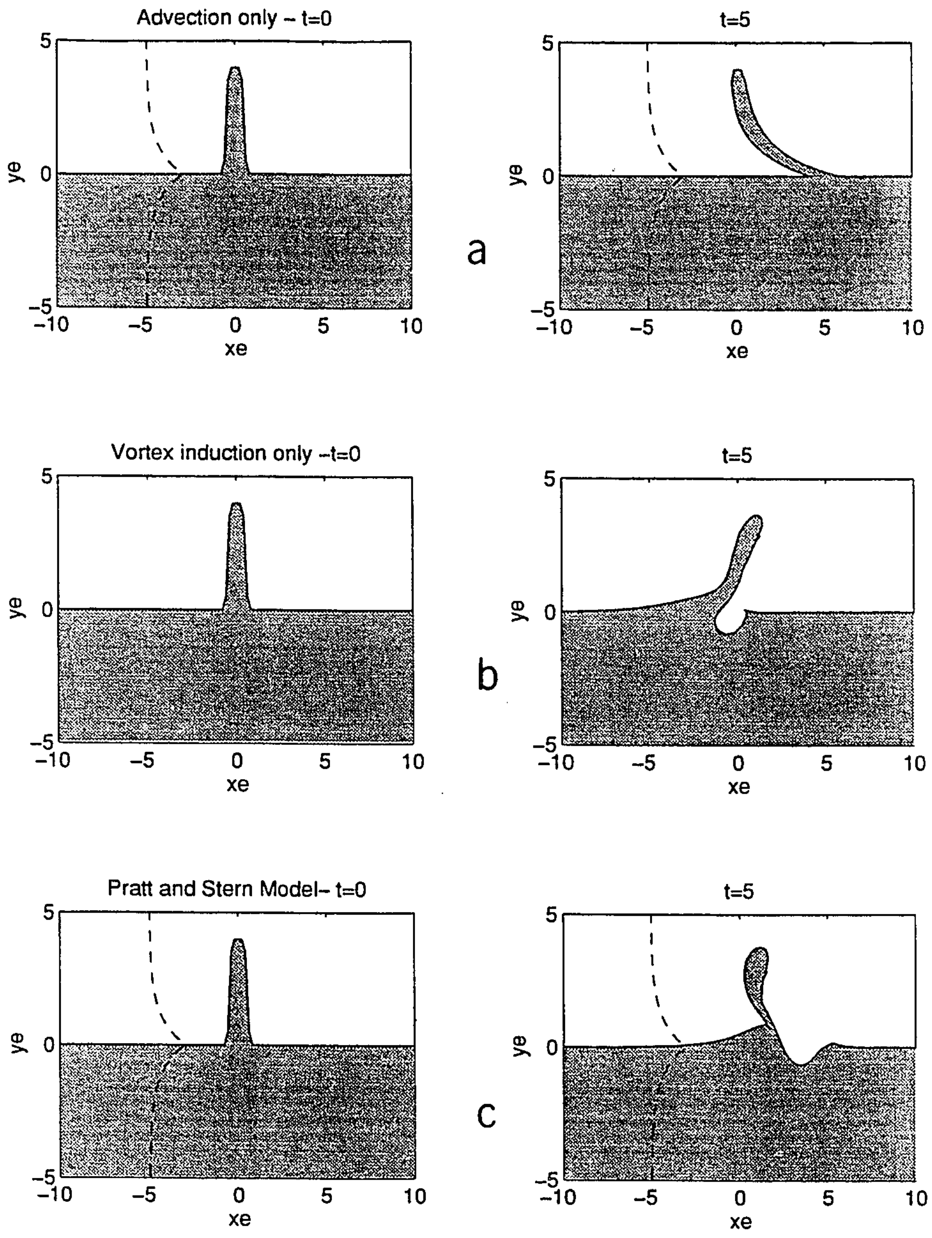

Figure 3.6: Physical processes involved in the evolution of a potential vorticity front: (a) advection of a passive front by the the background shear flow; (b) vortex induction mechanisms where the basic shear flow has been "turned off"; and (c) the *Pratt and Stern* [1986] balance which is a superposition of the effects in (a) and (b). The basic jet profile is represented by the dashed line

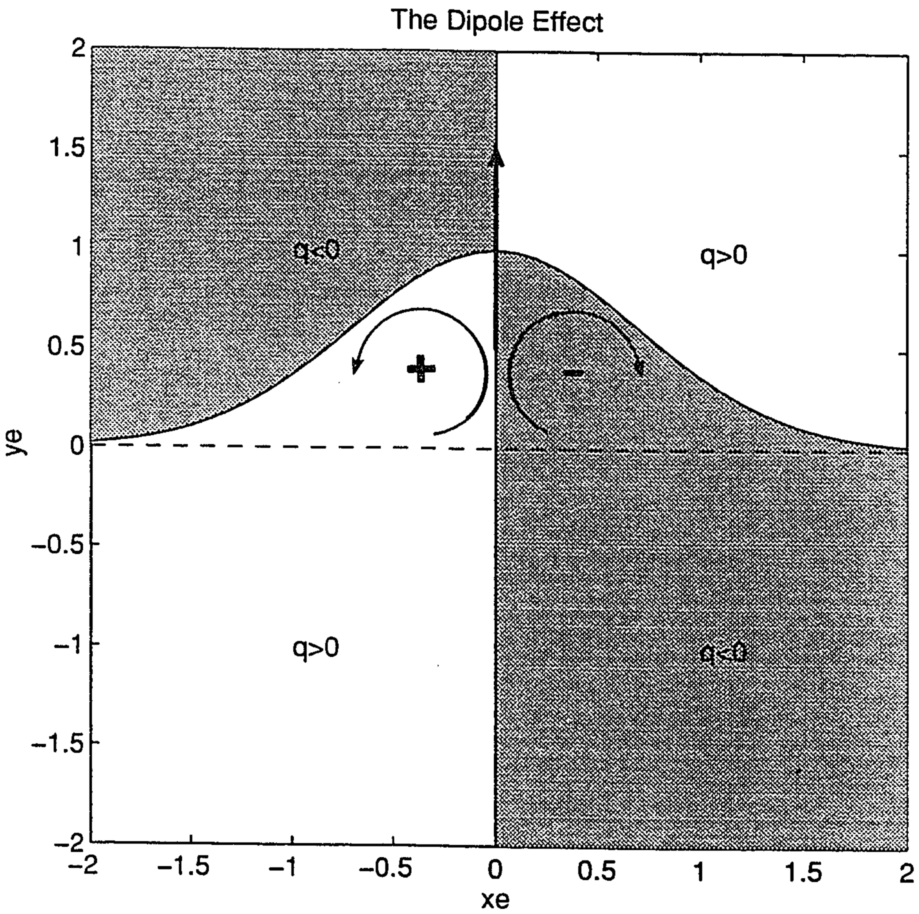

Figure 3.7: The dipole effect associated with the presence of a boundary in a anticyclonic anomaly. In an inviscid system, the zero normal flow condition at the boundary is satisfied by pairing of the vortex with its image. The net result is the movement of an anticyclonic anomaly along the boundary, toward larger y-values. The net motion is in the opposite direction for a cyclonic anomaly.

(decreases) an average a thousandth of a percent per time step.

3.2.2 The Asymmetric Front Model

Now consider the asymmetric case, in which the potential vorticity in the lower half of the model ($q = -1 - \alpha$) and in the upper half ($q = 1 - \alpha$) can differ in magnitude. The range for the asymmetry parameter is $-1 < \alpha < 1$, where positive (negative) values correspond to a stronger current in the lower (upper) half of the domain. In contrast to the symmetric model, in which the "undisturbed" contour is a straight line connected to the coast and the center streamline in the jet corresponds to $\psi_0 = 0$, the asymmetric model center jet streamline corresponds to $\psi_0 = \alpha$. This is easily seen by considering the inversion relationship for the meridional western boundary case (Eq. 3.6b) in the far-field limit as $x \to \infty$ with asymmetric forcing:

$$\begin{aligned}(\frac{\partial^2}{\partial y^2} - 1)\psi_0 &= 1 - \alpha \quad \text{for } y > 0 \\ &= -1 - \alpha \quad \text{for } y < 0 \,,\end{aligned} \tag{3.18}$$

for which the solution is

$$\psi_0 = \alpha + sign(-y)(1 - e^{|-y|}) \,. \tag{3.19}$$

The evaluation of Eq. (3.19) at $y = 0$ yields the $\psi_0 = \alpha$ result. Figure 3.4 shows that all streamlines for the symmetric model, other than $\psi_0 = 0$, have hyperbolic shapes. We would not expect that the asymmetric model streamlines will differ much from this. Hence, if a steady asymmetric front exists, it would also have a hyperbolic-like shape, as do the streamlines in Figure 3.4. Thus, it would not be connected to the coast, but rather extend southward paralleling the coast. The $\bar{y}$ contour should then approach the $\psi_0 = \alpha$ streamline as $x \to \infty$, and $y \to -\infty$ (for $\alpha > 0$) or $y \to \infty$ (for $\alpha < 0$). For example, consider the $\alpha > 0$ case, in which the

$\psi_0 = \alpha$ streamline approaches a cross-shore distance of $x = x_0$ as $y \rightarrow -\infty$. The inversion relationship for the boundary current is

$$
\begin{aligned}
(\frac{\partial^2}{\partial x^2} - 1)\psi_0 &= -1 - \alpha \quad \text{for } x > x_0 \\
&= 1 - \alpha \quad \text{for } x < x_0 \, .
\end{aligned} \tag{3.20}
$$

Assuming $\psi_0 = 0$ at the coast, Eq. (3.20) has a solution of the form

$$
\begin{aligned}
\psi_0 &= (1 + \alpha) + ae^{-x} \quad \text{for } x > x_0 \\
&= (-1 + \alpha) + be^{-x} + ce^{x} \quad \text{for } x < x_0 \, ,
\end{aligned} \tag{3.21}
$$

where the constants a, b and c are

$$
\begin{aligned}
a &= (1 - \alpha) - (e^{x_0} + e^{-x_0}) \\
b &= -\alpha + (1 - e^{x_0}) \\
c &= e^{-x_0}
\end{aligned}
$$

and x_0 is

$$
x_0 = -\ln(1 - \alpha) \, . \tag{3.22}
$$

The corresponding "undisturbed" contour $\bar{y}(x, y)$ is then formally defined as the asymptotes of a hyperbolic streamline,

$$
\begin{aligned}
\bar{y}(x, y) &= y \quad \text{for } y < 0 \, , \; x = x_0 \\
&= -(x - x_0)\tan\theta \quad \text{for } y \geq 0 \, , \; x > x_0 \, .
\end{aligned} \tag{3.23}
$$

Analogous expressions can be derived for the case in which $\alpha < 0$.

The asymmetric model q and its components are sketched in Figure 3.8. The formalism of the asymmetric model is not presented here due to a more complicated form of the potential vorticity front as described by $\bar{y} = \bar{y}(x, y)$ and $\eta = \eta(x, y, t)$. It suffices to say that the asymmetric model is conceptually and numerically similar to the symmetric version (as a comparison between Figures 3.3 and 3.8 suggests). Actually, the symmetric model can be regarded as the asymmetric model in the limiting case of $x_0 \rightarrow 0$ or $\alpha \rightarrow 0$. The ψ_0 field is calculated by iteration. For example, the boundary conditions needed to determine ψ_0 for the $\alpha > 0$ case on the iterative scheme are

$$\begin{aligned}
\psi_0 &= 0 \quad \text{at } x = 0 \\
&= (-1 + \alpha)(1 - e^{-x}) \quad \text{as } y \rightarrow \infty \\
&= (1 + \alpha) + ae^{-x} \quad \text{for } x > x_0 \\
&= (-1 + \alpha) + be^{-x} + ce^{x} \quad \text{for } x < x_0 \,, \\
&= \alpha + sign(-y)(1 - e^{|-y|}) \quad \text{as } x_e \rightarrow \infty
\end{aligned}$$

Notice that the last condition establishes that the zonal jet profile in the ocean interior for the asymmetric model is still the same as PS86's. The velocities associated with ψ_1 are computed by contour integrals identical to Eq. (3.16), and the ψ_β component is the same as in the symmetric case.

The cases of small and $O(1)$ α values will be explored considering the same θ values as in the symmetric model. Figure 3.9 shows the ψ_0 fields for $\alpha = 0.65$ as an example. Notice that in contrast to the symmetric model, the asymmetric model has a northward (and stronger) boundary current velocity core which is not located at the coast, but centered offshore at $x = x_0$. This is a consequence of the fact that asymmetry has introduced a potential vorticity band of different signs (between $x = 0$ and $x = x_0$) in the stronger current region. An unanswered question is how realistic this q band near the coast is. However, the velocity structure in the asymmetric model seems more like observed cases than in the symmetric model.

The flow structure in the asymmetric model is similar to the one in the viscous, barotropic model by *Cessi* [1991]. As in the present model, *Cessi*'s [1991] was

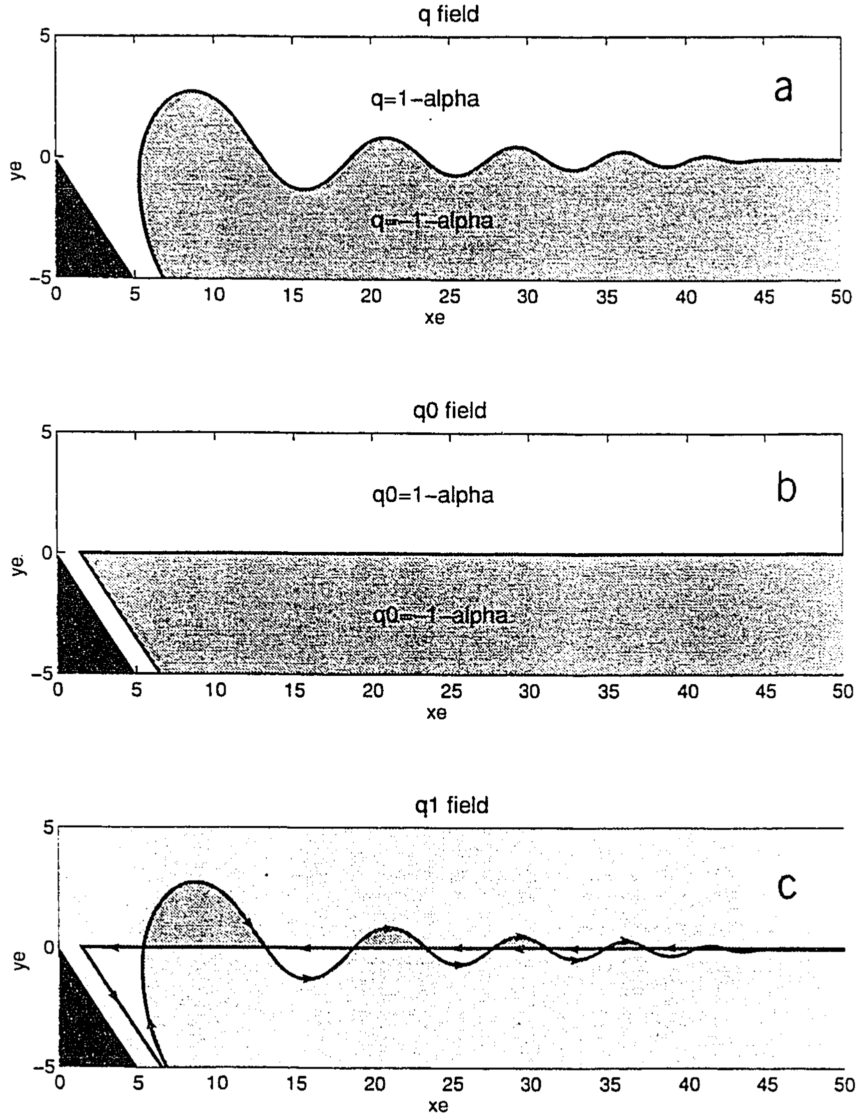

Figure 3.8: (a) The total potential vorticity field q for the asymmetric model is composed of: (b) q_0, the part of the field associated with the "undisturbed" position $\bar{y}(x)$ of the front; and (c) q_1, the part of the field associated with the deviations from the "undisturbed" field q_0 field. The arrows indicate the integration direction.

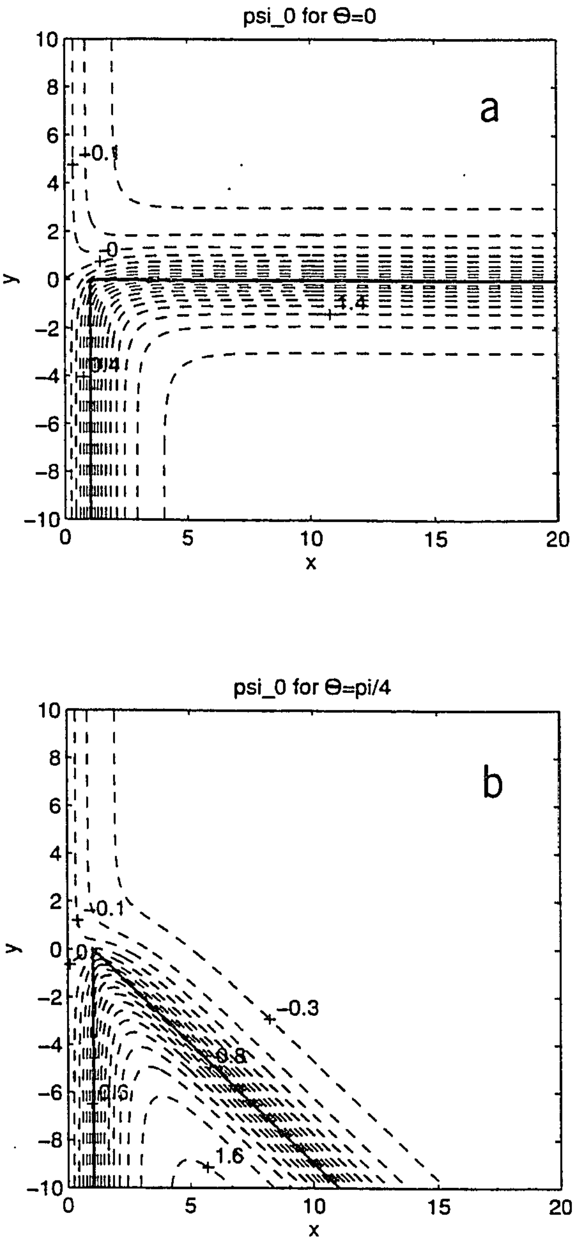

Figure 3.9: The "undisturbed" stream function ψ_0 solution for the asymmetric model ($\alpha = 0.65$), in which: (a) $\theta = 0$, and (b) $\theta = \pi/4$. Results are expressed in the model coordinates (x, y). The potential vorticity discontinuity is represented by a solid line, and the streamlines by dashed lines.

characterized by two asymmetric boundary currents that formed a separating zonal jet. Since *Cessi*'s [1991] model included friction, no-slip conditions were used in the western boundary and the boundary current velocity cores were placed at some distance from the coast. In our inviscid model, we have free-slip boundary conditions and the coastal current maximum velocities occur at the q contour.

3.3 Numerical Experiments

3.3.1 The Symmetric Model Results

A series of numerical experiments were conducted with the symmetric model. In this subsection, we describe and discuss the results. Table 3.2 defines the initial value problems performed.

The meridional boundary case

The known steady state solution for the meridional boundary case, represented by $\psi_0 + \beta\psi_\beta$, is given in Section 3.2.1. There, a qualitative description of how advection and vortex induction mechanisms may govern the contour motion close to the coast was presented. Here, some of PS86's experiments are repeated by perturbing the contour with isolated finite amplitude disturbances. The goal is to determine the effect of the boundary in the system dynamics. As in PS86's work, these disturbances are of the order of the deformation radius, in an attempt to make advection and vortex induction mechanisms of the same order.

To better understand vortex induction mechanisms as a combination of wave motion tendency and dipole effect, we "turn off" the shear flow in the model (i.e., ψ_0 is set to zero) and let $\beta = 0$. The contour is perturbed upward with a half Gaussian bump, which has the form

$$\eta(x, 0) = Ae^{-x^2} , \tag{3.24}$$

Table 3.2: Summary of numerical experiments with the symmetric model

Run	θ	β	Initial Conditions
s1	0	0	Eq.(24), A=0.5
s2	0	0	Eq. (24), A=2.0
s3	0	0.1	Eq.(24), A=0.5
s4	0	0.05	Eq. (24), A=2.0
s5	0	0	Eq.(25),
s6	0	0	Eq. (26), A=2, d=1.5
s7	0	0.1	Eq.(26), A=2, d=1.5
s8	$\pi/4$	0	$\psi_0 = 0$ streamline shape
s9	$\pi/4$	0.1	$\psi_0 = 0$ streamline shape

where $A = 0.5$. This disturbance represents an anticyclonic anomaly which has a velocity structure similar to that of the perturbed infinite jet problem on the east side (compare Figure 3.10a with Figure 3.6b). The difference is, of course, the presence of the boundary on the west side. The no-normal-flow condition at the boundary $[u_1(0,t) = 0]$ is created by pairing the anomaly with its image to the west of the boundary (or landward side of the model) as shown previously (Figure 3.7). Thus the northward velocity v_1 is enhanced. As time progresses, the westward wave propagation tendency creates a westward velocity in the southeast corner of the anomaly. The velocity is large enough to cause wave breaking and sequential detachment of the anomaly from the zonal front (Figure 3.10b). Meanwhile, in the northwest corner, the anomaly continues to be pushed northward. After separation the eddy continues to move northward (Figure 3.10c).

We now solve the complete problem, in which the basic state is a shear flow with zero β (Figure 3.4a), using the same initial condition as above (*Run s1* in Table 3.2). Figure 3.11 shows clearly that the advective effects of the southward coastal current overcome the dipole effect, and the anomaly is squashed against the x-axis. Waves are generated at the ocean side of the bump. The waves travel eastward, with shorter wavelengths outrunning the large ones, resembling a spatially damped wave pattern. After some time (t=100), the disturbance amplitude at the coast is approximately zero.

There are two ways to increase the relative effect of the vortex induction mechanisms (the dipole effect in particular) in the model. One is to increase the size of the disturbance in the initial conditions [PS86]. The other is to include β, which in a piecewise constant potential vorticity field weakens the restoring capability of the ψ_0 field.

In *Run s2*, the size of the amplitude initial disturbance is set to four times that of *Run s1*, i.e., $A = 2$ in Eq. (3.24) (Figure 3.12). With much larger anomalous velocities (u_1, v_1), the Gaussian bump is squashed more slowly. At t=100, the

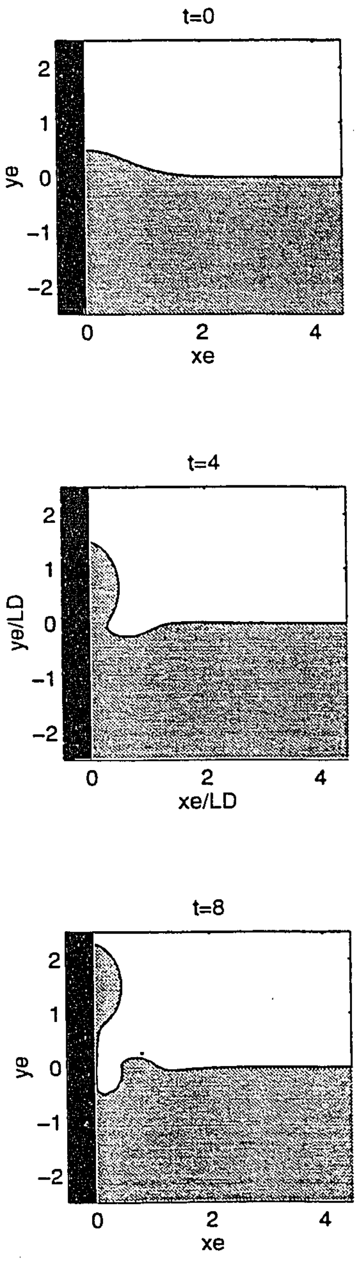

Figure 3.10: The "anomaly" model run, in which only vortex mechanisms are present, for: (a) $t = 0$, (b) $t = 4$, and (c) $t = 8$.

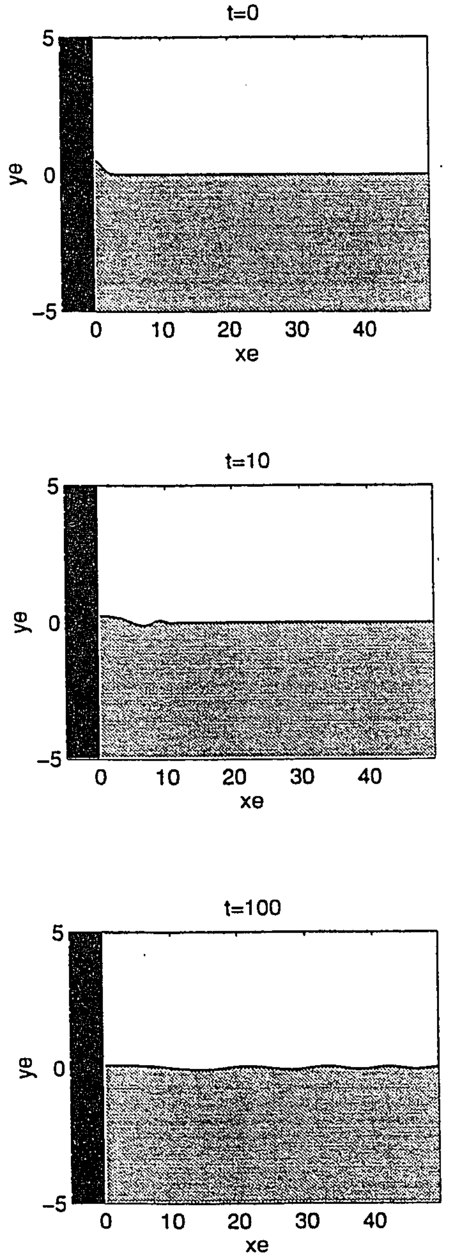

Figure 3.11: Symmetric model experiment with $\theta = 0$ and $\beta = 0$. Initial conditions given by Eq. (3.24) in main text with a disturbance amplitude of $A = 0.5$ (*Run s1*). The y-axis scale is amplified about four times relative to the x-axis scale.

amplitude of the bump is about a quarter of its initial value. However, we do not observe any significant difference between the wave pattern in this experiment and that in *Run s1*. Of course, the amplitudes are larger, but the waves have approximately the same wavelengths as the previous case.

Note also that at $t = 10$ (Figure 3.12), *Runs s1* and *s2* (in particular) resemble the model output when the basic shear is turned off (Figure 3.10, $t = 4$). However, in the presence of basic shear, the eastward advection velocity u_0 overcomes the westward wave velocity u_1 in the trough to the east of the initial bump, so that no eddy detachment occurs. Given the symmetry between the upper and lower halves of the model, a cyclonic Gaussian bump (i.e., $A = -2$) yields a pattern like those of *Runs s1* and *s2* (see Figures 3.11 and 3.12), with $\eta(x,t)$ being replaced by $-\eta(x,t)$.

In *Run s3*, the size of the initial disturbance in *Run s1* is retained, but β is given a value of 0.1. This β is about five times the typical mid-latitude value, but it is of the right order of magnitude for more tropical cases such as the North Brazil Current retroflection around 7°-8° N [*Brown et al.*, 1991]. As this case demonstrates, exaggerating β is analogous in some ways to the use of a larger initial disturbance (*Run s2*), because the "beta" velocity field opposes and thus weakens the "undisturbed" velocity field. As a consequence, the dipole effect is able to balance (at around $t = 10$) and eventually overcome the southward advection (see Figure 3.13). In contrast to results of the previous experiment, we obtained a slowly (temporally) growing, spatially damped wave pattern which slowly propagates away from the coast. The wavelengths in this case are somewhat shorter than the ones in the $\beta = 0$ cases.

In *Run s4* (results not shown), we consider the same bump amplitude as in *Run s2* and a smaller β value (0.05) than *Run s3*. The results are qualitatively identical to the *Run s3* except that it has a higher growth rate due to a larger initial disturbance.

In *Run s5*, the effect of steepening the slope of the disturbance is investigated

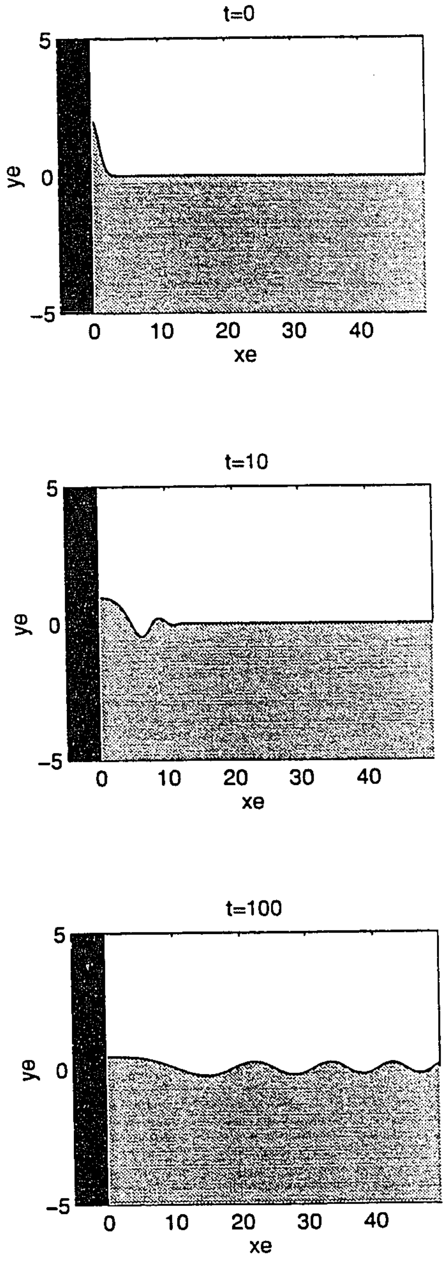

Figure 3.12: Same as Figure 3.11, but using a disturbance amplitude of $A = 2$ (*Run s2*). The y-axis scale is amplified about four times relative to the x-axis scale.

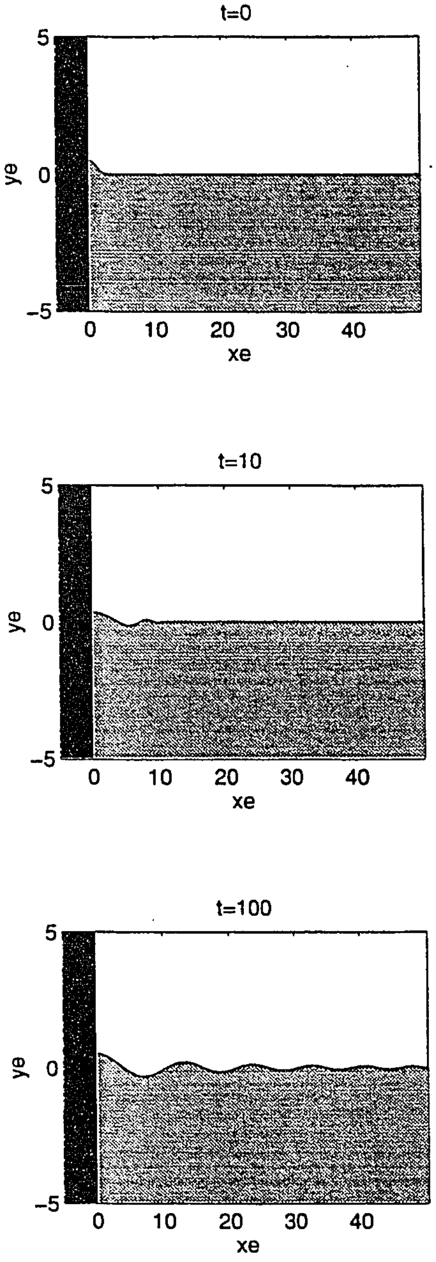

Figure 3.13: Same as Figure 3.12, but using $\beta = 0.1$ (*Run s3*). The y-axis scale is amplified about four times relative to the x-axis scale.

by starting with

$$\eta(x,0) \;=\; 2\{1-\tanh[10(x-1)]\}\ , \tag{3.25}$$

and $\beta = 0$. PS86 found this type of initial condition more efficient in causing eddies to detach in the infinite jet problem (as in Figure 3.6). In our case, however, the results are very similar to those of *Run s2* (Figure 3.12), but with slightly larger wave amplitudes.

In an effort to pinch off an eddy, we used PS86's two lobe initial disturbance (*Run s5*), given by

$$\eta(x,0) \;=\; -A(x-d)e^{-(x-d)^2}\ , \tag{3.26}$$

where $A = 0.5$, $d = 0.5$. The calculations were initialized with a large positive potential vorticity anomaly to the east and a negative one near the coast. This represents an attempt to initially provide enough westward u_1 at the southeast corner of the anticyclonic bump to overcome the positive u_0 and to develop a pattern similar to the one depicted in Figure 3.10. However this initial condition failed to result in a detached eddy. Instead, it produces a pattern similar to that in *Run s2* (Figure 3.12), but with an enlarged trough to the east of the anticyclone at the coast. In a final case, with the same initial disturbance and $\beta = 0.1$ (*Run s7*, not shown), the model again fails to pinch off a coastal eddy.

The results from the previous experiments contrast with the infinite jet case where nonlinear effects are important. PS86 showed that, for an initial disturbance with dimensions of the deformation radius, the competition between advection and vortex induction could lead to meandering and eddy shedding (Figure 3.6). In our case, the presence of the boundary imposes a different balance between the mechanisms, and hence the qualitatively different results are obtained here. For example, in *Run s2* an amplitude disturbance as large as in PS86's experiments certainly creates "disturbed" velocities large enough to prevent the bump from being squashed quickly. However, since there is obviously no zonal advection at $x = 0$, there is no possibility of backward wave breaking (in a way similar to Figure 3.6a). The dipole effect, which accounted for the eddy shedding on the "anomaly" model run, is opposed and overcome by the southward current advection. On the northeast side of the bump, the alongshore velocities associated with westward wave motion tendencies and advection have the same sign. As described above, no westward cross-shore velocity is created, making forward wave breaking unlikely. When β is included (*Runs s3* and *s4*), the effects of the "undisturbed" velocity field are weakened by the "beta" and dipole effect velocity fields. On the eastward side of the disturbance, the westward "beta" velocity is not large enough to allow a pattern similar to the one in Figure 3.10b to develop.

Our model results also show that perturbing the front at the coast excites fairly sinusoidal long waves. There is very little indication of nonlinear steepening, suggesting a predominantly linear behavior. A linearized version of the contour dynamics model is presented in the Appendix and reproduces qualitatively the results obtained in this section.

The wave pattern obtained in this work resembles the ones obtained by *Pratt* [1988], which dealt with the long wave limit of the PS86 model. The former author obtained the same fairly slowly dispersing wave pattern on an infinite domain, as found for initial disturbance amplitudes considered here. It should be emphasized that he explicitly filtered out short wavelengths which our model does not. The presence of the western boundary and the zonal shear region it creates seems to somehow impose the long wave approximation. To verify this finding, we use a simple linear calculation that considers an infinite jet similar to PS86's, but with a linear zonal gradient in some region of the domain. The role of such structure is to mimic the boundary effect. The center jet velocity is then given by

$$u(x,0) = mx\ , \tag{3.27}$$

where m is a constant coefficient.

The linearized PS86's potential vorticity front evolution equation is

$$\frac{\partial \eta}{\partial t} + \frac{\partial}{\partial x}[u\eta - \psi] = 0 \tag{3.28}$$

where ψ satisfies

$$(\nabla^2 - 1)\psi = -2\delta(y)\,\eta(x,t)\,. \tag{3.29}$$

If we assume a solution for η of the form

$$\eta = Ae^{i[k(t)x - \omega(t)t]}\,, \tag{3.30}$$

use the Green's function method in Eq. (3.29) to solve for ψ, and apply Eq. (3.27), we obtain

$$x(\frac{\partial k}{\partial t} + mk) = \frac{\partial}{\partial t}(\omega t) + im - \frac{k}{\sqrt{k^2+1}}\,. \tag{3.31}$$

By collecting the $O(x)$ terms, we determine the wavenumber evolution:

$$\frac{\partial k}{\partial t} = -mk \quad , \tag{3.32}$$

which has a solution of the form

$$k(t) = k_0 e^{-mt} \quad , \tag{3.33}$$

where k_0 is the dominant wavenumber in the initial disturbance. This result indicates that if the jet is perturbed in a region of the along-jet shear, the wave structure will have progressively smaller (larger) wavenumbers (wavelengths) no matter how large k_0 is. Therefore, the system will rapidly approach the long wave limit, in accordance with our model results.

We may again use linear theory to explain why the β-plane experiments yielded shorter waves than the f-plane results. The (non-dimensional) linearized phase speed c expression (derived by PS86 for the infinite jet problem and modified to include β)

$$c = 1 - \frac{1}{(k^2+1)^{\frac{1}{2}}} - \beta \tag{3.34}$$

is plotted in Figure 3.14 for $\beta = 0$ (solid curve) and $\beta = 0.1$ (dashed curve). Our model results indicate that the coastline causes the waves with phase speed close to zero to be favored. From Figure 3.14, we see that the slowest waves are shorter when β is nonzero.

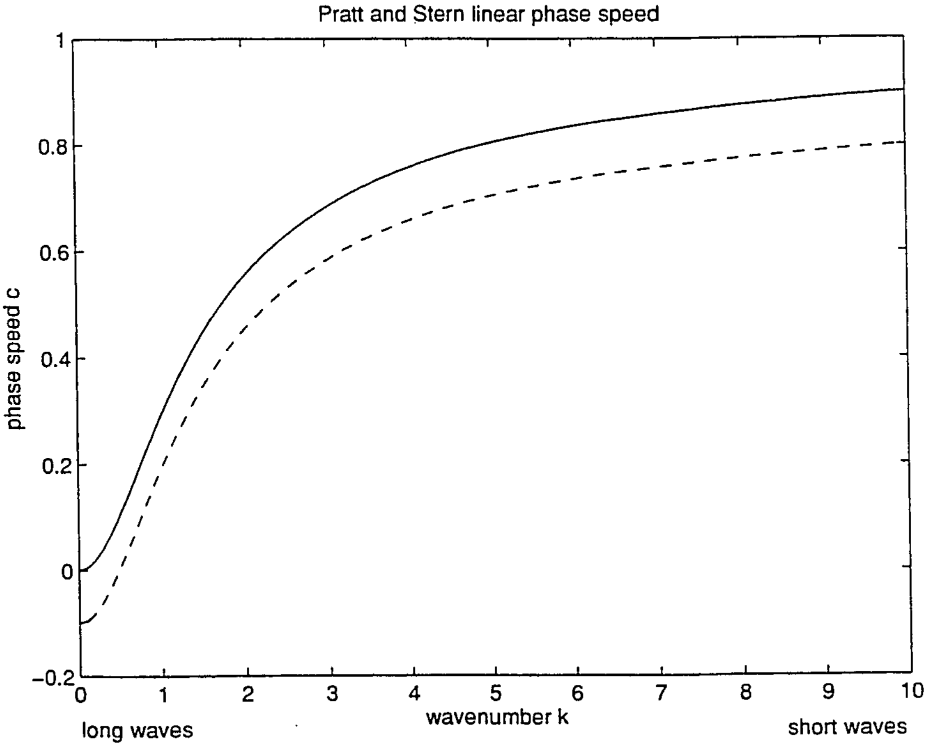

Figure 3.14: Linearized phase speed for *Pratt and Stern*'s [1986] infinite jet, using: $\beta = 0$ (solid curve), and $\beta = 0.1$ (dashed curve).

The tilted boundary case

Now we consider the case in which the boundary is tilted. In contrast to the cases in the previous section where large input disturbances caused a momentum imbalance and a quasi-stationary wave pattern, here the tilt is responsible for the imbalance. The details of the momentum imbalance in the tilted boundary case are made explicit in the linear model formulation, which is presented presented and discussed in the Appendix.

In *Run s8*, the case for $\beta = 0$ and a tilt of $\theta = \frac{\pi}{4}$ is considered first. The initial condition used simply corresponds to the shape of the $\psi_0 = 0$ streamline. Figure 3.15 shows that when the model is "turned on," a positive potential vorticity anomaly develops close to the coast, and a negative anomaly develops to the east side. Long waves are then excited (as in the cases of the previous section) and a spatially damped wave pattern results. However, in contrast to the $(\theta = 0, \beta = 0)$ cases, a slow linear temporal growth occurs.

Analogously to the meridional coast case, the results from the contour dynamics model do not differ qualitatively from the linear solution (see the Appendix), where a temporally growing, spatially damped long wave pattern is also obtained. The average linear growth, given in terms of the the time rate of change of latitude of a front particle at the coast is -0.028 and may be regarded as the time variation in the separation latitude between the two current systems.

The next model experiment (*Run s9*) repeats *Run s8*, except with $\beta = 0.1$. The same wave pattern is obtained (Figure 3.16), but with a higher linear growth. As in the $\theta = 0$ experiments with nonzero β, the waves excited are about 30-40% shorter than the f-plane cases [see Eq. (3.34) and Figure 3.14]. The amplitudes are about 20% higher.

A simple explanation to the linear growth in the long wave amplitudes that may be given is to regard the steady momentum input as a forcing. Then, the linear

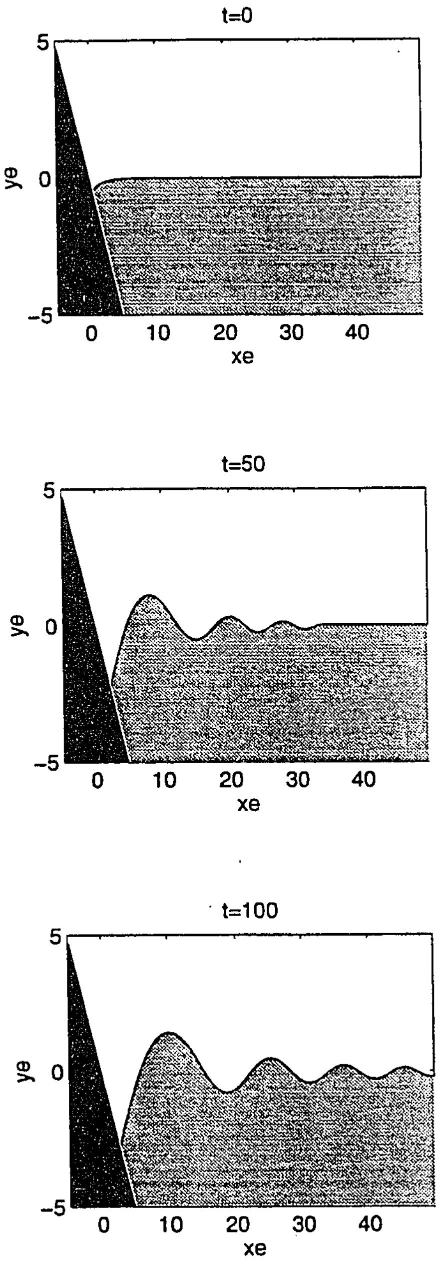

Figure 3.15: Symmetric model experiment with $\theta = \pi/4$, $\beta = 0$ (*Run s8*) Initial conditions given by the shape of the streamline $\psi_0 = 0$. The y-axis scale is amplified about four times relative to the x-axis scale.

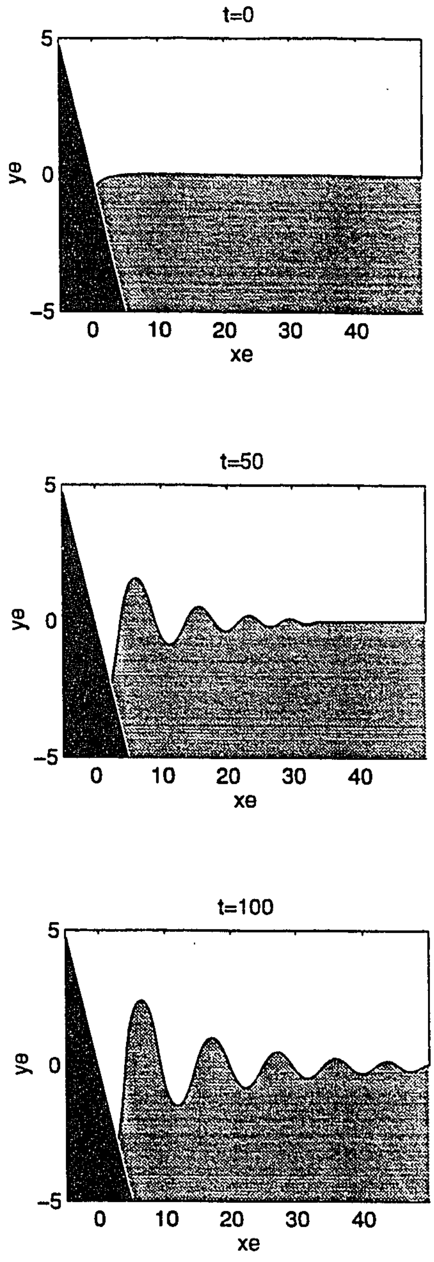

Figure 3.16: Same as Figure 3.15, but using $\beta = 0.1$ (*Run s9*). The y-axis scale is amplified about four times relative to the x-axis scale.

growth would occur due to resonant nearly stationary waves (close to zero phase speed) being excited. The role of "forcing" of the coastline tilt becomes particularly clear when the contour evolution equation in the linear model (Eq. A18 in the Appendix) is examined. There, the coastline tilt effect explicitly acts as a steady forcing term and drives the slowly growing long waves in the linear experiments. We believe that this is a result of unbalanced alongshore momentum fluxes in the "undisturbed" velocity fields.

The southwestward migration of the separation latitude in unbalanced converging current systems was also obtained by *Agra and Nof*'s [1993] model. These authors examined steady states for converging jets that were made possible by the steady migration of the whole current system.

Our results are also somewhat similar to those from the barotropic broad jet model by *Campos and Olson* [1991]. Those authors studied quasi-stationary wave patterns on a spatially constant zonal mean flow, using a model which included a meridional western boundary and lateral Laplacian dissipation. Despite the different physics, they obtained temporally growing spatially damped wave patterns similar to our results. In that model, the frictional boundary works as a permanent sink of potential vorticity. In the inviscid model considered here, the tilt creates a source of potential vorticity which excites the near-stationary waves. Another interesting similarity between the two models is the fact that larger β values were associated with shorter damped waves despite the different representations of the β-effect.

3.3.2 The Asymmetric Model Results

In this section, we will emphasize f-plane asymmetric model experiments (Table 3.3). Examples of asymmetric currents on the β-plane will be reported in Section 3.4.

Table 3.3: Summary of numerical experiments with the asymmetric model

Run	θ	α	Initial Conditions
a1	0	0.05	$\psi_0 = \alpha$ streamline shape
a2	0	0.22	$\psi_0 = \alpha$ streamline shape
a3	0	0.65	$\psi_0 = \alpha$ streamline shape
a4	π / 4	0.05	$\psi_0 = \alpha$ streamline shape
a5	π / 4	-0.05	$\psi_0 = -\alpha$ streamline shape
a6	π / 4	0.22	$\psi_0 = \alpha$ streamline shape
a7	π / 4	-0.22	$\psi_0 = -\alpha$ streamline shape
a8	π / 4	0.65	$\psi_0 = \alpha$ streamline shape
a9	π / 4	-0.65	$\psi_0 = -\alpha$ streamline shape
a10	π / 4	-0.38	$\psi_0 = -\alpha$ streamline shape

The meridional boundary case

In order to isolate the effect of asymmetry, we consider experiments with $\theta = 0$ and only positive α values, given the symmetry between the two halves of the model domain. All experiments used the shape of the streamline $\psi_0 \doteq \alpha$ as initial conditions.

In the first experiment (*Run a1*), a very small asymmetry ($\alpha = 0.05$) is considered. This results in the northward current being about 10% more intense than the southward one (Figure 3.17a). There is a striking similarity to the tilted boundary problem: slowly temporally growing, dispersing waves that resemble a damped wave pattern are generated. Similar patterns are obtained in the experiments with increasing asymmetry, corresponding to $\alpha = 0.22$ (*Run a2*, Figure 3.17b) and 0.65 (*Run a3*, Figure 3.17c), respectively.

In Figure 3.18, we plot the latitude of the northernmost particle in the front for the three experiments at $t = 100$ (circles). We included the three corresponding $\alpha < 0$ cases, given

$$\bar{y}(x,y,-\alpha) + \eta(x,y,t,-\alpha) = -[\bar{y}(x,y,\alpha) + \eta(x,y,t,\alpha)] \, .$$

The zero α case corresponds to the symmetric model steady state result.

It is seen in Figure 3.18 that the asymmetry strengths and wave amplitudes vary linearly. The wavelengths excited are approximately the same in the three experiments. These results clearly indicate that the asymmetry in current transport plays a role similar to that of the coastline tilt. In other words, the asymmetry introduces a momentum imbalance in the alongshore direction as in the symmetric, tilted boundary model. This imbalance causes near-stationary waves to be excited as before. Therefore, it is possible to think of the asymmetry effect also as a "forcing", related here to some sort of inertial overshoot.

Agra and Nof [1993] were able to find steady state solutions for asymmetric, inviscid converging jets in the f-plane. In their model, a static steady state was

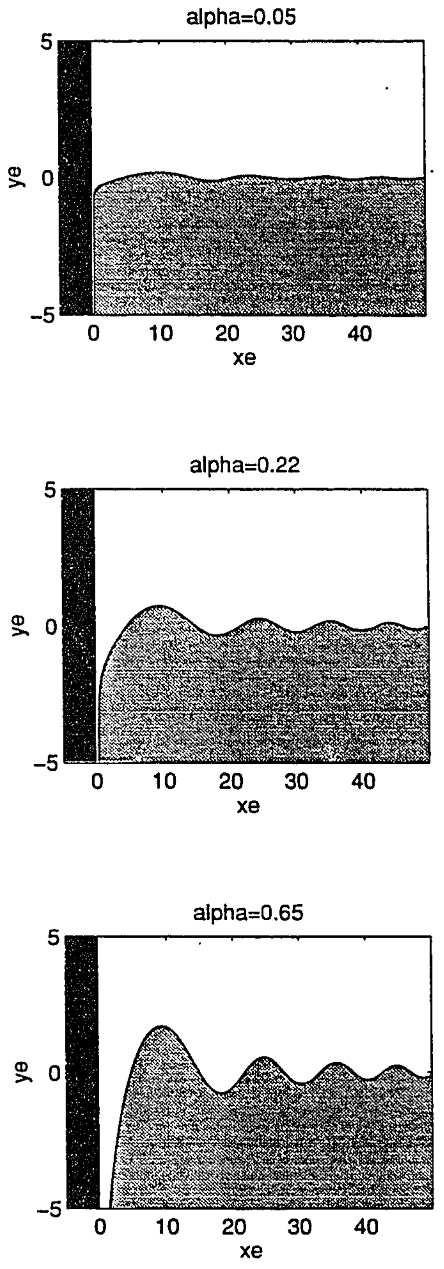

Figure 3.17: Asymmetric model experiment results with $\theta = 0$, $\beta = 0$ at $t = 100$ for: (a) $\alpha = 0.05$ (*Run a1*), (b) $\alpha = 0.22$ (*Run a2*), and (c) $\alpha = 0.65$ (*Run a3*). The y-axis scale is amplified about four times relative to the x-axis scale.

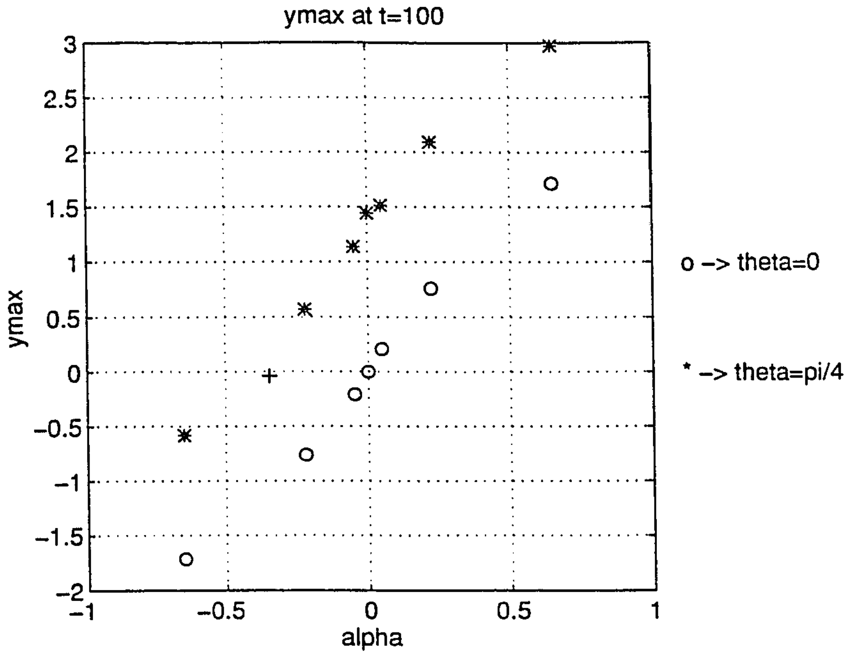

Figure 3.18: Position of the northernmost particle in the front at $t = 100$ as a function of the asymmetry parameter α for $\theta = 0$ (circled curve) and $\theta = \pi/4$ (starred curve). The black cross corresponds to the steady solution found at $\alpha = -0.38$. β is zero for all the simulations.

possible only when the converging currents had the same velocity at the coast. When the velocities were different, they found a steady migration of the stronger current system toward the weaker one. Unlike the model presented in this work, the departing jet veering angle is a result of their calculations. In ours, it is prescribed at infinity to make the jet zonal in the ocean interior. This assumption probably sustains the alongshore momentum imbalance that triggers the long waves.

Cessi [1991] found steady states in her viscous barotropic quasi-geostrophic converging jet model. Retroflection patterns were obtained, as in our results. In some of her experiments, a steady retroflection eddy was formed at the western boundary. If the statement about the momentum imbalance in our model is correct, *Cessi*'s [1991] result may be indicative that friction is needed to obtain steady states in an asymmetric converging jet system.

The tilted boundary case

In this series of experiments the coast is tilted in the presence of asymmetric coastal currents. In doing so, the symmetry in the geometry of the upper and lower halves of the model is lost and experiments with positive and negative α values are conducted.

The results from the two previous sections suggest that the forcing by the tilt and asymmetry will be additive when $\alpha > 0$ and will oppose each other for the $\alpha < 0$ cases.

The first pair of experiments employed a very small α, but with opposite signs. *Run a4* (Figure 3.19a) corresponds to $\alpha = 0.05$, and *Run a5* (Figure 3.19b) to $\alpha = -0.05$. As expected, the forcing by the tilt is much larger than the asymmetry effect and both results resemble the $\alpha = 0$ case (Figure 3.17), with the waves having slightly higher (lower) amplitudes in the positive (negative) α values. Also, the wave pattern is evidently translated by a distance x_0 from the coast.

When we make $\alpha = \pm 0.22$ (*Runs a6 and a7*, Figures 3.19c and 3.19d, respectively), about a third of the θ value, the forcing by asymmetry comes more effectively

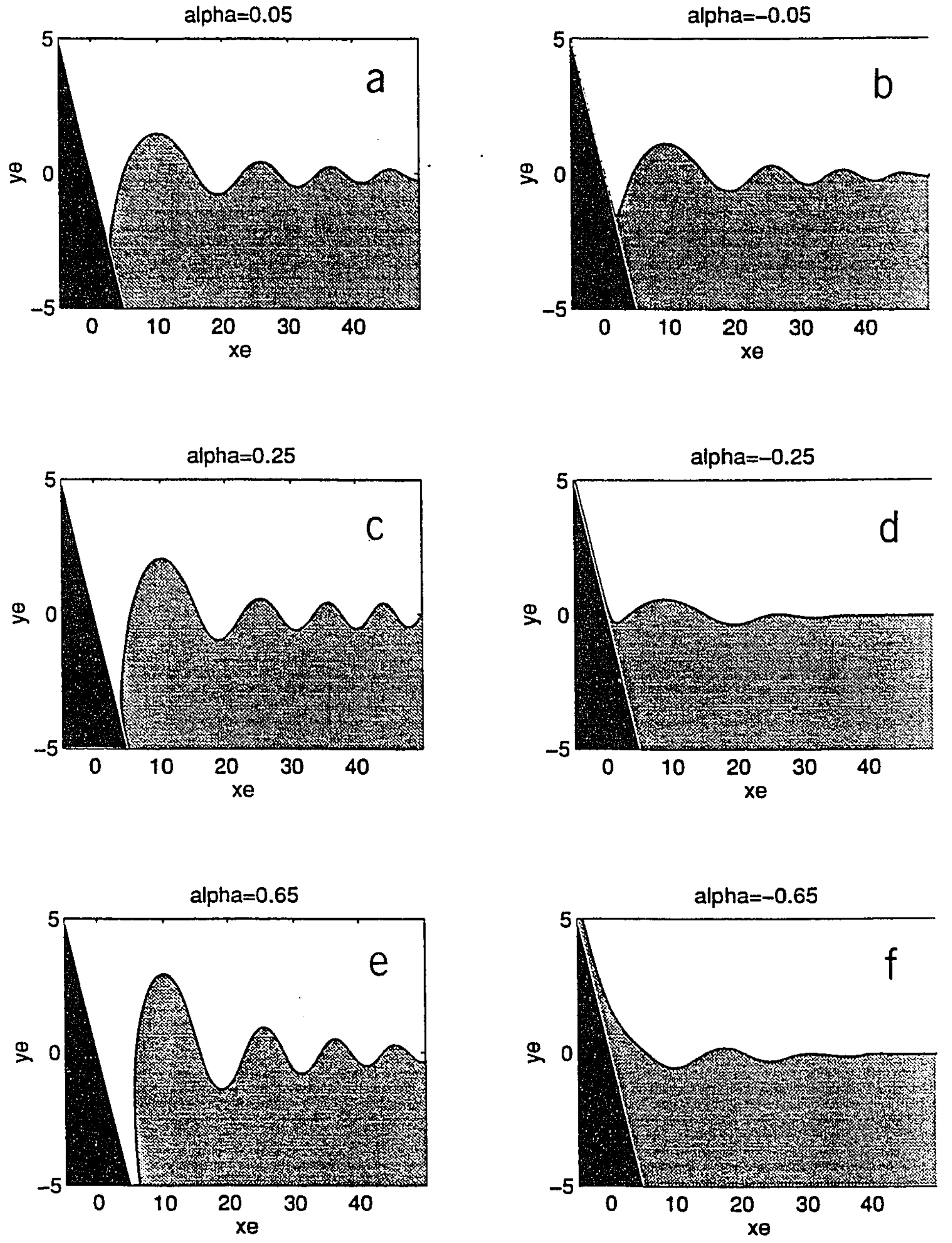

Figure 3.19: Asymmetric model experiment results with $\theta = \pi/4$, $\beta = 0$ at $t = 100$ for: (a) $\alpha = 0.05$ (*Run a4*), (b) $\alpha = -0.05$ (*Run a5*), (c) $\alpha = 0.22$ (*Run a6*), (d) $\alpha = -0.22$ (*Run a7*), (e) $\alpha = 0.65$ (*Run a8*) and (f) $\alpha = -0.65$ (*Run a9*).The y-axis scale is amplified about four times relative to the x-axis scale.

into play. The much smaller wave amplitudes and different pattern make evident the competition between the opposing forcing effects of tilt and asymmetry in Figure 3.19d, for which α is negative.

The asymmetry is of the same order as θ in *Runs a8 and a9* (Figures 3.19e and 3.19f), with $\alpha = \pm 0.65$. As expected, when the two $O(1)$ asymmetry and tilt effects add up, the highest amplitude waves among all f-plane experiments in this work are produced. On the other hand, when $\alpha < 0$, the asymmetry effect dominates and the wave amplitudes (Figure 3.19f) resemble the ones obtained for the meridional boundary, small asymmetry case. The dominance of asymmetry in the balance is due the fact that the front is separated by about one deformation radius from the coast ($x_0 = 1.05$) and the effect of the tilted coastline decays eastward (see Figure A1 in the Appendix). In other words, even with both effects having approximately the same strength, they are applied at different locations, and the front is closer to the influence of the asymmetry forcing.

From Figure 3.18 (circled curve) we could infer that no steady state is possible for an asymmetric converging current system when the western boundary is oriented meridionally. The results from Section 3.3.1.2 also suggest that there is no steady state for a symmetric converging current system when the coastline is slanted. However, when the tilt and asymmetry parameters have opposite signs (see Figure 3.18), it is possible that the effects cancel each other, making a steady solution possible. There are rigorous ways in the literature to find steady states based on potential vorticity conservation [e.g., *Wu et al.*, 1984]. In this work, we simply take advantage of the quasi-linear relationship between asymmetry and maximum wave amplitude (in an absolute sense). We then perform a linear fit using the starred curve in Figure 3.18 and estimate the parameter α for the zero amplitude value. After some tests to adjust the values using the linear fit error bounds, we find a numerical steady state solution for the $\alpha = -0.38$ and $\theta = \frac{\pi}{4}$ values (black cross in Figure 3.18), within our standard contour dynamics model resolution. The results of *Run a10* are presented in Figure 3.20.

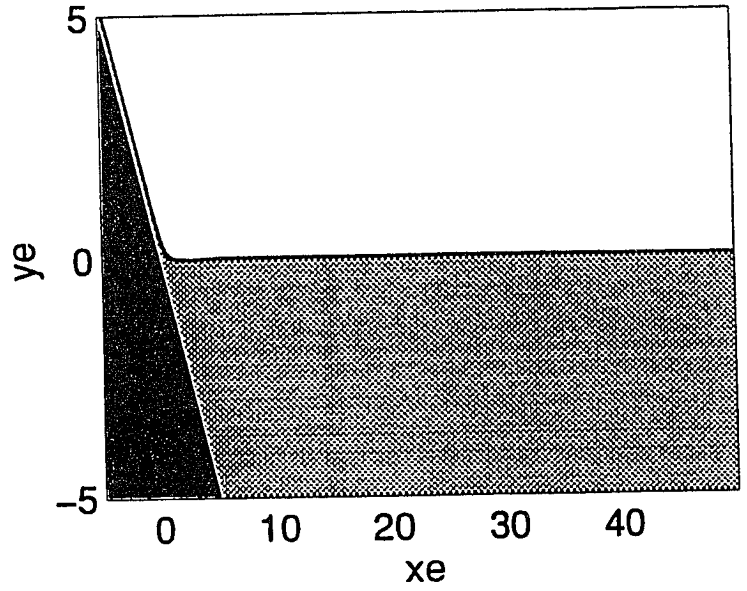

Figure 3.20: The steady state obtained for asymmetric model experiment *Run a10*, with $\theta = 0$, $\beta = 0$ and $\alpha = -0.38$. The y-axis scale is amplified about four times relative to the x-axis scale.

3.4 Applications

In this section, we apply the model to three well known western boundary current systems: the Gulf Stream, the Brazil Current, and the North Brazil Current. The variable scales and nondimensional parameters used in the three cases are presented in Table 3.4. The horizontal velocity scales U were estimated by matching the jet transport of our model with the observed transports.

Table 3.4: Scales and nondimensional parameters for the three study cases

current system	Length/scale (km)	$U(\mathrm{ms}^{-1})$	θ	α	β
Gulf Stream	30 [a]	1.2 [b]	$-\pi/4$	0.55 [c]	0.014
Brazil Current	30 [d]	0.5 [e]	$\pi/6$	0.33 [f]	0.033
North Brazil Current	110 [g]	0.8 [h]	$\pi/4$	0.3 [i]	0.348

[a] estimated R_d from *Hall and Fofonoff* [1993]

[b] estimated from *Schmitz and McCartney* [1993]

[c] estimated from *Schmitz and McCartney* [1993]

[d] estimated as R_d from *Houry et al.* [1987]

[e] estimated from *Gordon and Greengrove* [1986]

[f] estimated from *Gordon and Greengrove* [1986]

[g] estimated as R_d from *Houry et al.* [1987]

[h] estimated from *Bub and Brown* [1996]

[i] same as above

3.4.1 The Gulf Stream

The Gulf Stream case is modeled as the convergence between the Gulf Stream and the Slope Water near Cape Hatteras to form the Gulf Stream Extension. *Schmitz and McCartney* [1993] find that the transport in the upper kilometer of the Gulf Stream near Cape Hatteras, where it leaves the coast, to be about 55 Sv ($1Sv = 10^6\, m^3\, s^{-1}$) when it leaves the coast, and that the Slope Water transport is about 15 Sv. In terms of this model, the separating Gulf Stream is an asymmetric current system with $\alpha = 0.55$. Since α and θ have opposite signs, the effects oppose each other, with the asymmetry effect dominating. Consistent with PS86's scaling analysis, the β parameter is virtually negligible compared to the current vorticity gradient (about 1/60).

The results for the *Gulf Stream Run* (Figure 3.21a) reveal small amplitude, long meanders ($\approx 15R_d$ or about $450km$). These wavelengths are similar to those seen in the mean satellite image composite of the north wall by *Cornillon et al.* [1986]. The maximum meander amplitude occurs at a distance of $10\, R_d$ from the coast, and for $t = 100$ it is about $0.35\, R_d$ or $10.5\, km$. Using the position of the northernmost particle in the front, we can estimate the speed at which the largest lobe is moving eastward. Dimensionally, the main lobe "phase speed" is $8.7\, km\, d^{-1}$. This value represents 62% of phase speeds of $14\, km\, d^{-1}$ observed by *Tracey and Watts* [1986] for the wavelength range of $450 - 500km$ close to Cape Hatteras.

It is not a surprise that a equivalent-barotropic, single-front model does not agree with many aspects of the observed configuration of the Gulf Stream Extension with its growing meanders and ring production. Using a two-layer version of the PS86 jet model, *Meacham* [1991] showed that baroclinic instability can produce large amplitude meanders and eddy-shedding of similar character to the ones observed for the Gulf Stream Extension. A barotropically unstable version of the PS86 model, presented by *Pratt et al.* [1991], also produced eddies that resembled the warm out-

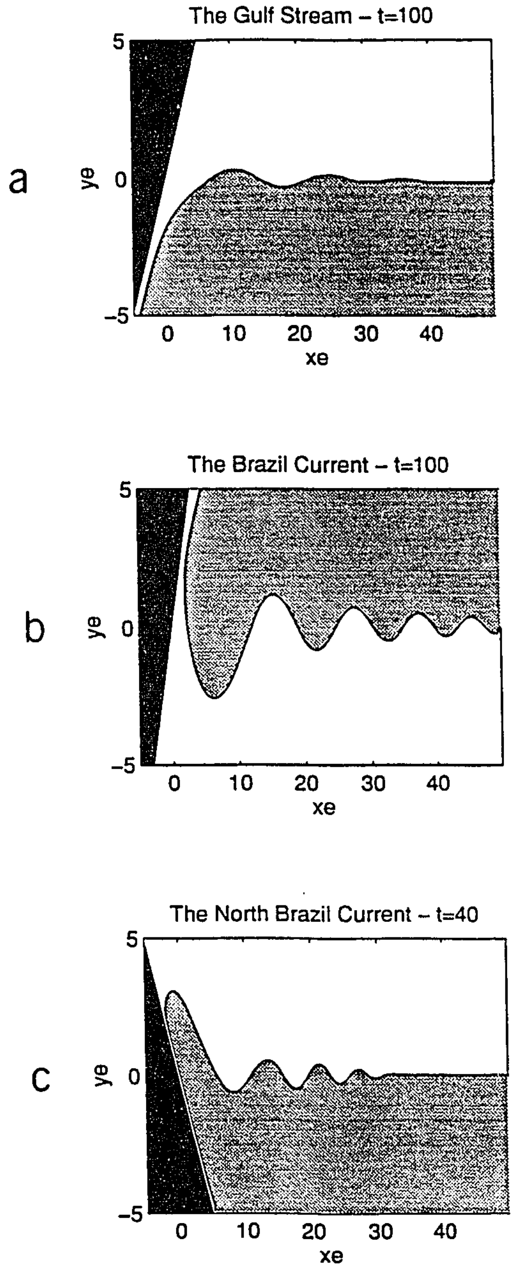

Figure 3.21: The boundary current applications: (a) the Gulf Stream case at $t = 100$ ($\theta = \pi/4$, $\beta = 0.014$, $\alpha = -0.55$); (b) the Brazil-Malvinas Confluence case at $t = 100$ ($\theta = \pi/6$ $\beta = 0.033$, $\alpha = 0.33$); and (c) the North Brazil Current case at $t = 40$ ($\theta = \pi/4$, $\beta = 0.348$, $\alpha = 0.3$).

break events in the Gulf Stream. However, our model lacks baroclinic and barotropic instability mechanisms. The incorporation of baroclinic instability mechanisms into a version of the present model is in progress.

3.4.2 The Brazil-Malvinas Confluence

The Brazil Current separates from the continental margin at approximately 38°S where its warm subtropical waters meet the cold subantarctic waters of the Malvinas Current to form the Brazil Current Extension, and later the South Atlantic Current [*Olson et al.*, 1988; *Stramma and Peterson*, 1990]. According to *Gordon and Greengrove* [1986], Brazil Current geostrophic transport in the upper 1000m is about 20 Sv and twice the transport for the Malvinas Current. Therefore, a Brazil Current experiment, analogous to the Brazil- Malvinas confluence (in the northern hemisphere, for convenience) with $\alpha = 0.33$, was conducted.

In contrast to the Gulf Stream situation, θ and α have the same sign in this case and therefore reinforce each other. Given the much less intense flow of the Brazil Current, its β scale is twice the value of its northern hemisphere counterpart.

The results for the *Brazil Current Run* (Figure 3.21b) are similar to the wavelength of about 450 km (at $\approx t = 100$) found for the larger lobes of the previous f-plane experiments (β is small). As the South American coast is less deviated from the north-south orientation, $\mid \theta \mid$ is smaller than for the Gulf Stream case. Thus, the maximum amplitude value of about 1.9 R_d (or 57 km) at $t = 100$ lies in between the two curves of Figure 3.18.

The width of the larger lobes is in agreement with the 500km found in *Olson et al.*'s [1988] analysis of satellite images. However, the amplitudes are reduced by a factor of 5. The large amplitude meanders and coastal eddy-shedding observed by *Gordon and Greengrove* [1986] and *Olson et al.* [1988] can be attributed to barotropic or baroclinic instabilities. Numerical experiments with the Miami model by *Campos and Olson* [1991] indicated that barotropic instability caused meandering growth and eddy-shedding in their simulations of the Brazil-Malvinas Confluence.

3.4.3 The North Brazil Current

We now model the separation of the near-equatorial North Brazil Current as the convergence of its $45Sv$ with a broader and slower southward branch of the North Equatorial Current, carrying about $35Sv$ [*Johns et al.*, 1991 and *Bub*, personal communication]. The convergence forms the western part of the North Equatorial Countercurrent. Since the separation occurs at about 7°N, the deformation radius is about four times larger than those for the mid-latitude examples. Also, the nondimensional Rossby parameter β is 0.35, one order of magnitude higher than the previous examples.

The results for the *North Brazil Current Run* (Figure 3.21c) show that the retroflection is reproduced and that the wavelengths present at $t = 40$ are about $700 - 900$km. These values are consistent with *Richardson and Reverdin* [1987] and *Richardson et al.* [1994]. The larger value of β causes the contour to be pushed against the boundary, and the main lobe grows northward (in a mechanism similar to the one described in *Run s3*). We acknowledge that the way the β-effect is modeled here is somewhat arbitrary, since one could move the $\psi_\beta = 0$ streamline north or south. However, the results on Figure 3.21c show striking resemblance to the maps of the North Brazil Current retroflection in charts derived from satellite images presented by *Johns et al.* [1990] and surface drifter tracks by *Richardson et al.* [1994]. In particular, the stretching of the retroflection bulge prior to shedding an eddy has been observed. Unfortunately, this model does not result in complete eddy detachment. Instead, it shows a slow linear stretch of the retroflection bulge northwestward.

In contrast to the previous current system examples, there is no evidence in the literature that either baroclinic or barotropic instabilities may play a role in the North Brazil Current eddy-shedding. It appears the processes governing the detachment in this case are yet to be uncovered.

3.5 Summary and Conclusions

In this paper we have explored the effect of coastline orientation and transport asymmetry in converging western boundary currents which form a zonal eastward inertial jet. A single-vorticity-front contour dynamics model based on PS86's infinite jet model is developed to explore this system. The β-effect is introduced in the model in such a way that the contour dynamics technique requirement of a piecewise constant potential vorticity field is satisfied. The β term is compensated for by including a time-independent flow field similar to the edge between two Fofonoff gyres. The parameter space of the model is spanned, including: the coastline tilt angle θ, the transport asymmetry α and the nondimensional Rossby parameter β.

For the case of a north-south coastline orientation ($\theta = 0$) and symmetric converging currents ($\alpha = 0$) that form a zonal jet, a steady state is known to exist. The PS86 experiments with isolated disturbances are repeated and the effect of the boundary is investigated. It is found that in the presence of the boundary, long waves are often excited and very little nonlinear steepening occurs as the flow evolves. The input of large potential vorticity anomalies leads to a slowly temporally decaying (growing) damped long wave pattern in our f-plane (β-plane) calculations. This pattern resembles the quasi-stationary wave motion observed in western boundary current extensions. Relatively shorter waves occurred in the β-plane experiments. Coastal eddy detachment in the present model is unlikely, even if fairly extreme boundary conditions are used. These results differ from the infinite jet experiments of PS86, where eddy shedding occurred when the same initial conditions were used. The presence of the western boundary (through the zonal gradient in the "undisturbed" cross-shore velocity component required to satisfy the zero normal flow condition at the coast) stretches the disturbances so that the long wave limit is reached rapidly, and prevents wave breaking on the west side of the anomaly.

When either a non-meridional coastline or converging current asymmetry are considered, a steady state seems not possible. The tilt in coastline orientation ($\theta \neq 0$) imposes a momentum imbalance that creates a steady source of potential vorticity at the coastward end of the departing jet. This source drives temporally growing, spatially damped long waves. The linear slow growth observed in the wave pattern is probably associated with the steady input of alongshore momentum in the model. If the tilt effect is thought of as a steady forcing, as the linear model in Appendix suggests, the quasi-stationary long waves excited are close to the resonance (zero) frequency and may account for the slow linear growth of the amplitudes. Similar responses can occur when there is asymmetry in the coastal current transports, without coastline tilt.

For the cases in which we allow both θ and α to be nonzero, the dynamical effects of asymmetry and tilt can reinforce or oppose each other. When the coastline is tilted westward relative to the stronger current direction, they reinforce each other, generating the "retroflection" type of separation (Figure 3.1b). When the coastline tilt is eastward following the stronger current, the two effects oppose each other, accounting for much smoother separations. These results agree with *Ou and De Ruijter*'s [1986] model results and *Campos and Olson*'s [1991] description of boundary current separations. Steady state solutions may be obtained for the latter case by means of total cancelation between tilt and asymmetry forcings.

The application of the model to three different separating boundary current systems qualitatively reproduces the separation patterns and the observed wavelengths are within the observed range.

We acknowledge that the model is unbalanced in all unsteady runs described above. However, we believe that the model has shown that an inertial system can reproduce the patterns observed in separating boundary currents by introducing a momentum imbalance locally (i.e., close to the coast) through tilting the coastline or making the current system asymmetric. The downstream condition of constraining the jet to be zonal is also in agreement with observations of most boundary current extension flow patterns. In the real ocean, we expect that other forces (such as pressure forces and friction) would balance the system as whole, and a retroflection pattern steady state may be possible.

Next chapter deals with a version of the present model which incorporates baroclinic instability mechanisms by considering a $2\frac{1}{2}$-layer configuration.

Appendix: The Linear Symmetric Model

The Model Formulation

The contour dynamics model developed in Section 3.2.1 allows the nonlinear investigation for any coastline tilt [the angle θ may be $O(1)$]. Here, we consider the linearized case in which the coast orientation is either meridional or only slightly tilted from the north-south direction , i.e., $\theta << 1$.

For easier manipulation of the equations, we first define a non-orthogonal coordinate system (x, ξ), where x is still the cross-shore direction and ξ is the cross-front direction defined by

$$\xi \;=\; y \;-\; \bar{y}(x) \tag{A1}$$

or, using Eq. (3.4),

$$\xi \;=\; y \;+\; x \tan\theta\,. \tag{A2}$$

In terms of the new coordinate system, Eq. (3.3) becomes

$$[\frac{\partial^2}{\partial x^2} + 2\tan\theta\frac{\partial^2}{\partial x \partial \xi} + (1+\tan^2\theta)\frac{\partial^2}{\partial \xi^2} - 1]\hat{\psi} + \beta\xi\cos\theta \;=\; -1 \;+\; 2\mathcal{H}(\xi - \hat{\eta})\,, \tag{A3}$$

where the hats denote the fields for the linearized model.

Eq. (3.17b) is also rewritten, with $\hat{v}$ as the new cross-front velocity:

$$\frac{d}{dt}\hat{\eta} \;=\; \frac{\partial \hat{\eta}}{\partial t} \;-\; \frac{\partial \hat{\psi}}{\partial \xi}\frac{\partial \hat{\eta}}{\partial x} \;=\; \hat{v}(x, \hat{\eta}, t). \tag{A4}$$

Under the $\theta << 1$ assumption, Eq. (A2) can be rewritten as

$$\xi = y - \theta x + O(\theta^2) \tag{A5}$$

and $\hat{\psi}$ can be expanded in the asymptotic series

$$\hat{\psi} = \hat{\psi}_0 + \theta\hat{\psi}_1 + O(\theta^2)\,. \tag{A6}$$

In the linear regime, $\hat{\eta}$ is $O(\theta)$, so that

$$\mathcal{H}(\xi - \hat{\eta}) = \mathcal{H}(\xi) - \delta(\xi)\hat{\eta} + O(\hat{\eta}^2) \ .$$

We can substitute Eqs. (A5) and (A6) into Eqs. (A3) and (A4) and collect the lowest terms to obtain

$$[\frac{\partial^2}{\partial x^2} + \frac{\partial^2}{\partial \xi^2} - 1]\hat{\psi}_0 + \beta\xi = -1 + 2\mathcal{H}(\xi)\,, \tag{A7}$$

and

$$\hat{\psi}_0(x, 0) = 0\,, \tag{A8}$$

respectively. No restriction was imposed on the size of β to allow the model to be applied for conditions where $\beta > \theta$.

The $\hat{\psi}_0$ field is partitioned into "undisturbed" $\hat{\psi}_{00}$ and "beta" $\hat{\psi}_{0\beta}$ parts that satisfy

$$[\frac{\partial^2}{\partial x^2} + \frac{\partial^2}{\partial \xi^2} - 1]\hat{\psi}_{00} = -1 + 2\mathcal{H}(\xi)\,, \tag{A9}$$

and

$$[\frac{\partial^2}{\partial x^2} + \frac{\partial^2}{\partial \xi^2} - 1]\hat{\psi}_{0\beta} = -\xi \ . \tag{A10}$$

respectively. Note that if we replace y with ξ and consider $\theta = \bar{y} = 0$, Eqs. (A9) and (A10) are of the same form as Eqs. (3.6) and (3.7). So are the boundary conditions and the solutions. Therefore, the solutions in Figures 3.4a and 3.5a also respectively represent the solutions for $\hat{\psi}_{00}$ and $\hat{\psi}_{0\beta}$ in the (x, ξ) space.

Defining

$$\hat{u}_0 = -\frac{\partial\hat{\psi}_0}{\partial\xi}\,, \tag{A11}$$

the $O(\theta)$ equations are:

$$[\frac{\partial^2}{\partial x^2} + \frac{\partial^2}{\partial \xi^2} - 1]\hat{\psi}_1 - 2\frac{\partial \hat{u}_0}{\partial x} = -2\delta(\xi)\hat{\eta}\,, \qquad \text{(A12)}$$

and

$$\frac{\partial \hat{\eta}}{\partial t} + \frac{\partial}{\partial x}(\hat{u}_0\hat{\eta}) = \frac{\partial \hat{\psi}_1}{\partial x} \ \text{ evaluated at } \xi = 0\,. \qquad \text{(A13)}$$

We can also split the $\hat{\psi}_1$ filed into $\hat{\psi}_{11}$ and $\hat{\psi}_{12}$, which satisfy

$$[\frac{\partial^2}{\partial x^2} + \frac{\partial^2}{\partial \xi^2} - 1]\hat{\psi}_{11} = 2\frac{\partial \hat{u}_0}{\partial x} \qquad \text{(A14)}$$

$$[\frac{\partial^2}{\partial x^2} + \frac{\partial^2}{\partial \xi^2} - 1]\hat{\psi}_{12} - \ = -2\delta(\xi)\hat{\eta}\,, \qquad \text{(A15)}$$

respectively. It can be seen in the equations above that all time dependence of $\hat{\psi}_1$ is contained in its $\hat{\psi}_{12}$ component through $\hat{\eta}(x,t)$. Hence the time-independent $\hat{\psi}_{11}$ is determined by iteration. The required boundary conditions for Eq. (A14) can be determined by considering the $\beta = 0$ case, in which the x-dependence of $\hat{u}_0$ is confined to small values of x and ξ (see Figure 3.4a). Thus it is reasonable to assume that $\hat{\psi}_{11}$ should also decay as $x \to \infty$ and $\xi \to \pm\infty$. The solution for $\hat{\psi}_{11}$ is shown in Figure A.1.

The $\hat{\psi}_{12}$ field is obtained in terms of Green's functions G_+ and G_-, as defined in Eq. (3.12), and written in the (x,ξ) space according to

$$\hat{\psi}_{12} = -2\int_0^\infty dx' \int_{-\infty}^\infty d\xi' [G_+ + G_-]\,\delta(\xi)\,\hat{\eta}(x',t)\,. \qquad \text{(A16)}$$

By applying the δ-function properties to Eq. (A16) and evaluating it at $\xi = 0$,

$$\hat{\psi}_{12} = \frac{1}{\pi}\int_0^\infty dx'\,[K_0(\mid x - x' \mid) - K_0(\mid x + x' \mid)]\,\hat{\eta}(x',t)\,, \qquad \text{(A17)}$$

The contour evolution Eq. (A13) for the linear model can be written in terms of $\hat{\psi}_{11}$ and $\hat{\psi}_{12}$,

$$\frac{\partial \hat{\eta}}{\partial t} + \frac{\partial}{\partial x}[\hat{u}_0\hat{\eta} - \hat{\psi}_{12}] = \frac{\partial \hat{\psi}_{11}}{\partial x} \qquad \text{(A18)}$$

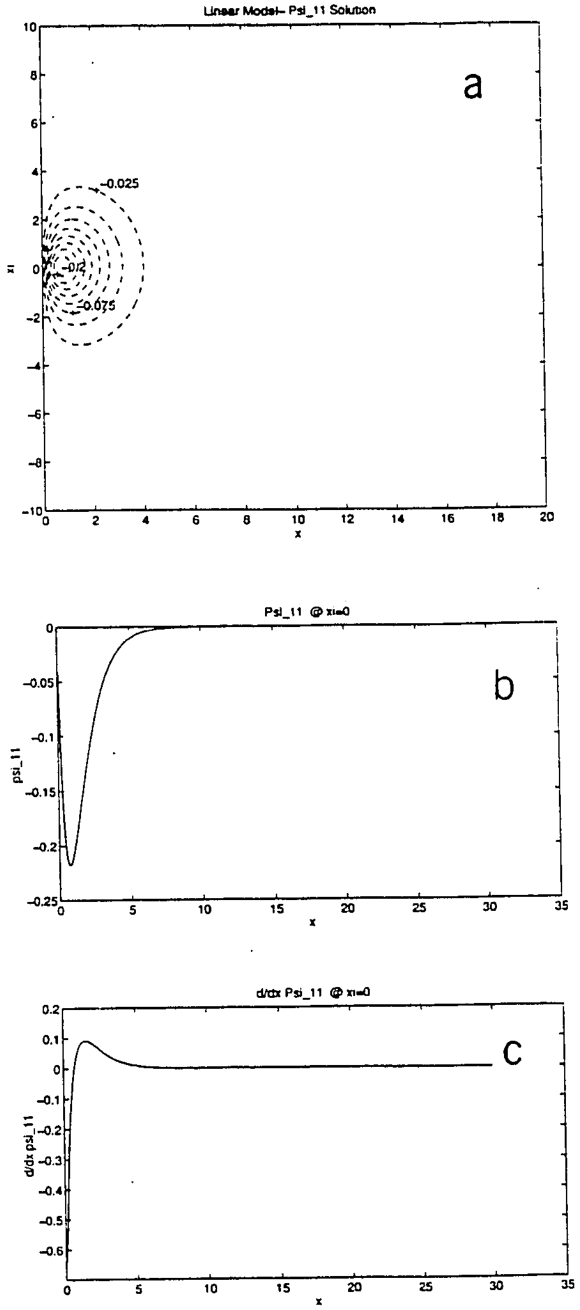

Figure A.1: The "mismatch" stream function $\hat{\psi}_{11}$ in the (x, ξ) space: (a) in the model domain, (b) along $\xi = 0$, and (c) its zonal gradient along $\xi = 0$.

or using Eq. (A16) to get

$$\frac{\partial\hat{\eta}}{\partial t} + \frac{\partial}{\partial x}\{\hat{u}_0\hat{\eta} - \frac{1}{\pi}\int_0^\infty dx'[K_0(| x - x' |) - K_0(| x + x' |] \hat{\eta}(x', t)\} = \frac{\partial\hat{\psi}_{11}}{\partial x} . \quad \text{(A19)}$$

Eq. (A18) [or Eq. (A19)] is a first order wave equation for $\hat{\eta}$, which is steadily forced by $\hat{v}_{11}(0)$ (Figure A.1). For the cases the coast is tilted, $\hat{\psi}_{11}$ exists and the time independent part of stream function field does not coincide with the contour. Thus the quantities in the linear model $\hat{\psi}_0 + \theta\hat{\psi}_{11}$, where $\hat{\psi}_{11}$ accounts for the mismatch between the contour and streamline (as seen in Figures 3.4b and 3.5b) can be related to the corresponding quantities in the nonlinear model: the $\psi_0 + \beta\psi_\beta$ field.

Prior to the discretization of Eq. (A18), the integrals in Eq. (A17), as in Eq. (3.15), need to have the logarithmic singularity removed. Here, the desingularization is done in a slightly different manner from the method employed on the contour dynamics scheme. We follow the PS86 method here.

As an example, consider the first integral of the right hand side of Eq. (A17). In the $| x - x' | \leq \epsilon$ interval where $\epsilon \ll 1$, the integral is singular. Hence, we can split the integral into non-singular and singular parts, as follows:

$$\begin{aligned} \int_0^\infty dx' K_0(| x - x' |)\hat{\eta}(x', t) &= \int_{|x-x'|>\epsilon} dx' K_0(| x - x' |)\hat{\eta}(x', t) \\ &+ \int_{x-\epsilon}^{x+\epsilon} dx' K_0(| x - x' |)\hat{\eta}(x', t) . \end{aligned} \quad \text{(A20)}$$

Note that the singularity is now confined to the second integral on the right hand side.

Using the $\epsilon \ll 1$ assumption, we can approximate $\hat{\eta}(x', t)$ in the singular integral of Eq. (A20) by

$$\hat{\eta}(x', t) = \hat{\eta}(x, t) + O(\epsilon) , \quad \text{(A21)}$$

which yields

$$\int_{x-\epsilon}^{x+\epsilon} dx' K_0(| x - x' |)\hat{\eta}(x', t) = -\hat{\eta}(x, t)\int_{x-\epsilon}^{x+\epsilon} dx' \ln(| x - x' |) + O(\epsilon) , \quad \text{(A22)}$$

given that $K_0(r) = -\ln(r) + O(\epsilon)$ for $r \leq \epsilon$.

The integral on the right hand side of Eq. (A22) can be easily integrated by parts to obtain

$$\int_{x-\epsilon}^{x+\epsilon} dx' \ln(\mid x - x' \mid) = -2\epsilon[\ln(\epsilon) - 1] + O(\epsilon) \,, \tag{A23}$$

With Eqs. (A22) and (A23) in Eq. (A20), we get

$$\begin{aligned} \int_0^\infty dx' \, K_0(\mid x - x' \mid) \, \hat{\eta}(x', t) &= \int_{|x-x'|>\epsilon} dx' \, K_0(\mid x - x' \mid) \hat{\eta}(x', t) \\ &- 2\epsilon[\ln(\epsilon) - 1]\hat{\eta}(x, t) + O(\epsilon) \,. \end{aligned} \tag{A24}$$

A similar procedure should be applied to the second integral on the right hand side of Eq. (A17).

Having desingularized the integrals in the $\hat{\psi}_{12}$ expression, we can discretize Eq. (A18). The numerical procedure used in this model is based on an Eulerian scheme, unlike the Lagrangian contour dynamics algorithm. Therefore, values for $\hat{\eta}(x, t)$ will be evaluated on a grid of fixed "x" values. Hence, considering

$$x_{(i)} = i\Delta x \quad \text{for} \quad i = 0, M \tag{A25a}$$

$$t^{(n)} = n\Delta t \quad \text{for} \quad n = 0, N \,, \tag{A25b}$$

we use a modified Lax finite difference scheme to approximate Eq. (A18) as

$$\begin{aligned} &\frac{\hat{\eta}^{(n+1)}_{(i)} - \frac{1}{2}[\hat{\eta}^{(n)}_{(i+1)} + \hat{\eta}^{(n)}_{(i-1)}]}{\Delta t} + \frac{\hat{u}_{0_{(i+1)}}\hat{\eta}^{(n)}_{(i+1)} - \hat{u}_{0_{(i)}}\hat{\eta}^{(n)}_{(i)}}{\Delta x} \\ &\qquad - \frac{\hat{\psi}^{(n)}_{12_{(i+1)}} - \hat{\psi}^{(n)}_{12_{(i)}}}{\Delta x} = \frac{\hat{\psi}_{11_{(i+1)}} - \hat{\psi}_{11_{(i)}}}{\Delta x} \,, \end{aligned} \tag{A26}$$

which is solved together with

$$\begin{aligned}\hat{\psi}^{(n)}_{12_{(i)}} &= \frac{\Delta x}{\pi}[\sum_{j\neq i} K_0(\mid x_{(i)} - x_{(j)} \mid)\,\hat{\eta}^{(n)}_{(j)} - (\ln\frac{\Delta x}{2} - 1)\hat{\eta}^{(n)}_{(i)} \\ &- \sum_{j\neq 0} K_0(\mid x_{(i)} + x_{(j)} \mid)\,\hat{\eta}^{(n)}_{(j)} + (\ln\frac{\Delta x}{2} - 1)\hat{\eta}^{(n)}_{(i)}\delta(j)\,],\end{aligned} \tag{A27}$$

where

$$\begin{aligned}\delta(j) &= 1 \quad \text{for } j = 0 \\ &= 0 \quad \text{otherwise}\end{aligned}$$

and ϵ was taken to be equal to $\frac{\Delta x}{2}$.

For the beginning of the domain ($i = 0$), we simply use

$$\frac{\hat{\eta}^{(n+1)}_{(0)} - \hat{\eta}^{(n)}_{(0)}}{\Delta t} + \frac{\hat{u}_{0_{(1)}}\hat{\eta}^{(n)}_{(1)} - \hat{u}_{0_{(0)}}\hat{\eta}^{(n)}_{(0)}}{\Delta x} - \frac{\hat{\psi}^{(n)}_{12_{(1)}} - \hat{\psi}^{(n)}_{12_{(0)}}}{\Delta x} = \frac{\hat{\psi}_{11_{(1)}} - \hat{\psi}_{11_{(0)}}}{\Delta x} \tag{A28}$$

The far-end boundary condition is obtained by choosing an M large enough to guarantee that $\hat{\eta}^{(n+1)}_{(M)} = 0$.

The numerical stability criteria is given by

$$\mid \frac{\Delta t}{\Delta x}\hat{u}_{0_{MAX}} \mid \leq 1 . \tag{A29}$$

Numerical Results

In this section we repeat some of the initial value problems described in Section 3.3.1 using the linear physics.

The meridional boundary case

For the $\theta = 0$ case, $\bar{y}(x)$ and $\hat{\psi}_{11}$ are also zero, and Eq. (A18) becomes homogeneous. We then perform the *Run l1* experiment, which is the linear analog of *Run s2*. In Figure A.2a, it can be verified that the same wave pattern as in the nonlinear model is obtained. The waves have approximately the same wavelengths, but the apparent spatial "damping" seem stronger.

The tilted boundary case

By including a slight tilt in the coastline, for example, $\theta = \frac{\pi}{40}$, the linear model also repeats the behavior of its contour dynamics counterpart. *Run l2* (Figure A.2b) and *Run l3* (Figure A.2c) represent the linear analogs of the *Run s8* and *Run s9*, respectively. The steady input of alongshore momentum is made explicit by the $\hat{v}_{11}$ velocity. Even though we just show the final time step of both model runs in Figure A.2, it is verified that the growth rate in the wave pattern is similar to the nonlinear calculations.

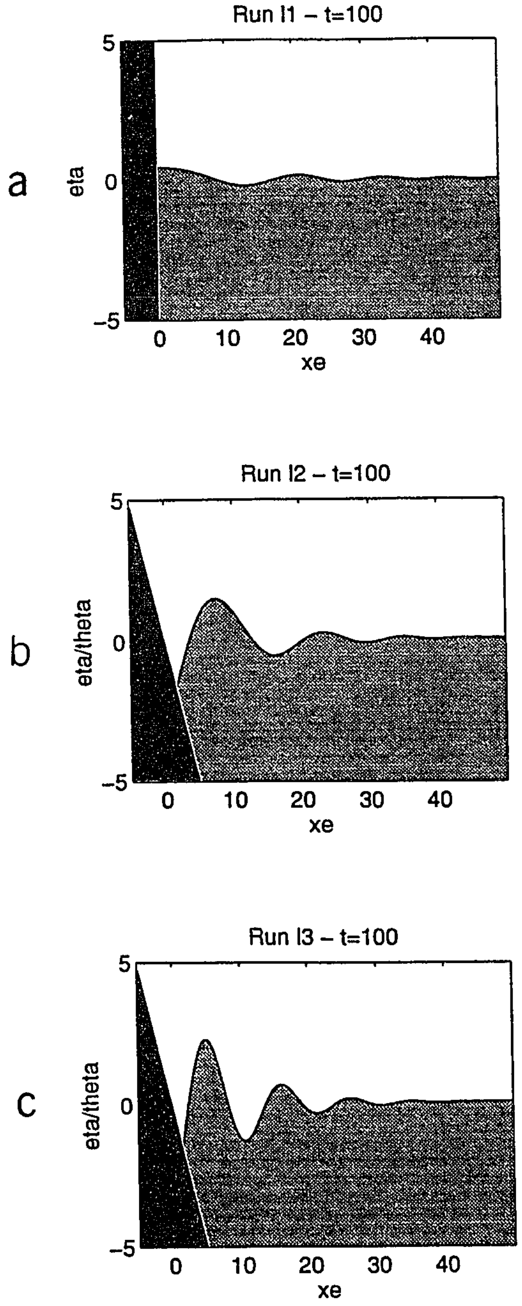

Figure A.2: Linear symmetric model experiment results at $t = 100$ for: (a) $\theta = 0$, $\beta = 0$ (*Run l1*), (b) $\theta = \frac{\pi}{4}$, $\beta = 0$ (*Run l2*), and (c)$\theta = \frac{\pi}{4}$, $\beta = 0.1$ (*Run l3*). The y-axis scale is amplified about four times relative to the x-axis scale.

References

Agra, C., and D. Nof, Collision and separation of boundary currents, *Deep-Sea Res. I, 40,* 2259-2282, 1993.

Bell, G.I., and L.J. Pratt, Eddy-jet interaction theorems of piecewise constant potential vorticity flows, *Dyn. Atmos. Oceans, 20,*, 285-314, 1994.

Bub, F.L. and W.S. Brown, Seasonal changes in the intermediate layer transport of mass and heat in the western tropical Atlantic Ocean, *submitted to J. Geophys. Res.*, 1996.

Campos, E.J.D., and D.B. Olson, stationary Rossby waves in western boundary current extensions, *J. Phys. Oceanogr., 21,* 1202-1224, 1991.

Cessi, P., Laminar separation of colliding western boundary currents, *J. Mar. Res., 49*, 697-717, 1991.

Cornillon, P., The effect of the New England seamounts on the Gulf Stream meandering as observed form satellite IR imagery, *J. Phys. Oceanogr., 16,* 386-389, 1986.

Gordon, A.L., and C.L. Greengrove, Geostrophic circulation of the Brazil-Falkland confluence, *Deep-Sea Res. I, 33,* 573-585, 1986.

Hall, M.M., and N.P. Fofonoff, Downstream development of the Gulf Stream from 68° to 55° W, *J. Phys. Oceanogr.*, 23, 225-249, 1993.

Houry, S., E. Dombrowsky, P. De Mey, and J. F. Minster, Brunt-Vaisala frequency and Rossby radii in the South Atlantic, *J. Phys. Oceanogr., 17,* 1619-1626, 1987.

Johns, W.E., T.N. Lee, F. Schott, R. Zantopp, and R. H. Evans, The North Brazil Current retroflection: Seasonal structure and eddy variability, *J. Geophys. Res., 95,* 22103-22120, 1990.

Meacham, S.P., Meander evolution on piecewise-uniform, quasi-geostrophic jets, *J. Phys. Oceanogr., 21,* 1139-1170, 1991.

Olson, D., G. Podesta, R. Evans, and O. Brown, Temporal variations in the separation of Brazil and Malvinas currents, *Deep-Sea Res. I, 35,* 1971-1980, 1988.

Ou, H.W., and W.P.M. De Ruijter, Separation of an inertial boundary current from a curved coastline, *J. Phys. Oceanogr., 16,* 280-289, 1986.

Polvani, L.M., Geostrophic vortex dynamics, PhD thesis, MIT/WHOI Joint Program, WHOI-88-48, 221p., 1988.

Polvani, L.M., N.J. Zabusky, and G.R. Flierl, Two-layer geostrophic vortex dynamics Part 1. upper-layer V-states and merger, *J. Fluid. Mech., 205,*, 215-242, 1989.

Pratt, L.J., Meandering and eddy detachment according to a simple (looking) path equation, *J. Phys. Oceanogr., 18,*, 1627-1640, 1988.

Pratt, L.J., and M. E. Stern, Dynamics of potential vorticity fronts and eddy detachment, *J. Phys. Oceanogr., 16,*, 1101-1120, 1986.

Pratt, L.J., J. Earles, P. Cornillon, and J. F. Cayula, The nonlinear behavior of varicose disturbances in a simple model of the Gulf Stream, *Deep-Sea Res. I, 38,* S591-S622, 1991.

Pullin, D.J., Contour Dynamics method, *Annu. Rev. Fluid Mech., 24,*, 89-115, 1992.

Richardson, P.L., and G. Reverdin, Seasonal cycle of the velocity in the Atlantic North Equatorial Countercurrent as measured by surface drifters, current meters, and ship drifts, *J. Geophys. Res., 92,*, 3691-3708, 1987.

Richardson, P. L., G. E. Hufford, R. Limeburner, and W. S. Brown, North Brazil Current retroflection eddies, *J. Geophys. Res., 99,* 5081-5093, 1994.

Schmitz, W. J. and M. S. McCartney, On the North Atlantic circulation, *Rev. Geophys., 31,*, 29-49, 1993.

Stern, M. E., and L. J. Pratt, Dynamics of vorticity fronts, *J. Fluid. Mech., 161,* 513-532, 1985.

Stern, M. E., and G. R. Flierl, On the interaction of a vortex with a shear flow, *J. Geophys. Res., 92,*,, 10733-10744, 1987.

Stramma, L., and R. G. Peterson, The South Atlantic current, *J. Phys. Oceanogr., 20,* 846-859, 1990.

Tracey, K. L., and D. R. Watts, On the Gulf Stream characteristics near Cape Hatteras, *J. Geophys. Res., 91,* 7587-7602, 1986.

Wang, X, Interaction of an eddy with a continental slope, PhD thesis, MIT/WHOI Joint Program, WHOI-92-40, 216p., 1992.

Wu, H. M., E. A. Overman, and N. J. Zabusky, Steady state solutions of the Euler equation in two dimensions. Rotating and translating v-states with limiting cases. I. Numerical results, *J. Comput. Phys., 53,* 42-71, 1984.

Zou, Q., E. A. Overman, H. M. Wu, and N. J. Zabusky, Contour dynamics for the Euler equations: curvature controlled initial node displacement and accuracy, *J. Comput. Phys., 78,* 350-372, 1988.

Chapter 4

Eddy Formation in $2\frac{1}{2}$-Layer Jets

Abstract

The formation of nonlinear eddies in unstable $2\frac{1}{2}$-layer, quasi-geostrophic jets is investigated using a piecewise constant potential vorticity, "contour dynamical" model. Both infinite and semi-infinite jet dynamics are explored. In the first category, we perform numerical experiments analogous to those of *Meacham* [1991], who used a double-front, two-layer model. Unlike *Meacham*'s [1991] model, ours has a two dynamical mode structure in the background jet. The lower layer jet transport ranges from westward to eastward (with the upper layer transport considered eastward in all cases) and a continuum of eddy shedding events is obtained. When dipolar vortex formation occurs, it develops very similarly to *Meacham*'s [1991] two-layer experiments. It is found that apparently there are no bounds for dipole formation in terms of lower layer transport direction. Even weakly unstable jets are able to shed dipolar eddies when initial conditions target the most unstable wavenumbers. In the second category, we build the $2\frac{1}{2}$-layer analog of the *Silveira et al.* [1996] equivalent-barotropic, separating western boundary current model. We then verify that coastal and retroflection eddies are shed when baroclinic instability mechanisms are included. However, it seems that the unstable waves must either

propagate westward or slowly in the eastward direction to allow this process to occur.

4.1 Introduction

Contour Dynamics (CD) has provided a useful framework for the investigation of the nonlinear dynamics of quasi-geostrophic (QG) jets. As discussed in *Stern and Pratt* [1985], geophysical jets are usually associated with potential vorticity (PV) fronts (i.e., a front separating regions of significantly different PV values), for which a step-function is a reasonable approximation. The CD method, based on PV conservation, consists exactly of solving initial value problems for PV fields with a stair-step profile with discontinuities (fronts) separating regions of uniform PV (i.e., piecewise constant PV distributions) [*Pullin*, 1992]. The Lagrangian form of the dynamical equations are solved to determine the evolution of the PV front regions [*Dritschel and Legras*, 1993]. The QG inversion relationships are used to determine the flow field from a known PV distribution. Since PV is made piecewise constant, the area integrals normally required to invert the PV expressions are replaced with contour integrals evaluated at the PV fronts [*Flierl and Meacham*, 1995; hereafter referred to as FM95]. Another appealing feature of the CD method is that is explicit about the contributions of the "background" and the "perturbed" parts of the flow in the evolution of the PV front [*Pratt and Stern*, 1986; *Pratt*, 1988].

The principal shortcoming of CD models is that they are restricted to investigating inviscid flow systems. Also, the piecewise constant PV fields of the CD approach makes it difficult to handle the planetary vorticity gradient (i.e., β-effect), which is a large-scale and smoothly varying PV gradient. *Yano and Flierl* [1992] attempted to circumvent the latter limitation for infinite domain models by adding a parabolic zonal flow that completely compensates for the β-term in the PV relation. They included a westward tendency in the background flow, but Rossby waves were still not possible. *Silveira et al.* [1996] (hereafter referred to as SFB96) followed the same procedure in their semi-infinite domain model, bounded by the western boundary, in which their "beta" flow structure resembled the edge between two Fofonoff gyres. Another approach is to approximate the planetary vorticity gradient by a series of zonal fronts, equally spaced by a distance Δy and with vorticity jumps of magnitude $\beta \Delta y$ [*Griffa and Virasoro*, 1988].

Alternately, there have been several f-plane QG jet studies in the literature. One of the first and simplest models to investigate nonlinear f-plane flows is *Stern* [1985], who considered a broad barotropic, infinite jet model associated with a single PV front. *Stern* [1985] successfully obtained shingle formation, similar to that observed in the Gulf Stream, by analyzing the evolution of large amplitude disturbances. The *Pratt and Stern* [1986] model incorporated the ocean stratification in its minimum form by examining the dynamics of a $1\frac{1}{2}$-layer (or equivalent barotropic), single PV front zonal jet. The background flow in their model had more "realistic" jetlike characteristics, with a cusped jet profile and a maximum velocity at the PV front, than *Stern*'s barotropic models. In *Pratt and Stern*'s [1986] experiments, the competition between advection by the background flow and vortex induction mechanisms associated with disturbances superimposed on the background flow led to meandering and eddy detachment. The *Pratt et al.* [1991] model added an additional PV front to the *Pratt and Stern* [1986] $1\frac{1}{2}$-layer jet model, allowing for the possibility of (equivalent) barotropic instability. Instability is possible for a piecewise constant PV configuration, because Rayleigh's necessary condition for instability is satisfied by simply setting the PV jumps to have opposite signs in the two contours. By matching their piecewise constant jet with observations of the Gulf Stream, *Pratt et al.* [1991] obtained detached eddies very similar in appearance to those associated with "warm outbreak" events in that current system.

Meacham [1991] (hereafter referred as M91) used *Polvani et al.*'s [1988] generalization of the CD method for the two-layer model, and examined several infinite jet configurations to understand how baroclinic instability could cause meandering and eddy detachment. *Pedlosky* [1979] showed that the necessary condition for a two-layer infinite zonal jet to be baroclinically unstable is to have opposite PV gradients in each layer. This condition in a piecewise uniform PV jet, as in M91 models, is reduced to PV jumps with opposite signs in each layer. The simplest PV structure considered by M91 was a double front model (one PV front in each layer) with an eastward upper layer jet and a westward-flowing lower layer. Meander growth occurred in quite a different fashion than those of *Pratt et al.*'s [1991] barotropically unstable model. M91 reported that, in this simple configuration, meander occlusion could give rise to a dipole structure (detached meanders with opposite signs in each layer) that might advect itself away from the jet structure, as observed in the Gulf Stream eddies. M91 also investigated mixed (barotropic and baroclinic) instability effects by considering multiple PV fronts in each layer.

None of baroclinically unstable configurations examined by M91 had barotropic PV in the far field. The background jet in M91's double front model had no barotropic component. M91 probably avoided dealing with barotropic vorticity in the far field because it would impose unrealistic jet configurations. For example, the barotropic jet component associated with a single front would have a triangular shape, with infinite velocity as the cross-stream coordinate approached infinity. A consequence of the lack of a background barotropic jet was that the lower layer motion was constrained to the opposite direction of the upper layer transport. Questions arising from M91's work are: Would the presence of more than one dynamical mode in the far field PV affect the evolution of meanders? Would meander growth and dipole formation differ if the transport in both layers were eastward? If yes, how?

We address these and other questions, by using FM95's multi-layer CD technique to develop a $2\frac{1}{2}$-layer model. The $2\frac{1}{2}$-layer approximation eliminates the barotropic mode, and, thus, we can only examine PV configurations involving the first and second baroclinic modes. The vertical structure of this model consists of a surface and a thermocline layer overlying an infinitely deep motionless third layer (Figure 4.1). This model has a double front model, which according to M91 produces the more realistic meander patterns. We will look at cases in which the upper layer transport will be eastward only, and the lower layer transport ranges from westward to eastward values.

We also aim to verify whether baroclinic instability can account for eddy-shedding close to the coast (as observed in the Brazil Current) or whether the eddies develop downstream (as in the Gulf Stream case), where the flow structure can be regarded as an infinite jet. In order to do that, we build a semi-infinite jet model by connecting the zonal baroclinic jet to a western boundary by coastal currents, as in SFB96's equivalent-barotropic model.

The PV inversion relationships and a discussion on the vertical structure parameters for the $2\frac{1}{2}$-layer model are presented in Section 4.2. The infinite zonal jet models are discussed in Section 4.3. The "separating" jet models, where a western boundary is included, are examined in Section 4.4. A summary of our main findings is presented in Section 4.5.

4.2 The $2\frac{1}{2}$-Layer Model Formulation

The flow in a contour dynamics model is governed by conservation of PV. Using the scales in Table 4.1, we can write conservation statements for PV in each of the two active layers in a nondimensional form to get

$$\frac{d}{dt}\boldsymbol{q} = \left[\frac{\partial}{\partial t} + \boldsymbol{u}\frac{\partial}{\partial x} + \boldsymbol{v}\frac{\partial}{\partial y}\right]\boldsymbol{q} = 0\,, \qquad (4.1)$$

The boldface variables denote column vectors such as

$$\boldsymbol{s} = \begin{bmatrix} s_1 \\ s_2 \end{bmatrix},$$

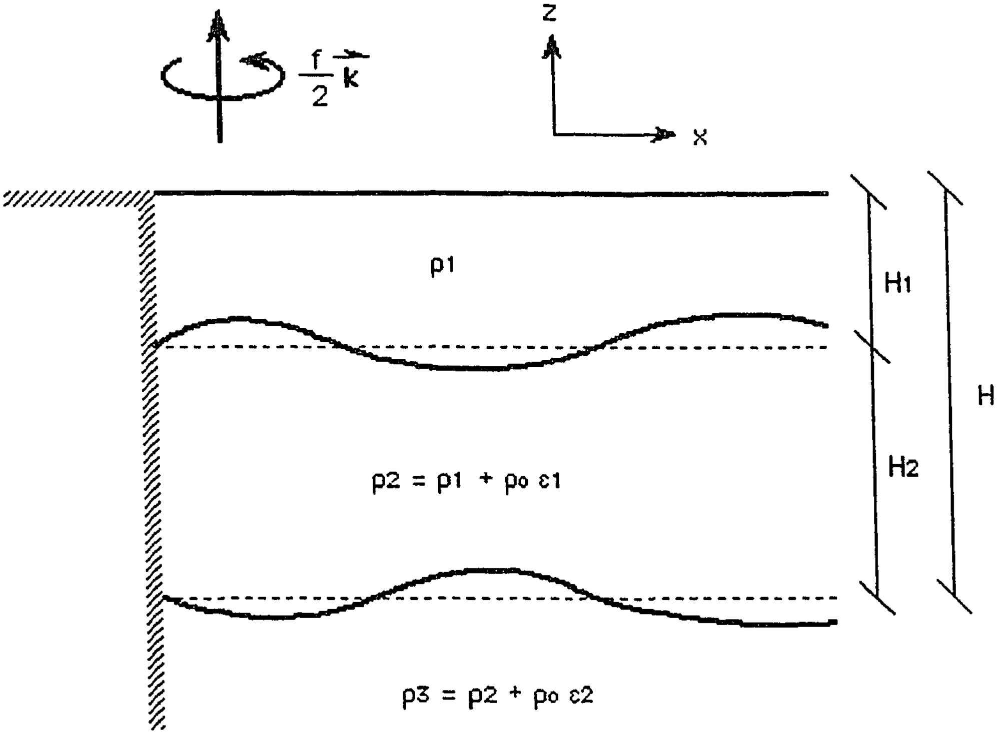

Figure 4.1: The quasi-geostrophic $2\frac{1}{2}$-layer model. The western boundary is included in the semi-infinite jet models of Section 4.3.

which is formed with values of the variable s_i in each of the two layers ($i = 1, 2$). We define q_i as the quasi-geostrophic *ith* layer potential vorticity, and the *ith* layer quasi-geostrophic velocity components (u_i, v_i) relate to the *ith* layer quasi-geostrophic stream function ψ_i by

$$[\boldsymbol{u}, \boldsymbol{v}] = \left[-\frac{\partial}{\partial y}, \frac{\partial}{\partial x}\right] \boldsymbol{\psi} \, . \tag{4.2}$$

The PV inversion relationships in the $2\frac{1}{2}$-layer model can be expressed as

$$M\boldsymbol{\psi} = \left[I\nabla^2 + Z\right] \boldsymbol{\psi} = \boldsymbol{q} \, , \tag{4.3}$$

where I is a 2×2 identity matrix and Z is the vertical structure matrix given by

$$Z = \begin{bmatrix} -\mu & \mu \\ \delta\mu & -(1+\epsilon)\delta\mu \end{bmatrix} . \tag{4.4}$$

The parameters μ, the layer thickness aspect ratio δ, and the density jump ratio ϵ are mathematically defined in Table 4.1. The physical interpretation of μ is not as straightforward as it is in the two-layer model. However, if the second layer is at rest, μ may also be interpreted as the inverse squared of the projection of the first deformation radius onto the upper layer. An alternative explanation follows *Polvani at al.* [1988], in which μ can be thought as the "rigidity" of the interface between the first and the second layers.

The matrix Z can be diagonalized to allow the decoupling of Eq. (4.3) and the writing of the dynamical system in terms of the first and second dynamical "mode" quantities. Hence,

$$Z\,F = -F\,\Gamma^2 \, , \tag{4.5}$$

where F is the 2×2 orthonormalized eigenvector matrix and

$$\Gamma^2 = \begin{bmatrix} {\gamma_1}^2 & 0 \\ 0 & {\gamma_2}^2 \end{bmatrix} \tag{4.6}$$

is the eigenvalue matrix. The eigenvectors F_{im} ($i, m = 1, 2$) can be interpreted as the amplitude of the *mth* dynamical mode in the *ith* layer. Expressions for F_{im}

Table 4.1: Scales and corresponding nondimensional quantities

Definition	Convention
depth scale	$H = H_1 + H_2$
(=total depth of upper + lower active layers)	
layer thickness	h_i
layer thickness aspect ratio	$\delta = h_1/h_2$
mean water density scale	ρ_0
layer water density	ρ_i
density jumps between layers	$\epsilon_i = \rho_{i+1} - \rho_i$
density jump ratio	$\epsilon = \epsilon_1/\epsilon_2$
Coriolis parameter	f_0
horizontal length scale	R_{d1}
(=first radius of deformation)	
layer coupling parameter	$\mu = {R_{d1}}^2{f_0}^2/(g\epsilon_1 H_1)$
eigenvalue ratio	$R = {\gamma_2}^2/{\gamma_1}^2 = {R_{d1}}^2/{R_{d2}}^2$
horizontal velocity scale	$\tilde{u}_1$
(=upper layer mean center jet velocity)	
layer velocity components	u_i, v_i
mode velocity components	U_i, V_i
stream function scale	$R_{d1}\tilde{u}_1$
layer stream function	ψ_i
mode stream function	Ψ_i
time scale	$R_{d1}{\tilde{u}_1}^{-1}$
potential vorticity scale	${R_{d1}}^{-1}\tilde{u}_1$
layer potential vorticity	q_i
mode potential vorticity	Q_i
potential vorticity jump scale	${R_{d1}}^{-2}\tilde{u}_1$
layer potential vorticity jump	Δ_i
mode potential vorticity jump	D_i

can be found by solving for the eigenvectors of matrix Z (via Eq. 4.5) with the orthonormal condition that

$$h_i F_{im} F_{in} = \delta_{mn} \,, \tag{4.7}$$

in which h_i is the ith-layer nondimensional thickness (when the fluid is at rest), and δ_{mn} is the Kronecker delta. Thus,

$$F_{1m} = \sqrt{(1+\delta)\left[\delta + \frac{(\mu - {\gamma_m}^2)^2}{\mu^2}\right]^{-1}} \tag{4.8a}$$

$$F_{2m} = \frac{\mu - \gamma_m}{\mu} F_{1m} \,. \tag{4.8b}$$

The eigenvalue ${\gamma_m}^2$ is defined in the literature as the inverse of the mth internal deformation radii squared [*Flierl*, 1978; *Pedlosky*, 1979]. Nondimensionalization using the scales of Table 4.1 leads to ${\gamma_1}^2 = 1$ and ${\gamma_2}^2 = R$.

The "layer" stream function ψ_i and potential vorticity q_i are related to the "mode" stream function Ψ_i and potential vorticity Q_i according to

$$[\boldsymbol{\psi}, \boldsymbol{q}] = F\,[\boldsymbol{\Psi}, \boldsymbol{Q}] \,, \tag{4.9}$$

which can be inverted to obtain

$$[\boldsymbol{\Psi}, \boldsymbol{Q}] = F^T \begin{bmatrix} h_1 & 0 \\ 0 & h_2 \end{bmatrix} [\boldsymbol{\psi}, \boldsymbol{q}] = \mathcal{F}\,[\boldsymbol{\psi}, \boldsymbol{q}] \,. \tag{4.10}$$

Therefore it is possible to map ψ_i (q_i), knowing Ψ_m (Q_m) and vice-versa. On one hand, if one starts with the "layer" quantities, then μ, δ and ϵ need to be known to obtain the "mode" quantities. On the other hand, if the starting point is the "mode" system, μ, then δ and R must be known to calculate the "layer" quantities.

How are the values for μ, δ, R (or ϵ) chosen to properly (and consistently) represent a continuously stratified ocean with the $2\frac{1}{2}$-layer approximation? Following *Flierl* [1978], we propose the following simple calibration scheme.

- The parameter R is chosen to match observations.

We force the eigenvalues in Eq. (4.5) to match the first and the second deformation radii estimated from data. See *Houry et al.* [1987] for a numerical method to compute the deformation radii from CTD data.

- The parameter δ or ϵ is chosen from previous knowledge of the study region.

  It is probably easier (and perhaps more accurate) to choose the layer thickness ratio δ based on water mass criteria and/or observed velocity structure than the density jump ratio ϵ.

- The parameter μ , given R, is calculated from

$$det(Z + \Gamma^2) \; = \; 0 \, . \tag{4.11}$$

  If one chooses to input the parameters R and δ, the solution for μ is given by

$$\mu \; = \; \frac{(1+R) \pm \sqrt{(1-R)^2 - 4\delta R}}{2(1+\delta)} \, . \tag{4.12}$$

  An expression for ϵ can also be obtained from manipulating Eq. (4.11), yielding

$$\epsilon \; = \; \frac{R}{\delta\mu^2} \, . \tag{4.13}$$

  Notice from Eq. (4.12) that since μ is real, a restriction must be imposed on the choice of δ, i.e.,

$$\delta \leq \frac{(1-R)^2}{4R} \, . \tag{4.14}$$

Houry et al.'s [1987] work suggests that R ranges from 2.5 in the tropics to 6.5 at mid-latitudes. The layer thickness aspect ratio range is probably $0 < \delta \leq 1$. The calibration scheme above provides two sets of values for μ and ϵ (see Eq. 4.12). The choice between the two sets depends on which the set that satisfies $\epsilon > 1$. However, there are cases in which both roots of Eq. (4.12) satisfy that condition. In those cases, the smaller μ value is associated with a larger ϵ value (via Eq. 4.13), implying that the vortex stretching/squashing of the second layer is due primarily to interactions with the upper layer. The larger μ root is usually associated with $\epsilon = O(1)$, which implies that the changes in the lower interface are of the same order as the the upper interface. Thus, we intuitively expect that a model applying the set with the smaller μ value should behave more like to the two-layer case.

4.3 Infinite Jets

In this section, we present the formalism and numerical results for f-plane infinite jets in this section. The derivation that follows is based on FM95's method for multi-layer, piecewise uniform jets. It is applied to the double front model in which there is one front in each active layer.

For this model, the PV field is given by

$$\mathbf{q} = \mathbf{q}_\circ + \mathcal{D}\boldsymbol{\mathcal{H}}(y - \bar{\mathbf{y}} - \boldsymbol{\eta}) , \tag{4.15}$$

where q_{0i} is the q_i value south of the front (contour) on the ith layer, $\mathcal{D}$ is a 2×2 diagonal matrix with the vorticity jumps Δ_1 and Δ_2 as its nonzero elements. The column vector $\boldsymbol{\mathcal{H}}(y - \bar{\mathbf{y}} - \boldsymbol{\eta})$ is given by

$$\boldsymbol{\mathcal{H}}(y - \bar{\mathbf{y}} - \boldsymbol{\eta}) = \begin{bmatrix} \mathcal{H}(y - \bar{y}_1 - \eta_1) \\ \mathcal{H}(y - \bar{y}_2 - \eta_2) \end{bmatrix} ,$$

where

$$\begin{aligned} \mathcal{H}(y) &= 0 \quad for \;\; y < 0 \\ &= 1 \quad for \;\; y > 0 \end{aligned}$$

is the Heaviside step function, $\bar{y}_i$ is the mean front latitudinal position, and η_i is the time-dependent deviation.

The PV field is then split into a basic state part $\bar{q}_i$ and a perturbed part q_i' according to

$$\bar{\mathbf{q}} = \mathbf{q}_\circ + \mathcal{D}\boldsymbol{\mathcal{H}}(y - \bar{\mathbf{y}}) , \tag{4.16}$$

and

$$\mathbf{q}' = \mathcal{D}\left[\boldsymbol{\mathcal{H}}(y - \bar{\mathbf{y}} - \boldsymbol{\eta}) - \boldsymbol{\mathcal{H}}(y - \bar{\mathbf{y}})\right] . \tag{4.17}$$

The parts of the corresponding basic stream function $\bar{\psi}_i(y)$ and $\psi_i'(x,y,t)$ relate to the basic and perturbed PV fields by

$$M\bar{\boldsymbol{\psi}} = \boldsymbol{q}_o + \mathcal{D}\mathcal{H}(y - \bar{\boldsymbol{y}}) \tag{4.18}$$

and

$$M\boldsymbol{\psi}' = \mathcal{D}\left[\mathcal{H}(y - \bar{\boldsymbol{y}} - \boldsymbol{\eta}) - \mathcal{H}(y - \bar{\boldsymbol{y}})\right] . \tag{4.19}$$

A PV inversion formula for the basic zonal $\bar{u}_i$ can be obtained by simply taking the $-\frac{\partial}{\partial y}$ of Eq. (4.18). This yields

$$M\bar{\boldsymbol{u}} = -\mathcal{D}\,\boldsymbol{\delta}(y - \bar{\boldsymbol{y}}) , \tag{4.20}$$

where $\boldsymbol{\delta}(y - \bar{\boldsymbol{y}})$ is a column vector given by

$$\boldsymbol{\delta}(y - \bar{\boldsymbol{y}}) = \begin{bmatrix} \delta(y - \bar{y}_1) \\ \delta(y - \bar{y}_2) \end{bmatrix} ,$$

with $\delta(y)$ representing the Dirac delta function.

The temporal evolution of the contour on the *ith* layer is then computed using the kinematic equations

$$\frac{d}{dt}\boldsymbol{x} = \boldsymbol{u} = \bar{\boldsymbol{u}} + \boldsymbol{u}' \tag{4.21a}$$

$$\frac{d}{dt}\bar{\boldsymbol{y}} + \boldsymbol{\eta} = \boldsymbol{v} = \boldsymbol{v}' . \tag{4.21b}$$

In following subsections, the linearized versions of Eqs. (4.19), (4.20) and (4.21) are used to determine the basic jet profiles and linear stability properties by employing FM95's method,, while the fully nonlinear system is stepped forward in time to determine the nonlinear evolution of the dynamical system.

4.3.1 Linear Stability

Eqs. (4.19), (4.20) and (4.21) can be linearized around $\bar{y}_i$ and by considering solutions proportional to $e^{k(x-ct)}$. In doing so, one obtains

$$M_k\,\boldsymbol{\psi}' = -\mathcal{N}[\mathcal{D}\,\boldsymbol{\delta}(y - \bar{\boldsymbol{y}})] , \tag{4.22}$$

$$M_0 \bar{\boldsymbol{u}} = -\mathcal{D}\,\delta(y - \bar{\boldsymbol{y}}) \,, \tag{4.23}$$

and

$$\mathcal{U}\eta - c\eta = \psi'(\bar{\boldsymbol{y}}) \,. \tag{4.24}$$

The matrix M_k is defined as

$$M_k = I\left(\frac{\partial^2}{\partial y^2} - k^2\right) + Z \,,$$

and M_0 is the M_k matrix applied to the $k = 0$ case. The matrix $\mathcal{N}$ ($\mathcal{U}$) is a 2×2 diagonal matrix with η_i (u_i), for $i = 1, 2$, as its nonzero elements.

Eqs. (22) and (23) can be solved using the method of Green's function, where the Green's function in this case should satisfy

$$M_k G_k(y \mid y') = I\delta(y - y') \,. \tag{4.25}$$

According to FM95, the elements of the G_k matrix have the form

$$(G_k)_{ij} = -\, h_i F_{im} F_{jm} \frac{1}{2\sqrt{k^2 + {\gamma_m}^2}} e^{\sqrt{k^2 + {\gamma_m}^2}\,|y - y'|} \,. \tag{4.26}$$

Applying Eq. (4.26) to Eqs. (4.22) and (4.23), yields

$$\psi'(y, t) = G_k(y \mid \bar{\boldsymbol{y}})[\mathcal{D}\,\eta] \,, \tag{4.27}$$

$$\bar{\boldsymbol{u}}(y) = G_0(y \mid \bar{\boldsymbol{y}})\,\boldsymbol{\Delta} \,. \tag{4.28}$$

We can solve for c in Eq. (4.24) by evaluating $(\psi'_i, \bar{u}_i)$ at $\bar{y}_i$. Moreover, FM95 proposed specifying the basic jet velocities at the contours instead choosing the Δ_i's. This is possible by inverting Eq. (4.28) to get

$$\boldsymbol{\Delta} = {G_0}^{-1}(\bar{\boldsymbol{y}} \mid \bar{\boldsymbol{y}})\,\bar{\boldsymbol{u}}(\bar{\boldsymbol{y}}) \,. \tag{4.29}$$

4.3.2 The Nonlinear Model

The fully nonlinear system, Eqs. (4.19), (4.20) and (4.21), is also solved for using the method of the Green's function. In this case, the solution of Eq. (4.19) becomes

$$\psi'(x, y, t) = \int\!\!\int_{\boldsymbol{A}} G(x, y \mid x', y')\,\boldsymbol{\Delta}\, dx'dy' \,, \tag{4.30}$$

where A_i is the area between the curves $\bar{y}_i + \eta_i$ and $\bar{y}_i$. The elements of the Green's function matrix now take the form of

$$G_{ij} \doteq - h_i F_{im} F_{jm} \frac{1}{2\pi} K_0(\gamma_m r) \, , \tag{4.31}$$

with

$$r = \sqrt{(x-x')^2 + (y-y')^2} \, .$$

The expressions for the perturbed velocities are obtained by differentiating Eq. (4.30), using the symmetry properties of the Green's function and applying the divergence theorem [*Pratt and Stern*, 1986; *Wang*, 1992]. The result is that

$$[\boldsymbol{u}', \boldsymbol{v}'] = \int_{\partial A} G(x,y \mid x',y') \, \boldsymbol{\Delta} \, [dx', dy'] \, , \tag{4.32}$$

where ∂A_i is the contour enclosing A_i. However, Eq. (4.32) contains a logarithmic singularity due to $K_0(z) \rightarrow -\ln(z)$ as $z \rightarrow 0$, which, following *Polvani et al.* [1988], we remove integrating the velocity expressions by parts. This yields

$$[\boldsymbol{u}', \boldsymbol{v}'] = - \int_{\partial A} \frac{\partial G(x,y \mid x',y')}{\partial r} \, \boldsymbol{\Delta} \, [(x-x'), (y-y')] \, dr \, . \tag{4.33}$$

The numerics of the contour dynamics algorithm described next are given by *Pratt and Stern* [1986]. The position of the fronts is determined by as a function of time t by tagging parcels along the contours at some initial time and following their motion using Eq. (4.21). A second-order Runge-Kutta scheme is employed in the discretization of Eq. (4.21). At each time step, $\bar{u}$, u' and v' must then be determined. The basic jet velocity $\bar{u}$ is calculated from Eq (28). The perturbed velocities u' and v' are evaluated from Eq. (4.33), which has been discretized using a midpoint integration rule, according to *Zou et al.* [1987] and *Polvani* [1988]. We use a simple particle insertion-deletion scheme to keep the front particles separated by a preselected average distance l. The integrations are carried out until the model breaks down. Our approach is sufficient, although we could have used more sophisticated techniques, such as contour surgery [see *Dritschel*, 1988 and 1989], to maintain the model's resolution and to separate (reconnect) eddies and PV filaments from (to) the fronts.

4.3.3 Numerical Results

For this work, we restrict our $2\frac{1}{2}$-layer infinite jet model experiments to baroclinically unstable configurations in which :

- The mean front latitudinal positions $\bar{y}_1$ and $\bar{y}_2$ are zero;
- The upper layer centerjet velocity $\bar{u}_1(0)$ is 1.0, and the lower layer centerjet velocity $\bar{u}_2(0)$ is allowed to vary.
- The eigenvalue ratio R is 6.25;

  (A value typical of the North Atlantic mid-latitudes and one which corresponds to a 50km first deformation radius and a 20km second deformation radius, making this choice for R sets the two length scales involved as far apart as they can realistically be).
- The layer thickness aspect ratio δ is either 1.0 or 0.2; and
- The jets are perturbed with (equivalent) barotropic disturbances of the form

  $$\eta(x,0) \;=\; A\,e^{-x^2/w^2}\,, \tag{4.34}$$

  where $A = 2,\ w = 2$ for all study cases. The actual conditions are given for the three different set of the numerical experiments are given in Experiment Set 1 (Table 4.2), Experiment Set 2 (Table 4.3), and Experiment Set 3 (Table 4.4). The disturbance with these A and w values contains significant power in wavenumbers $k \leq 2.5$ and, as we shall see later, within the unstable k range for all the cases in the three experiment sets to be discussed in this section.

Calibrated Vertical Parameters and Linear Model Results

Our initial set of results have $\delta = 1.0$, which means that the vortex stretching/squashing associated with changes in the first interface depth are felt equally in both layers. The calibration scheme provides two sets of values for μ satisfying the $\epsilon > 1$ condition:

$$\textbf{Experiment Set 1}: \mu = 2.21 \quad , \quad \epsilon = 1.28$$

$$\textbf{Experiment Set 2}: \mu = 1.41 \quad , \quad \epsilon = 3.13 \quad .$$

As noted in Section 4.2, the first set of values causes the coupling between the first and second layer to be relatively stronger, and the changes on the lower interface to be of the same order as the changes on the upper interface. The second set of values causes the coupling between the two layers to be weaker, and the upper density jump be stronger than the lower one.

Our choices for $\bar{u}_2(0)$ and the corresponding vorticity jumps for Experiment Set 1 (Set 2) computed by the linear model are presented in Table 4.2 (Table 4.3). The basic jet profiles and growth rates, also from the linear theory, are shown in Figure 4.2 (Experiment Set 1) and Figure 4.3 (Experiment Set 2).

The presence of the two dynamical modes is evident in the background jet profiles (Figures 4. 2a and 4.3a), particularly in the lower layer jets with counterflow regions. Figures 4.2 and 4.3 shows that by shifting the lower layer transport from regressive to progressive (relative to the upper layer), the growth rates diminish and the most unstable waves get longer. As expected, the growth rates of Experiment Set 1 are higher than those of Experiment Set 2 because of the stronger coupling between the layers.

It is possible to relate growth rates and transport directions to magnitudes of the layer-integrated PV jumps $| h_i \Delta_i |$ (note that for the $\delta = 1$ case, $h_1 = h_2$ and $h_i \Delta_i$ and Δ_i are obviously equivalent). For cases where $| h_2 \Delta_2 | > | h_1 \Delta_1 |$, we obtain the largest westward lower layer jet transports and the highest growth rates. As $| h_2 \Delta_2 |$

Table 4.2: Experiment Set 1: $\delta = 1$, $R = 6.25$, $\mu = 2.21$ and $\epsilon = 1.28$

Run	$\bar{u}_2(0)$	Δ_1	Δ_2	Summary of Results
j1	-1.0	3.96	-5.57	dipole formation on primary crest eddies shed by $t \approx 23$, upper layer first
j2	-0.50	3.33	-3.42	same as above eddies shed by $t \approx 28$, lower layer first
j3	-0.25	3.01	-2.34	same as above eddies shed by $t \approx 35$, upper layer first
j4	0.0	2.69	-1.26	eddy detached from lower layer primary crest at $t \approx 30$
j5	0.10	2.57	-0.83	dipole formation on primary trough eddies shed from lower layer primary crest and trough
j6	0.25	2.38	-0.19	dipole formation on secondary crest upper layer disturbance dispersed quickly shingle formation on lower layer

Table 4.3: Experiment Set 2: $\delta = 1$, $R = 6.25$, $\mu = 1.41$ and $\epsilon = 3.13$

Run	$\bar{u}_2(0)$	Δ_1	Δ_2	Summary of Results
kl	-1.0	3.04	-5.57	dipole formation on primary crest eddies shed by $t \approx 35$, upper layer first
k2	-0.35	2.50	-2.49	dipole formation on primary trough eddies shed by $t \approx 65$, upper layer first
k3	-0.25	2.32	-1.29	eddy detached from lower layer primary crest at $t \approx 60$ dipole formation on primary trough
k4	0.0	2.24	-0.81	eddies shed from lower layer primary crest no dipole formation
k5	0.1	2.16	-0.33	upper layer disturbance dispersed quickly shingle formation on lower layer

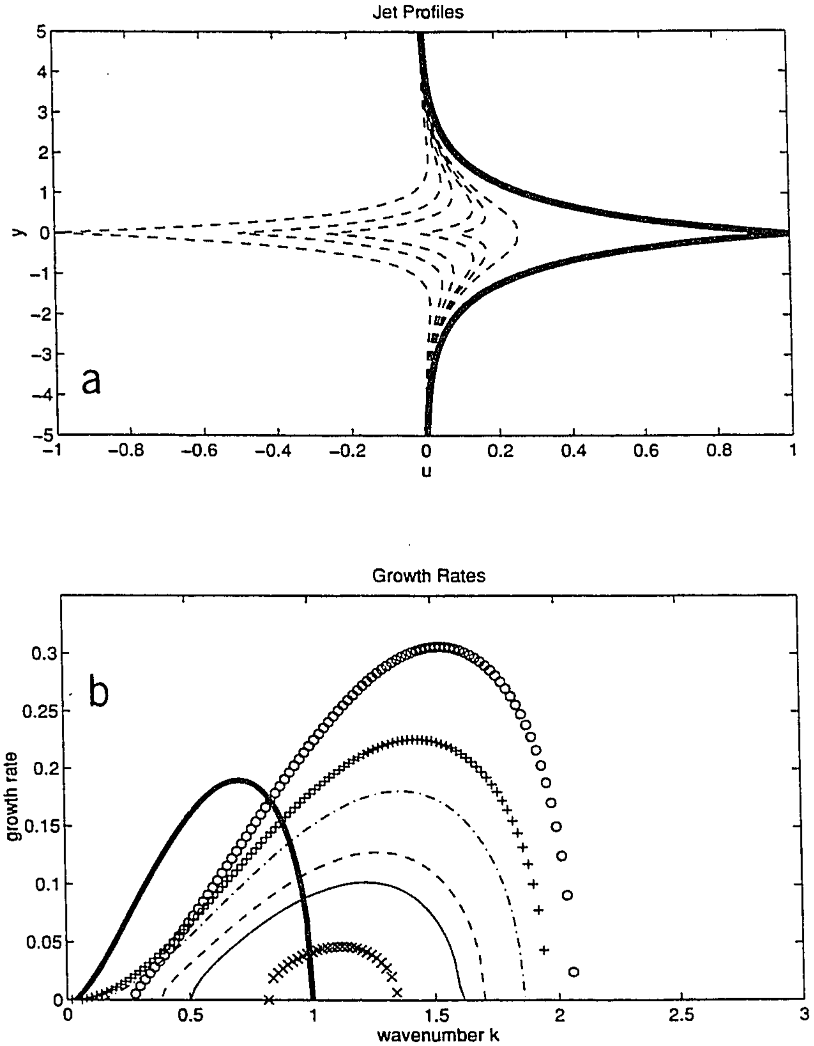

Figure 4.2: Experiment Set 1 ($\delta = 1$, $R = 6.25$, $\mu = 2.21$, and $\epsilon = 1.28$)-linear model results. (a) Jet profiles: the lower layer jets (dashed curves), from left to right, correspond to $\bar{u}_2(0)$ = -1.0 (*Run j1*), -0.5 (*Run j2*), -0.25 (*Run j3*), 0.0 (*Run j4*), 0.1 (*Run j5*), and 0.25 (*Run j6*). The upper layer jets are very similar in all cases and the thick solid line should be regarded as an envelope enclosing all six profiles. (b) Growth rates corresponding to $\bar{u}_2(0)$ = -1.0 ('o' curve, *Run j1*), -0.5 ('+' curve, *Run j2*), -0.25 ('.-.' curve, *Run j3*), 0.0 ('–' curve, *Run j4*), 0.1 ('-' curve, *Run j5*), and 0.25 ('x' curve, *Run j6*). The thick solid line represents the growth rate for M91's two-layer model with $\delta = 1$ and $\bar{u}_2(0)$ = -1.0.

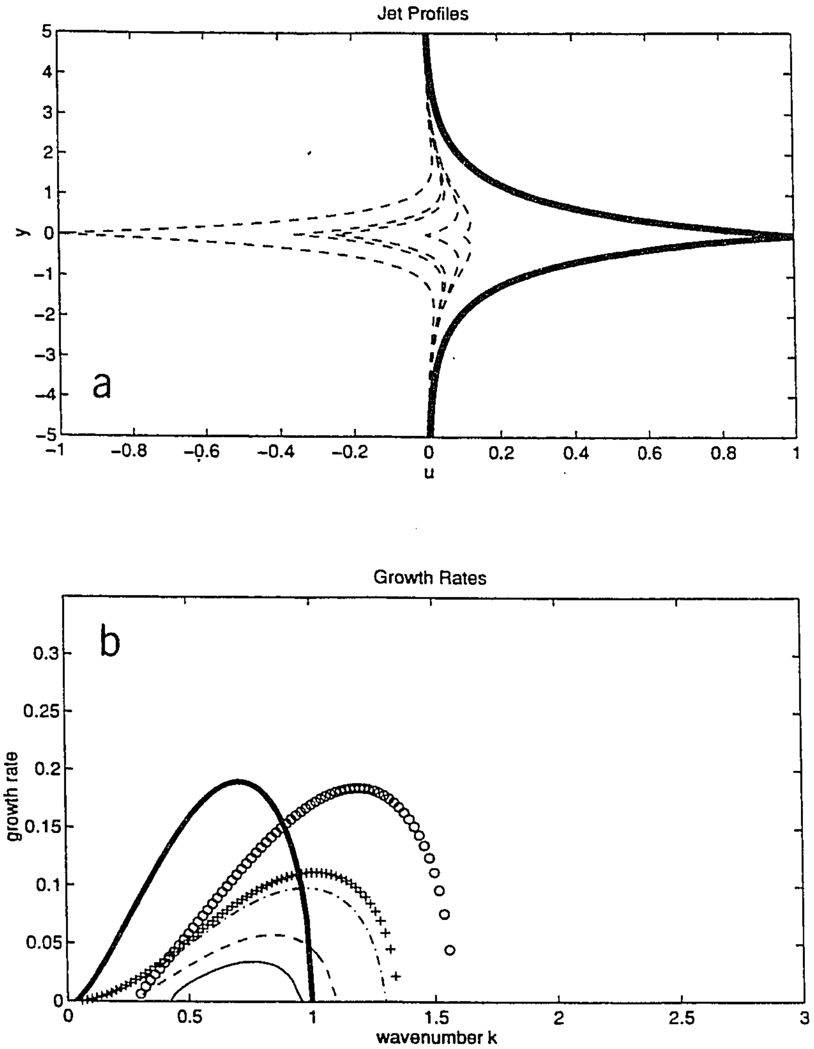

Figure 4.3: Experiment Set 2 ($\delta = 1$, $R = 6.25$, $\mu = 1.41$, and $\epsilon = 3.13$)-linear model results. (a) Jet profiles: the lower layer jets (dashed curves), from left to right, correspond to $\bar{u}_2(0)$ = -1.0 (*Run k1*), -0.35 (*Run k2*), -0.25 (*Run k3*), 0.0 (*Run k4*), 0.1 (*Run k5*). The upper layer jets are very similar in all cases and the thick solid line should be regarded as an envelope enclosing all five profiles. (b) Growth rates corresponding to $\bar{u}_2(0)$ = -1.0 ('o' curve, *Run k1*), -0.35 ('+' curve, *Run k2*), -0.25 ('.-.' curve, *Run k3*), 0.0 ('–' curve, *Run k4*), and 0.1 ('-' curve, *Run k5*). The thick solid line represents the growth rate for M91's two-layer model with $\delta = 1$ and $\bar{u}_2(0)$ = -1.0.

is decreased relative to $| h_1\Delta_1 |$, the westward lower layer transport decreases and the most unstable wavenumber gets longer. When $| h_2\Delta_2 |=| h_1\Delta_1 |$, the net lower layer transport is zero, and there is no unstable long wave cutoff (see the *Run j2* curve in Figure 4.2b, and the *Run k2* curve in Figure 4.3b). For $| h_2\Delta_2 |<| h_1\Delta_1 |$, the net lower layer transport is eastward.

We can also compare the linear stability properties between our $2\frac{1}{2}$-layer cases and M91's $\delta = 1$, $\bar{u}_2(0) = -1$, double-front, two-layer model (the reader is referred to the Appendix for a brief review of M91's model). The growth rate corresponding to that of M91's $\delta = 1$, $\bar{u}_2(0) = -1$, two-layer model is represented by the thick solid lines in Figures 4.2b and 4.3b. It can be seen that for *Run j1* ($\bar{u}_2(0) = -1$, Experiment Set 1), the unstable wave range is larger than its two-layer counterpart, with growth rates about two times higher (Figure 4.2b, circled curve). The most unstable waves for the *Run j1* configuration are somewhat shorter than for the corresponding M91 $\delta = 1$ two-layer model. In *Run k1* ($\bar{u}_2(0) = -1$, Experiment Set 2); Figure 4.3b, circled curve, we confirm that for large ϵ cases, the growth rates and unstable wavenumber range are comparable to M91's $\delta = 1$ two-layer model. However, the most unstable waves in *Run k1* are shorter than in its two-layer counterpart, and relatively longer than the stronger coupling case *Run j1*. In terms of the layer-integrated PV gradient structure, the M91 model is constrained to $| h_1\Delta_1 |=| h_2\Delta_2 |$, but unlike our $2\frac{1}{2}$-layer model results, the lower layer transport is westward.

Now we examine the linear stability properties using a more realistic layer aspect ratio, say $\delta = 0.2$. In particular, we are interested in relatively weaker (westward and eastward) lower layer jets, probably closer to the currents observed in the ocean. The calibration scheme again provides two sets of values for μ (ϵ) that satisfy the $\epsilon > 1$ condition:

Experiment Set 3 : $\mu = 5.00 \ , \ \epsilon = 1.04$

Experiment Set 4 : $\mu = 1.25$, $\epsilon = 28.80$.

The growth rates obtained for Experiment Set 3 (Table 4.4, Figure 4.4) are comparable to those in Experiment Set 1. Interestingly, the values of the coupling parameter μ in Experiment Set 1(= 2.21) and in Experiment Set 3 (= 5.0) can be thought of as the two roots of the calibration scheme version using $R = 6.25$, $\epsilon \approx 1.25$ as input parameters. In other words, we discussed in Section 4.2 how the calibration could be performed using either R, δ or R, ϵ as input parameters. If we solve for μ in Eq. (4.11) inputting ($R = 6.25$, $\epsilon = 1.25$), the two δ values are approximately ≈ 1.0 and 0.2. We believe that this result exemplifies the flexibility of the calibration scheme and confirms that the $\epsilon = 0(1)$ case usually provides more unstable jets. Three cases listed in Table 4.4 correspond to different layer-integrated PV structures: $| h_2\Delta_2 | > | h_1\Delta_1 |$ (*Run l1*), $| h_2\Delta_2 | \approx | h_1\Delta_1 |$ (*Run l2*), and $| h_2\Delta_2 | < | h_1\Delta_1 |$ (*Run l3*).

We omit here the results for Experiment Set 4 because the growth rates are small even if fairly large negative values of $\bar{u}_2(0)$ are considered. Neutral stability occurs for a $\bar{u}_2(0)$ value of about -0.05.

It remains to discuss the effect of changing the eigenvalue ration R in the linear stability properties. As we said, the $R = 6.25$ represents an upper bound and is typical of mid-latitudes. To reduce R implies examining a more equatorward jet system. For example, $R = 3.11$ corresponds to the average R over the 20°N band in the Atlantic Ocean estimated from the *Houry et al.* [1987] data set. The first and second deformation radii in this case are 61.76 km and 34.98 km, respectively. As discussed in Section 4.2, the calibration imposes a maximum bound on the layer aspect ratio, with smaller δ's for smaller R's. This agrees with the fact that pycnoclines become shallower equatorward. From calibration (Eq. 4.12), we expect that for a chosen δ, the smaller R is, the closer are the two roots for the coupling parameter μ. As the previous results show, the larger μ root strengthens the coupling between the layers and causes the lower interface to wobble as much as the upper

Table 4.4: Experiment Set 3: $\delta = 0.2$, $R = 6.25$, $\mu = 5.0$ and $\epsilon = 1.25$

Run	$\bar{u}_2(0)$	Δ_1	Δ_2	Summary of Results
11	-0.50	5.71	-1.93	dipole formation on primary crest eddies shed by $t \approx 30$, upper layer first
12	-0.125	4.64	-0.91	dipole formation on primary crest eddies shed by $t \approx 50$, lower layer first
13	0.0	4.286	-0.57	dipole formation on primary trough eddies shed by $t \approx 65$, upper layer first

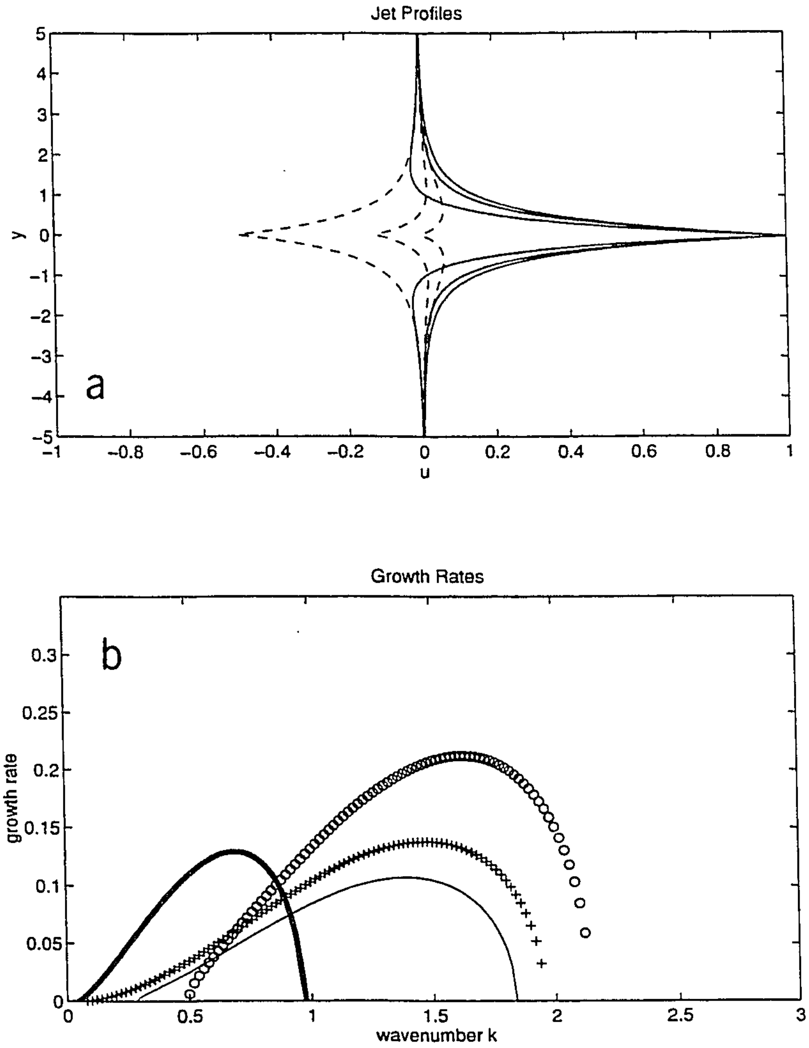

Figure 4.4: Experiment Set 3 (δ = 0.2, R = 6.25, μ = 5.0, and ϵ = 1.25)-linear model results. (a) Jet profiles: the lower layer jets (dashed curves), from left to right, correspond to $\bar{u}_2(0)$ = -0.5 (*Run l1*), -0.125 (*Run l2*), and 0.0 (*Run l3*). From left to right, the upper layer jets (solid curves) also correspond to *Runs l1, l2* and *l3*. (b) Growth rates corresponding to $\bar{u}_2(0)$ = -0.5 ('o' curve, *Run l1*), -0.125 ('+' curve, *Run l2*), and 0.0 ('-' curve, *Run l3*). The thick solid line represents the growth rate for M91's two-layer model with δ = 0.2 and $\bar{u}_2(0)$ = -0.2.

one (the density contrasts are similar). This creates what we consider to be more typical of the $2\frac{1}{2}$-layer model behavior, with more unstable jet configurations.

Nonlinear Model Results

The results of the temporal evolution of the initial disturbance given by Eq. (4.34) for all cases in the three experiment sets are summarized in Tables 4.2, 4.3 and 4.4. It can be seen that a continuum of eddy shedding events is obtained, and dipole formation occurs on either side of the fronts. As we shift the lower layer transport shifts from westward to eastward, the jets become more linearly stable, with both growth rates and unstable wavenumber range diminishing. The most unstable jet configurations shed dipolar eddy structures from the primary crest (i.e., from the initially Gaussian disturbance). As the lower layer transport becomes eastward and the jets less unstable, the dipole pinches off from the primary trough (i.e, from the first trough to the right of the initial disturbance) or the secondary crest. As the jet configurations approach neutral stability, short-lived eddies and/or shingles are shed in the lower layer only, and the upper layer meander disperses quickly eastward.

Since evolutionary patterns of the disturbances are similar among the three experiment sets as $\bar{u}_2(0)$ is varied, we restrict ourselves to discussing the details of five distinct cases.

Dipole formation on the primary crest

Run j1 (Experiment Set 1, $\bar{u}_2(0) = -1$) corresponds to a $\mid h_2\Delta_2 \mid > \mid h_1\Delta_1 \mid$ structure. For this case (Figure 4.5), the meander evolution and eddy occlusion proceed identically to M91's experiments, only much faster because of the larger growth rates (Figure 4.2b). As soon as the model is 'turned on ($t = 0$, Figure 4.5a), the vertical shift of the disturbance starts triggering baroclinic instability mechanisms ($t = 10$, Figure 4.5b). The primary crest then begins to grow, as the wave structure develops. The dipole structure is formed by interactions between the opposite sign vortex patches in the two layers and tries to advect itself northward away from the jet axis ($t = 20$, Figure 4.5c). Eddy detachment occurs first in the upper layer, as the vortices become more rounded and keep moving northward ($t = 25$, Figure 4.5d).

Dipole formation on the primary trough

For *Run j4* (Experiment Set 1, $\bar{u}_2(0) = 0$), the upper layer-integrated vorticity jump is about twice the magnitude of the lower layer jump. As it grows, the upper layer disturbance seems to disperse faster than that in the lower layer ($t = 15$, Figure 4.6b). The lower layer primary crest pinches off as the primary trough in both layers grows and deepens ($t = 30$, Figure 4.6c). Since there is no mechanism to advect the eddy pinched off from the primary crest, it does not move away from the jet and will be reentrained in the jet later on. A dipole structure is formed on the primary trough, and it advects itself from the jet axis ($t = 50$, Figure 4.6d). The eddies in this case have a cyclonic (anticyclonic) circulation on the upper (lower) layer.

Dipole formation on the secondary crest

For *Run j5* (Experiment Set 1, $\bar{u}_2(0) = 0.1$), the lower layer PV front is about three times weaker than the upper layer front (Table 4.2). The upper layer disturbance disperses quickly, but there is some growth in the waves excited ($t = 25$, Figure 4.7b). Eddies are shed on the lower layer primary crest and troughs ($t = 45$, Figure 4.7c). The upper layer secondary crest grows noticeably through interactions with the lower layer counterpart ($t = 60$, Figure 4.7d). The lower layer secondary crest develops long fringes. The upper layer secondary crest occludes and forms a dipolar structure, with filaments emerging from the lower layer counterpart. The dipole advects itself from the jet axis ($t = 80$, Figure 4.7e).

Isolated lower layer eddies

For *Run k4* (Experiment Set 2, $\bar{u}_2(0) = 0$), the lower layer-integrated PV jump is about a third of that of the upper layer, as in *Run j5*. However, as predicted by linear theory, the growth rates are lower and the most unstable wavenumber is shorter than that of *Run j5* and the meander evolution here occurs differently than

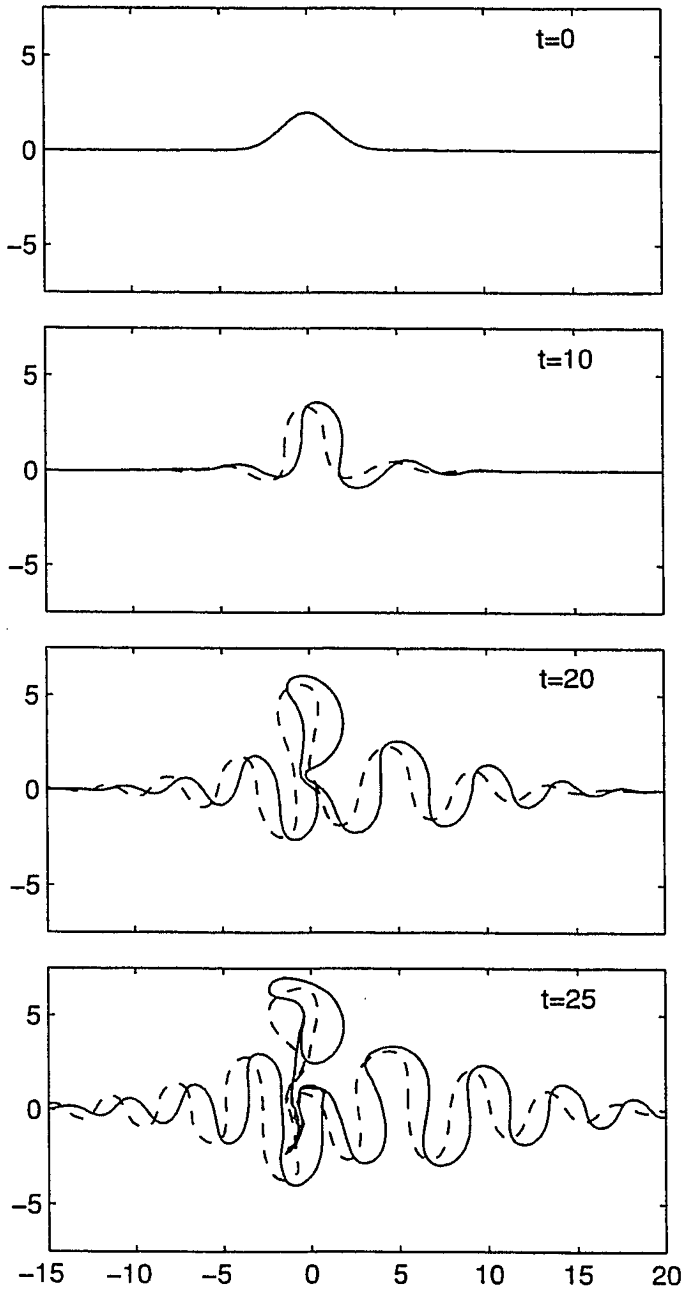

Figure 4.5: *Run j1*: (a) t=0, (b) t=10, (c) t=20 and (d) t=25.

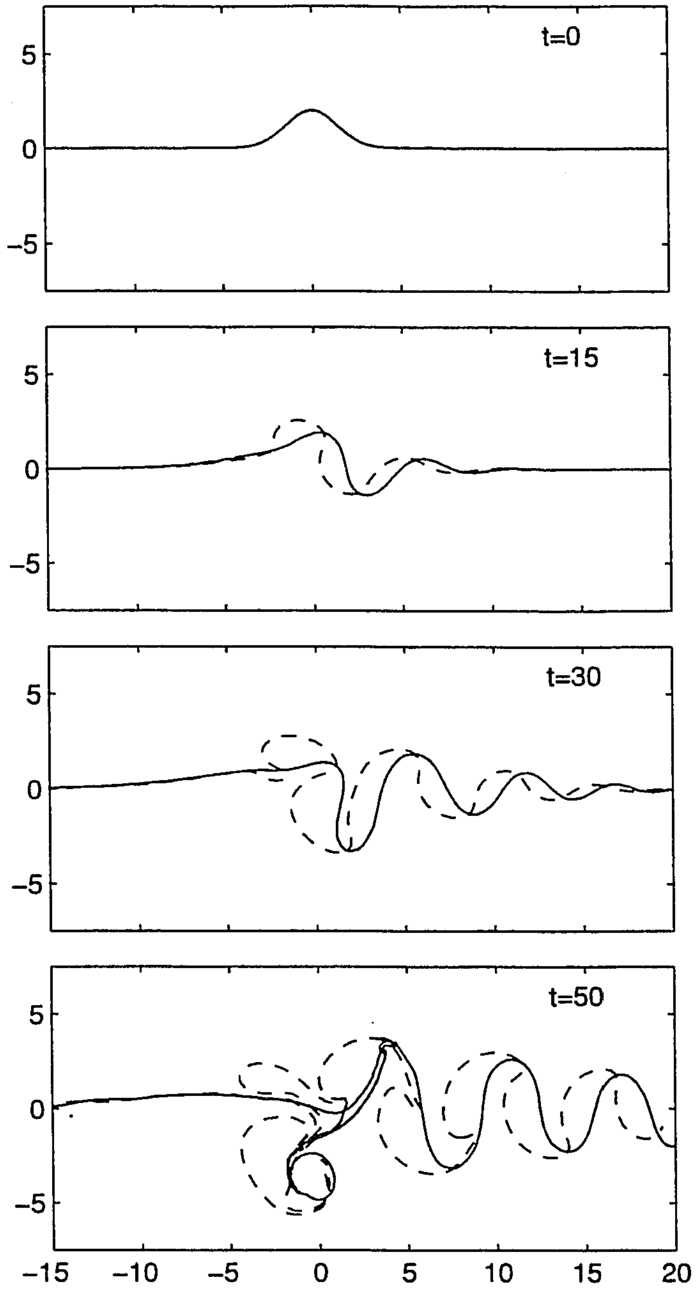

Figure 4.6: *Run j4*: (a) t=0, (b) t=15, (c) t=30 and (d) t=50.

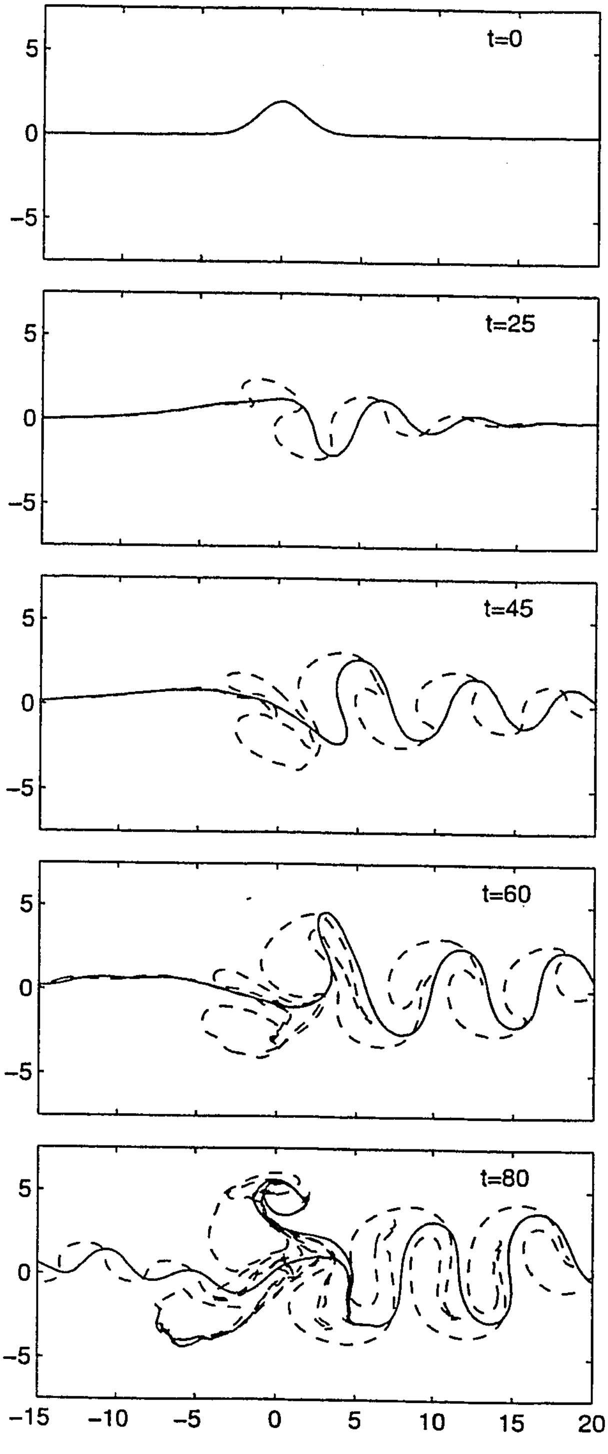

Figure 4.7: *Run j5*: (a) t=0, (b) t=25, (c) t=45, (d) t=60, and (d) 80.

in the previously discussed case. An eddy is shed from the lower layer primary crest (Figure 4.8). The upper layer does not exhibit eddy detachment but the fairly sinusoidal waves that are excited grow as they propagate eastward (Figures 4.8b and 4.8c). We expect the lower eddies be reabsorbed into the jet since they lack mechanisms to advect themselves away from it.

Shingle formation in the lower layer

Run j6 (Experiment Set 1, $\bar{u}_2(0) = 0.25$) represents a marginally unstable configuration (neutral stability is obtained for $\bar{u}_2(0) = 0.3$), in which $\mid h_2 \Delta_2 \mid$ is only about 10% of $\mid h_1 \Delta_1 \mid$ (Table 4.2). As a consequence, the upper layer vortex patches feel very little the interaction with the lower layer (Figure 4.9). The upper layer disturbance disperses quickly downstream, while some moderate growth occurs in the lower layer ($t = 15$, Figure 4.9b). Shingle formation happens in the lower layer where the eastward lower layer jet shears out the grown meanders ($t = 50$, Figure 4.9c).

Thus, we have shown that when the transports in the two layers are either in the same or opposite directions, dipoles can be formed from a initially equivalent barotropic Gaussian meander. In particular for eastward flowing lower layers, the eddy shedding occurred when the jet core was westward (such as in *Runs j3 and k3*), stagnant (as in *Runs j4 and l3*) or eastward (as in *Run j5*).

Can we define bounds for dipole formation to happen, based on PV frontal structure or linear stability properties? In Experiment Sets 1, 2 and 3 , we use the same initial condition in all runs. As mentioned previously, the disturbance in Eq. (4.34) (with $A = w = 2$) contains power distributed in the range $k \leq 2.5$. The most unstable wavenumbers are mostly in this range but get smaller as the model approaches neutral stability (Figures 4.2b, 4.3b, and 4.4b). For instance, consider the results of *Run k2* (Table 4.3), where the dipole formation occurred on the primary trough (contrasting with the primary crest dipole in *Run k1*). M91 found a similar behavior when he perturbed his two-layer jet with a tall but narrow

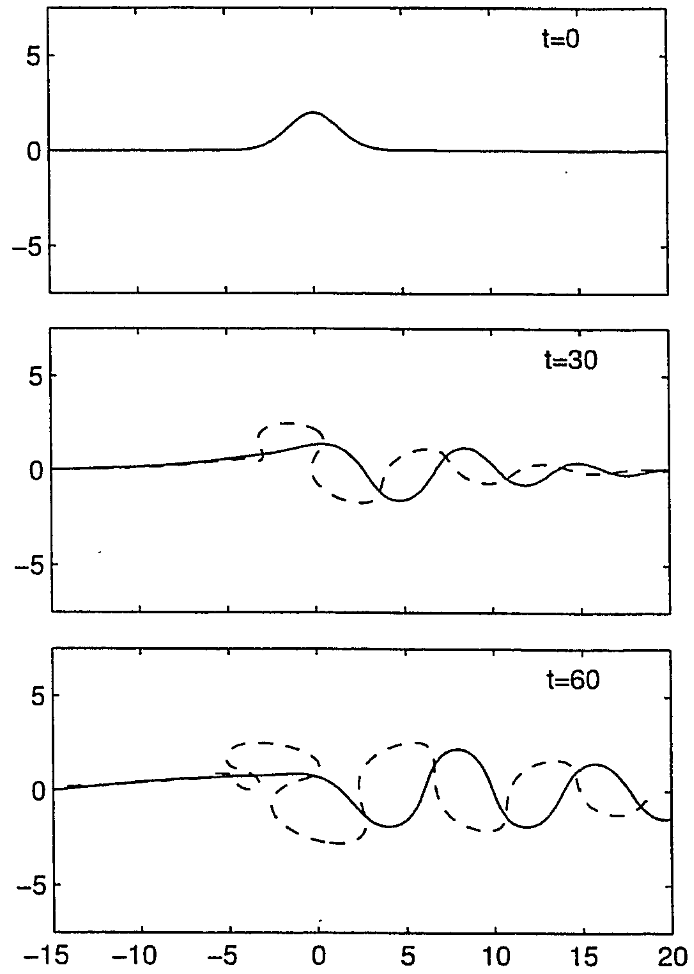

Figure 4.8: *Run k4*: (a) t=0, (b) t=30, and (c) t=60.

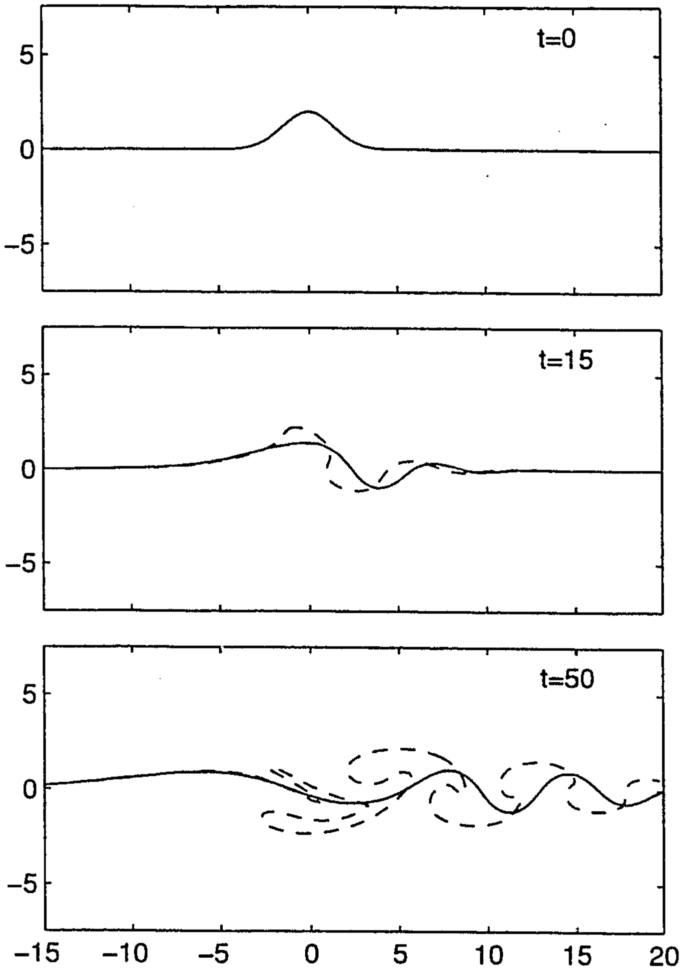

Figure 4.9: *Run j6*: (a) t=0, (b) t=15, and (c) t=50.

disturbance (width $< R_{d_1}$). His meander contained power in wavenumbers larger than the most unstable ones. Then, he was also able to shift the dipole formation from the primary crest to the primary trough. In our case, the most unstable waves in *Run k2* are somewhat longer than in *Run k1*. Since the Gaussian meander is the same, the effect is analogous to narrowing the initial condition. Therefore, it is possible that the eddy shedding regime described in the previous paragraph is particular to the initial condition used, which did not necessarily target the most unstable wavenumbers.

To test this hypothesis, we explore the jet configuration in *Run k2* (Table 4.3), in which the dipolar vortex is formed on the primary trough. Since the most unstable wavenumber is $k \approx 1.25$ (Figure 4.3b), we now perturb the jet with a wider Gaussian meander, say $w = 3$ (*Run k6*). This particular disturbance contains more power closer to the most unstable k than does the $w = 2$ bump. Thus, by targeting the most unstable k's, we are able to shift the dipole formation to the primary crest (Figure 4.10), and excite longer waves than in *Run k2*.

Now, consider the weakly unstable jet configuration in *Run k4* which developed no dipole formation with the $A = w = 2$ Gaussian anomaly. In this case, its most unstable wavenumber ($k \approx 0.85$) is targeted with a more complicated disturbance shape, given by

$$\eta(x,0) \quad = \quad 3\, e^{(-x^2/w^2)} \cos(k_0 x) \; .$$

This multi-lobed bump, formulated by *Pratt* [1988], sets k_0 as the dominant wavenumber, and the width w determines the extent to which wavelengths neighboring k_0 are present. We obviously choose $k_0 = 0.85$ and $w = k_0/2\pi$ (*Run k7*, Figure 4.11a). The disturbed jet evolution obtained on the upper layer resembles *Pratt*'s [1988] experiments with equivalent barotropic jets, with some moderate growth on secondary crests. The lower layer primary crest elongates as the left side secondary crest necks off ($t = 30$, Figure 4.11b). The primary crests in both layers drift apart, as the

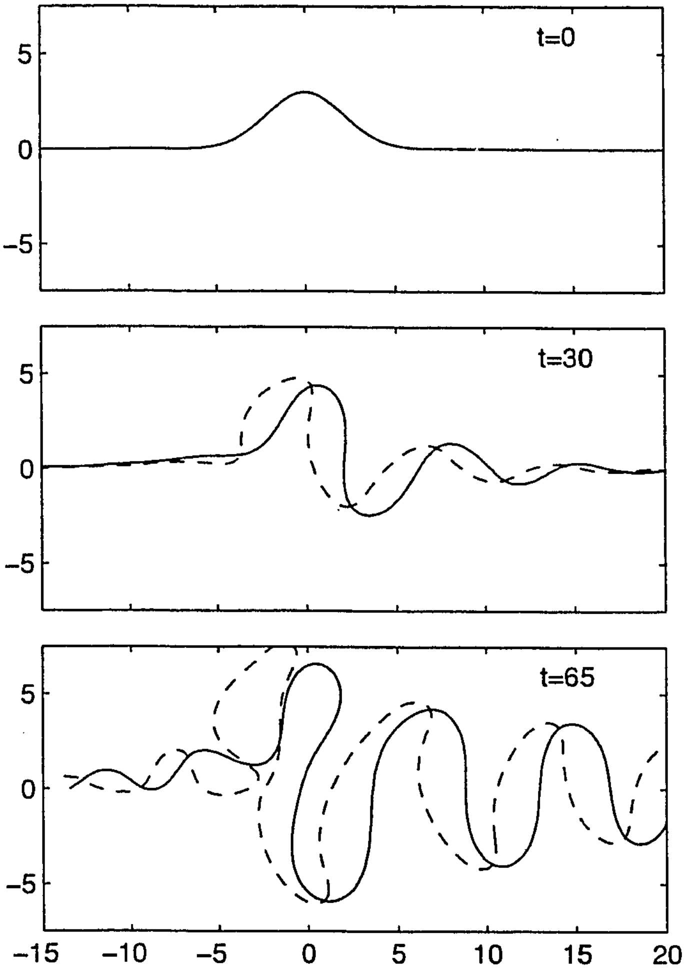

Figure 4.10: *Run k6*: (a) t=0, (b) t=30, and (c) t=65.

lower layer crest grows fringes that interact with the upper layer crest ($t = 45$, Figure 4.11c). The upper layer primary crest pinches off an eddy. Its interaction with the elongated lower layer primary crest and its fringes creates mechanisms that allow the upper layer anticyclonic eddy to propagate away from the jet ($t = 60$, Figure 4.11d). Unfortunately, our simple CD insertion-deletion particle control does not allow us to carry the integration much farther and verify what happens to the lower layer primary crest. Nevertheless we conclude that this experiment shows the ability of weakly unstable jets to generate propagating eddies. Thus, the results above suggest that there are apparently no rigid bounds to be defined for development of dipolar vortices in $2\frac{1}{2}$-layer unstable jets. The results of Experiment Sets 1-3 are needed to illustrate the several ways this process can occur.

4.4 Separating Jets

In this section, we aim to understand if/how baroclinic effects change the results obtained by the SFB96 $1\frac{1}{2}$-layer separating jet model. In particular, we want to verify whether coastal eddy shedding is possible in double-front, $2\frac{1}{2}$-layer jets. Thus, here we examine semi-infinite jet models which include a western boundary and connect a zonal jet to a coastal current system. The formulation to be described in the next subsections follows SFB96's model. Also it should be emphasized that away from the coast, the jet profile is identical to those given by Eq. (4.28). We restrict our investigation to configurations with converging upper-layer coastal currents that form an eastward separating jet.

We start by redefining the coordinate system and rotating the frame of reference described in Section 4.3 by an angle θ to make the y-axis parallel to the western boundary. Hence,

$$\begin{aligned} x_* &= x\,cos\theta + y\,sin\theta \\ y_* &= y\,cos\theta - x\,sin\theta\ , \end{aligned}$$

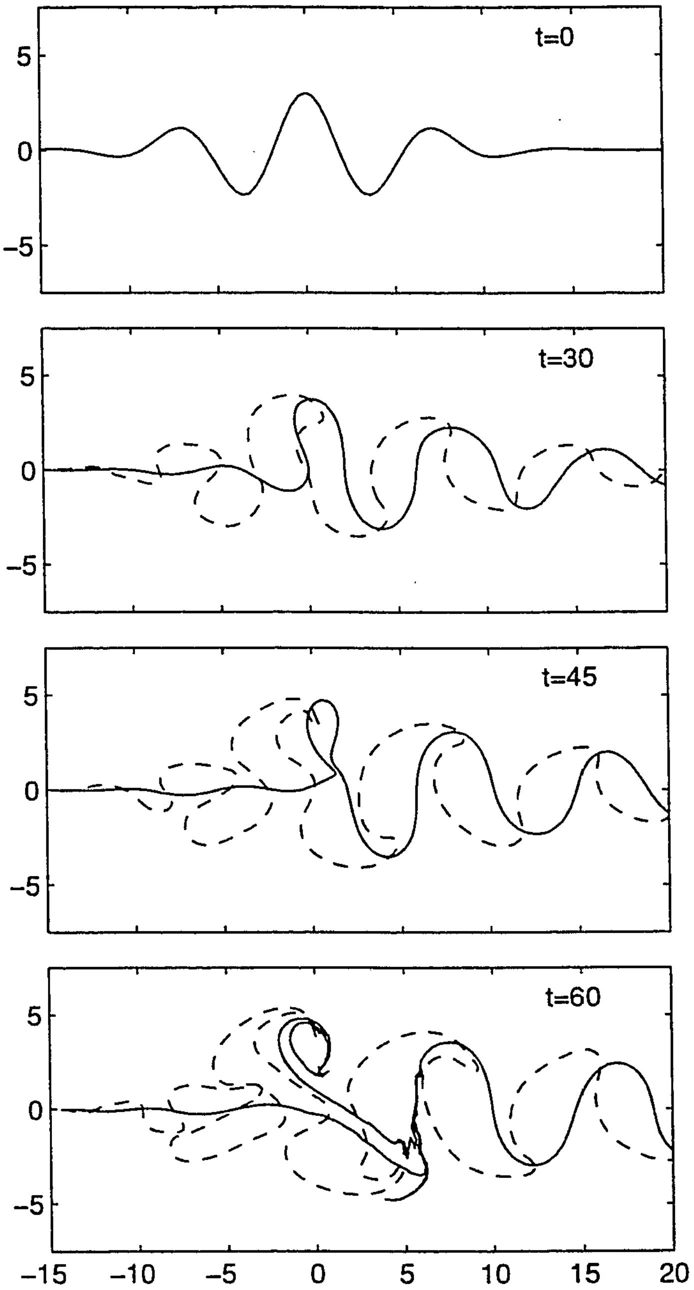

Figure 4.11: *Run k7*: (a) t=0, (b) t=30, (c) 45 and (d) t=60.

where x_* and y_* are the new cross-shore and alongshore coordinates. Therefore, $x_* = 0$ corresponds to the boundary, and the model is limited to positive x_* values only. As in SFB96, we limit the study to cases where $\theta = 0$ and $\theta = \pi/4$.

The PV field is still given by Eq. (4.15). However, in contrast to the infinite jet case, q_{0_i} is not a free parameter and its value alters the background flow pattern. For example, if $q_{0_i} = -\frac{1}{2}\Delta_i$, the southern and northern coastal currents are symmetric, or a mirror image of each other. In cases where $q_{0_i} = -\frac{1}{2}\Delta_i - \alpha_i$, one coastal current is stronger than the other. We designate as the "symmetric" separating jet model, configurations of the particular case for which $q_{0_i} = -\frac{1}{2}\Delta_i$ and thus, in which q_i has same magnitude (and opposite sign) in each side of the PV front. The formalism and numerical experiments for this case are presented in Section 4.4.1. We designate as the "asymmetric" jet model, configurations for which q_{0_i} differs from $-\frac{1}{2}\Delta_i$ by a quantity α_i. The formalism and experiment results for the asymmetric model are reported in Section 4.4.2.

4.4.1 The Symmetric Model

Model Formulation

The PV field for the symmetric model is obtained by rewriting Eq. (4.15) using $q_{0_i} = -\frac{1}{2}\Delta_i$. This yields

$$\boldsymbol{q} = -\frac{1}{2}\boldsymbol{\Delta} + \mathcal{D}\mathcal{H}(y - \bar{\boldsymbol{y}} - \boldsymbol{\eta}) , \tag{4.35}$$

where now,

$$\bar{y}_i = \bar{y}_i(x) = x \tan\theta$$

and the *'s are dropped. By evaluating $\bar{y}_i(0) = 0$, it can be seen that the PV front is connected to the coast in both layers.

SFB96 showed that when $\theta \neq 0$, an alongshore momentum imbalance is introduced. For those cases, the coastline tilt acts as a forcing, creating a steady PV anomaly close to the confluence region. The anomaly drives linearly growing wave patterns, making steady states unlikely. However, given the linear nature of the inversion formulae Eq. (4.3), we can still split, for any θ, the q_i field into a background and time-independent part $\bar{q}_i$, and a part q_i' associated with the time-dependent deviations from $\bar{q}_i$. It should be emphasized that $\bar{q}_i$, which is associated with the "straight" position of the front, does not (necessarily) represent a steady state, By partitioning the PV field, analogous expressions to Eq. (4.16) and Eq. (4.17) can be written for the symmetric, semi-infinite jet model considered in this section. However because the background (or "straight") flow pattern is much more complex here than in the infinite jet case, it is difficult to find an analytical solution like Eq. (4.28). Thus, the $\bar{\psi}_i$ field is solved numerically. Following SFB96, we actually solve numerically for the orthogonalized "mode" stream function $\bar{\Psi}_m$, and as in Section 4.2, we use Eq. (4.10) to relate the "mode" stream function and PV to the corresponding "layer" fields. Hence, the "mode" background inversion relationship (equivalent to Eq. 4.18) is

$$[I\nabla^2 - \Gamma^2]\,\bar{\boldsymbol{\Psi}} \;=\; -\frac{1}{2}\boldsymbol{D} + \mathcal{D}_{\perp}\mathcal{H}(y-\bar{y})\,, \tag{4.36}$$

where according to Eq. (4.10),

$$\boldsymbol{D} \;=\; \mathcal{F}\boldsymbol{\Delta}\,, \tag{4.37}$$

and $\mathcal{D}_{\perp}$ is a 2×2 diagonal matrix with the "mode" vorticity jumps D_1 and D_2 as its nonzero entries.

The four boundary conditions required to solve for Ψ_m are: the zero normal flow at the boundary,

$$\Psi_m(0,y) \;=\; 0\,; \tag{4.38}$$

the specified symmetric and opposing coastal current profiles,

$$\Psi_m(x,\pm\infty) \;=\; \mp\frac{D_m}{2{\gamma_m}^2}(1-e^{-\gamma_m x})\,; \tag{4.39}$$

and the condition that as $x \rightarrow \infty$, the background velocity structure becomes identical to that of the infinite jet model (just rotated by the angle θ). Once Ψ_m is determined numerically by iteration, it can be mapped back into the ψ_i fields via Eq. (4.9). The velocities $\bar{u}_i$ and $\bar{v}_i$ are computed using a finite difference approximation of the stream function Eq. (4.2).

The perturbed "layer" stream function solution is given by Eq. (4.30). To satisfy the condition that $\psi_i'(0,y,t) = 0$, the Green's function Eq. (4.31) needs to be modified, taking the form

$$G_{ij} = - h_i F_{im} F_{jm} \frac{1}{2\pi} \left[K_0(\gamma_m r) - K_0(\gamma_m \tilde{r}) \right] , \tag{4.40}$$

with $\tilde{r}$ being

$$\tilde{r} = \sqrt{(x+x')^2 + (y-y')^2} \, .$$

Expressions for u_i' and v_i' are obtained by substituting Eq. (4.40) into Eq. (4.33). The contour evolution equations, analogous to Eq. (4.21), now include a $\bar{v}_i$ contribution in Eq. (21b) due to the coastal currents and the coastline tilt (i.e., $d\bar{y}_i/dt$).

The CD code is also identical to the one for the infinite jets (see Section 4.3.2, last paragraph), with the only difference being that $\bar{u}_i$ and $\bar{v}_i$ are now interpolated within the grids obtained by the iterative scheme.

Numerical Results

We investigate of the symmetric model using the three PV front structures of Experiment Set 3 with the coastline tilt parameter θ either 0 or $\pi/4$. The initial conditions used are:

- For a meridionally oriented coastline ($\theta = 0$), a $A = w = 2$ half Gaussian disturbance (Eq. 4.34) placed at $x = 0$;
- For a tilted coastline ($\theta = \pi/4$), $\eta(x,0) = 0$, given no steady state is known.

Table 4.5: Experiment Set 4: Symmetric Separating Jets ($\delta = 0.2$, $R = 6.25$, $\mu = 5.0$ and $\epsilon = 1.25$)

Run	$\bar{u}_2(\infty, 0)$	θ	Initial Condition	Summary of Results
ml	-0.50	0	Eq. (34), $A = w = 2.0$	coastal eddy shedding by $t = 20$
m2	-0.50	$\pi/4$	$\eta(x, 0) = 0.0$	coastal eddy shedding by $t = 20$
m3	-0.125	0	Eq. (34), $A = w = 2.0$	dipole formation on primary trough eddies shed at $x = 5.0$ by $t = 55$
m4	-0.125	$\pi/4$	$\eta(x, 0) = 0.0$	retroflection dipolar eddies shed by $t = 60$
m5	0.0	0	Eq. (34), $A = w = 2.0$	dipole formation on primary trough eddies shed at $x = 10.0$ by $t = 65$
m6	0.0	$\pi/4$	$\eta(x, 0) = 0.0$	eddy shed from lower layer retroflection bulge dipole formation on primary trough at $x = 10.0$ by $t = 85$

The results of these experiments are summarized in Table 4.5 and described below.

In *Run m1* ($\theta = 0$), The upper layer eastward (lower layer westward) jet is connected to the coast by converging (diverging) coastal currents. Away from the coast, the jet configuration is as in *Run l1.* As soon as the model is turned on ($t = 0$, Figure 4.12a), the lower layer meander is sheared northward by the lower layer coastal current. This sets a vertical phase shift, and the meander in both layers start to grow ($t = 10$, Figure 4.12b). In the upper layer, the bulge at the coast interacts with both the lower layer PV patch and its image, creating a northward tendency that overcomes a possible squashing by the southward coastal current ($t = 15$, Figure 4.12c). In the lower layer, the meander interaction with its image creates a southward tendency that is overcome by both the northward advection by the lower layer coastal current and the northward motion through interaction with the upper layer.

The result is that coastal eddies are pinched off in both layers as the primary trough reaches the boundary ($t = 20$, Figure 4.12d). The eddies will continue propagating northward. The westward propagation of baroclinically unstable waves in this experiment account for a coastal eddy shedding, which was not possible in SFB96's equivalent-barotropic model (see Figure 4.13, circled curve). In the SFB96 model, unlike in stable infinite jets, the presence of the boundary could have been responsible for dipole formation due to interactions of the anomaly with its image. However, the results of *Run m1* emphasize the importance of both baroclinic effects and westward wave motion for dipole formation.

Run m2 is the tilted coastline ($\theta = \pi/4$) version of *Run m1.* When the model is turned on, waves are excited due to the presence of a tilted coastline. As the long waves (both unstable and stable) propagate westward, a pattern similar to the one in *Run m1* is obtained. In SFB96's equivalent-barotropic model, a realistic retroflection pattern (consisting of a spatially damped wave on the jet with an anticyclonic upper-layer bulge close to the coast) developed when the tilt effect was

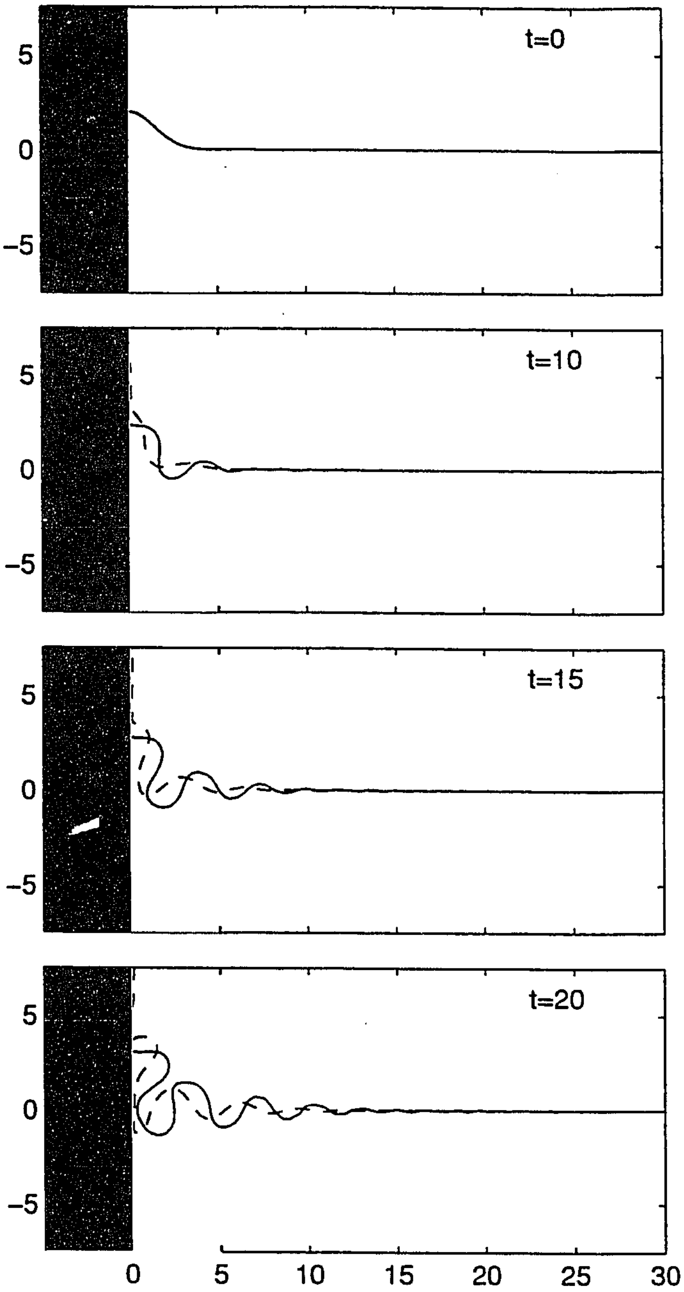

Figure 4.12: *Run m1*: (a) t=0, (b) t=10, (c) t=15 and (d) t=20.

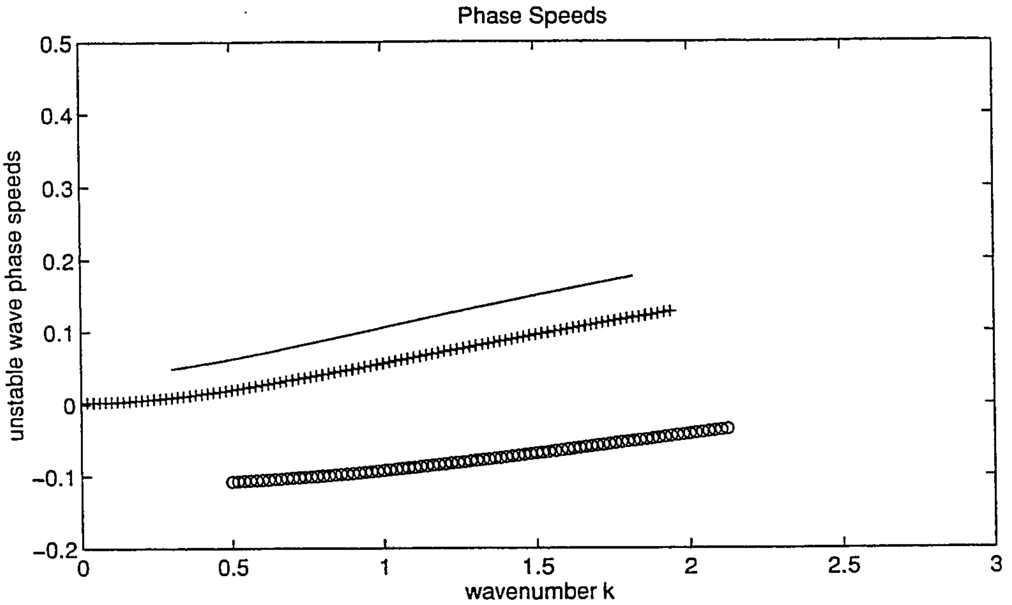

Figure 4.13: Phase speeds for the unstable waves of Experiment Set 3, corresponding to $\bar{u}_2(0)$ = -0.5 ('o' curve, *Run l1*), -0.125 ('+' curve, *Run l2*), and 0.0 ('-' curve, *Run l3*).

introduced. However, the waves in SFB96's $1\frac{1}{2}$-layer jets propagated eastward.

In *Run m3* ($\theta = 0$), we look at the case in which, away from the coast, the jet configuration is as in *Run l2* (Table 4.4). The linear theory tells us that the waves slowly propagate eastward (Figure 4.13, crossed curve). It can be seen (Figure 4.14) that in early stages after initialization, the wave structure is similar to that of SFB96's equivalent-barotropic model. The meander in both layers is slowly squashed against the y-axis ($t = 10$, Figure 4.14b). The eastward traveling waves form a spatially damped pattern, with shorter wavelengths outrunning the longer ones. With meander dispersion occurring faster in the upper layer, a vertical phase shift develops on the ocean side of the bump, triggering baroclinic instability ($t = 25$, Figure 4.14c). The meanders then start to grow. The original bump continues to be stretched in both layers, being about five deformation radii wide at $t = 40$ (not shown).

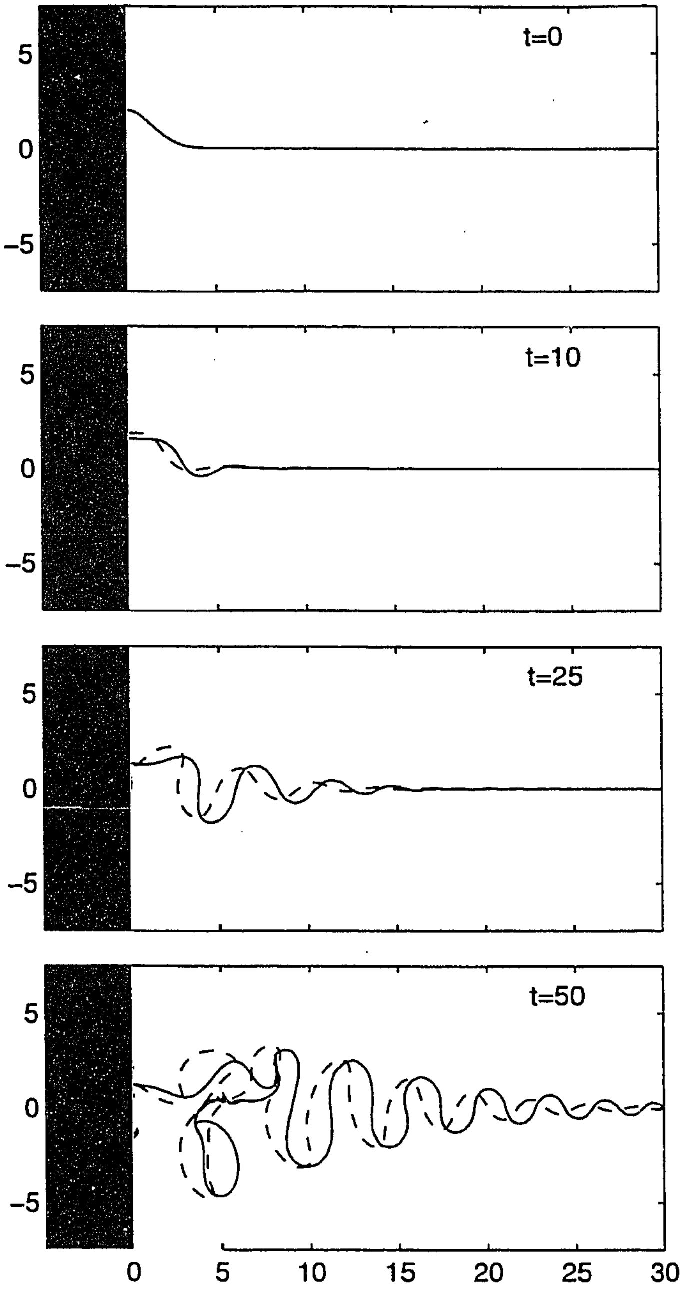

Figure 4.14: *Run m3*: (a) t=0, (b) t=10, (c) t=25 and (d) t=50.

The primary trough necks off in both layers and forms a dipolar vortex ($t = 50$, Figure 4.14d). The dipole is shed at some distance from the coast ($x > 5$) so that it feels very little the influence of the boundary. This may be a case in which the presence of the boundary actually inhibits dipole formation. SFB96 showed that the cross-shore gradient in the cross-shore velocity is responsible for the stretching of the initial meander, favoring long wave patterns. This is exactly what happens with the upper layer meander, which by $t = 10$ is about five deformation radii wide. Recalling that separating jets tend to excite long waves, we build a semi-infinite version of M91's model, which for the corresponding $\delta = 0.2$ case exhibit considerably longer unstable waves (see Figure 4.4b, thick line). The goal is to try to match the wave growth rate with the meander stretching rate and verify the possibility of dipole formation on the primary crest. The results shown on the Appendix (*Run a1*) repeat those of *Run m3*, indicating that the time scale on which the bump widens is shorter than the meander growth, and thus dominates the evolution process.

In *Run m4* is the tilted coastline case ($\theta = \pi/4$) of *Run m3*. In contrast to the previous case, retroflection eddies (i.e., eddies pinching off from the retroflection bulge) are obtained in this case (Figure 4.15). We believe that meander growth (due to baroclinic instability) adds to the linear growth (due to the steady input of alongshore momentum), as in the wave pattern of SFB96's model, combine effects to control the widening of the primary crest, and thus allowing the pinching off (the primary crest is about 35% narrower at $t = 25$ than in the $\theta = 0$ case).
Sometime later (see Figure 4.15d), the whole retroflection bulge appears to pinch off in both layers when the primary trough reaches the coast. We don not actually see it happening because we are limited by the simplicity of our CD code. Regarding the dipolar vortex, We speculate that, since the dipolar vortex is shed about four deformation radii from the coast, its self-induced motion will prevail over that due to the opposing coastal currents, and it will move northwestward. If the dipole approaches the coast, it will feel a stronger upper layer coastal current, but the

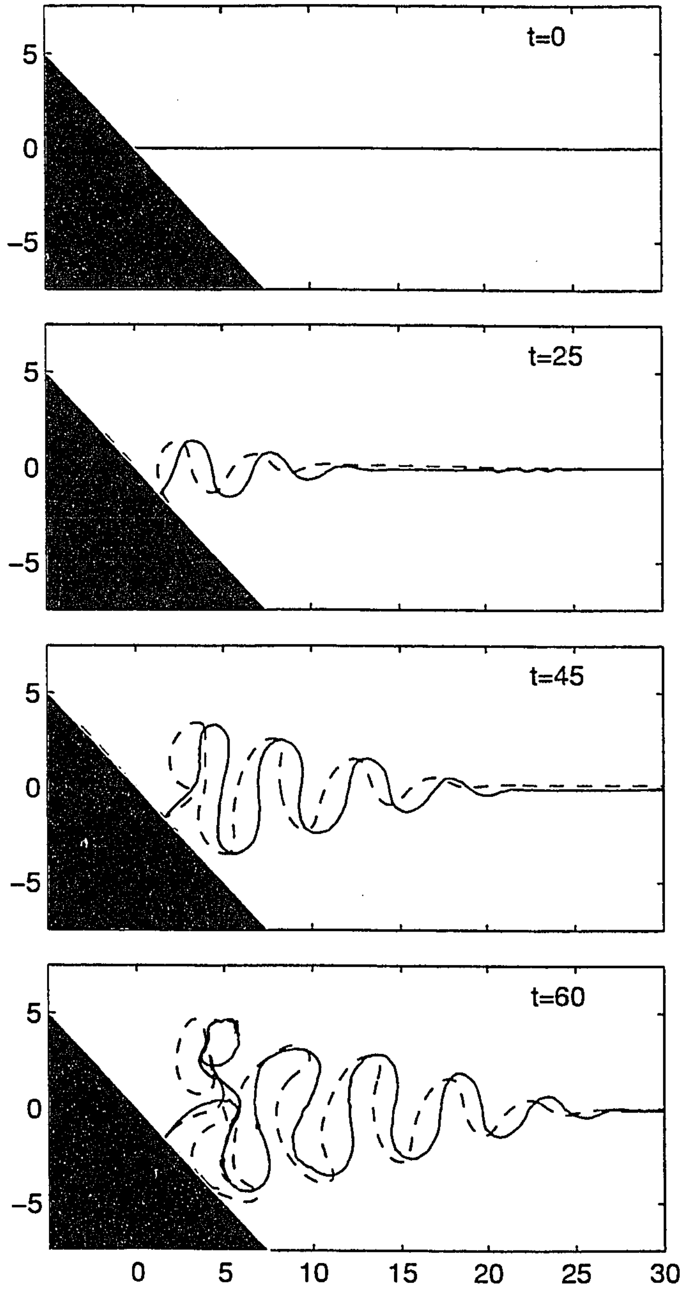

Figure 4.15: *Run m4*: (a) t=0, (b) t=25, (c) t=45, and (d) t=60.

northward tendency due to the image effect will also be enhanced.

For *Run m5* ($\theta = 0$), the jet configuration, away from the coast, is as in *Run l3*. There is no westward flow in either of the layers (Figure 4.4a). The waves propagate eastward faster than in *Run m3* configuration (see also Figure 4.13, solid curve). The results obtained are very similar to those of *Run m3*. For example, as shown in Figure 4.16b, the faster eastward traveling waves cause a fast dispersion of the initial meander toward the ocean interior. There is little vertical phase shift on the anomalies close to the coast. The dipolar vortex is formed on the primary trough at about ten deformation radii distance from the boundary, where the jet is essentially a free jet ($t = 50$, Figure 4.16c).

Run m6 is the tilted boundary ($\theta = \pi/4$) version of *Run m5*. The evolution follows the meridional boundary analog (Figure 4.17). The main difference is that an eddy pinches off from the retroflection bulge on the lower layer, and is later reentrained in the jet.

The results of *Run m5* and *m6* strongly suggest that either westward or weakly eastward propagating waves are necessary for dipole formation on the primary crest of separating symmetric jets.

More precisely, we find that retroflection/coastal eddy formation occurs when the dynamical system satisfies *Farrell's* [1982] criteria for absolute instability. This author developed "the pinch singularity method", which is an extension of the method of the stationary phase to the complex plane. He defined that a system is absolutely unstable if the local envelope growth rate ν is positive for $x/t = 0$. The wave envelope then grows as $exp(\nu t)$ at the point of excitation. In Figure 4.18, we present the calculations of ν for *Runs m1* and *m2* (thick solid line), *Runs m3* and *m4* (solid line), *Runs m5* and *m6* (dashed line). There, it can be seen that *Runs m5* and *m6* are the only case which are not absolutely unstable.

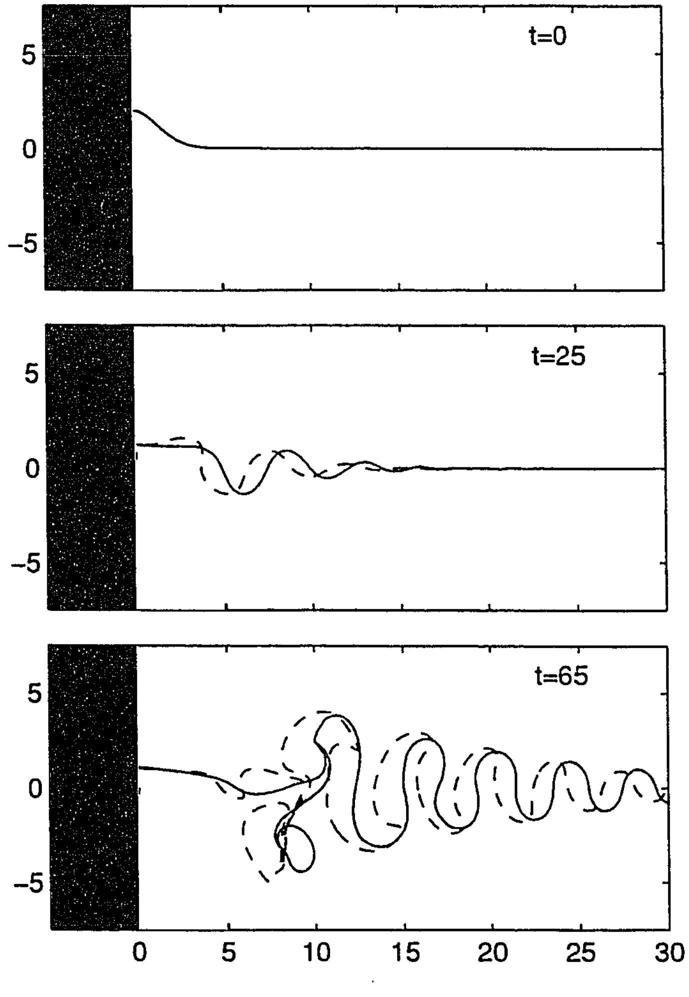

Figure 4.16: *Run m5*: (a) t=0, (b) t=25, and (c) t=65.

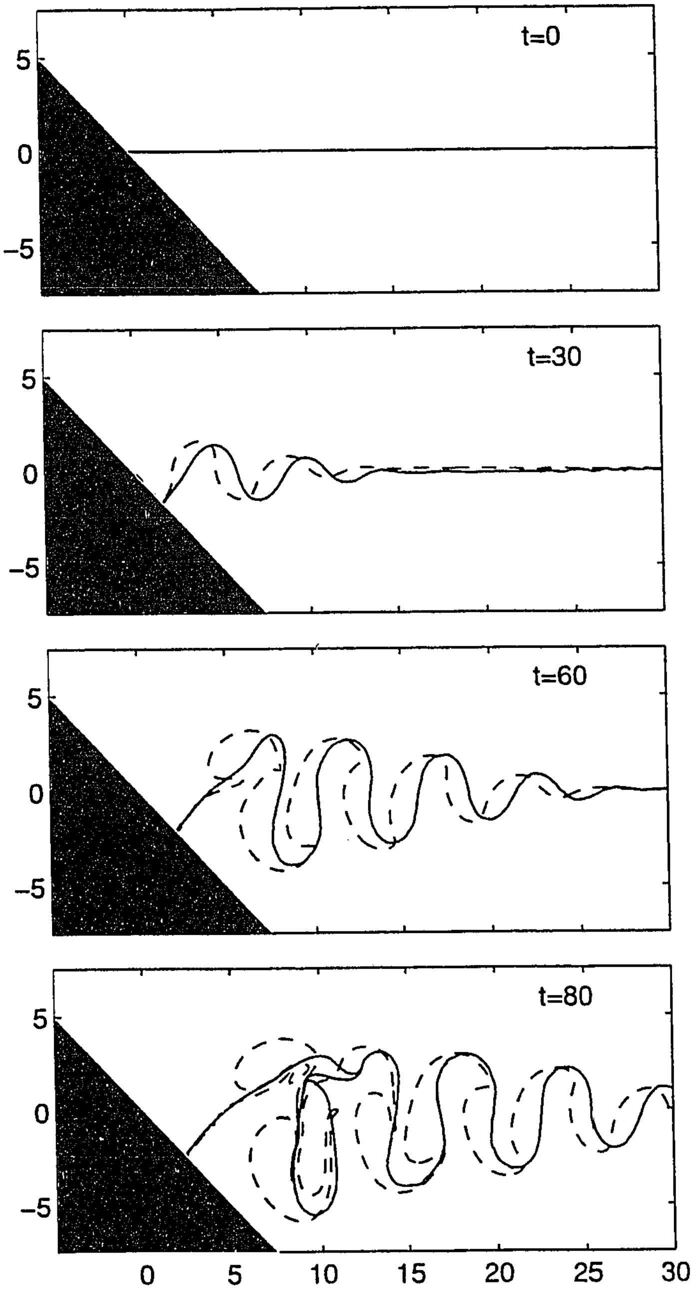

Figure 4.17: *Run m6*: (a) t=0, (b) t=30, (c) t=60 and (d) t=80.

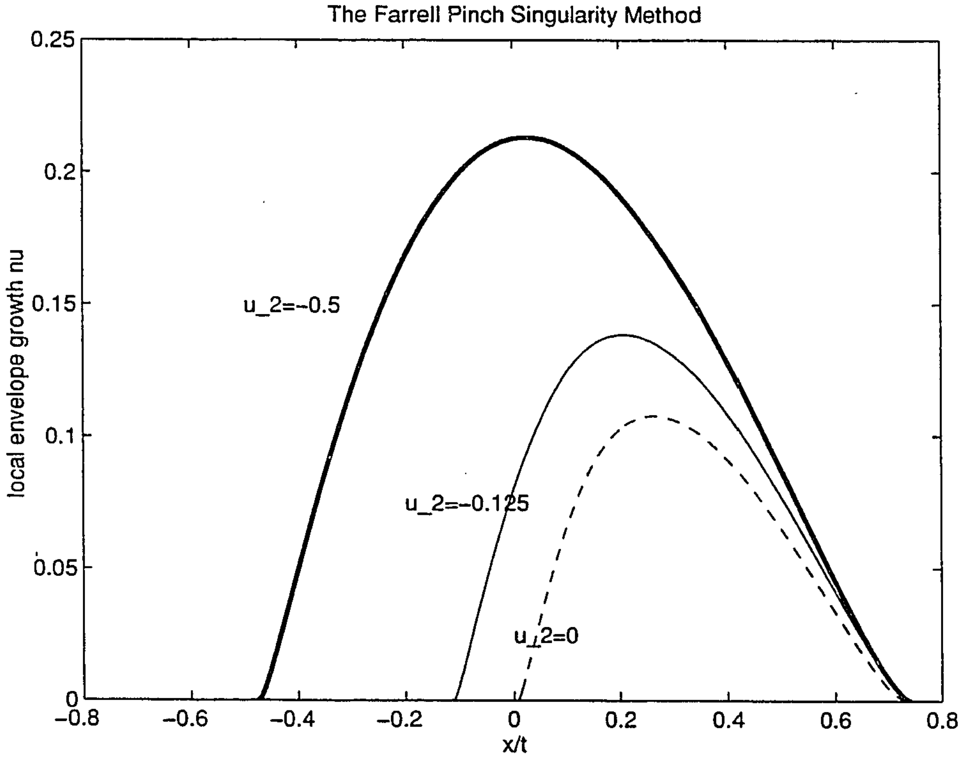

Figure 4.18: *Farrell's* [1982] pinch singularity method: the local envelope growth rate ν, corresponding to $\bar{u}_2(\infty, 0)$ = -0.5 (thick curve, *Runs m1* and *m2*), -0.125 (solid curve, *Runs m3* and *m4*), and 0.0 (dashed curve, *Runs m5* and *m6*).

4.4.2 The Asymmetric Model

Model Formulation

Now we consider cases where one coastal current is stronger than its counterart, and therefore, $q_{0_i} = -\frac{1}{2}\Delta_i - \alpha_i$. We formulate the asymmetric model similarly to the symmetric model, following SFB96. The q_i (ψ_i) field is split into a background part, $\bar{q}_i$ ($\bar{\psi}_i$), associated with the "straight" position of the front, and a time-dependent part, q_i' (ψ_i'). The jet profile in the ocean interior is given by Eq. (4.28). However, because of the asymmetric coastal current configuration, the centerjet streamline does not correspond to $\psi_i = 0$. Rather, the centerjet streamline value depends somehow on the asymmetric parameter α_i.

The model requires that $\psi_i(0, y) = 0$ at the boundary, and the front in these cases is not connected to the coast. If there is a steady asymmetric front, it would have a hyperbolic shape and would asymptotically approach some distance $\bar{x}_i(\alpha_i)$ from the coast. Therefore, close to the boundary, the fronts in each layer extend northward or southward, depending on the value of α_i. Another important distinction of the asymmetric model is that the maximum velocity of the coastal currents is not at the coast, but rather at $x = \bar{x}_i(\alpha_i)$. It turns out that computationally, it is more accurate to specify $\bar{x}_i$ instead of α_i because $\bar{\psi}_i$ is determined numerically using finite differences. More exactly, we choose $\bar{x}_1$ and $\bar{x}_2$ to be in the mid-point between two grid values. Therefore, we have two additional parameters ($\bar{x}_1$ and $\bar{x}_2$) to consider by including asymmetry. Like the symmetric model, it is convenient to solve for the "mode" background stream functions instead of the "layer" system in the asymmetrical model.

The simplest of the asymmetric cases that in which both fronts approach the same distance $\bar{x}_1 = \bar{x}_2 = x_0$ from the coast, as $y \to -\infty$. There is a converging pair of coastal currents in the upper layer in which the southern current is stronger. In the lower layer, the presence of counterflows and more complex jet patterns does not permit us to make general statements regarding transport strengths. Thus, they will be discussed on a case-by-case basis.

For the $\bar{x}_1 = \bar{x}_2 = x_0$ case, the "mode" asymmetric parameters are obtained by using Eq. (4.10):

$$\boldsymbol{a} = \mathcal{F}\boldsymbol{\alpha}\,. \tag{4.41}$$

The PV inversion relationship for the limit $y \to -\infty$ can be written as

$$[I\frac{\partial^2}{\partial x^2} - \Gamma^2]\,\bar{\boldsymbol{\Psi}} = -\frac{1}{2}\boldsymbol{D} - \boldsymbol{a} + \boldsymbol{D}\mathcal{H}(x - x_0)\,. \tag{4.42}$$

Using the assumptions $\bar{\Psi}_m(0, y) = 0$ and $\bar{\Psi}_m(x_0, -\infty) = \frac{a_m}{\gamma_m{}^2}$, one finds:

$$\Psi_m = \begin{cases} \frac{1}{\gamma_m{}^2}(\frac{D_m}{2} + a_m) + c_1 e^{-\gamma_m x}\,, & x > x_0 \\ (-\frac{D_m}{2} + a_m) + c_2 e^{-\gamma_m x} + c_3 e^{\gamma_m x}\,, & x < x_0\,, \end{cases} \tag{4.43}$$

where the constants c_1, c_2 and c_3 are

$$\begin{aligned} c_1 &= \frac{1}{\gamma_m{}^2}(\frac{D_m}{2} - a_m) - \frac{D_m}{2\gamma_m{}^2}(e^{-\gamma_m x_0} + e^{\gamma_m x_0}) \\ c_2 &= \frac{D_m}{2\gamma_m{}^2}(1 - e^{\gamma_m x_0}) - \frac{a_m}{\gamma_m{}^2} \\ c_3 &= \frac{D_m}{2\gamma_m{}^2}(e^{-\gamma_m x_0})\,. \end{aligned}$$

The expression for x_0 is given by

$$x_0 = -\frac{1}{\gamma_m}\ln(1 - \frac{2}{D_m}a_m)\,. \tag{4.44}$$

We can again invoke the linear nature of Eq. (4.3) to define a new "straight" position of the front $\bar{y}_m(x, y)$ in terms of the asymptotes of the hyperbolic centerjet streamline $\bar{\Psi}_m = \frac{a_m}{\gamma_m{}^2}$, yielding

$$\bar{y}_m(x, y) = \begin{cases} y\,, & \text{for } y < 0,\ x = x_0 \\ -(x - x_0)\tan\theta\,, & \text{for } y \geq 0,\ x > x_0 \end{cases}\,. \tag{4.45}$$

As with the symmetric model, the $\bar{\Psi}_m$ field, is determined numerically by iteration subject to four boundary conditions given by Eqs. (28), (38), (39) and (43).

Accuracy problems in the iteration scheme are minimized by choosing x_0 and inverting Eqs. (4.44) and (4.41) to obtain the a_m's and α_i's, respectively. This yields

$$\boldsymbol{a} \;=\; \frac{1}{2}\mathcal{D}_{\perp}\begin{bmatrix} 1 - e^{-\gamma_1 x_0} \\ 1 - e^{-\gamma_2 x_0} \end{bmatrix} \tag{4.46}$$

and

$$\boldsymbol{\alpha} \;=\; F\,\boldsymbol{a}. \tag{4.47}$$

The formulation for the background stream functions in cases where $\bar{x}_1 \neq \bar{x}_2$ is not as straightforward as the $\bar{x}_1 = \bar{x}_2$ case. For $\bar{x}_1 \neq \bar{x}_2$, the layer PV fields $\bar{q}_1$ and $\bar{q}_2$ have two PV value regions as before, but not the corresponding mode $\bar{Q}_1$ and $\bar{Q}_2$. For example, consider the cases in which the upper and lower layer fronts asymptotically approach distances $\bar{x}_1 > \bar{x}_2$ as $y \longrightarrow -\infty$. The background PV field is then given by

$$\bar{q}_i \;=\; \begin{cases} -\frac{\Delta_i}{2} - \alpha_i & x > \bar{x}_i \\ \frac{\Delta_i}{2} - \alpha_i & x < \bar{x}_i \;. \end{cases} \tag{4.48}$$

Using Eq. (4.10), the mode background PV field becomes

$$\bar{Q}_m \;=\; \begin{cases} h_i F_{im}(-\frac{\Delta_i}{2} - \alpha_i) & x > \bar{x}_i \\ h_1 F_{1m}(-\frac{\Delta_1}{2} - \alpha_1) + h_2 F_{2m}(-\frac{\Delta_2}{2} - \alpha_2) & \bar{x}_2 < x < \bar{x}_1 \\ h_i F_{im}(\frac{\Delta_i}{2} - \alpha_i) & x < \bar{x}_2 \;. \end{cases} \tag{4.49}$$

We can use Eqs. (4.37) and (4.47) to rewrite Eq. (4.49) and get

$$\bar{Q}_m \;=\; \begin{cases} (-\frac{D_m}{2} - a_m) & x > \bar{x}_i \\ h_1 F_{1m}(-\frac{\Delta_1}{2} - \alpha_1) + h_2 F_{2m}(-\frac{\Delta_2}{2} - \alpha_2) & \bar{x}_2 < x < \bar{x}_1 \\ (\frac{D_m}{2} - a_i) & x < \bar{x}_2 \;. \end{cases} \tag{4.50}$$

It is then clear that the $\bar{x}_1 \neq \bar{x}_2$ assumption creates a third PV value region in the $\bar{Q}_m$ field. As consequence, there is no simple relationship between $\bar{x}_i$ and a_m (or α_i), such as Eq. (4.44).. We also can no longer use the fact that we know the centerjet streamline value in the mode space. However, the condition

$$\bar{\psi}_i(\bar{x}_i, -\infty) = \bar{\psi}_i(\infty, \bar{y}_i) \tag{4.51}$$

still holds in the layer space. After some tedious algebra and some switching back and forth between the layer and mode spaces through Eq. (4.10), one is able to derive expressions for $\bar{\psi}_i$ in terms of $\bar{q}_i$ and $\bar{x}_i$ for the limits indicated in Eq. (4.51). We then solve a 4×4 linear system using the two expressions in Eq. (4.51) and the two constraints stating that Δ_i is the jump across the front in each layer ($i = 1, 2$). Once α_i is determined, the mode PV field (Eq. 50) is known and $\bar{\Psi}_m$ is determined iteratively. Then $\bar{\psi}_i$ is found from $\bar{\Psi}_m$ using Eq. (4.9).

Asymmetry does not alter the calculation of the perturbed "layer" stream function given by Eqs. (4.30) and (4.40). The numerics of the CD algorithm for the asymmetric model also follows those for the symmetric case described in Section 4.4.1.

Numerical Results

The asymmetric model has six parameters: $\bar{u}_2(0)$, R, δ, θ, $\bar{x}_1$ and $\bar{x}_2$. As our goal here is to verify that retroflection eddies are formed in presence of asymmetry coastal flows. We consider only those jet profiles in the ocean interior used in *Run l2* ($\bar{u}_2(0) = -0.125$, $R = 6.25$, and $\delta = 0.2$). We use as initial conditions the shape of the respective background centerjet streamlines in the two layers. Table 4.6 summarizes the values and the results of the experiments performed.

In order to isolate the effect of asymmetry, we focus mainly on the results of cases a meridional boundary (θ=0) is considered. One example of the combined effect of coastline tilt-asymmetry is given at the end of this section.

The $\bar{x}_1 = \bar{x}_2$ cases

In *Run n1*, we consider $\bar{x}_1(-\infty) = \bar{x}_2(-\infty) = 0.15$. In the upper layer, the southern coastal current is 30% stronger than its opposing northern counterpart. In the lower layer, the transport of both northern and southern coastal currents is southward, with the northern current being also about 30% stronger. The lower layer flow structure of this case is very different form that of the analogous symmetric case

Table 4.6: Experiment Set 5: Asymmetric Separating Jets ($\delta = 0.2$, $R = 6.25$, $\mu = 5.0$, $\bar{u}_2(\infty, 0) = -0.125$)

Run	θ	$\bar{x}_1$ ($\bar{y}_1$)	α_1	$\bar{x}_2$ ($\bar{y}_2$)	α_2	Summary of Results
n1	0	0.15 ($-\infty$)	0.71	0.15 ($-\infty$)	-0.16	dipole shed from the tip of retroflection bulge at $t \approx 65$
n2	0	0.55 ($-\infty$)	1.70	0.55 ($-\infty$)	-0.37	dipole shed from the tip of retroflection bulge at $t \approx 70$
n3	0	0.55 ($-\infty$)	1.24	0.15 ($-\infty$)	-0.29	dipole shed from secondary trough at $t \approx 65$
n4	0	0.55 ($-\infty$)	0.86	0.15 (∞)	-0.17	dipole shed from secondary trough at $t \approx 65$
n5	$\pi/4$	0.55 ($-\infty$)	1.70	0.55 ($-\infty$)	-0.37	retroflection bulge pinches off at $t \approx 45$

(*Run m3*). The layer-integrated PV jumps are equal, and the lower layer transport of the zonal jet in the ocean interior is approximately zero. The same is true for the symmetric coastal current configuration where, as seen in Figure 4.19a, the northward (southward) counterflows compensate for the opposing coastal jet core in the southern (northern) borders. In the present case (Figure 4.19b), the asymmetry causes the jet core to be displaced to the $\bar{x}_1$ ($\bar{x}_2$) position, as the y approaches $-\infty$ in the upper (lower) layer. The lower layer southern coastal current transport then becomes negative, as does the northern coastal current transport since the northward jet core at the coast is weakened.

As shown by SFB96, a consequence of having asymmetric coastal current configurations and a zonal jet in the ocean interior is the introduction of an alongshore momentum imbalance that triggers linearly growing long waves, similar to the effect of tilting the coastline. This can be verified in the results of this experiment displayed in Figure 4.20. After the model is turned on ($t = 0$, Figure 4.20a), slowly eastward propagating long waves are excited and the retroflection pattern develops ($t = 15$, Figure 4.20b). As these long waves are unstable, the vertical phase shift starts the baroclinic instability and the meanders grow ($t = 40$, Figure 4.20c). A retroflection dipolar vortex pinches off at about $x = 5$ ($t = 65$, Figure 4.20d).

It seems that as in *Run m4*, the linear growth (due to asymmetry here) and baroclinic instability combine in controlling the retroflection bulge widening, which allows the necking off of its tip. It should be noticed that in these two cases the dipole is shed at about the same distance from the coast: about five deformation radii. However, there seems to be no indication in *Run n1* that the whole retroflection bulge will occlude some time later, as in *Run m4*.

The question that arises from the results above is whether the pinching off of the whole retroflection bulge is related to the increase in the asymmetry effect. To address this question, we then consider the case with $\bar{x}_1(-\infty) = \bar{x}_2(-\infty) = 0.55$. In the upper layer, the southern coastal current transport is 80% larger than the

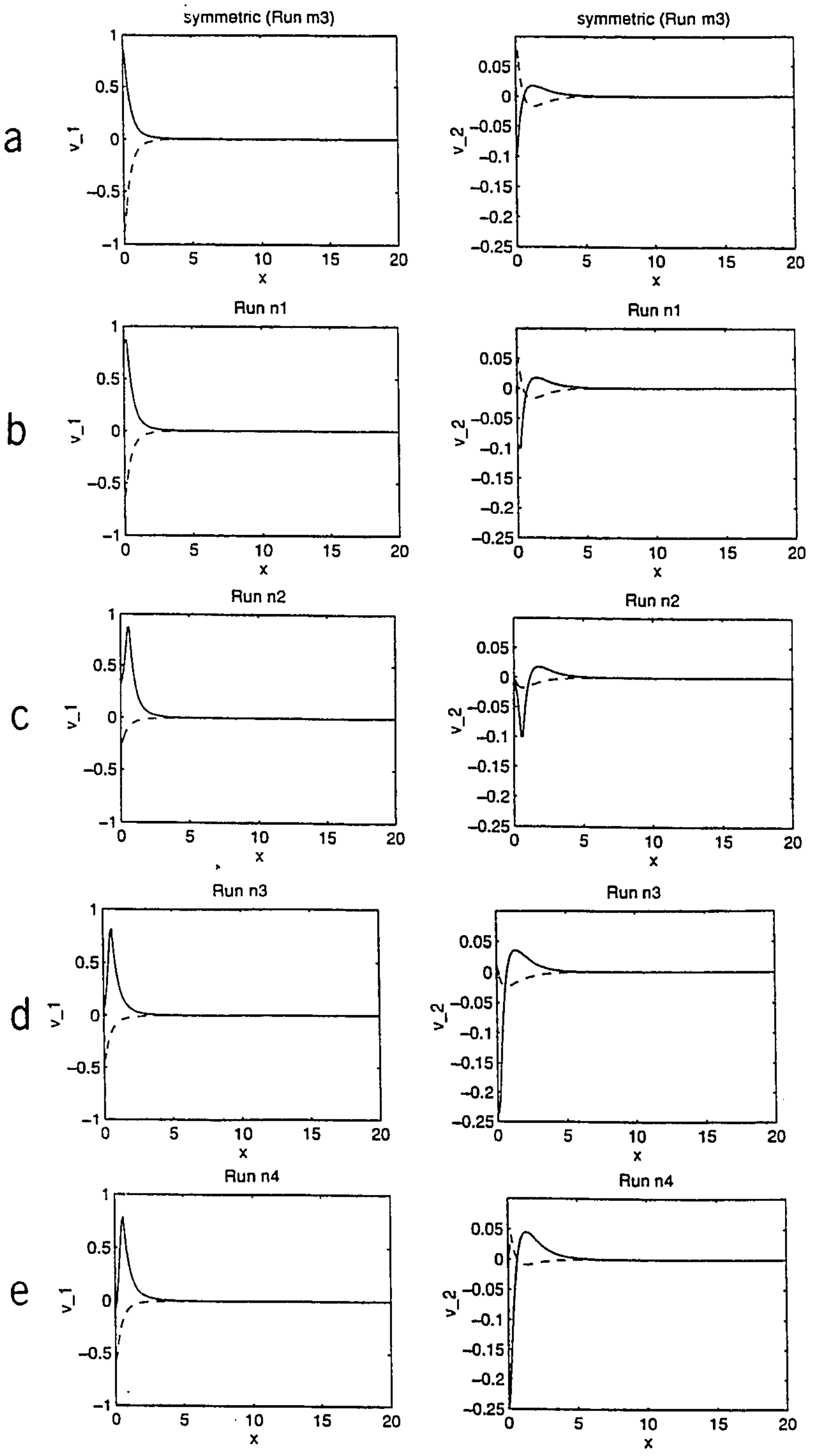

Figure 4.19: Background coastal current profiles as $y \to \infty$ (dashed line) and $y \to -\infty$ (solid line) for *Runs*: (a) *m3*, (b) *n1*, (c) *n2*, (d) *n3*, and (e) *n4*. Left (right) panels correspond to upper (lower) layer currents.

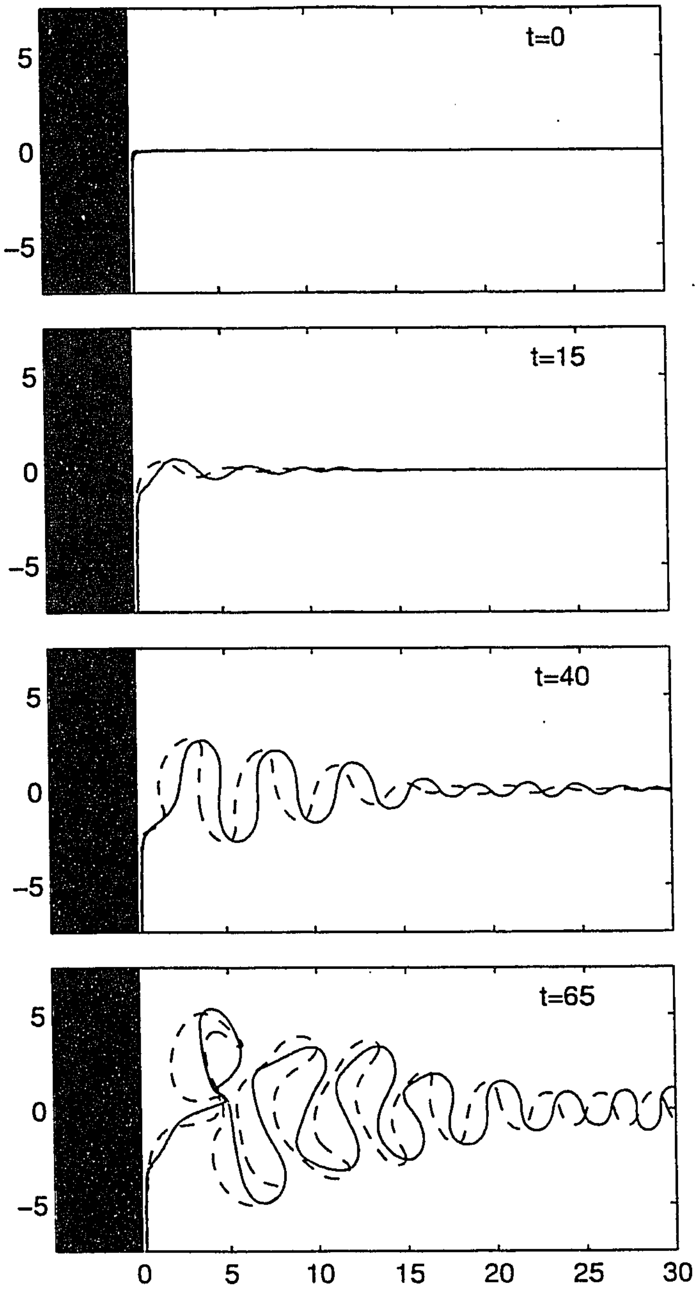

Figure 4.20: *Run n1*: (a) t=0, (b) t=15, (c) t=40 and (d) t=65.

northern one (Figure 4.19c, left panel). In the lower layer, both coastal current transports are southward, but the northern current is about 70% stronger. However the results shown in Figure 4.21 indicate only slight differences from those of *Run n1*: no retroflection bulge pinch-off. There seems to be more elongation on the retroflection bulge but only the tip pinches off. The upper layer vortex occludes later than $t = 65$. Also, as the background front is now placed at about $x = 0.55$, the wall effect is weakened, allowing cross-shore velocities to develop and wave patterns to form in its coastal side.

The $\bar{x}_1 \neq \bar{x}_2$ cases

In *Run n3*, we consider $\bar{x}_1(-\infty) = 0.55$ and $\bar{x}_2(-\infty) = 0.15$. By regarding the values of $\bar{x}_1$ and $\bar{x}_2$ as indicative of asymmetry strength, we should expect that the present case should lie between *Runs n1* and *n2*. This can be confirmed by the values of the asymmetric parameters presented in Table 4.6. In the upper layer, the southern coastal current transport is about 60% stronger than its northern counterpart. In the lower layer, the flow pattern becomes much more complex. As shown in Figure 19d, the lower layer southern coastal current presents a jet core which is 1.5 times more intense than in the previous cases. The associated counterflows are also about two times broader and more intense, creating a strong anticyclonic circulation cell on the southwest side of the domain. The results for this experiment are shown in Figure 4.22.

Unlike the previous cases, the dipole vortex does not pinch off from retroflection bulge. Rather, it is pinched off from the primary trough centered at $x = 7.5$, which occludes first in the upper layer. Intuitively, one would expect that since the background fronts are vertically displaced, baroclinic instability would be triggered earlier than in the previous experiments and somehow more effective in the eddy formation process. However, we attribute the inhibition of dipole shedding in the primary crest to the more complex lower layer background flow. Notice that in *Runs n1* (Figure 4.20) and n2 (Figure 4.21), the necking off process in the lower

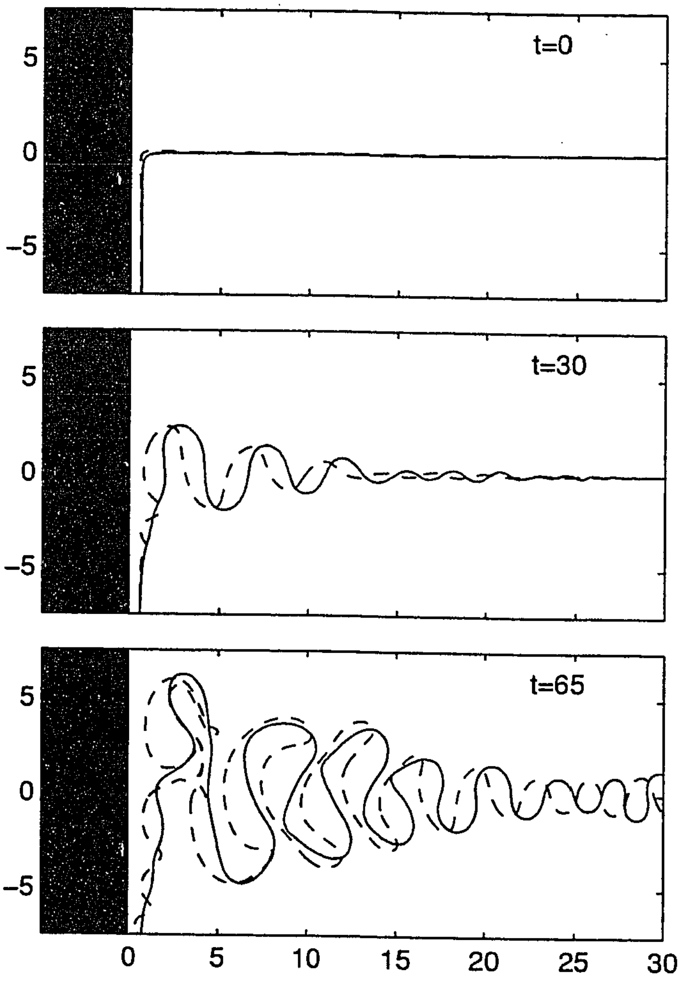

Figure 4.21: *Run n2*: (a) t=0, (b) t=30, and (c) t=65.

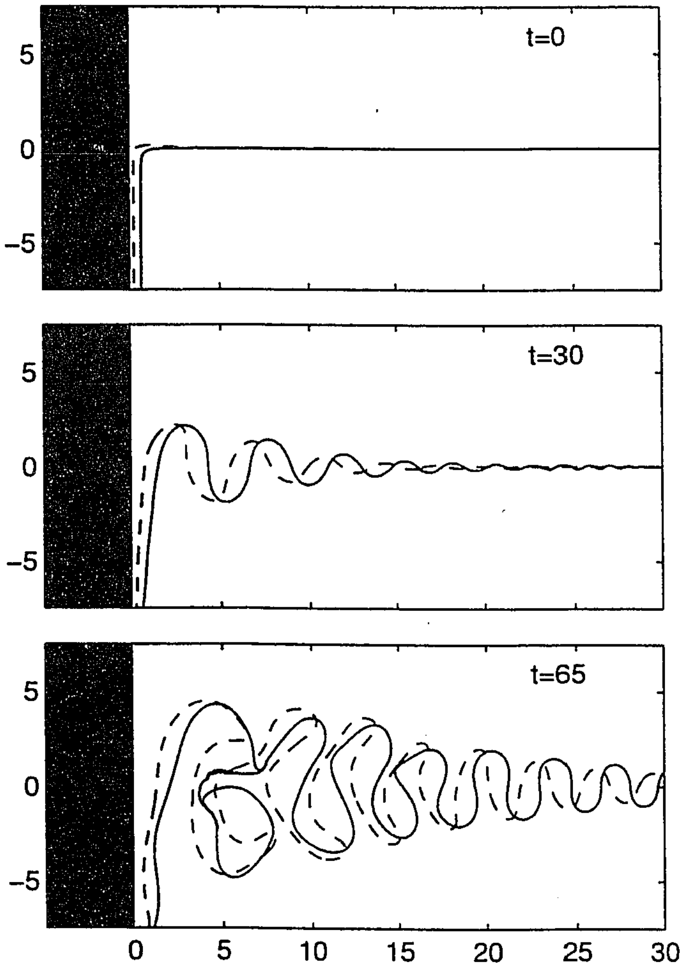

Figure 4.22: *Run n3*: (a) t=0, (b) t=30, and (c) t=65.

layer retroflection bulge begins on its western side by developing a trough. In the present case (Figure 4.22), the formation of this west side trough is absent. It is probable that the southward jet core of the southern coastal current, which is much stronger than in the previous cases, advects the perturbations formed on the west side of the bulge southward. Also, the dipole is shed at a greater distance than in the previous cases, away from the eastern edge of the strong anticyclonic cell in the southwest region of the model domain.

When a case in which $\bar{x}_1(-\infty) = 0.55$ and $\bar{x}_2(\infty) = 0.15$ is considered, we find that the values for the asymmetry parameters are only larger than those of *Run n1* (Table 4.6). The upper layer southern coastal current is about 50% stronger than its northern counterpart. The transports of both northern and southern lower layer coastal currents are southward, with the northern coastal current being only 30% stronger than the southern. Notice that the profiles of the coastal jets in the present case are similar to the ones in *Run n3* (compare Figures 4.19d and 4.19e). The main difference is the northward core centered at $\bar{x}_2(\infty)$ in the lower layer northern coast current. It is observed that, as the model is turned on ($t = 0$, Figure 4.23a), the retroflection pattern begins to develop, the tip of the lower layer is captured by the intense southward coastal current in the lower half of the domain ($t = 10$, Figure 4.23b). This part of the lower layer front is then quickly advected southward, as the meanders on its ocean side grow ($t = 25$, Figure 4.23c). The final result is a pattern identical to the one in *Run n3*, with the dipole being shed in the primary trough ($t = 65$, Figure 4.23d). This apparently confirms that the absence of "retroflection eddies" is due to the complex lower layer flow pattern.

Finally, we perform an experiment considering a both a tilted coastline ($\theta = \pi/4$), and asymmetry as in *Run n2* $\bar{x}_1(-\infty) = \bar{x}_2(-\infty) = 0.55$. The results of *Run n5*, shown in Figure 4.24, indicate that the linear growth due to both asymmetry and tilt effects adds up to the exponential meander growth due to baroclinic instability to occlude the retroflection bulge in both layers. The occlusion occurs faster than

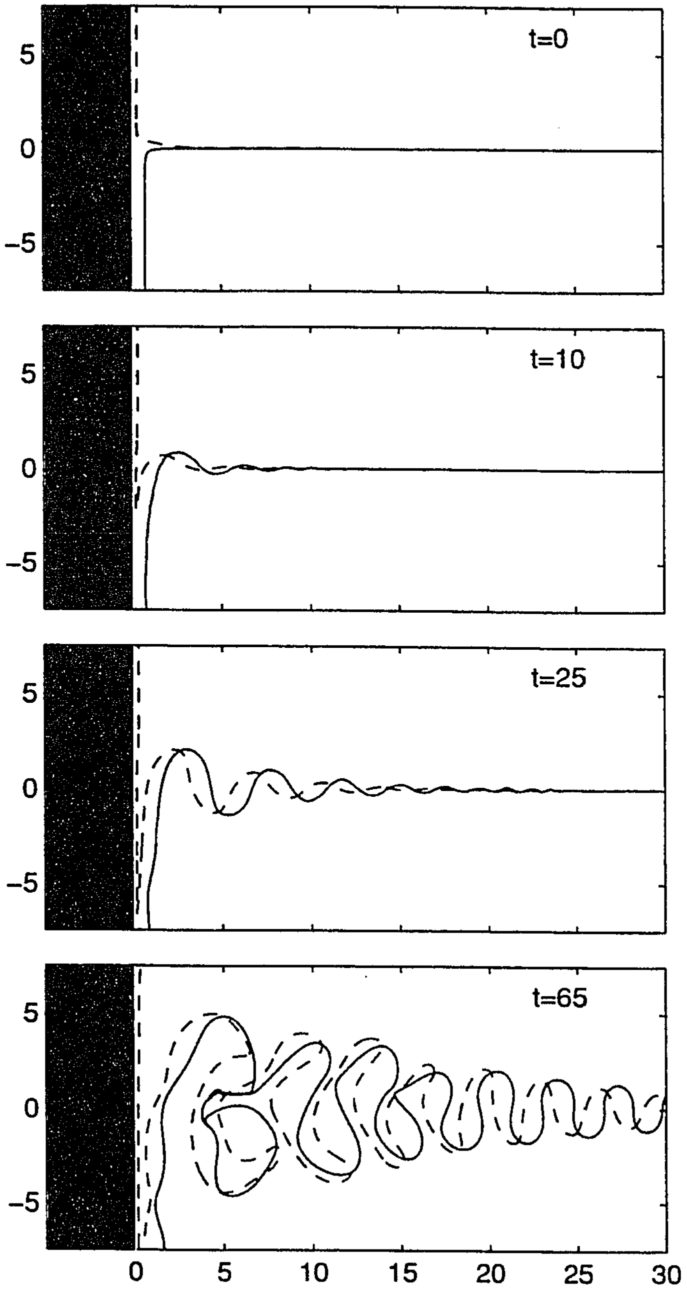

Figure 4.23: *Run n4*: (a) t=0, (b) t=10, (c) t=25 and (d) t=65.

in the tilted boundary symmetric case *Run m4*.

4.5 Summary and Conclusions

In this paper we have investigated eddy formation and detachment in piecewise-constant, baroclinically unstable f-plane quasi-geostrophic jets. Using FM95's multi-layer CD technique, we have built a $2\frac{1}{2}$-layer version of M91's double front, two-layer infinite jet model. We also consider a $2\frac{1}{2}$-layer jet adjacent to a western boundary. The latter model is a baroclinic version of SFB96's equivalent-barotropic separating jet model. Our goal in this work is to address two issues:

- M91's double front model has a background jet configuration in which only the first baroclinic mode structure is present. A consequence of such a condition is that it constrains the lower layer transport to the opposite direction of the upper layer. So, if we include more than one mode structure in the background flow (and thereby allow the lower layer transport to be in any desired direction), do the eddy shedding and dipolar vortex formation still occur?
- SFB96's model was able to reproduce some characteristics of separating boundary currents, such as the development of a retroflection pattern. However, it lacked the formation of coastal or retroflection eddies, which are known to occur in real current systems (e.g., the Brazil Current). Thus, can baroclinic instability mechanisms combine with SFB96's physics to produce coastal/retroflection eddy shedding?

However, the $2\frac{1}{2}$-layer formulation is somewhat more complex than the two-layer version, especially regarding the vertical structure parameters. For example, as discussed in Section 4.2, the layer coupling parameter is not simply the projection of the first deformation radius onto the upper layer, and there are two density jumps instead of one. An arbitrary choice for this set of parameters would probably

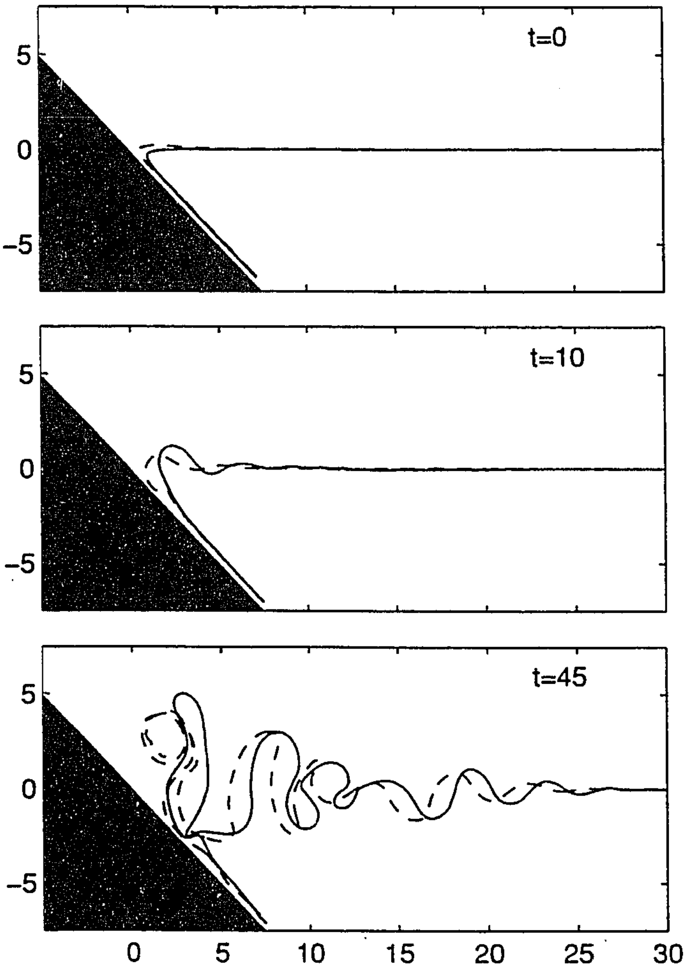

Figure 4.24: *Run n5*: (a) t=0, (b) t=10, and (c) t=45.

jeopardize a more accurate comparison with the two-layer analog. We therefore build on some of *Flierl*'s [1978] ideas and propose a simple "calibration" method for the $2\frac{1}{2}$-layer configuration that provides dynamically consistent values for the coupling parameter and density jump ratio. In this simple scheme, more familiar parameters are input: the layer aspect ratio and the ratio between the first and second deformation radii squared. With some freedom left in the scheme, two sets of values for the coupling parameter and density jump ratio emerge from a choice for one layer aspect ratio and one deformation radius ratio. The larger root for the coupling parameter is usually associated with a density jump ratio of $O(1)$, which means that the two interface vertical displacements are of the same order. The smaller root is usually associated with a much larger density jump between the first and second layers. While the smaller root provides sometimes a more realistic density profile and a behavior closer to the two-layer case, the larger root and the corresponding stronger coupling are associated with much larger unstable ranges. We believe that the latter is representative of a more truly $2\frac{1}{2}$-layer regime. Both roots are explored in this paper, but focus is be given to the larger set of values.

The first issue is addressed through exploration of the $2\frac{1}{2}$-layer infinite jet model. We use the FM95 method to determine the PV structure of the model by choosing the vertical structure parameters and the centerjet zonal velocities in both layers. We constrain our experiments to eastward-flowing upper layer jets. Also, we restrict the deformation radius (or eigenvalue) ratio to 6.25, the maximum realistic value that seems to us to be appropriate in comparisons with M91's results (i.e., it provides the largest contrast possible between the two length scales involved). The experiment results reveal that eddy shedding and dipole formation occur when the net lower layer transport is westward, zero or eastward. Even weakly unstable jet configurations are able to shed dipolar vortices when initial conditions targeting the most unstable wavenumber (determined by linear theory) are used. Nevertheless, the meander evolution in all study cases that led to dipole formation occur in a very similar way to the cases reported by M91 with his two-layer model. Linear theory shows that the most unstable wavenumbers in all cases analyzed in this work are somewhat larger than the ones of M91's model. An interesting characteristic of the $2\frac{1}{2}$-layer cases analyzed in this work is that when the centerjet velocities are chosen to provide approximately equal layer integrated PV jumps, the net lower layer transport is close to zero and there is no unstable long wave cutoff.

The second issue is addressed by examining balanced and unbalanced configurations of the semi-infinite jet model, which is bounded by the western boundary. The model allows varying the (straight) coastline orientations and asymmetry in the boundary current transports. We then obtain coastal and retroflection eddy shedding when baroclinic instability mechanisms are present. Also, more realistic meander amplitudes for retroflecting currents are obtained than those of SFB96's model. However, these phenomena seem to be contingent on a combination of relatively high growth rates and either westward or slowly eastward propagating unstable waves. When the unstable waves travel westward, the wall effect (in which the vortex anomaly pairs with its image) dominates over meander growth due to baroclinic instability and cause the detachment of a dipole that propagates northward along the boundary after occlusion. When the unstable waves travel slowly eastward and unbalanced configurations are considered, it is possible that a dipolar vortex is shed from parts of the retroflection bulge. In some cases, the whole retroflection bulge pinches off and will propagate along the coast. Baroclinic instability mechanisms dominates the process for those cases. All study cases that produced coastal/ retroflection eddies were absolutely unstable systems, according to *Farrell*'s [1982] pinch singularity method.

As future work, we intend to explore further the $2\frac{1}{2}$-layer separating jet model. In particular, we would like to search for steady states in cases where the coastline is tilted and the coastal currents are asymmetric. Also, we would like to apply the model to real boundary current systems, especially to the Brazil-Malvinas Confluence region. In this case, we would estimate the vertical structure parameters from hydrographic data, match the transports of the theoretical jet profiles to the observed ones to find the characteristic centerjet velocities. The inclusion of "contour surgery" and multiple fronts in each layer is also intended.

Appendix: Two-layer Separating Jets

In this appendix we described the results of M91's double front, two-layer jets when the western boundary is included. Both the formalism of the two-layer model and the results of the numerical experiments are presented here.

The Meacham [1991] Double Front Model: A Brief Review

The two-layer PV equations are easily recovered from Eq. (4.3) by placing the ocean floor at the second interface (see Figure 4.1). This is equivalent to setting an infinite density contrast between the second layer and the ocean floor, which makes $\epsilon \rightarrow 0$. Thus, the vertical structure matrix Z (Eq. 4) takes the form of

$$Z = \begin{bmatrix} -\mu & \mu \\ \delta\mu & -\delta\mu \end{bmatrix} . \tag{A1}$$

By diagonalizing Z (as done via Eq. 4.5), the eigenvalue matrix simply becomes

$$\Gamma^2 = \begin{bmatrix} {\gamma_0}^2 & 0 \\ 0 & {\gamma_1}^2 \end{bmatrix} = \begin{bmatrix} 0 & 0 \\ 0 & 1 \end{bmatrix} . \tag{A2}$$

Note that the zero eigenvalue is related to the barotropic mode and the external deformation radius. Besides, $R \rightarrow \infty$ if one regards R as the ratio between the lowest (the zeroth) eigenvalue and the highest (the first) also in the two-layer model. As a matter of fact, this is the reason why we concentrate our analysis of the $2\frac{1}{2}$-layer jets on $R = 6.25$. As discussed in Section 4.2, the latter R value corresponds to the maximum realistic ratio between the first two deformation radii and is probably more adequate for direct comparisons with M91's model.

The eigenvector matrix also acquires a simpler form in the two-layer case, being given by

$$F = \begin{bmatrix} 1 & 1/\sqrt{\delta} \\ 1 & -\sqrt{\delta} \end{bmatrix} . \tag{A3}$$

An expression for the coupling parameter μ is found by applying Eq. (A1) and (A2) to Eq. (4.11). The result is

$$\mu = \frac{{\gamma_1}^2}{(1+\delta)} = \frac{1}{(1+\delta)} , \tag{A4}$$

meaning the inverse squared projection of the first deformation radius onto the upper layer.

Regarding the PV structure, the M91 model requires the absence of barotropic vorticity in the far field. This assumption is satisfied by setting the barotropic vorticity jump equal to zero on the two-layer analog of Eq. (4.10). This results in the condition

$$\Delta_2 = -\delta \Delta_1 . \tag{A5}$$

As a consequence, the layer-integrated vorticity jumps are equal in the M91 model for all δ values.

The background jet profile and linear stability properties are still determined by Eqs. (4.22)-(4.28). The only difference relative to the $2\frac{1}{2}$-layer model resides in the Green's function (Eq. 4.4.26), which for the special case $k = {\gamma_0}^2 = 0$ becomes

$$(G_0)_{ij} = h_i F_{im} F_{jm} \frac{1}{2} \mid y - y' \mid . \tag{A6}$$

The basic zonal jet profile has the form

$$\bar{u}(y) = \begin{bmatrix} 1 \\ -\delta \end{bmatrix} \Delta_1 \frac{1}{2} e^{-|y|} . \tag{A7}$$

In Figure A.1, we plot the jet profiles and the growth rates for several δ values. In Figure A.2, we show the corresponding phase speeds for the same δ range of Figure A.1.

The nonlinear model (Eqs. 30-33) also has the Green's function altered in the limiting case of ${\gamma_0}^2 \rightarrow 0$ to become

$$G_{ij} \;=\; h_i F_{im} F_{jm} \frac{1}{2\pi} \ln(r) \,. \tag{A8}$$

Separating Jets: Numerical Results

The separating jet model (in both symmetric and asymmetric cases) follows the development presented in Section 4.4. We restrict ourselves to cases where $\delta = 0.2$. We also consider $\Delta_1 = 2$, yielding $\bar{u}_1(0) = 1.0$ and $\bar{u}_2(0) = -0.2$ (via Eq. 4.A5).

We perform two experiments with the two-layer symmetric separating jet model: one case with $\theta = 0$ (*Run a1*) and one with $\theta = \pi/4$ (*Run a2*).

Run a1 (Figure A.3) corresponds then to the balanced, meridional boundary case. The initial condition is the same half $A = w = 2$ Gaussian bump used in in Section 4.4.1. Note that the meander evolution approximately follows the pattern in *Run m3*. The fact that the unstable wave range is somewhat longer than the $2\frac{1}{2}$-layer model does not affect the results. Neither does the use of a larger and wider initial condition change the pattern depicted in Figure A.3. We ran experiments considering $A = w = 3, 4$ (not shown), and the dipolar eddies were shed at distances greater than five deformation radii from the coast. Therefore, coastal eddy shedding seems just possible to occur in the meridional boundary case when the unstable wave speeds are either zero or in the westward direction.

Run a2 (Figure A.4) is the experiment with the tilted boundary and hence includes the linear growth due to the alongshore momentum imbalance. As in *Run m4*, we are able to shed retroflection eddies. The dipole does not go far because the upper layer anticyclone will collide with the secondary crest. Also, the whole

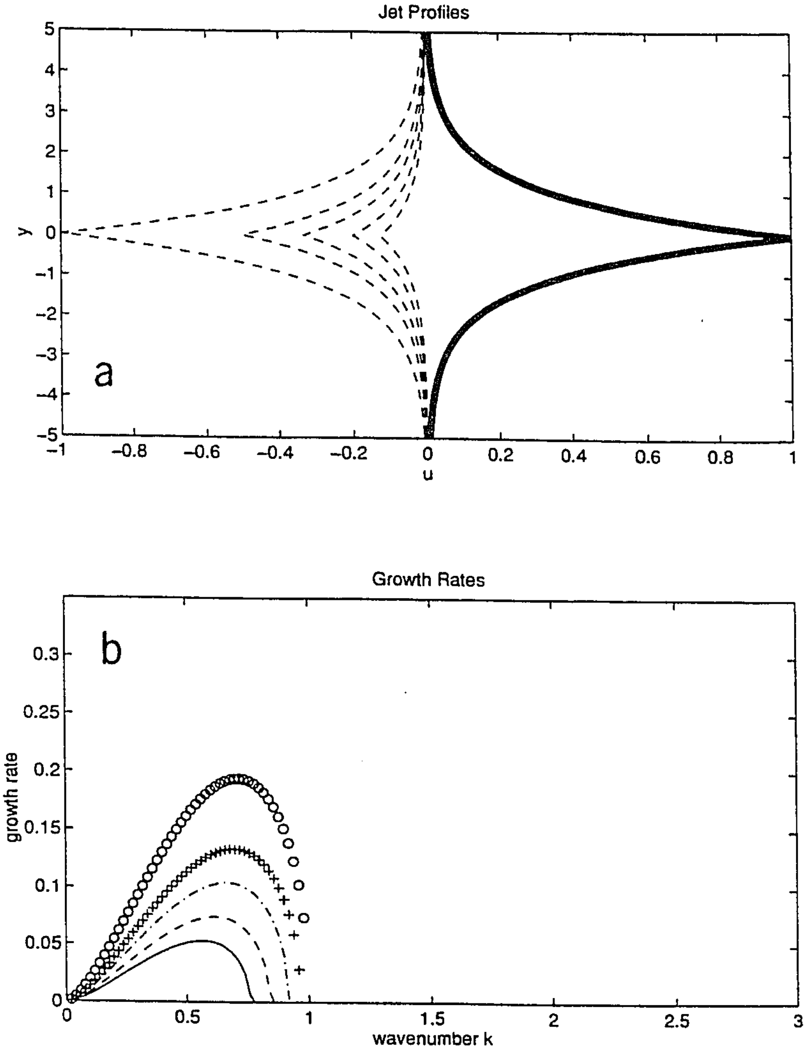

Figure A.1: The *Meacham* [1991] double front, two-layer model- (a) Jet profiles: the lower layer jets (dashed curves), from left to right, correspond to $\bar{u}_2(0) = -\delta$ -1.0, -0.50, -0.33, -0.20, -0.125; the upper layer center jet $\bar{u}_1(0)$ is equal to 1.0 in all cases (solid curves). (b) Growth rates,corresponding to $\bar{u}_2(0) = -\delta$=-1.0 ('o' curve), -0.5 ('+' curve), -0.33 ('.-.' curve), -0.2 ('–' curve), and -0.125 ('-' curve).

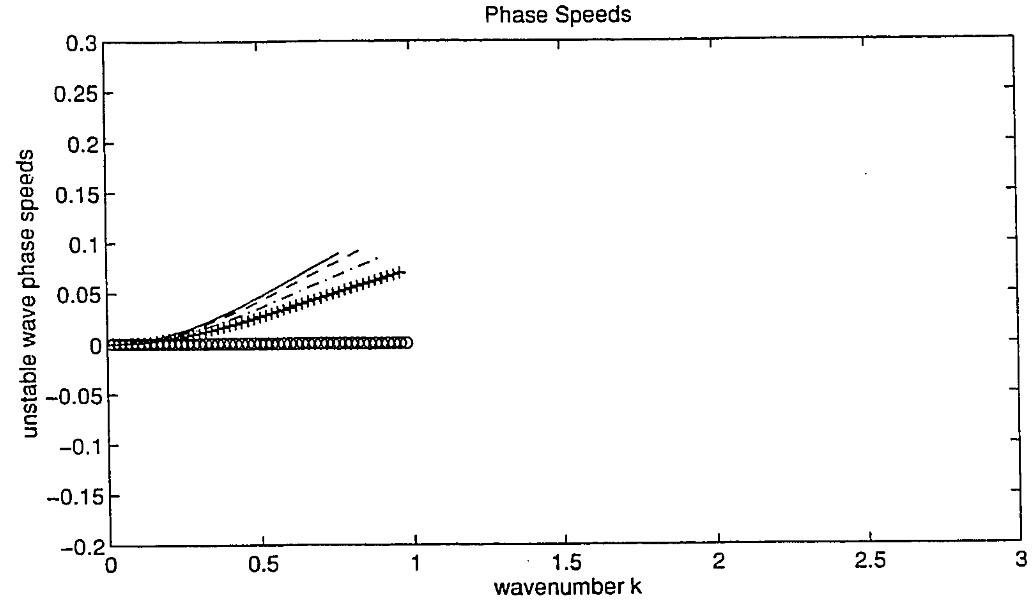

Figure A.2: The *Meacham* [1991] double front, two-layer model– phase speeds of unstable waves, corresponding to $\bar{u}_2(0) = -\delta$=-1.0 ('o' curve), -0.5 ('+' curve), -0.33 ('.-.' curve), -0.2 ('–' curve), and -0.125 ('-' curve).

retroflection bulge is separated from the front when the primary crest folds enough to reach the western boundary. But again, we show that the additional growth due to the coastline tilt effect is crucial in compensating for the meander widening and allowing coastal eddy shedding in jet configurations with eastward traveling unstable waves.

In the two-layer asymmetric model, unlike the $2\frac{1}{2}$-layer version, only the asymmetry type $\bar{x}_1 = \bar{x}_2$ is possible (see Section 4.4.2). As Eqs. (4.48)-(4.50) indicate, the $\bar{x}_1 \neq \bar{x}_2$ condition requires a two modal structure in the background PV field, which is not possible in M91's two-layer model.

In *Run a3* (Figure A.5), we consider $\theta = 0$ and $\bar{x}_i = 1.05$, which leads to southern coastal currents 80% stronger than the northern ones in both layers. As shown in Figure A.6, the retroflection bulge gets extremely elongated, but no eddies pinch off from it within the time range of *Run a2*. The dipole will be shed at $t > 100$

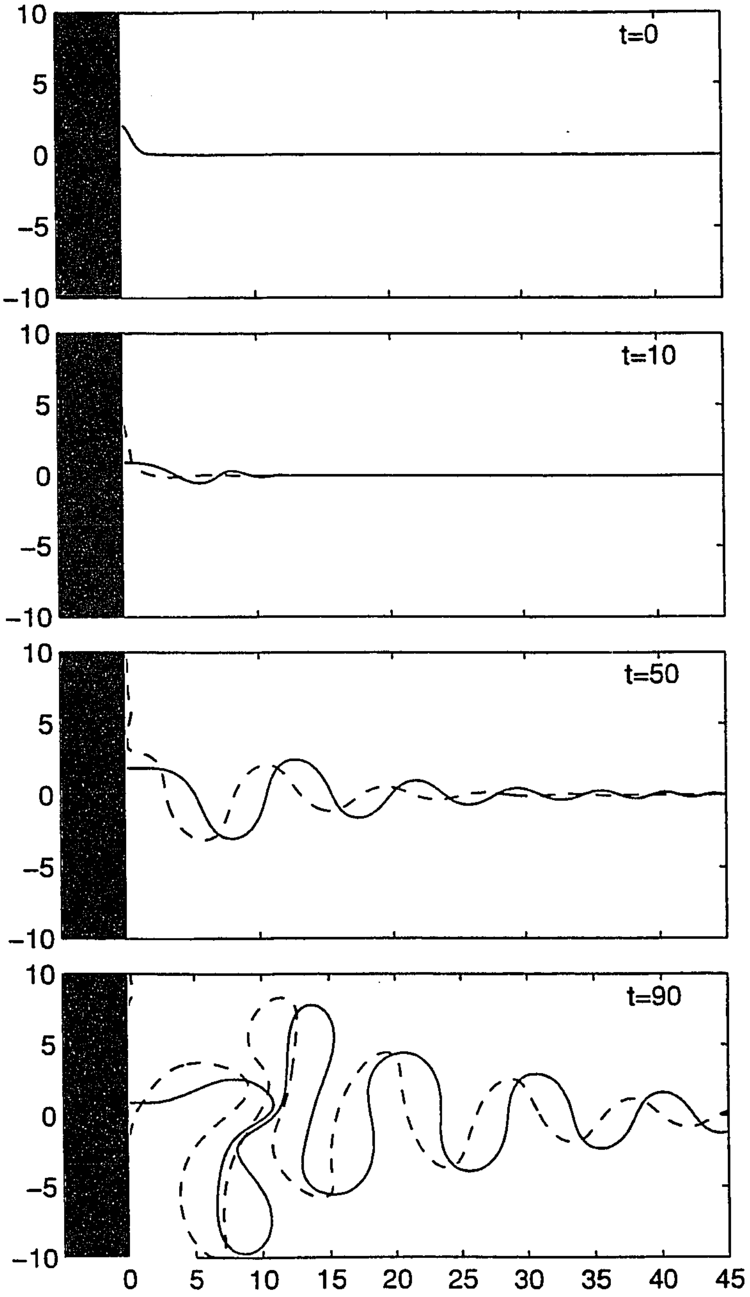

Figure A.3: *Run a1*: (a) t=10, (b) t=20, (c) t=50 and (d) t=90.

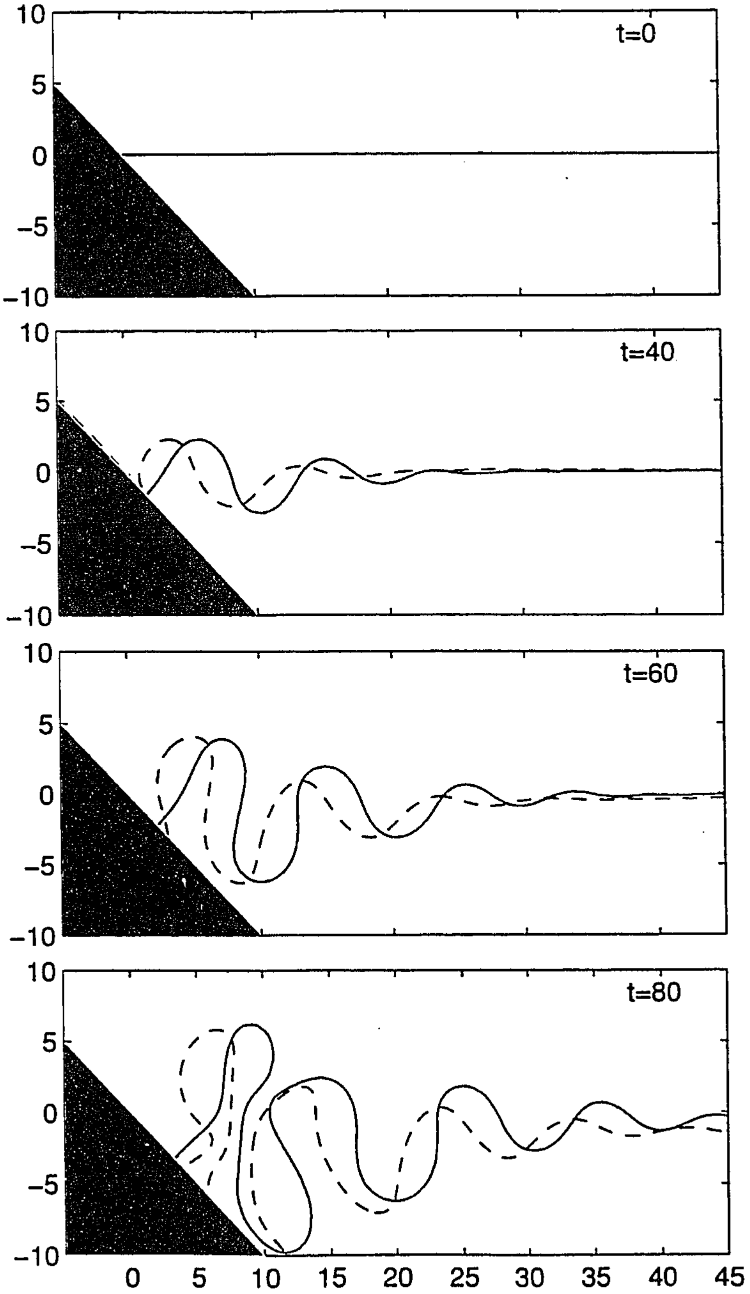

Figure A.4: *Run a2*: (a) t=0, (b) t=40, (c) t=60, and (d) t=80.

(not shown). The reason for such a result is not clear to us. We expected that the combination of meander growth due to baroclinic instability and asymmetry would develop a pattern similar to the one in Figures 4.22-4.23, in the time range of *Run a2*.

On the other hand, when the linear growths due to asymmetry ($\bar{x}_i = 1.05$) and tilt ($\theta = \pi/4$) combine with the exponential growth due to baroclinic instability in *Run a4* (Figure A.6), the whole retroflection bulge pinches off. This case apparently shows a more nonlinear wave pattern than the other cases. Even an upper layer small nondipolar eddy is shed downstream.

Except for *Run a4*, the two-layer separating jet experiments behaved very similarly to their $2\frac{1}{2}$-layer counterparts. A noticeable difference is the much larger wave patterns, which are consistent with the linear growth rate calculations displayed in Figure A.1a.

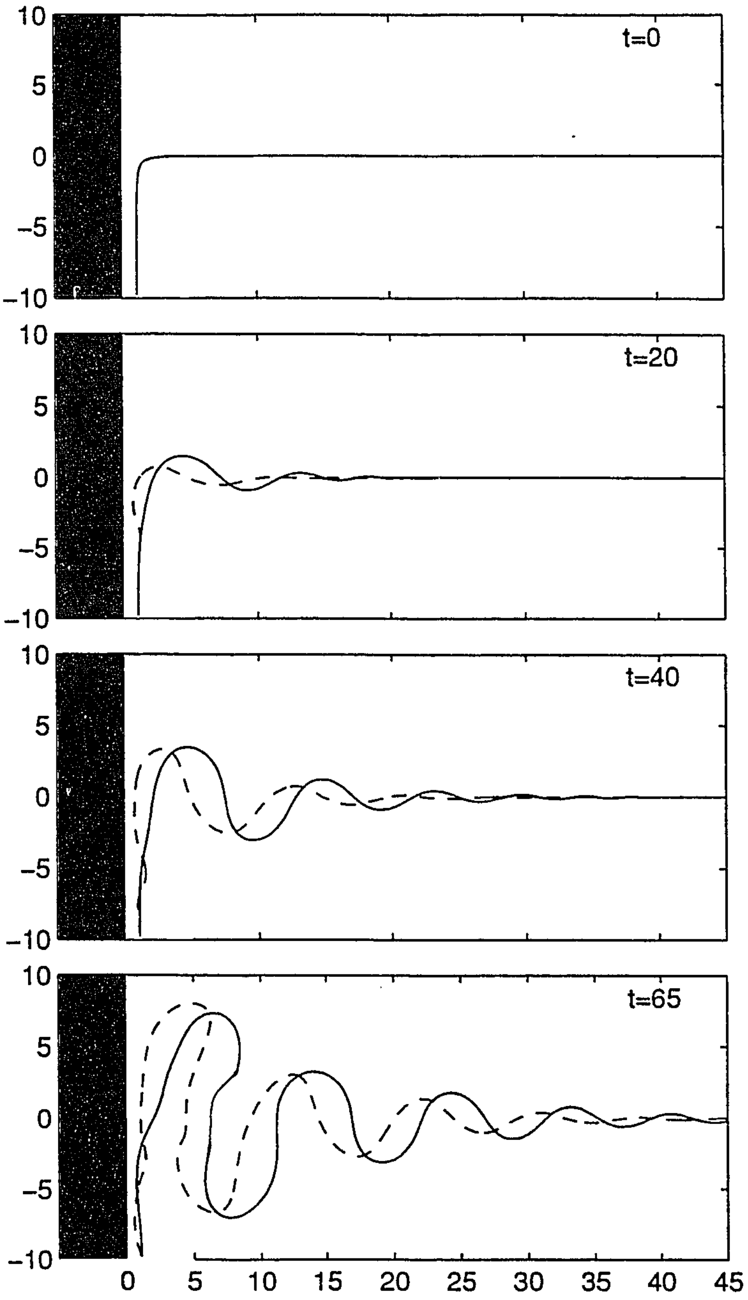

Figure A.5: *Run a3*: (a) t=0, (b) t=20, (c) t=40, and (d) t=100.

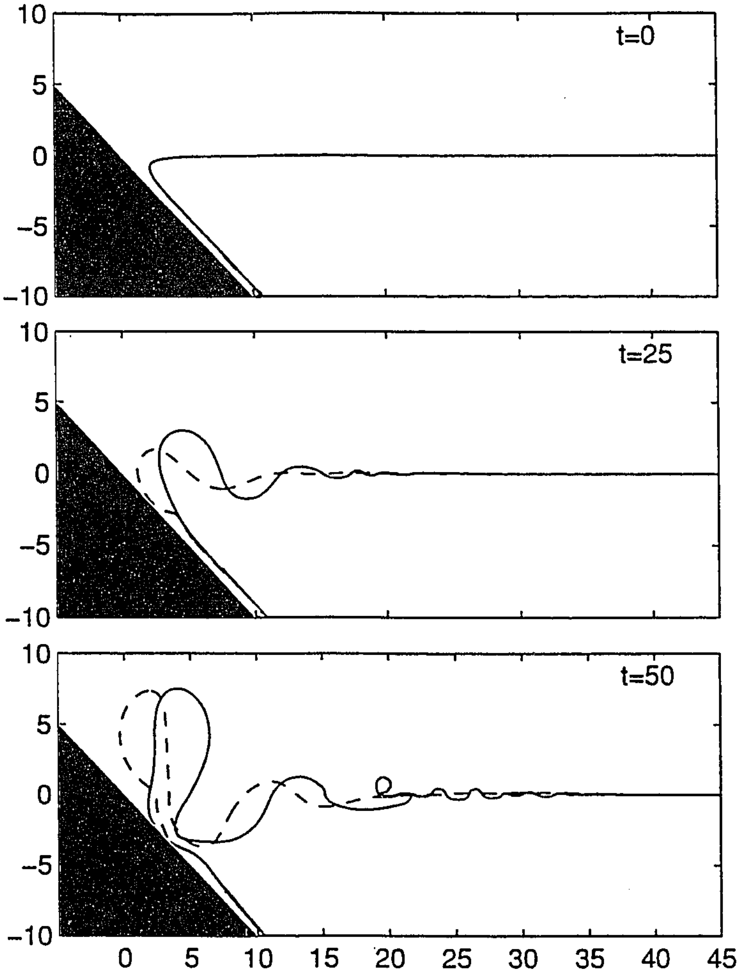

Figure A.6: *Run a4*: (a) t=0, (b) t=40, and (c) t=50.

References

Dritschel, D. G., Contour surgery: a topological reconnection scheme for extended integrations using contour dynamics, *J. Comput. Phys., 77*, 240:266, 1988.

Dritschel, D. G., Contour dynamics and contour surgery: numerical algorithms extended high-resolution modeling of vortex dynamics in two-dimensional, inviscid, incompressible flows, *Comput. Phys. Rep., 10*, 79-146, 1989.

Dritschel, D. G., and B. Legras, Modeling oceanic and atmospheric vortices, *Physics Today*, March issue, 44-51, 1993.

Farrell, B. F., Pulse Asymptotics of the Charney Baroclinic Instability Problem, *J. Atmos. Sci., 39*, 507-517, 1982.

Flierl, G. R., Models of vertical structure and the calibration of the of two-layer models, *Dynam. Atmos. Oceans, 2*, 341-381, 1978.

Flierl, G. R., and S. P. Meacham, Instabilities and waves on thin jets, (submitted to *J. Phys. Oceanogr.*)

Griffa, A. and M. A. Virasoro, A variational approach to a model for the Gulf Stream Rings, *Geophys. Astrophys. Fluid Dynamics, 42,* 115-150, 1988.

Houry, S., E. Dombrowsky, P. De Mey, and J. F. Minster, Brunt-Vaisala frequency and Rossby radii in the South Atlantic, *J. Phys. Oceanogr., 17,* 1619-1626, 1987.

Meacham, S.P., Meander evolution on quasigeostrophic jets, *J. Phys. Oceanogr., 21,* 1139-1170, 1991.

Pedlosky, J., Geophysical Fluid Dynamics, Springer-Verlag, 624 pp, 1979.

Polvani, L. M., Geostrophic vortex dynamics, PhD thesis, MIT/WHOI Joint Program, WHOI-88-48, 221p., 1988.

Polvani, L. M., N. J. Zabusky, and G. R. Flierl, Two-layer geostrophic vortex dynamics Part 1. upper-layer V-states and merger, *J. Fluid. Mech., 205,*, 215-242, 1989.

Pratt, L. J., Meandering and eddy detachment according to a simple (looking) path equation, *J. Phys. Oceanogr., 18,*, 1627-1640, 1988.

Pratt, L.J., and M. E. Stern, Dynamics of potential vorticity fronts and eddy detachment, *J. Phys. Oceanogr., 16,*, 1101-1120, 1986.

Pratt, L.J., J. Earles, P. Cornillon, and J. F. Cayula, The nonlinear behavior of varicose disturbances in a simple model of the Gulf Stream, *Deep-Sea Res. I, 38,* S591-S622, 1991.

Pullin, D. J., Contour Dynamics method, *Annu. Rev. Fluid Mech., 24,*, 89-115, 1992.

Silveira, I. C. da, G. R. Flierl, W.S. Brown, Dynamics of separating western boundary currents, (submitted to *J. Phys. Oceanogr.*)

Stern, M. E., Lateral wave breaking and "shingle" formation in large-scale shear flow, *J. Phys. Oceanogr., 15*, 1274-1283, 1985.

Stern, M. E., and L. J. Pratt, Dynamics of vorticity fronts, *J. Fluid. Mech., 161,* 513-532, 1985.

Stern, M. E., and G. R. Flierl, On the interaction of a vortex with a shear flow, *J. Geophys. Res., 92*, 10733-10744, 1987.

Wang, X, Interaction of an eddy with a continental slope, PhD thesis, MIT/WHOI Joint Program, WHOI-92-40, 216 pp, 1992.

Wu, H. M., E. A. Overman, and N. J. Zabusky, Steady state solutions of the Euler equation in two dimensions. Rotating and translating v-states with limiting cases. I. Numerical results, *J. Comput. Phys., 53,* 42-71, 1984.

Yano, J.-I., and G. R. Flierl, Isolated potential vorticity patches in quasi-geostrophic zonal shear flows, *Dynam. Atmos. Oceans, 16*, 439-472, 1992.

Zou, Q., E. A. Overman, H. M. Wu, and N. J. Zabusky, Contour dynamics for the Euler equations: curvature controlled initial node displacement and accuracy, *J. Comput. Phys., 78,* 350-372, 1988.

Complete List of References

Agra, C., and D. Nof, Collision and separation of boundary currents, *Deep-Sea Res. I, 40,* 2259-2282, 1993.

Arnault, S., Tropical Atlantic geostrophic currents and ship drifts, *J. Geophys. Res., 92(C5)*, 5076-5088, 1987.

Arnol'd, V.I., On the a priori estimate in the theory of hydrodynamical instability, *Isv, Vyssh Uchebn. Zaved. Mat., 54(5)*, 3-5, 1966.

Bell, G. I., and L. J. Pratt, Eddy-jet interaction theorems of piecewise constant potential vorticity flows, *Dyn. Atmos. Oceans, 20,*, 285-314, 1994.

Bretherton, F.P., R.E. Davis and C.B. Fandry, A technique for objective analysis and design of oceanographic experiments applied to MODE-73, *Deep-Sea Res., 23*, 559-582, 1976.

Brown, W.S., W.E. Johns, K.D. Leaman, J.P. McCreary, R.L. Molinari, P.L. Richardson and Rooth, C., A western tropical Atlantic experiment (WESTRAX), *Oceanography 5(1)*, 73-77, 1992.

Bruce, J.G., Comparison of eddies off the North Brazilian and Somali Coasts, *J.Phys.Oceanogr., 14*, 825-832, 1984.

Bruce, J.G. and J.L. Kerling, Near equatorial eddies in North Atlantic. *Geophys. Res. Lett., 11(8)*, 779-782, 1984.

Bub, F.L. and W.S. Brown, Intermediate layer water masses in the Western Tropical Atlantic Ocean, *accepted for publication in J. Geophys. Res.*, 1996.

Bub, F.L. and W.S. Brown, Seasonal changes in the intermediate layer transport of mass and heat in the western tropical Atlantic Ocean, *submitted to J. Geophys. Res.*, 1996.

Campos, E.J.D., and D.B. Olson, stationary Rossby waves in western boundary current extensions, *J. Phys. Oceanogr., 21,* 1202-1224, 1991.

Carter, E.F. and A.R. Robinson, Analysis models for the estimation of oceanic fields, *J.Atm.Oc.Tech., 4(1)*, 49-74, 1987.

Cessi, P., Laminar separation of colliding western boundary currents, *J. Mar. Res., 49*, 697-717, 1991.

Cornillon, P., The effect of the New England seamounts on the Gulf Stream meandering as observed form satellite IR imagery, *J. Phys. Oceanogr., 16,* 386-389, 1986.

Cochrane, J.D., F.J. Kelly and C.R. Olling, Subthermocline countercurrents in the western equatorial Atlantic Ocean. *J.Phys.Oceanogr., 9*, 724-738, 1979.

Davis, C.A. and K.A. Emanuel, Potential vorticity diagnostics of cyclogenesis, *Mon. Wea. Rev., 119 (8),* 1929-1953, 1991.

Davis, R.E., Predictability of sea surface temperature and sea level pressure anomalies over the North Pacific Ocean, *J.Phys.Oceanogr., 6(3)*, 249-266.

Didden, N, and F. Schott, Seasonal variations in the western tropical Atlantic: surface circulation from Geosat altimetry and WOCE model Results, *J. Geophys. Res., 97(C3)*, 3529-3541, 1992.

Didden, N, and F. Schott, Eddies in the North Brazil Current retroflection region observed by Geosat altimetry, *J. Geophys. Res., 98*, 20121-02131, 1993.

Dritschel, D.G., Contour surgery: a topological reconnection scheme for extended integrations using contour dynamics, *J. Comput. Phys., 77*, 240:266, 1989.

Dritschel, D.G., Contour dynamics and contour surgery: numerical algorithms extended high-resolution modeling of vortex dynamics in two-dimensional, inviscid, incompressible flows, *Comput. Phys. Rep., 10*, 79-146, 1988.

Dritschel, D.G., and B. Legras, Modeling oceanic and atmospheric vortices, *Physics Today*, March issue, 44-51, 1993.

Farrell, B.F., Pulse Asymptotics of the Charney Baroclinic Instability Problem, *J. Atmos. Sci., 39*, 507-517, 1982.

Flierl, G.R., Models of vertical structure and the calibration of two-layer models, *Dyn. Atm. Oceans., 2*, 341-381, 1978.

Flierl, G.R., and S.P. Meacham, Instabilities and waves on thin jets, (submitted to *J. Phys. Oceanogr.*)

Fratantoni, D.M., W.E. Johns and T.L. Townsend, Rings of the North Brazil Currents: Their structure and behavior inferred from observations and a numerical simulation, *J. Geophys. Res., 100(C6)*, 10633-10654, 1995.

Garzoli, S.L. and Z. Garrafo, Transports, frontal motions and eddies at the Brazil-Malvinas currents confluence, *Deep-Sea Res., 36(5),* 681-702, 1989.

Gill, A.E., Atmosphere-ocean dynamics, *Academic Press*, 652 pp., 1982.

Gordon, A.L., Brazil-Malvinas Confluence–1984, *Deep-Sea Res., 36(3),* 359-384, 1989.

Gordon, A.L., and C.L. Greengrove, Geostrophic circulation of the Brazil-Falkland confluence, *Deep-Sea Res. I, 33,* 573-585, 1986.

Griffa, A. and M.A. Virasoro, A variational approach to a model for the Gulf Stream Rings, *Geophys. Astrophys. Fluid Dynamics, 42,* 115-150, 1988.

Hall, M.M., Horizontal and vertical structure of velocity, potential vorticity and energy in Gulf Stream, Ph.D. thesis, WHOI/MIT Joint Program in Oceanography, WHOI-85-16, 165pp, 1985.

Hall, M.M., and N.P. Fofonoff, Downstream development of the Gulf Stream from 68° to 55° W, *J. Phys. Oceanogr.*, 23, 225-249, 1993.

Hoskins, B.J., M.E. McIntyre, and A. W. Roberson, On the use and significance of isentropic potential vorticity maps, *Quart. J. R. Met. Soc., 111,* 877-946, 1985.

Houry, S., E. Dombrowsky, P. De Mey, and J.F. Minster, Brunt-Vaisala frequency and Rossby radii in the South Atlantic, *J. Phys. Oceanogr., 17,* 1619-1626, 1987.

Hua, B.L., McWilliams, J.C., and Owens, W.B., An objective analysis of the POLYMODE local dynamics experiment. Part II: stream function and potential vorticity fields during the Intensive Period, *J.Phys.Oceanogr., 16*, 506-522.

Johns, W.E., T.N. Lee, F. Schott, R. Zantopp and R.H. Evans, The North Brazil Current retroflection: seasonal structure and Eddy Variability, *J. Phys. Oceanogr., 95 (C12)*, 22103-22120, 1990.

Klinck, J.M., EOF analysis of central Drake Passage currents from DRAKE 79, *J.Phys.Oceanogr., 15*, 288-298, 1984.

McClean, J.L. and J.M. Klinck, Description and Vorticity Analysis of the 50-day Oscillations in the Western Tropical Atlantic Region of the CME Model, *J. Phys. Oceanogr., 25*, 2498-2517.

Meacham, S.P., Meander evolution on quasigeostrophic jets, *J. Phys. Oceanogr., 21,* 1139-1170, 1991.

Molinari, R.L., B. Voituriez and P. Ducan, Observations in the subthermocline undercurrent of the equatorial South Atlantic Ocean: 1978-1980, *Oceanologica Acta, 4(4)*, 451-456, 1981.

Olson, D., G. Podesta, R. Evans and O. Brown, Temporal variations in the separation of Brazil and Malvinas currents, *Deep-Sea Res., 35,* 1971-1980, 1988.

Ou, H.W., and W.P.M. De Ruijter, Separation of an inertial boundary current from a curved coastline, *J. Phys. Oceanogr., 16,* 280-289, 1986.

Pedlosky, J., Geophysical Fluid Dynamics, Springer-Verlag, 624 pp, 1979.

Pinardi, N and A.R. Robinson, Dynamics of deep thermocline jets in the POLYMODE region, *J.Phys.Oceanogr., 17(8)*, 1163-1188.

Polvani, L.M., Geostrophic vortex dynamics, PhD thesis, MIT/WHOI Joint Program, WHOI-88-48, 221p., 1988.

Polvani, L.M., N.J. Zabusky, and G.R. Flierl, Two-layer geostrophic vortex dynamics Part 1. upper-layer V-states and merger, *J. Fluid. Mech., 205,*, 215-242, 1989.

Pratt, L.J., Meandering and eddy detachment according to a simple (looking) path equation, *J. Phys. Oceanogr., 18,*, 1627-1640, 1988.

Pratt, L.J., and M.E. Stern, Dynamics of potential vorticity fronts and eddy detachment, *J. Phys. Oceanogr., 16,*, 1101-1120, 1986.

Pratt, L.J., J. Earles, P. Cornillon, and J. F. Cayula, The nonlinear behavior of varicose disturbances in a simple model of the Gulf Stream, *Deep-Sea Res. I, 38,* S591-S622, 1991.

Pullin, D.J., Contour Dynamics method, *Annu. Rev. Fluid Mech., 24,*, 89-115, 1992.

Richardson, P.L., Gulf Stream ring trajectories, *J. Phys. Oceanogr., 10,* 90-104, 1980.

Richardson, P.L., Tracking Ocean Eddies, *American Scientist, 81*, 261-271, 1993.

Richardson, P.L. and T.K. McKee, Average seasonal variation of the Atlantic equatorial currents from historical ship drifts, *J.Phys.Oceanogr., 14(7)*, 1226-1238, 1984.

Richardson, P.L., and G. Reverdin, Seasonal cycle of velocity in the Atlantic North Equatorial Countercurrent as measured by surface drifters, current meters, and ship drifts, *J. Geophys. Res., 92,* 3691-3708, 1986.

Richardson, P.L., G.E. Hufford, R. Limeburner, and W.S. Brown, North Brazil Current retroflection eddies, *J. Geophys. Res., 99 (C3),* 5081-5093, 1994.

Schmitz, W.J. and M.S. McCartney, On the North Atlantic circulation, *Rev. Geophys., 31,*, 29-49, 1993.

Schott, F., and C.W. Böning, The WOCE model in the western equatorial Atlantic: upper layer circulation, *J. Geophys. Res., 96(C4)*, 6993-7004, 1991.

Silveira, I.C.A. da, W.S. Brown and Flierl, G.R., A Quasi-geostrophic study of the North Brazil Current retroflection eddies (abstract), *EOS Trans. AGU, 75(3),* Ocean Sciences Meeting Suppl., 225, 1994.

Silveira, I.C.A da, G.R. Flierl, W.S. Brown, Dynamics of separating western boundary currents, (submitted to *J. Phys. Oceanogr.*)

Silveira, I.C.A. da, and Flierl, G.R., Eddy formation in $2\frac{1}{2}$-layer, quasi-geostrophic jets (in preparation)

Springer, S.R. and M. Kawase, Nonlinear and dissipative dynamics in the connection region between western boundary currents and equatorial currents, *J. Geophys. Res., 98*, 12511-12525, 1993.

Stern, M. E., Lateral wave breaking and "shingle" formation in large-scale shear flow, *J. Phys. Oceanogr., 15*, 1274-1283, 1985.

Stern, M. E., and L. J. Pratt, Dynamics of vorticity fronts, *J. Fluid. Mech., 161,* 513-532, 1985.

Stern, M. E., and G. R. Flierl, On the interaction of a vortex with a shear flow, *J. Geophys. Res., 92*, 10733-10744, 1987.

Stramma, L., and R. G. Peterson, The South Atlantic current, *J. Phys. Oceanogr., 20,* 846-859, 1990.

Tracey, K. L., and D. R. Watts, On the Gulf Stream characteristics near Cape Hatteras, *J. Geophys. Res., 91,* 7587-7602, 1986.

Wang, X, Interaction of an eddy with a continental slope, PhD thesis, MIT/WHOI Joint Program, WHOI-92-40, 216 pp, 1992.

Wu, H.M., E.A. Overman, and N.J. Zabusky, Steady state solutions of the Euler equation in two dimensions. Rotating and translating v-states with limiting cases. I. Numerical results, *J. Comput. Phys., 53,* 42-71, 1984.

Yano, J.-I., and G. R. Flierl, Isolated potential vorticity patches in quasi-geostrophic zonal shear flows, *Dynam. Atmos. Oceans, 16*, 439-472, 1992.

Young, W.R., Baroclinic theories of the wind driven circulation, in *General circulation of the ocean*, pp.134-200, H.D.I. Abarbanel and W.R.Young, Springer-Verlag, 1987.

Zou, Q., E.A. Overman, H.M. Wu, and N.J. Zabusky, Contour dynamics for the Euler equations: curvature controlled initial node displacement and accuracy, *J. Comput. Phys.*, *78*, 350-372, 1988.